ROYAUME DU MAROC
Université Mohammed V - RABAT -
جامعة محمد الخامس – الرباط –
Faculté des sciences
كلية العلوم
CENTRE D'ÉTUDES DOCTORALES - SCIENCES ET TECHNOLOGIES

N°d'ordre : 3926

THÈSE

*en vue de l'obtention du :***DOCTORAT**

Structure de Recherche : Équipe de Physique des Hautes Énergie-Modélisation et Simulation

Discipline : Physique

Spécialité : Physique des Matériaux et Énergies Renouvelables

Présentée et Soutenue le : *01 / 06 / 2024*

par :

Salma LAGHZAOUI

First-principles study of the electronic, magnetic, optical, and thermoelectric properties of $Sn_{1-2x}Mn_xA_xO_2$ (A=Mo/Tc), Double Perovskites, and $Zn_{1-x}TM_xO$ Nanosheets: Promising half-metallic materials for energy conversion

JURY

Mohammed GAROUM	PES	Ecole Normale Supérieure, Université Mohammed V - Rabat	Président
El Houssaine EL RHALEB	PES	Faculté des Sciences, Université Mohammed V - Rabat	Examinateur/Rapporteur
Abdelmajid EL MANSOURI	PH	Institut Supérieur des Métiers de l'Audiovisuel et du Cinéma - Rabat	Examinateur/Rapporteur
Lalla Btissam DRISSI	PES	Faculté des Sciences, Université Mohammed V - Rabat	Examinateur/Rapporteur
Rachid MASROUR	PES	Faculté des Sciences, Université Sidi Mohamed Ben Abdellah - Fès	Examinateur/Rapporteur
Hamid SAUFI	PH	Ecole Normale Supérieure, Université Mohammed V - Rabat	Examinateur
Rachid AHL LAAMARA	PES	Faculté des Sciences, Université Mohammed V - Rabat	Co-Directeur de thèse
Abdelmajid FAKHIM LAMRANI	PH	Ecole Normale Supérieure, Université Mohammed V – Rabat	Directeur de thèse

Année Universitaire : 2023 - 2024

Dedications

I dedicate this thesis,

To one of the finest ladies I have ever met, my mom **Rachida SAMRAOUY**, who has never ceased to believe in me and has given me support, love, and understanding.

To my deceased father **Souilem LAGHZAOUI**, I hope you are proud of me.

Remerciements

Tout d'abord, je remercie le Dieu tout-puissant de m'avoir donné la volonté d'accomplir ce travail, le courage, ainsi que l'audace pour dépasser toutes les difficultés.

Le travail présenté dans cette thèse a été réalisé au sein du Laboratoire de Physique des Hautes Energies-Modélisation et Simulation (LPHE-MS), Faculté des sciences de l'Université Mohammed V à Rabat, sous la direction de Monsieur **Rachid AHL LAAMARA**, Professeur d'Enseignement Supérieur à la Faculté des Sciences de l'Université Mohammed V à Rabat.

Je souhaite exprimer ma gratitude envers mon directeur de thèse Monsieur **Abdelmajid FAKHIM LAMRANI**, Professeur d'Habilité à l'École Normale Supérieure de Rabat, qui m'a proposé cette thèse et qui m'a guidé tout au long de ce travail. Je le remercie pour sa rigueur scientifique, sa disponibilité et sa volonté de partager son expérience ainsi que ses connaissances avec moi.

Je souhaite également exprimer ma reconnaissance envers mon co-directeur de thèse Monsieur **Rachid AHL LAAMARA**, Professeur d'Enseignement Supérieur à la Faculté des Sciences de l'Université Mohammed V à Rabat, pour sa précieuse attention et son soutien. Je lui exprime ma plus chaleureuse gratitude pour ses précieux conseils.

Je souhaite exprimer ma gratitude envers Monsieur **Mohammed GAROUM**, Professeur d'Enseignement Supérieur à l'École Normale Supérieure de Rabat, pour avoir accepté de présider le jury. Je vous prie, Monsieur, d'accepter l'expression de mon respect et de ma profonde gratitude.

Je tiens à exprimer mes sincères remerciements à Monsieur **El Houssaine EL RHALEB**, Professeur d'Enseignement Supérieur à la Faculté des Sciences de l'Université Mohammed V à Rabat, pour avoir accepté d'assumer le rôle de rapporteur pour cette thèse. Je suis profondément reconnaissant de l'honneur qu'il m'a accordé en acceptant de participer à ce jury malgré ses engagements professionnels.

Je tiens également à exprimer ma gratitude envers Monsieur **Abdelmajid EL MANSOURI**, Professeur d'Habilité à l'Institut Supérieur des Métiers de l'Audiovisuel et du Cinéma à Rabat, pour avoir accepté d'assumer le rôle de rapporteur pour cette thèse. C'est pour moi un grand honneur d'avoir pu bénéficier de sa participation au sein de mon jury de soutenance.

J'exprime toute ma reconnaissance à Madame **LALLA Btissam DRISSI**, Professeur d'Enseignement Supérieur à la Faculté des Sciences de l'Université Mohammed V à Rabat, pour sa participation exceptionnelle dans l'avancement de cette thèse. Je tiens également

à la remercier chaleureusement pour son rôle en tant que rapporteur et examinateur de ce travail.

Je tiens à vous exprimer ma plus sincère gratitude à Monsieur **Rachid MASROUR**, Professeur d'Enseignement Supérieur à la Faculté des Sciences Dhar El Mahraz de l'Université Sidi Mohamed Ben Abdellah à Fès, pour avoir accepté de participer en tant que rapporteur de cette thèse. Votre expertise et votre dévouement ont grandement contribué à la réussite de ce travail de doctorat.

Je remercie vivement et chaleureusement Monsieur **Hamid SAUFI**, Professeur d'Habilité à l'École Normale Supérieure de Rabat, d'avoir bien voulu examiner ce travail et de faire partie du jury. Je lui exprime toute ma reconnaissance pour l'intérêt porté à ce travail.

Je suis reconnaissant envers toutes les personnes qui m'ont apporté leur aide, que ce soit de manière directe ou indirecte, tout au long de ce travail. Je tiens particulièrement à exprimer ma gratitude envers ma mère, qui m'a encouragé et soutenu sans relâche.

MERCI à tous...

Résumé

Cette thèse présente une étude modélisatrice de l'effet du dopage par des impuretés magnétiques simples et doubles sur les propriétés électroniques, magnéto-optiques, et thermoélectriques des matériaux: $Sn_{1-2x}Mn_xA_xO_2$, doubles pérovskites, et $Zn_{1-x}TM_xO$ nanofeuilles. Nous avons utilisé une méthode construite au sein de la théorie de la fonctionnelle densité (DFT) dite, FP-LAPW. En effet, nos travaux de recherche s'articulent autour des alliages demi-métalliques ayant des applications dans le domaine spintronique ainsi que dans le domaine des énergies renouvelables, et particulièrement du type photovoltaïque et thermoélectrique. Plusieurs approches ont été utilisées pour définir le potentiel d'échange et de corrélation, notamment GGA, GGA+U, TB-mBJ, YS-PBE0 et GGA+SOC. L'une des principales propriétés de nos résultats, que ce soit dans le bulk ou dans la nanofeuille, est la « demi-métallicité », où les électrons de conduction sont polarisés à 100% en spin en raison d'un écart étroit au niveau de Fermi. Selon nos résultats, les composés demi-métalliques sont capables d'absorber le maximum de lumière visible. En outre, les propriétés de transport en fonction de la température et du potentiel chimique garantissent une excellente conductivité électrique, une faible conductivité thermique et une meilleure figure de mérite (ZT), ce qui conduit à des performances thermoélectriques plus élevées. Cela nous pousse à prédire que ces alliages ont tout le pouvoir d'effectuer la conversion photovoltaïque à haute efficacité dans les cellules solaires.

Mots-clés: Demi-métallique ferromagnétique et Antiferromagnétique, structure 3D et les nanofeuilles 2D, Spintronique, conversion photovoltaïque, propriétés thermoélectriques.

Abstract

This thesis presents a modeling study of the effect of doping by single and double magnetic impurities on the electronic, magneto-optical, and thermoelectric properties of materials: $Sn_{1-2x}Mn_xA_xO_2$ (A=Mo/Tc), double perovskites, and $Zn_{1-x}TM_xO$ nanosheets. We used a method built within density functional theory (DFT) called FP-LAPW. Indeed, our work focuses on half-metallic alloys with applications in the spintronic domain as well as in the field of renewable energies, particularly of the photovoltaic and thermoelectric types. Several approaches have been used to define exchange and correlation potential, including GGA, GGA+U, TB-mBJ, YS-PBE0, and GGA+SOC. One of the main properties of our results, whether in the bulk or nanosheet, is "half-metallicity", where the conduction electrons are 100% spin polarization due to a narrow gap at the Fermi level. According to our results, half-metallic compounds are able to absorb the maximum amount of visible light. Furthermore, the transport properties as a function of the temperature and the chemical potential ensure excellent electrical conductivity, low thermal conductivity, and better figure of merit (ZT), which leads to higher thermoelectric performance. This leads us to predict that these alloys have the power to perform the high-efficiency photovoltaic conversion in solar cells.

Keywords : Half-metallic ferromagnet and Antiferromagnet, 3D structure and 2D nanosheets, Spintronics, photovoltaic conversion, thermoelectric properties.

List of Publications

1. S. Laghzaoui, A. Fakhim Lamrani, R. Ahl Laamara, E. Maskar, Botir Qonishevich Tuxtamishev, Amel Laref, and D. P. Rai, Electronic, magnetic, optical and thermoelectric properties of co-doped $Sn_{1-2x}Mn_xA_xO_2$ (A=Mo, Tc): a first principles insight, RSC Advances 12 (2022) 28451.
https://doi.org/10.1039/D2RA04499D

2. S. Laghzaoui, A. Fakhim Lamrani, R. Ahl Laamara, E. Maskar, Amel Laref, Mohammed Ezzeldien, and D. P. Rai, Realization of half-metal antiferromagnetic (HM-AFM) behaviour in double perovskite Sr_2CrReO_6 on substitution of Tc at Cr site: Promising material for optoelectronics and thermoelectric applications via DFT framework, Inorganic Chemistry Communications 146 (2022) 110172.
https://doi.org/10.1016/j.inoche.2022.110172

3. S. Laghzaoui, A. Fakhim Lamrani, R. Ahl Laamara, E. Maskar, Amel Laref, Mattipally Prasad, J. Sivakumar, and D. P. Rai, Study of electronic, magneto-optical and transport properties of double perovskite Ca_2XMnO_6 (X = Ti, Cr) under uniaxial compressive strain by using a DFT method, Modern Physics Letters B 37 (2023) 2350026.
https://doi.org/10.1142/S0217984923500264

4. S. Laghzaoui, A. Fakhim Lamrani, R. Ahl Laamara, Robust half-metallic ferromagnet in doped double perovskite Sr_2TiCoO_6 by rare-earth elements for photovoltaic and thermoelectric conversion: A DFT method, Journal of Physics and Chemistry of Solids 183 (2023) 111639.
https://doi.org/10.1016/j.jpcs.2023.111639

5. S. Laghzaoui, A. Fakhim Lamrani, R. Ahl Laamara, Excellent optical and thermoelectric features of two-dimensional half-metallic ferromagnet $Zn_{1-x}TM_xO$: A first principle investigation, Physica B: Condensed Matter 668 (2023) 415241.
https://doi.org/10.1016/j.physb.2023.415241

Abbreviations list

DFT: Density Functional Theory

FM: Ferromagnetic

AFM: Antiferromagnetic

HM: Half-Metallic

DMS: Diluted Magnetic Semiconductors

HF: Hartree-Fock

LDA: Local Density Approximation

GGA: Generalized Gradient Approximation

GGA+U: Generalized Gradient Approximation with Hubbard correction

TB-mBJ: Tran-Blaha modified Becke Johnson Potential

SOC: Spin Orbit Coupling

APW: Augmented Plane Wave

FP-LAPW: Full Potential-Linearized Augmented Plane Wave

RKKY coupling: Ruderman-Kittel-Kasuya-Yoshida coupling

MT: Muffin-Tin

RMT: Muffin-Tin Radius

DOS: Density of States

TDOS: Total Density of States

PDOS: Partial Density of States

TM: Transition Metals

BC: Conduction Band

BV: Valence Band

List of Figures

List of Tables

Contents

General Introduction

General context

The study of and use of the characteristics of matter is the focus of the multidisciplinary area of materials science. It involves establishing a link between the desirable features and the comparative effectiveness of a material in a particular application. Recent years have seen a concentration of research in novel fields, including nanotechnology, electronics, optics, and thermoelectric systems, which requires an in-depth investigation of the diverse range of material classes. Particle, atom, and molecular behavior are explained at the microscopic level by quantum physics theory. This theory made it possible to theoretically describe the physical properties of matter depending on the laws that govern the interactions of particles. The Hamiltonian of the system describes these interactions. To obtain a deeper comprehension of the origin of the physical, magnetic, electronic, optical, and thermoelectric characteristics of materials in general, we must employ accurate and efficient computations for a complex system with high correlation. However, the Schrödinger equation cannot be solved analytically, except in basic situations such as the hydrogen atom. For this reason, we need to use theoretical approximations to have more exact properties close to reality. Theoretically, density functional theory, which makes it possible to quantify the ground state energy and electron density of the substance, may explain electron behavior and the atoms that make up condensed matter. Pierre Hohenberg [1], Walter Kohn, and Lu Sham [2] developed the equations that form the basis of this theory in 1960. The FP-LAPW approach (Full Potential-Linearized Augmented Plane Wave), adopted in the Wien2K code, is among the more precise for determining the electronic property of condensed matter in a ground state.

In recent decades, scientific research into novel materials at the nanotechnology scale has led to a significant modernization of daily life due to technological advancements. For decades, the electron charge was the only factor considered when calculating the physical properties. Recently, the electron spin is a second fundamental property. It is the angular momentum associated with the electric charge. This new characteristic is used to data storage, a long-standing application for ferromagnetic materials. Electron spin has grown as bit density on hard drives has increased. The first spintronics products

to be commercially successful were giant magnetoresistance (GMR) read heads. For the finding of the GMR effect [3, 4], 2007 saw the Nobel Prizes awarded to P. Grünberg and A. Fert. Recalling this achievement is crucial since it was the first to employ electron spin polarization with charge transport in electronics. When an external excitation, such as the magnetic field, is introduced to a device, it uses the quantum effect of electron spin to control the magnetization orientation. This influence first appeared by Motte in 1936. Both experimental and theoretical evidence demonstrated this fact towards the end of 1960. A technological advancement called tunnel magnetoresistance (TMR) has improved the functionality of modern hard disk systems [5, 6]. Since TMR is the foundation for all modern hard drive read heads, this new branch has already had a significant influence. Using materials with high polarization maximizes tunnel magnetoresistance (TMR). Magnetic Random Access Memories (MRAM) also make use of this effect. At present, Spin Electronics is searching for novel materials to address several technological issues that limit the development of new products. The most promising substances for creating significant-performance magnetic recording media with high densities of writing and reading are half-metallic ones. Potential uses in spintronics have drawn interest in ferromagnetic half-metals (HM-FM) [7].

In the field of spin electronics, integrating spinning devices with GMR or TMR in microelectronics is another crucial challenge. This integration is challenging due to the difference in electrical resistivity between metallic and semiconductor materials commonly used in microelectronics. A workaround for this issue would be to employ magnetic semiconductor materials instead of the typically used metallic ferromagnetic materials as ferromagnetic electrodes in TMR systems. The first suggested the notion of half-metallic ferromagnet in 1983 by De Groot et al. [8]. Doping a conventional wide-gap semiconductor, such as ZnO, SnO_2, TiO_2, etc., with transition metals (TM= Cr, Fe, Co, Ni...) is the easiest method of making a semiconductor magnetic. The fabrication of TiO_2 thin layers doped with Co that display ferromagnetism at ambient temperature in 2001 [9] represents the first significant breakthrough in the field from an experimental perspective. Also, in 2001, thin films of Co-doped ZnO that were ferromagnetic at room temperature were produced [10]. Dilute magnetic semiconductors (DMS) have higher curie temperatures because the dopant causes long-range magnetic order that passes via the carrier [11]. Finding room-temperature ferromagnetism in semiconductors doped with magnetic elements is a significant challenge for researchers engaged in this subject. Localized transition metal d electrons are the primary source of magnetic moment in half-metallic ferromagnetic HMF materials. Many studies on semiconductors with band gaps above 3eV, especially SnO_2 and ZnO, have been spurred by an investigation by Dietl et al. [12]. Wide band gap semiconductors have already generated much interest outside their potential use as DMS.

Furthermore, some double perovskite oxides exhibit half-metallic properties with 100% spin polarization conduction electrons. The existence of magnetoresistance, or more specifically, the TMR at room temperature, has been found in Sr_2FeMoO_6 by Kobayashi et al. [13], indicating potential uses in spin-based technologies, MRAM, and DRAM. Double perovskites have a relatively high curie temperature (Tc), which implies that conduction electrons are more spin-polarized. Among them, Sr_2CrReO_6 has a Curie temperature of Tc = 635K [14, 15]. These materials provide a fascinating option for spintronic uses.

Researchers have become increasingly interested in utilizing "renewable" resources that derive energy from the sun. Daily radiation from the sun gives the world a comparable amount of energy, thousands of times more than what humanity needs for all of its current activities. As a result, trying to profit from it is reasonable. Photovoltaic energy converts solar electromagnetic radiation to electricity, making it a renewable energy source. In a photovoltaic cell, sunlight is directly transformed into electric current by charge separation on a p-n junction employing a semiconductor material. This cell functions by using the characteristics of both radiation and semiconductors. Technological advancements can increase the efficiency of photovoltaic cells to meet growing energy demands. High light absorptions and extended diffusion dimensions, among other qualities, have also shown to be very helpful in solar cell development [16].

Thermoelectricity is also one of these new sources of renewable energy. Thermoelectric materials are exceptional because they can directly transform the thermal flow into electrical energy (Seebeck effect) and, in the other direction, an electric current into thermal flow (Peltier effect). Since thermoelectricity offers the opportunity to recycle energy lost as heat into electricity, its application appears especially prudent. As a result, research into lowering the price and increasing the efficiency of thermoelectric materials is crucial. There are two approaches to enhancing thermoelectric efficiency while reducing dependency on network thermal conductivity and electrical properties. One is to modify the electronic band gap to increase the electrical power factor (PF) [17]. The other option is to reduce thermal conductivity by adding defects (substitution, interstitial, vacancy) or phonon scattering centers in many dimensions. DMS and double perovskite materials have become recommended for TE uses because of their remarkable temperature stability and environmental friendliness.

The process of characterizing materials involves a multitude of metrics and qualities, with one of the key influencing factors for this process being the system dimensionality. The advent of novel technology increases the likelihood of discovering and producing new material types. The example of the first two-dimensional material ever synthesized in the laboratory is graphene in 2004 [18, 19, 20]. The possibility of creating 2D materials was

long thought to be unattainable. In that field, theorists like Landau and Peierls [21, 22] proposed that any two-dimensional crystal was thermodynamically unstable. Andre Geim and Kostya Novoselov of Manchester University successfully isolated a graphene sheet having a single layer of carbon atoms using the "Scotch tape" method after 2004 [23, 24]. 2010 saw this outcome win the Nobel Prize in Physics. Graphene is well-known due to its unique characteristics, which include a 0eV band gap, an unusual electrical band structure, and high transparency [25]. Nevertheless, the 0eV band gap of graphene restricts its use in optoelectronics. Future generations of nanoelectronics need to decrease the size of circuit parts without sacrificing quality. Using monoatomic thin layers of 2D materials and their fusion quality can more effectively control electrostatic conductivity. In addition, the charge carrier dispersion in 2D materials is less than in their bulk counterparts because there are fewer dangling bonds [26]. The decrease in dimensionality can cause a band gap opening due to the quantum confinement phenomenon [27, 28]. This result suggests that the two-dimensional material has considerable potential and remarkable chemical and physical capabilities. Zinc oxide (ZnO) nanosheets are one of the most transparent, non-toxic, and abundant 2D materials found in nature. Recent efforts have enabled the doping of ZnO nanosheets to produce half-metallic ferromagnetic behavior. According to Zheng et al. [29], ZnONS may take on a half-metallic appearance when nonmagnetic atoms are added, which makes them valuable for spintronics applications.

Objective of the thesis

The primary objective of the research work of this doctoral thesis is to realize half-metallic materials that can absorb as much solar light as possible, especially in the visible spectrum. These materials also can convert heat into electricity. This thesis presents a study by modeling and simulation of the magnetic, electronic, thermoelectric, and optical properties of SnO_2 co-doped with Mn and A=Mo/Tc, ZnO nanosheets doped by (Fe, Co, Ni, or Cu), and double perovskite oxides, using the methods of first principles so-called ab-initio which are among the most accredited simulation methods. Applying the FP-LAPW method, we treated the exchange-correlation potential via YS-PBE0, mBJ-GGA, GGA, GGA+SOC, and GGA+U approximations employing the Wien2k computation code. The ability of these methods to accurately and consistently provide results in modeling the electronic property in addition to the optical, thermoelectric, and magnetic characteristics of these materials has been proven. Doping with single or double impurities makes it possible to achieve half-metallic ferromagnetic behavior in our materials. The combination of spintronics and optoelectronics fields has yet to be fully explored and remains a stranded domain. Although ferromagnetic materials are not yet used to create solar cells, they may prove crucial in future generations as solar cell technology advances. To that end, we have examined how ferromagnetic behavior affects optical performance in sunlight, specifically

in the visible spectrum, and how it may be advantageous in photovoltaic applications within solar cells. In addition, this study sheds light on antiferromagnetic half-metallic Sr_2TcReO_6, which have remarkable properties such as the spin polarization of the carriers being 100% close Fermi level with a total magnetization equal to zero. These materials are desirable for manufacturing spin-polarized scanning tunneling microscopes. Indeed, they serve in the manufacture of local magnetic order probes without altering the total magnetic character of the system.

Structure of the thesis

We have organized this thesis into five chapters:

Chapter 1: Theoretical investigation: Concepts and Methodologies

The first chapter covers the basics of the Kohn-Sham equations, density functional theory (DFT), and several methods for figuring out the exchange potential and correlation. This makes it possible to examine the electronic properties of materials as well as their magnetic, optical, and thermoelectric characteristics.

Chapter 2: Generality of Dilute magnetic semiconductors (DMS) and the application of half-metallic materials

The second chapter covers the most common uses of ferromagnetic half-metallic materials, which include thermoelectric, solar cells, and spintronic applications. We have reviewed certain fundamental concepts about the numerous optical and thermoelectric characteristics employed in this investigation and the many magnetic semiconductor families and types of magnetic interactions present in DMS.

Chapter 3: Study of the structural, electronic, magnetic, optical, and thermoelectric properties of SnO_2 coupled with double substitutions Mn and A=Mo/Tc

The third chapter presents the results of the electronic, structural, magnetic, thermoelectric, and optical characteristics of co-doped SnO_2 with Mn and A=Mo or Tc along with an interpretation of the findings and a comparison with previous theoretical studies.

Chapter 4: Study of the structural, electronic, magnetic, optical, and thermoelectric properties of Half-metallic Double Perovskites

The fourth chapter focuses on the structural, magnetic, electronic, optical, and thermoelectric properties of the ferromagnetic Ca_2CrMnO_6, Sr_2RECoO_6 (RE=Dy, Ho, Er, or Tm) and antiferromagnetic Sr_2TcReO_6 materials.

Chapter 5: Study of electronic, magnetic, optical, and thermoelectric properties of doped two-dimensional ZnO nanosheets

The fifth chapter discusses the magnetic, optical, electronic, and thermoelectric characteristics of two-dimensional doped ZnO nanosheets with TM (=Fe, Co, Ni, and Cu).

We finalize this thesis with a general conclusion and perspectives.

Chapter 1

Theoretical investigation: Concepts and Methodologies

1.1 First-principles computations

In recent years, ab initio, or first-principles, approaches have become a potent tool for examining the microscopic properties of the material. These approaches allow one to process large systems and model materials quantitatively and dependably. They, therefore, allow comparison with experimental results. Density functional theory (DFT) transforms the many-body quantum problem into a problem focusing on electronic density. As a result, it is the most common method for investigating the physical characteristics of solids in their ground state. To address the fundamentals of the DFT method, we will present several approaches needed to resolve the Schrödinger equation in this chapter. We will be discussing the methods used to calculate energy and exchange-correlation potential.

1.1.1 Schrödinger equation

To describe a quantum system (a collection of particles, such as atoms, molecules, etc.), determine its ground state, and determine its properties, it is necessary to resolve the Schrödinger equation for a wave function Ψ with N particles.

$$H\Psi = E\Psi \tag{1.1}$$

With H represents the Hamiltonian of the system and E denotes the energy of the system, we can express H using the terms:

$$H = \frac{-\hbar^2}{2}\sum_i \frac{\bigtriangledown^2 \overrightarrow{r_i}}{m_e} - \frac{1}{4\pi\varepsilon_0}\sum_{i,j}\frac{e^2 Z_i}{\left|\overrightarrow{R_i} - \overrightarrow{r_j}\right|} + \frac{1}{8\pi\varepsilon_0}\sum_{i\neq j}\frac{e^2}{|\overrightarrow{r_i} - \overrightarrow{r_j}|} - \frac{\hbar^2}{2}\sum_i \frac{\bigtriangledown^2 \overrightarrow{R_i}}{M_n} + \frac{1}{8\pi\varepsilon_0}\sum_{i\neq j}\frac{e^2 Z_i Z_j}{\left|\overrightarrow{R_i} - \overrightarrow{R_j}\right|} \tag{1.2}$$

$$H = T_e + V_{ne} + V_{ee} + T_n + V_{nn} \tag{1.3}$$

With:

$T_e = \frac{-\hbar^2}{2}\sum_i \frac{\bigtriangledown^2 \overrightarrow{r_i}}{m_e}$: The kinetic energy of the N electrons of mass m_e.

$V_{ne} = -\frac{1}{4\pi\varepsilon_0}\sum_{i,j}\frac{e^2 Z_i}{\left|\overrightarrow{R_i} - \overrightarrow{r_j}\right|}$: The potential energy between the nucleus and the electron.

$V_{ee} = \frac{1}{8\pi\varepsilon_0}\sum_{i\neq j}\frac{e^2}{\left|\overrightarrow{r_i} - \overrightarrow{r_j}\right|}$: The potential energy between electron-electron.

$T_n = -\frac{\hbar^2}{2}\sum_i \frac{\bigtriangledown^2 \overrightarrow{R_i}}{M_n}$: The kinetic energy of the M nuclei of mass M_n.

$V_{nn} = \frac{1}{8\pi\varepsilon_0}\sum_{i\neq j}\frac{e^2 Z_i Z_j}{\left|\overrightarrow{R_i} - \overrightarrow{R_j}\right|}$: The potential energy between nucleus-nucleus.

Only in the case of the hydrogen atom is it possible to precisely resolve the Schrödinger equation. In most cases, it is necessary to resort to approximations.

1.1.2 Born-Oppenheimer approximation

The Born-Oppenheimer approximation centers on the idea that each nucleus has a mass significantly higher than an electron [30]. Because of this, the movement of the nuclei is neglected compared to that of the electrons. The nucleus appears frozen in their respective locations, where their Coulomb energy (V_{nn}) resulting from their repulsions becomes a constant, and their kinetic energy ($T_n = 0$) is zero. The challenge is to solve the electronic Schrödinger equation in the field of the nuclei supposedly fixed, with the location of the nuclei acting as a parameter. Thus, the following is the electronic Hamiltonian:

$$H_e = T_e + V_{ne} + V_{ee} + (V_{nn} = cte) \tag{1.4}$$

$$H_e = \frac{-\hbar^2}{2}\sum_i \frac{\bigtriangledown^2 \overrightarrow{r_i}}{m_e} - \frac{1}{4\pi\varepsilon_0}\sum_{i,j}\frac{e^2 Z_i}{\left|\overrightarrow{R_i} - \overrightarrow{r_j}\right|} + \frac{1}{8\pi\varepsilon_0}\sum_{i\neq j}\frac{e^2}{|\overrightarrow{r_i} - \overrightarrow{r_j}|} + \left(\frac{1}{8\pi\varepsilon_0}\sum_{i\neq j}\frac{e^2 Z_i Z_j}{\left|\overrightarrow{R_i} - \overrightarrow{R_j}\right|} = cte\right) \tag{1.5}$$

The Schrödinger equation (1.5) cannot be resolved using this approach alone because of the dependence on electron movements and the existence of interactions. It relies on the fact that electrons travel in a field of stationary nuclei. Therefore, using different approximations is required.

1.1.3 Hartree approximation

Due to the numerous particles involved, it is impossible to resolve the electronic part. By approaching the N-body problem as if it only included one particle, it is possible to consider the wave function as the direct product of one-particle wave functions developed by Hartree in 1928 [31].

$$\Psi\left(\overrightarrow{r}\right) = \Pi_{i=1}^{n}\Psi_i\left(\overrightarrow{r}\right) \tag{1.6}$$

This approximation relies on the presumption that electrons are free, which ignores the interactions between electrons and spin states. The Schrödinger equation with n electrons simplifies to n Schrödinger equations with 1 electron in this simplified model, where each electron is accounted for individually.

$$\left(-\frac{1}{2}\overrightarrow{\bigtriangledown}_i^2 + V_{ext}\left(\overrightarrow{r_i}, \overrightarrow{R}\right) + V_H\left(\overrightarrow{r}_i, \overrightarrow{r}_j\right)\right)\Psi_i\left(\overrightarrow{r}\right) = E\Psi_i\left(\overrightarrow{r}\right) \tag{1.7}$$

Where V_{ext} is the attractive interaction that exists between the electron of coordinate $\overrightarrow{r_i}$ and the nucleus of coordinate $\overrightarrow{R}$, and $V_H\left(\overrightarrow{r}_i, \overrightarrow{r}_j\right)$ is the Hartree potential leading to the repulsive Coulomb interaction among an electron of coordinate $\overrightarrow{r_i}$ involved in the field mean of the another electrons of coordinates $\overrightarrow{r_j}$. As the Hartree approximation ignores the Pauli Exclusion law and the indistinguishability of electrons (anti-symmetric functions), it is unlikely to create the ground state.

1.1.4 Hartree–Fock approximation

The Hartree-Fock approximation incorporates the Pauli principle, which leads us to investigate the anti-symmetry of the wave function of a quantum electronic structure, including:

$$\Psi\left(r_1, ...r_a, ...r_b, ...r_N\right) = -\Psi\left(r_1, ...r_b, ...r_a, ...r_N\right) \tag{1.8}$$

The Slater determinant expresses the anti-symmetric wave function:

$$\Psi_{HF} = \frac{1}{\sqrt{N!}} \begin{vmatrix} \varphi_1\left(r_1\right) & \varphi_1\left(r_2\right) & ... & \varphi_N\left(r_1\right) \\ \varphi_2\left(r_1\right) & \varphi_2\left(r_2\right) & ... & \varphi_N\left(r_1\right) \\ ... & ... & ... & ... \\ \varphi_N\left(r_1\right) & \varphi_N\left(r_2\right) & ... & \varphi_N\left(r_N\right) \end{vmatrix} \tag{1.9}$$

1.1.5 Density Functional Theory (DFT)

The fundamental studies for DFT was published in 1927 by Thomas [32] and Fermi [33]. The DFT uses electronic density to represent the system of interacting electrons instead of the wave functions of each electron. The two essential theorems of Hohenberg and Kohn form the foundation of the DFT, which connects the ground state's energy to its electronic density [1].

1.1.5.1 Hohenberg-Kohn theorems

To describe the energy contributions to the overall energy, Hohenberg, and Kohn (HK) [1] created a rigorous formalism. Two theorems compose this formalism:
* The unique function of the density $\rho(r)$ is the ground state energy.

$$E = E\left(\rho\right) \tag{1.10}$$

* The overall energy minimum is represented by the ground state density.

$$E_0 = \min E\left(\rho\right) \tag{1.11}$$

This density is the same as the ground state density for one particle:

$$E_0 = E\left(\rho_0\right) \tag{1.12}$$

where ρ_0 denotes the ground state density. The function of the overall energy of the ground state has the following expression:

$$E\left[\rho\left(r\right)\right] = \int V_{ext}\left(r\right)\rho\left(r\right)dr + F\left[\rho\right] \tag{1.13}$$

With $V_{ext}(r)$ represents the external potential acting on the particles. $F[\rho(r)]$ holds true for every system with more than one electron based only on electron density. For a given external potential, the variational method makes it simple to calculate the ground state electron density and overall energy as long as the $F[\rho(r)]$ is known. Sadly, the form of $F[\rho(r)]$ is not indicated by the Hohenberg and Kohn theorem.

1.1.5.2 Kohn-Sham equations

It is possible for an auxiliary system made up of independent particles to reproduce the ground state density of N particles in interaction, according to the Kohn-Sham theory [2]. A Real system consisting of electrons in interaction is replaced by a hypothetical collection of independent particles developing an effective potential. As a result, the hypothetical system maintains the energy and electron density of the real system.
Schrödinger equation and the Kohn and Sham equation (KS) have a similar form, which is as follows:

$$H\psi_i = E\psi_i \tag{1.14}$$

The following is the form of Hamiltonian of this system:

$$H = -\frac{\hbar^2}{2m} \triangle + V_{KS}(r) \tag{1.15}$$

With:

$$V_{KS} = V_{eff} = V_{ext}(r) + V_H(r) + V_{xc}(r) \tag{1.16}$$

$V_{ext}(r)$ is the electron-nuclei Colombian interaction.

$V_H(r) = \int \frac{\rho(r,r')}{|r-r'|} d^3r'$ represents the Colombian interaction between the electrons described through their load density.

$V_{xc}(r) = \frac{\partial E_{xc}[\rho(r)]}{\partial \rho(r)}$ represents the interaction of exchange and correlation.

The KS equations become:

$$\left(-\frac{\hbar^2}{2m} \triangle + V_{KS}(\overrightarrow{r})\right) \psi_i(\overrightarrow{r}) = E\psi_i(\overrightarrow{r}), i = 1, 2, ..., N \tag{1.17}$$

With :

$$V_{KS}(r) = -\sum_I \frac{Ze^2}{|r - R_I|} + \int \frac{\rho(r,r')}{|r-r'|} dr' + \frac{\partial E_{xc}[\rho(r)]}{\partial \rho(r)} \tag{1.18}$$

Every many-body interaction exists in an exchange and correlation functional dependent on the electron density presented by:

$$\rho(\overrightarrow{r}) = \sum_{i=1}^{N} |\psi_i(\overrightarrow{r})|^2 \tag{1.19}$$

The accuracy of the exchange and correlation energy, whose analytical formulation is unknown, is necessary for the Kohn-Sham method to be effective. The equations (1.17), (1.18), and (1.19) that make up the KS equations are self-consistently resolved. Indeed, utilizing a test density as a starting point, we can solve equation (1.17) to get a potential V_{KS} and a new electron density. The process continues until the targeted level of accuracy is obtained [34] (see Figure 1.1).

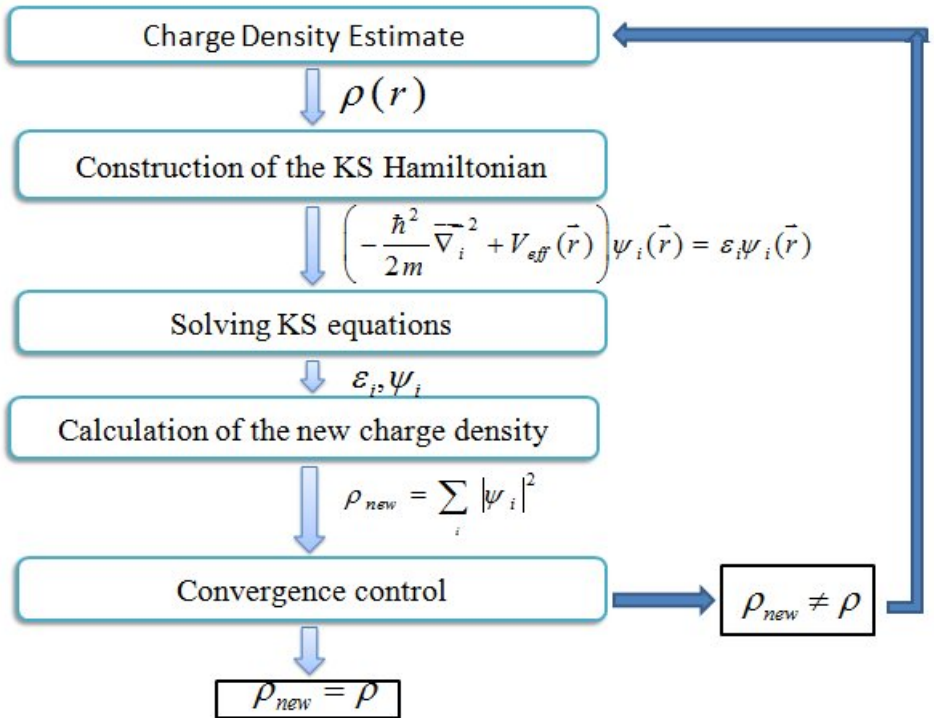

Figure 1.1: Iterative scheme of the self-consistent technique for resolving the KS equations

We now have a workable solution to the electronic problem of ground states. If one knows the electron density, one may use the Khon-Sham technique to calculate every system characteristic. It became possible thanks to the model of independent electrons. However, the function of the $E_{xc}[\rho(\overrightarrow{r})]$ remains unknown and ill-defined. Thus, it is necessary to use approximations.

1.1.6 Approximations of the exchange and correlation functional

The point that the exchange-correlation function corresponds to the sole density function that is still unknown within this formalism can now be underlined thanks to the development of the Kohn-Sham equations. Local density approximation, which views an electronic system as a locally uniform gas of electrons, was the first approximation developed historically. To enhance the treatment of the exchange and correlation indicated through the LDA, several approximations have been developed.

1.1.6.1 Local Density Approximation (LDA)

The idea that the terms of the exchange and correlation rely just on the local value of $\rho(r)$ is the foundation of the Local Density Approximation (LDA). In other words, it treats inhomogeneous systems as being locally homogeneous. The exchange-correlation energy formula is shown as follows:

$$E_{xc}^{LDA}\left[\rho(r)\right] = \int \rho(r)\varepsilon_{xc}^{LDA}\left[\rho(r)\right] d^3r \tag{1.20}$$

Assuming uniform distribution, $\varepsilon_{xc}^{LDA}\left[\rho(r)\right]$ represents the energy of correlation and exchange for each electron in an electron gas. The LDA assumes that the $\varepsilon_{xc}^{LDA}\left[\rho(r)\right]$ is purely local. Two terms describe this energy:

$$\varepsilon_{xc}^{LDA}\left[\rho(r)\right] = \varepsilon_x\left[\rho(r)\right] + \varepsilon_c\left[\rho(r)\right] \tag{1.21}$$

With $\varepsilon_x\left[\rho(r)\right]$ represents the exchange energy, and $\varepsilon_c\left[\rho(r)\right]$ denotes the correlation energy. This approximation is precise in the limit of a uniformly dense free electron gas. One would anticipate this approximation to work reasonably well in the case of a slowly varying density ρ.
Local Spin-polarized Density Approximation (LSDA) is an extension of LDA that might potentially accommodate spin-polarized systems [35, 36]:

$$E_{xc}^{LSDA}\left[\rho_\uparrow(r), \rho_\downarrow(r)\right] = \int \rho(r)\varepsilon_{xc}\left[\rho_\uparrow(r), \rho_\downarrow(r)\right] d^3r \tag{1.22}$$

Remember that the excited states of electronic systems are not described by the LDA, only for the ground state. This approximation underestimates the width of the forbidden bands of semiconductors and insulators. Certain systems with strong correlation effects (narrow f or d bands) have properties that are hard to describe with the LDA approximation.

1.1.6.2 Generalized Gradient Approximation (GGA)

Compared to the LDA, the Generalized Gradient Approximations (GGA) [37, 38] provide an improvement. The GGA approximation expresses the potential of the exchange and correlation as a function of the local electron density $\rho(\overrightarrow{r})$ and its gradient $\bigtriangledown\rho(\overrightarrow{r})$:

$$E_{xc}^{GGA}\left[\rho(\overrightarrow{r})\right] = \int \rho(\overrightarrow{r}) f\left[\rho(\overrightarrow{r}), \bigtriangledown\rho(\overrightarrow{r})\right] d\rho(\overrightarrow{r}) \tag{1.23}$$

With: $f\left[\rho(\overrightarrow{r}), \bigtriangledown\rho(\overrightarrow{r})\right]$ is the exchange and correlation function dependent on the gradient and electron density. Perdew and Wang (PW91) [39, 40] and Perdew, Burke, and Ernzerhof (PBE) [41, 42] are the two most often used versions of the GGA. For the volumes at equilibrium, the cohesion energies, and the total energies, the GGA approx-

imation frequently yields better outcomes than LDA. Still, the width of the forbidden bands of insulators and semiconductors remains far too low. The description of systems with strong correlations (narrow d or f bands) is weak.

1.1.6.3 Approximation of local density and generalized gradient with the adjustment of Hubbard (LDA+U and GGA+U)

When the d or f orbitals are firmly packed together, the localized electrons exhibit strong intra-site Coulomb repulsion, which corresponds through the Hubbard parameter U throughout the width of the band. The powerful screened intra-site Coulomb interactions between d electrons have been added using the DFT+U, which blends the DFT with a Hubbard Hamiltonian, $\hat{h}_{Hubbard}$ [43, 44, 45, 46]. Based on the basic DFT+U version made available by Dudarev et al., the Hamiltonian can be expressed as follows [45]:

$$\hat{h}_{Hubbard} = \frac{U}{2} \sum_{m,m',\sigma} \widehat{n}_{m,\sigma} \widehat{n}_{m',-\sigma} + \frac{(U-J)}{2} \sum_{m \neq m',\sigma} \widehat{n}_{m,\sigma} \widehat{n}_{m',\sigma} \tag{1.24}$$

Where $\widehat{n}_{m,\sigma}$ is the operator that indicates how many electrons are present in an orbital at a given site with spin σ and magnetic quantum number m. U is the spherically averaged value that represents the energy required to insert an additional electron. J is the energy of the screened exchange. Coulomb repulsion inside a site is characterized by parameters U and J. This method uses their difference ($U_{eff} = U - J$) rather than U and J intervening independently.

1.1.6.4 Modified Becke-Jonshon Approximation (MBJ)

Tran and Blaha [48] have published an updated form of the exchange potential, which was initially introduced by Becke and Johnson [47]. The most recent ab initio Wien2k code incorporates mBJ potential ("modified Becke Johnson Potential"), commonly known as the TB potential ("Tran-Blaha" potential). The expression of the mBJ method is as follows:

$$U_{x,\sigma}^{mBJ}(r) = cU_{x,\sigma}^{BR}(r) + (3c-2)\frac{1}{\pi}\sqrt{\frac{5}{12}}\sqrt{\frac{2t_\sigma(r)}{\rho_\sigma(r)}} \tag{1.25}$$

Where $\rho_\sigma(r) = \sum_{1=1}^{n_\sigma} |\psi_{i,\sigma}(r)|^2$ represents the electron density and $t_\sigma(r) = \frac{1}{2}\sum_{1=1}^{n_\sigma} \bigtriangledown\psi_{i,\sigma}^*(r) \bigtriangledown \psi_{i,\sigma}(r)$ denotes the kinetic energy density. $U_{x,\sigma}^{BR}$ is the potential suggested to simulate the Coulomb potential generated by the exchange hole, or Becke-Roussel (BR) potential [49].

$$U_{x,\sigma}^{BR} = -\frac{1}{b_\sigma(r)}(1 - e^{-x_\sigma(r)} - \frac{1}{2}x_\sigma(r)e^{-x_\sigma(r)}) \tag{1.26}$$

The term x_σ in equation (1.26) was determined from $\rho_\sigma(r)$, $\bigtriangledown\rho_\sigma(r)$, $\bigtriangledown^2\rho_\sigma(r)$, and $t_\sigma(r)$; while term $b_\sigma(r)$ was calculated using the following relationship:

$$b_\sigma(r) = \left[\frac{x_\sigma^3(r)e^{-x_\sigma(r)}}{8\pi\rho_\sigma(r)}\right]^{\frac{1}{3}} \tag{1.27}$$

The index σ is the spin notation.
In equation (1.25), the choice was made for c to rely linearly on the square root of the mean of $\frac{\bigtriangledown\rho(r)}{\rho(r)}$:

$$c = \alpha + \beta\left(\frac{1}{V_{cell}}\int_{cell}\frac{|\bigtriangledown\rho(r')|}{\rho(r')}d^3r'\right)^{\frac{1}{2}} \tag{1.28}$$

α and β are adjustable parameters ($\alpha = -0.012$ (dimensionless) and $\beta = 1.023 Bohr^{\frac{1}{2}}$), and V_{cell} represents the unit cell volume.
Compared with some popular computation modes, such as LDA or PBE (the solids version of GGA), the modified Tran and Blaha functional (TB-mBJ) quickly established its effectiveness and popularity, even if its self-consistent converges slowly and so necessitates more iterations.

1.1.6.5 Hybrid functionals

Becke presented hybrid functionals to address the flaws in DFT and Hartree-Fock (HF). Combining the precise exchange of HF with the DFT term is a practical strategy. Functions PBE0 [51] and HSE [52, 53] are the two hybrid functions that are currently most commonly used. Full-range hybrid functionals PBE0, which are a linear combination of the DFT and HF exchange, are written as [50]:

$$E_{xc}^{PBE0} = \alpha E_x^{HF} + (1-\alpha)E_x^{PBE} + E_c^{PBE} \tag{1.29}$$

With:
E_{xc}^{PBE0}: Exchange and correlation function of the PBE0.
E_x^{HF}: HF exchange.
E_x^{PBE}: Exchange function of the PBE.
E_c^{PBE}: Correlation function of the PBE.
α: a mixing coefficient obtained from perturbation theory [42, 54].

1.1.6.6 Spin Orbit Coupling (SOC)

In a non-relativistic description, spin-orbit coupling is missed. But these interactions appear in the completely relativistic description of the system, given by the Dirac equation, which appears in several references [55]. Relativistic treatment of the heavy element core electrons is necessary because of the importance of the DOC. The following represents

the Dirac-Hamiltonian equation :

$$H^{sr}\psi + \frac{1}{2}\zeta(\overrightarrow{\sigma}\,\overrightarrow{l})\psi = E\psi \tag{1.30}$$

with:
H^{sr}: The relativistic scalar Hamiltonian.
ζ: The spin-orbit coupling constant.

1.1.7 Calculation methods

Several methods of electronic structure calculation exist. The self-consistent resolution of the Kohn and Sham equations is what unites them. Their differences lie in the details of their different representations of potential, electronic density, and especially the mono-electronic orbitals of Sham and Kohn.

The Augmented Plane Wave (APW) approach created by Slater [57, 58] was improved upon by Andersen [56] with the development of the Linearized Augmented Plane Wave (LAPW) method.

Augmented plane wave (APW) method

Slater first described the APW in his article from 1937 [59, 60], where he assumed that the wave functions and potential close to the atomic nucleus are comparable to those in an isolated atom. They almost seem spherical. In contrast, because the electrons that are far from the nucleus are considered free, their behavior is described by plane waves. To characterize the crystal potential, also known as the "Muffin-Tin" potential, the APW approach relies on the "Muffin-Tin" approximation [61]. There are two zones. Crystal waves have different functions in different bases: Plane waves in the interstitial zone and radial solutions of the Schrödinger equation inside the MT sphere (See Figure 1.2).

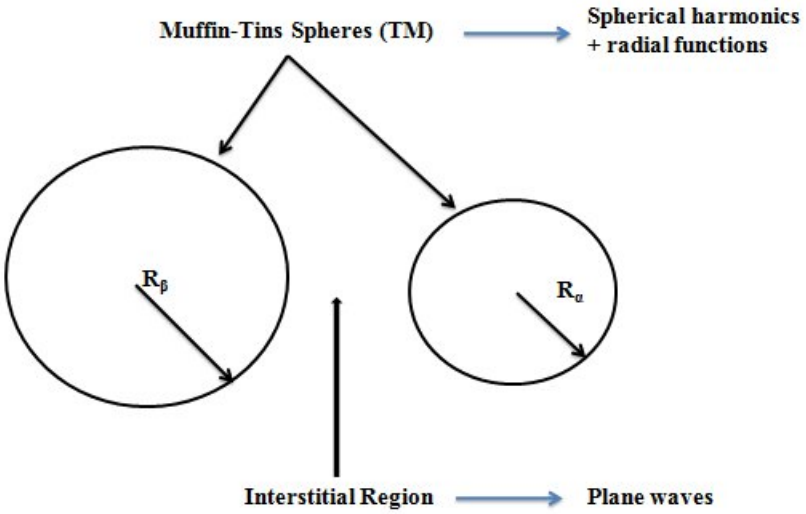

Figure 1.2: Distribution of the unit cell, an interstitial region, and spherical regions: $\alpha-$ and $\beta-$ spheres of muffin-tin radii R_α and R_β, respectively.

Then wave function $\varphi(r)$ is:

$$\varphi(r) = \left\{ \begin{array}{c} \frac{1}{\Omega^{\frac{1}{2}}} \sum_G C_G e^{i(G+K)r}, r > R_{MT} \\ \sum_{l,m} A_{l,m} U_l(r,E) Y_m^l(r), r < R_{MT} \end{array} \right\} \tag{1.31}$$

Ω is the cell volume, C_G represents the plane wave development coefficients, Y_m^l are the spherical harmonics, $A_{l,m}$ are the coefficients of the spherical harmonics, K represents the wave vector in the irreducible Brillouin zone (IBZ), G represents the reciprocal space vector, and the function U_l denotes a regular solution of the radial Schrödinger equation. It is expressed as follows:

$$\left\{ -\frac{d^2}{dr^2} + \frac{l(l+1)}{r^2} + V(r) - E_l \right\} r U_l(r) = 0 \tag{1.32}$$

V(r) represents the Muffin-Tin potential, and E_l is the linearization energy.
To support his choice of functions, Slater employed the plane waves as solutions of the Schrödinger equation in the case of a constant potential. The radial functions are solutions in the situation of a spherical potential where E_l is an eigenvalue.
For the function to remain continuous on the surface of the sphere MT, the plane wave coefficients C_G that are present in the interstitial areas must evolve the coefficients $A_{l,m}$. The following expression can be employed to describe it:

$$A_{l,m} = \frac{4\pi i^l}{\Omega^{\frac{1}{2}} U_l(R_\alpha)} \sum_G C_G j_l(|K+g| R_\alpha) Y_{l,m}^*(K+G) \tag{1.33}$$

After being formed in this way, the APW approach has some issues with the function $U_l(R_\alpha)$ that shows up in the denominator of equation (1.34). The separation of radial functions from plane wave functions occurs at the surface of the sphere MT, where the value of $U_l(R_\alpha)$ might become zero based on the value of the parameter E_l. The APW method has undergone several modifications to address this issue, especially those suggested by Andersen [56] and Koelling [62]. This modification results in the LAPW technique, which is the wave function $\varphi(r)$ within the spheres represented by a linear combination of the radial functions $U_l(r)$ and their derivatives with respect to the energy $\mathring{U}$.

Fundamentals of the Full Potential Linearized Augmented Plane Wave (FP-LAPW) method

Based on the radial functions $U_l(r)Y_{lm}(r)$ and their energy-related derivatives $\mathring{U}_l(r)Y_{lm}(r)$, the basis functions in the MT spheres of the LAPW method are linear combinations. The APW method defines the U_l functions, and the function must fulfill this equation:

$$\left\{-\frac{d^2}{dr^2}+\frac{l(l+1)}{r^2}+V(r)-E_l\right\}r\mathring{U}_l(r)=rU_l(r) \tag{1.34}$$

In the non-relativistic situation, $U_l(r)$ and $\mathring{U}(r)$ preserve continuity with the outer plane waves on the surface of the sphere MT. The augmented wave functions serve as the basis functions (LAPW) for the LAPW method:

$$\varphi(r)=\left\{\begin{array}{c}\frac{1}{\Omega^{\frac{1}{2}}}\sum_G C_G e^{i(G+K)r}, r>R_{MT}\\ \sum_{l,m}[A_{l,m}U_l(r)+B_{lm}\mathring{U}_l(r)]Y_m^l(r), r<R_{MT}\end{array}\right\} \tag{1.35}$$

These coefficients, B_{lm}, are the same as A_{lm} and relate to the function $\mathring{U}_l$. The LAPW in the interstitial zones are just plane waves, exactly like in the APW. LAPW functions are more appropriate inside spheres than APW functions.

All-electron methods and supposedly pseudo-potential approaches are the two primary divisions of DFT methods. Similarly, there are two main classes of potentials: all-electron potentials and pseudo-potentials. The FP-LAPW (full potential -LAPW) approach is one of the all-electron methods. This technique, which adapts the fundamental functions and their derivatives to the radial function and its derivative, is adequate. Consequently, the potential at the surface of the sphere MT is guaranteed to be continuous using the following method:

$$V(r)=\left\{\begin{array}{c}\sum_K V_K e^{ikr}, r>R_{MT}\\ \sum_{lm}V_{lm}(r)Y_{lm}(r), r<R_{MT}\end{array}\right\} \tag{1.36}$$

The core electrons are accounted for in the computation, as opposed to methods that use

pseudo-potentials. The most precise approach is FP-LAPW, although it is computationally heavy.

In this work, we examined various characteristics of our compounds by the FP-LAPW incorporated in the Wien2k code.

1.2 Wien2k Simulation Program

The WIEN code, an ensemble of programs created by Blaha, Schwarz, and their associates [63], includes the FP-LAPW approach. This code exists in several versions, including WIEN97 [64], which was later updated to give WIEN2k [65]. It has enabled the successful treatment of quantum chemistry on periodic solids and condensed matter physics. The Wien2k code consists of different independent programs (see Figure 1.3). Initialization consists of executing auxiliary programs which generate:
NN: aids in calculating the radius of the Muffin-Tin sphere in addition to providing the distances among the closest neighbors.
SGROUP: obtains the space group of the structure described in the file case.struct and outputs the file case.struct-sgroup.
LSTART: chooses how to treat the various orbitals (like core and valence states, with or without local orbitals...) and creates the atomic densities when calculating the band structure.
SYMMETRY: establishes the point group of specific atomic sites, produces the lattice harmonics LM expansion, and establishes local rotation matrices, in addition to generating symmetry operations for space groups.
KGEN: creates a Brillouin zone mesh k.
DSTART: superimposes the atomic densities produced in LSTART to provide a beginning density for the SCF cycle.

**** Self-consistent calculation***

In this step, the energies and ground state electronic density are calculated according to a convergence criterion (energy, charge density, force). The subprograms used are:
LAPW0: generates the Poisson potential for calculating the density.
LAPW1: allows you to calculate valence bands, eigenvalues, and eigenvectors.
LAPW2: determines for each eigenvector the valence densities.
LCORE: computes densities and core states.
MIXER: combines the input and output densities (starting, valence, and core).

The ground state characteristics (charge density, electronic band structure, magnetic

characteristics, etc.) are then calculated following the completion of the self-consistent calculation.

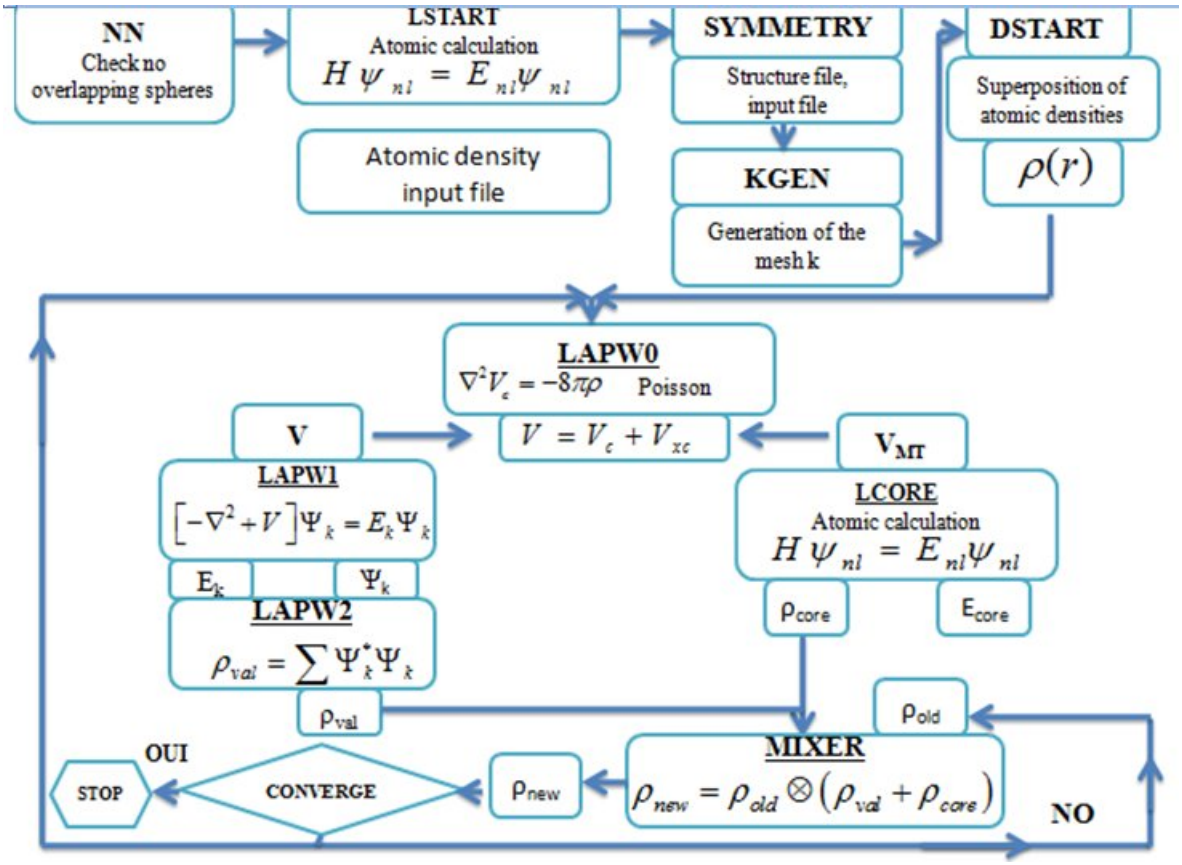

Figure 1.3: WIEN2k code flowchart.

1.3 BoltzTraP code

Calculating the semi-classical transport coefficients requires the execution of the program Boltzmann Transport Properties (BoltzTraP) [66]. This code, which interfaces with Wien2k, utilizes a grid of band energies. The algorithm uses a Fourier extension of the band energies to keep the space group symmetry.

1.3.1 Boltzmann Transport Equation

According to the Boltzmann transport equation (BTE), thermoelectricity transforms heat into electricity [67, 68]. The semi-classical transport equation is a theoretical method for carrying out such an investigation of the transport characteristics. The BTE is employed to analyze the classical transport of charge carriers, which describes how the local concentration of carriers varies over time in the state k near the point r. This equation

describes the various ways that the state of the particles can change:

* Collisions: the motion of electrons results in the entrance or departure of carriers of any volume element near r.

* The impact of outside forces.

* Diffusion: Electrons will move from one state k to another as a result of diffusion processes.

The following equation, which describes how the distribution function changes when these various actions are present, was created:

$$\frac{\partial}{\partial r} f.\nu(k) + \frac{\partial}{\partial k} f.\frac{F}{\hbar} + \frac{\partial}{\partial t} f = \left(\frac{\partial f}{\partial t}\right)_c \tag{1.37}$$

With:
* $\frac{\partial}{\partial r} f.\nu(k)$: shows diffusion caused by a gradient $\frac{\partial}{\partial r} f$ via a volume element d^3r around point r in phase space. .

* $\frac{\partial}{\partial k} f.\frac{F}{\hbar}$: shows diffusion caused by a gradient $\frac{\partial}{\partial k} f$ via a volume element d^3r around point r in phase space.

* $\frac{\partial}{\partial t} f$: represents the concentration gradient.

* $\left(\frac{\partial f}{\partial t}\right)_c$: represents the collision term and explains how electrons diffuse from a point k.

These semi-classical equations describe the path of an electron in momentum space (r, k). When electron diffusion is absent, collisions are not introduced, the earlier equation is zero, and we get:

$$\frac{\partial}{\partial r} f.\nu(k) + \frac{\partial}{\partial k} f.\frac{F}{\hbar} + \frac{\partial}{\partial t} f = 0 \tag{1.38}$$

The semi-classical Boltzmann transport equation will be solved using the BoltzTraP code [66], and the transport coefficients will be determined using this solution under the assumption of a constant relaxation time. Applying the DFT and Boltzmann transport theory, we may ascertain the transport properties based on the electronic structure.

1.3.2 Solving the Boltzmann Transport Equation

The BoltzTraP, an open-source program, solves the Boltzmann equation to determine the semi-classic transport parameters. It provides an even analytical representation of the

bands by performing a Fourier expansion of the band energies using symmetry-conserving star functions. It is possible to compute band-structure-dependent values and derivatives of band-structure-dependent quantities using the analytical representation of the bands. In theory, the relaxation time depends on both temperature T and energy. Moreover, BoltzTraP assumes that the relaxation time is constant by default. Additionally, this thesis will consider the electronic contribution, even though the phonon contribution should be considered when computing the transport characteristics in theory.

1.4 Conclusion

This chapter covers the fundamentals of DFT, including the many approaches used to compute the exchange-correlation potential and energy. This work employed the FP-LAPW included in the Wien2k code with the BoltzTrap code interfaces with Wien2k based on the electronic structure. Several characteristics of the atomic systems are calculated utilizing these codes and will be discussed later.

Chapter 2

Generality of Dilute magnetic semiconductors (DMS) and the application of half-metallic materials

Introduction

The growing need for information storage and quick access to data has stimulated the search for novel devices and materials with unique magnetic properties for electronics of spin. Therefore, the use of substances with high polarized spin is necessary for the future development of spintronics. Half-metal materials have enormous potential for use in spintronic components like magnetic logic and magnetic random access memories (MRAM). It appears that some materials are half-metals, such as Double Perovskites and Dilute Magnetic Semiconductors (DMS). The researchers are also at the forefront of creating new energy technologies, such as solar electricity generation systems.Materials that can convert heat flow directly to electricity or the reverse serve to make the most of thermoelectric technology now in production. This chapter will cover some general aspects of Ferromagnetic half-metallic materials and their uses in spintronics, solar energy, and thermoelectricity devices. Additionally, we will cover certain fundamental concepts about optical, thermoelectric, and magnetic properties.

2.1 Diluted Magnetic Semiconductors (DMS)

Electronics depends on the movement of charge of carriers, like electrons or holes, in semiconductors like silicon. The growing need for processing power and data storage is one of the main issues facing science and technology today. It is possible to integrate various features into a single device when ferromagnetic materials combine their magnetic, optical, and thermoelectric characteristics with their electronic ones. This is one of the trendiest subjects in spin electronics. Diluted magnetic semiconductors (DMS) are an exclusive category of material made possible by the ability to dope semiconductors with magnetic elements. The emergence of localized magnetic moments caused by electron-hole interaction is one of the distinctive features of DMS. This results in intriguing characteristics like, for example, a rise in charge carriers or new excitations like magnetic polarons. However, ferromagnetism seldom occurs in semiconductors due to the low carrier density and preponderance of super-exchange between local magnetic moments. Magnetic semiconductors typically have low Curie temperatures.

2.1.1 Classification of magnetic semiconductors

There are two different categories of magnetic semiconductors:

**** Semiconductors where magnetic elements form a network periodic:***

This class involves adding large quantities of magnetic elements (transition metals or

rare earths) to semiconductor materials. The crystalline network formed by the matrix atoms and the magnetic atoms is arranged on a periodic network and is thus perfectly defined (Figure 2.1(a)). These materials are sometimes called CMS (Concentrated Magnetic Semiconductors). The principal representatives of this family are chalcogenides ($CdCr_2Se_4$ [69, 70], $FeCr_2S_4$ [71], EuO [72]) and certain manganites. Although several of these CMS materials exhibit ferromagnetic properties and higher ordering temperatures than ambient temperature, integrating them into current microelectronics systems can be challenging. The use of diluted magnetic semiconductors (DMS) appears more promising.

**** Semiconductors where magnetic elements randomly substitute cations (DMS):***

The DMS approach differs considerably from the earlier one. In this case, magnetic ions, mostly transition metals, can be introduced to a semiconductor matrix, but only in small enough to prevent the crystal structure of the matrix from changing (Figure 2.1(c)). Several different types of DMS can be categorized based on their host semiconductor matrices:

- Type III-V like GaMnAs and InMnAs.
- Type IV based on Si or Ge doped with Mn, Ni, Cr, or Fe.
- Type IV-VI like $Pb_{1-x}Sn_xMn_xTe$.
- Type II-VI like ZnTMO and CdTMTe (TM=ion of the transition metal series).
- Oxide semiconductors like TiO_2, SnO_2, and HfO_2.

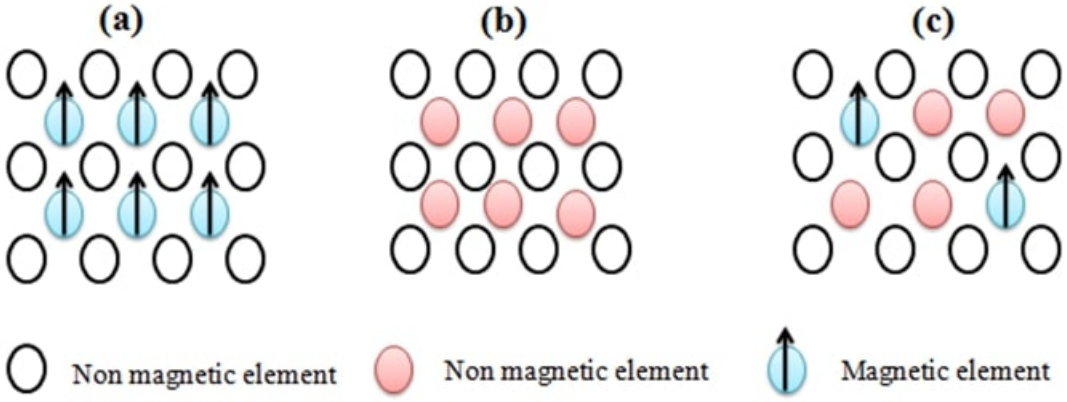

Figure 2.1: Schematic illustration of (a) Semiconductors where magnetic elements form a network periodic, (b) Traditional semiconductors without magnetic elements, and (c) Dilute magnetic semiconductors where the magnetic elements are distributed randomly.

DMS are of great interest today because they are prospective materials for spintronics and computer memory applications. DMSs are correlated electron systems due to carriers

interacting with localized magnetic ions, generating ferromagnetism.

2.1.2 Dilute magnetic oxides (DMO)

Numerous teams have conducted experimental studies on DMO in the wake of Dietl et al. The first important discovery in this field dates from 2001 with the fabrication of thin layers of ferromagnetic Co-doped TiO_2 at room temperature [9]. In 2001, researchers also created ferromagnetic Co-doped ZnO thin films at ambient temperature [10]. Since then, ferromagnetism has been observed in numerous DMOs (in thin layers in the vast majority) of:

- Fe, V, Co, Ni, or Cr doped TiO_2 [9, 73, 74];
- Mn, Cr, V, Co, or Fe doped SnO_2 [75 - 77];
- Cu, V, Ti, Fe, Cr, Ni, Mn, or Co doped ZnO [10, 78, 79, 80, 81];
- Fe doped HfO_2 [82];
- Fe, Cr, V, Ni, Co, or Mn doped In_2O_3 [83 - 88];
- N, or Co doped CeO_2 [89 - 91];

The first explanation that comes to mind to clarify the ferromagnetism of DMOs is the precipitation of magnetic dopants in a ferrimagnetic or ferromagnetic phase like Fe_3O_4 or metallic Co. In this case, the ferromagnetism of the DMO is not intrinsic but is related to the coupling mechanism between magnetic dopants dispersed in the matrix. To begin with, we need to understand the coupling mechanisms that can account for the ferromagnetism of DMOs.

2.2 Half-metallic ferromagnet materials

It was Groot and associates [8] who initially presented the proposal of a ferromagnetic half-metal. It is a substance having a single spin population around the Fermi level, ensuring that only "up" (or "down" spins) can conduct, making the current 100% spin-polarized. Furthermore, there is only one spin orientation (up or down) for the electron contribution around the Fermi level. There is an enormous demand for half-metallic ferromagnet systems in spintronics technologies.

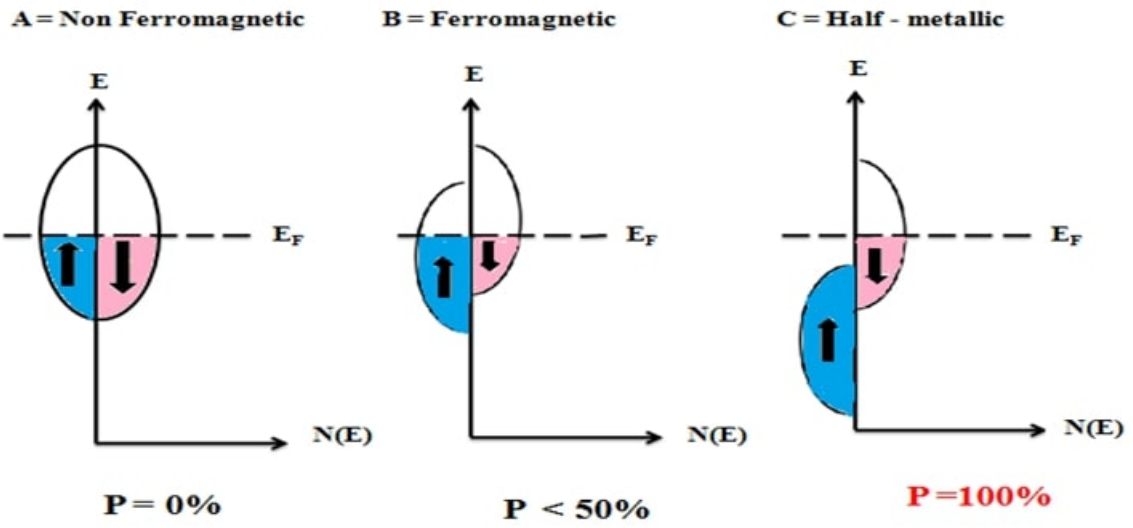

Figure 2.2: Schematic presentation comparing the densities of states and spin polarization of (A) non-magnetic, (B) ferromagnetic, and (C) half-metallic materials.

Figure 2.2 (B) displays the density of states for a ferromagnetic material. In one spin orientation, a ferromagnetic half-metal (HMF) functions as an insulator, while in the other, like a metal (Figure 2.2(C)).

2.3 Magnetic interactions

The mechanisms most used to describe the magnetic interactions in DMS are super-exchange, the Ruderman-Kittel-Kasuya-Yoshida (RKKY) interaction and double Zener exchange. These exchange interactions leading to ferromagnetic interaction occur indirectly, without direct overlap of closest neighboring orbitals (direct exchange).

2.3.1 Super-exchange interaction

When two magnetic ions (cations), nearest neighbors, interact indirectly through an oxygen ion (anion), it's called super-exchange. Research has demonstrated that $LaMnO_3$ crystals display antiferromagnetism due to super-exchange interaction [92, 93]. The exchange interaction correlates the magnetic moments of ions and valence band p. In this case, there is no orbital overlap between the nearest neighboring magnetic ions. Super-exchange does not require the presence of delocalized charge carriers. Goodenough et al. formalized the super-exchange interaction [93] in insulating materials based on the configuration of the d orbitals of magnetic ions and the bond angle (magnetic ion-oxygen-magnetic ion), which gave rise to the Goodenough Kanamori rules. At 180°, Figure 2.3

shows a variety of cation-anion arrangements. In the first situation, a half-full e_g orbital oriented in the direction of the anion is present in both cations. In this case, the coupling is direct and gives strong antiferromagnetism by the rules of Hund. The antiferromagnetism is weak when both eg orbitals are empty, as the electrons of the cation have an identical and non-zero probability of being on the empty orbital e_g (case 2). However, in case 3, one of the cations has a half-filled e_g orbital, and the other has an empty one. The electron can pass from one cation to another if the two cations have parallel spins. This virtual passage gives rise to weak ferromagnetic interaction.

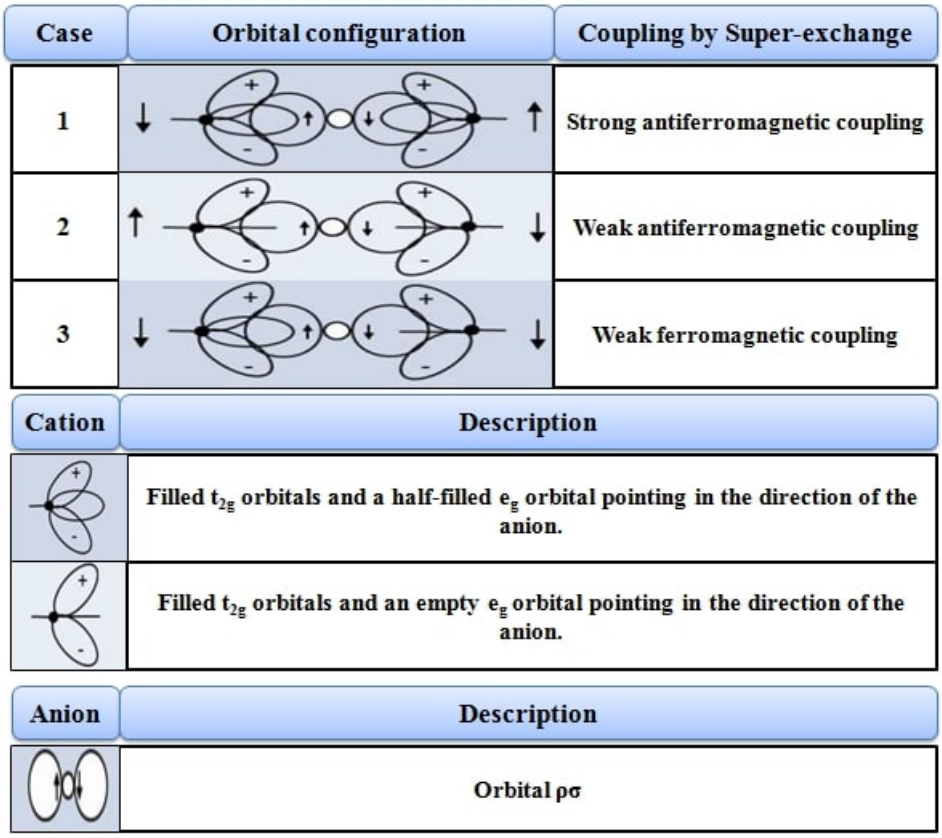

Figure 2.3: Magnetic order depending on the type of orbital of neighboring cations. A stable 180° angle exists between two cations [9].

2.3.2 Double exchange interaction

In 1951, Zener [94, 95] proposed the double exchange model to explain ferromagnetism in manganites (perovskites), such as $La_{0.7}Sr_{0.3}MnO_3$. This model involves oxygen ions to ensure the transport of electrons between manganese cations with different charge states that are too far apart and for which the direct exchange (cation-cation) is zero. When two cations of the same species but different valences meet, a ferromagnetic interaction known as the double exchange interaction occurs. A non-magnetic atom facilitates the exchange

of a third shell electron. For example, an oxygen ion separates Mn^{4+} and Mn^{3+}. Comparing the orientation of the localized electrons' spins, Zener reasoned, would allow one to establish the ground state using Hund's rules. Electron delocalization and ferromagnetic interactions should result from the electron's movement in a parallel spin environment. He studied the interaction mechanism like electronic transfer between manganese ions via the oxygen ion through the initial Ψ_1 to Ψ_2. He called this transfer the double exchange.

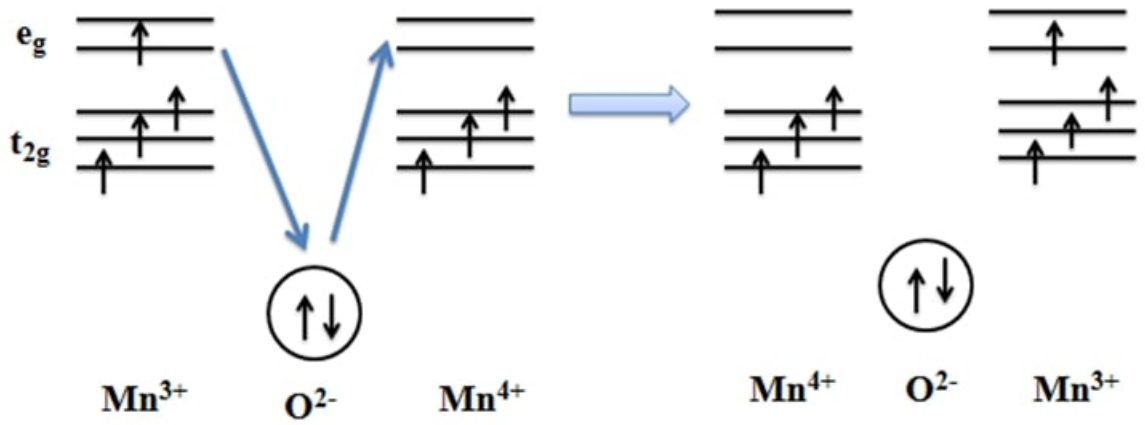

Figure 2.4: Double exchange mechanism.

2.3.3 RKKY coupling (Ruderman-Kittel-Kasuya-Yoshida)

An exchange coupling between a magnetic ion and the conduction band electrons is the cause of RKKY interaction [96]. This interaction is strong between the localized moments carried by the d orbitals of the inner layer. Charge carriers free (roaming electrons or holes) must be present for this type of interaction.

A d electron spin interacts with a conduction electron. The latter interacts with a different d electron spin, resulting in an energy correlation between the two electrons. The spin of the conduction electron orients in the environment of the magnetic ion, and its polarization decreases in an oscillatory fashion with increasing separation from the magnetic ion. This concept was applied to explain the ferromagnetic/antiferromagnetic interaction between two thin ferromagnetic metal layers that are separated from another by a thin non-magnetic metal layer. There is either an antiferromagnetic or ferromagnetic coupling between the two layers, depending on how thick the non-magnetic layer is [97]. The RKKY theory calculates indirect exchange interactions between localized magnetic moments in impurity electrons and holes in DMS [98].

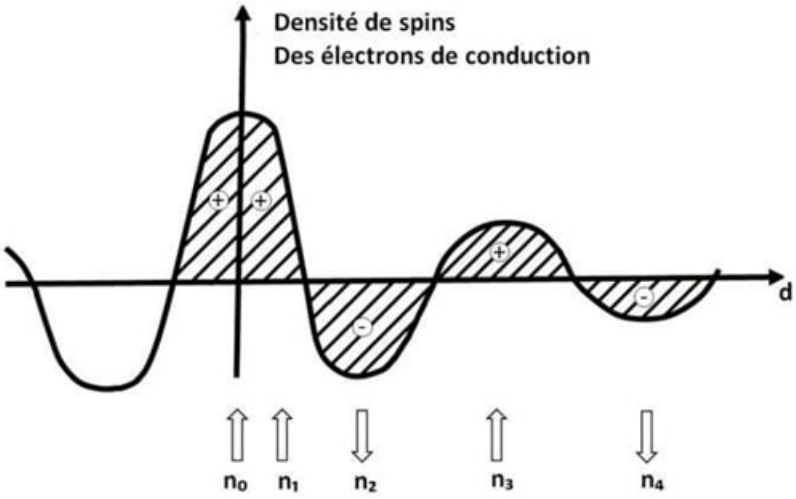

Figure 2.5: Diagrammatic illustration of the indirect RKKY interaction. The conduction electron polarization at site n_0 is represented by (+) et (−), depending on the distance d from the magnetic ion. ↑ and ↓ represent the orientation of the magnetic moments [96].

2.4 Optical properties

The optical properties of a substance are intimately related to its electronic structure. Electrons and radiation interact to produce these characteristics. The complex dielectric function allows for an analysis of the optical characteristics of solids.

2.4.1 Complex dielectric function

The dielectric constant ε remains an indicator of the incident photon energy when the electric field passes through a dispersive material medium at frequencies that are analogous to the medium's inherent electronic or molecular vibration frequencies. The $\varepsilon(\omega)$ is expressed in the complex form, and we adopt the following convention to describe it [99, 100]:

$$\varepsilon(\omega) = \varepsilon_1(\omega) + i\varepsilon_2(\omega) \tag{2.1}$$

With $\varepsilon_1(\omega)$ and $\varepsilon_2(\omega)$ represent the real and imaginary components of the complex dielectric function, respectively.

$\varepsilon_2(\omega)$ depends on electronic transition at origin of the absorption. The following relation gives the $\varepsilon_2(\omega)$ [101]:

$$\varepsilon_2(\omega) = \frac{4\pi^2 e^2}{m^2\omega^2} \sum \int \frac{2dk}{(2\pi)^3} \left|\varphi_{fk} \left\langle |e.p| \right\rangle \varphi_{ik}\right|^2 \delta(E_f(\omega) - E_i(\omega) - \hbar\omega) \tag{2.2}$$

With e represents the electron charge and m its mass, φ_{ik} denotes the initial state filled with energy E_i, and φ_{fk} represents the final empty state of energy E_f.

$\varepsilon_1(\omega)$ can be obtained from $\varepsilon_2(\omega)$ via the Kramers-Kronig relation [102]:

$$\varepsilon_1(\omega) = 1 + \frac{2}{\pi} \int_0^\infty \frac{\omega' \varepsilon_2(\omega') d\omega'}{\omega'^2 - \omega^2} \tag{2.3}$$

The dielectric function represents a fundamental physical characteristic for the light-matter interaction study, but its use is often limited to the area of solid-state physics.

2.4.2 Absorption coefficient

The absorption coefficient, $\alpha(\omega)$, measures the strength of electromagnetic radiation as it travels through any substance. $\alpha(\omega)$ is obtained from the following relation:

$$\alpha(\omega) = 4\pi \frac{k(\omega)}{\lambda} = 2\pi \frac{1}{n(\omega)\lambda} \varepsilon_2(\omega) \tag{2.4}$$

With λ represents the wavelength of the incident photon.

2.4.3 Complex refractive index

When a plane wave travels between two mediums with different dielectric constants, it splits into a refracted wave, and the other is a reflected wave. The following provides the complex refractive index N [99, 102]:

$$N(\omega) = n(\omega) + ik(\omega) \tag{2.5}$$

With:

$$N^2(\omega) = \varepsilon(\omega) \tag{2.6}$$

With $n(\omega)$ is the real refractive index and $k(\omega)$ is the attenuation index, commonly known as the extinction coefficient.

From the previous formula, it is also possible to calculate the $\varepsilon_1(\omega)$ and $\varepsilon_2(\omega)$ according to the equations:

$$\varepsilon_1(\omega) = n^2(\omega) - k^2(\omega) \tag{2.7}$$

And:

$$\varepsilon_2(\omega) = 2n(\omega)k(\omega) \tag{2.8}$$

Where the $n(\omega)$ can be given by:

$$n(\omega) = \sqrt{\frac{\sqrt{\varepsilon_1(\omega)^2 + \varepsilon_2(\omega)^2} + \varepsilon_1(\omega)}{2}} \tag{2.9}$$

And the $k(\omega)$ is equal to:

$$k(\omega) = \sqrt{\frac{\sqrt{\varepsilon_1(\omega)^2 + \varepsilon_2(\omega)^2} - \varepsilon_1(\omega)}{2}} \tag{2.10}$$

2.4.4 Reflectivity

Reflectivity is another important optical property that may be determined from the complex index. This crucial parameter, which defines the portion of energy reflected at the solid-surface interface, is as follows:

$$R(\omega) = \left(\frac{\sqrt{\varepsilon(\omega)} - 1}{\sqrt{\varepsilon(\omega)} + 1}\right)^2 \tag{2.11}$$

2.4.5 Loss function

Moving the electrons through the valence band to the conduction band caused the photon's energy to be lost during the interaction between light and matter. An energy loss function is used to identify this energy loss in the electron transfer. The following is an expression of the energy loss function relationship:

$$L(\omega) = \frac{\varepsilon_2(\omega)}{\varepsilon_1(\omega)^2 + \varepsilon_2(\omega)^2} \tag{2.12}$$

2.5 Thermoelectric properties

The direct and reversible energy conversion of heat to electricity through the application of solid-state conductive materials is known as thermoelectricity [103]. An introduction to thermoelectricity in the context of thermoelectric effects will open up this part of the chapter.

2.5.1 Thermoelectric effects

2.5.1.1 Seebeck effect

Thomas Johann Seebeck first observed the Seebeck effect in 1821. It is the process via which an electric current appears at the junction of two distinct conductors or semicon-

ductors when heat transfer occurs [104]. A potential difference appears at the connection of the two substances exposed to the temperature gradient. An inherent material attribute known as thermoelectric power in the past and the Seebeck coefficient (S) now relate to the proportion of an electric field to a temperature gradient.

$$E = S_{AB} \bigtriangledown_r T \tag{2.13}$$

Where S_{AB} represents the difference in the substances' Seebeck coefficients, and E denotes the electric field produced by temperature gradient $\bigtriangledown_r T$.

2.5.1.2 Peltier effect

Later, in 1834, the French physicist Jean Peltier discovered the reciprocal effect, which states that depending on which direction an electric current runs at the connections of two distinct substances, heat energy is either released or absorbed [105, 106]. The power absorbed or released is given by:

$$Q = \Pi_{AB} I \tag{2.14}$$

Where Q is the heat absorbed or released at the interface, Π_{AB} represents the Peltier coefficient, and I denotes the current.

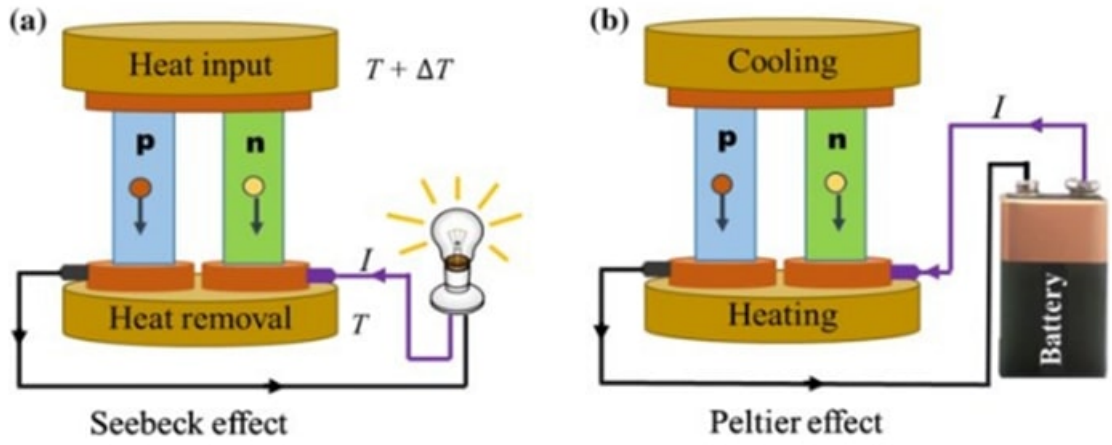

Figure 2.6: Diagrammatic concept of a) Seebeck effect and b) Peltier effect [107].

2.5.1.3 Thomson effect

In 1851, the English physicist William Thomson (Lord Kelvin) showed that the Seebeck and Peltier effects are linked. The generation or absorption of heat in each thermocouple segment becomes apparent when a temperature gradient and an electric current are

applied concurrently. The fundamental difference between the first two effects is that the latter does not concern a single material and does not require the presence of a junction. In each segment dX of the material, the heat flux gradient is given by:

$$\frac{dQ}{dX} = I.\tau.\frac{dT}{dX} \tag{2.15}$$

Where τ denotes the Thomson factor, and X represents the spatial coordinate, given by the relation:

$$\tau_a - \tau_b = T\frac{dS_{AB}}{dT} \tag{2.16}$$

The relation between the three absolute coefficients S, Π, and τ is as follows:

$$\Pi = \tau.S.T \tag{2.17}$$

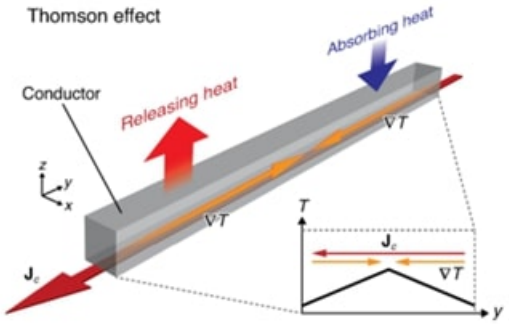

Figure 2.7: Schematic principle of Thomson effect [108].

The Thomson effect causes charge carriers to be heat carriers. The movement of the carriers caused by the temperature gradient generates a current or a potential difference, and vice versa.

2.5.2 Thermoelectric coefficients

Three characteristics define thermoelectric materials:

- The Seebeck coefficient (V/K)
- Electrical conductivity $(\Omega^{-1}.m^{-1}$
- Thermal conductivity $(W/m.K)$

Excellent thermoelectric materials have a substantial Seebeck coefficient, minimal thermal conductivity, and significant electrical conductivity. A parameter called the figure of

merit ZT defines the qualities of a thermoelectric substance specified by the relation:

$$ZT = T\frac{S^2\sigma}{K} \tag{2.18}$$

The variables T, K, S, and σ are the temperature (in Kelvin), thermal conductivity, Seebeck coefficient, and electrical conductivity, respectively. For an excellent thermoelectric material, $ZT \succeq 1$ must be. The power factor ($PF = \sigma S^2$) represents the result of multiplying the electrical conductivity σ by the squared Seebeck coefficient. It explains how much power a substance can generate electricity. To create a better thermoelectric material, the ZT must be improved. For this, it is necessary to decrease thermal conductivity and raise the power factor (PF). The thermal conductivity is the sum of:

$$K = K_e + K_l \tag{2.19}$$

Where K_e denotes the thermal conductivity of electrons, and K_l is the thermal conductivity of atoms (phonons). According to the law of Wiedemann and Franz, the electrical conductivity σ and the electronic thermal conductivity are proportionate:

$$K_e = LT\sigma \tag{2.20}$$

Where L is the Lorentz constant.

In comparison to metals with higher conductivities, semiconductors perform better thermoelectrically. The BoltzTraP code [66] is used in theoretical calculations to establish the intrinsic thermoelectric characteristics, like Seebeck coefficient S, electrical conductivity, and electronic thermal conductivity K_e.

2.6 Applications of half-metal materials

Half-metallic ferromagnetic materials have recently undergone extensive research to take advantage of the 100% spin polarization that spontaneous magnetization induces, which is distinct from magnetic materials (like EuO and (Ga, Mn)As) based on magnetic field-induced ferromagnetism. This family of materials forms an attractive group, offering many potential uses, particularly in spintronics, photovoltaic solar cells, and thermoelectric applications.

2.6.1 Spintronic (Spin electronics)

Traditional electronics rely on semiconductors and the fundamental characteristic of the electron, its electrical charge. A field of study known as spintronics or spin electronics

uses the quantum property of electron spin. This new branch of electronics links the spin state "up" or "down" of the carriers and the dependency on the spin conduction in specific magnetic materials rather than being purely based on the carrier charge as in traditional electronics. Essentially, spintronics is the study of how spin affects electron motion in ferromagnetic materials by putting them in the way of electrons. This influence, first suggested by Mott in 1936, was then demonstrated experimentally and described theoretically over the years. The most common uses of spintronics are writing magnetic memory (MRAM: Magnetoresistive Random Access Memory) in contemporary computers, reading hard disks using GMR, and using Tunnel Magnetoresistance (TMR).

Giant Magnetoresistance (or GMR) was discovered by Albert Fert [3] and P. Grunberg [4] (co-Nobel in physics, 2007). This discovery of GMR and TMR led to a significant technological upheaval in the microcomputing sector. The creation of novel hard disk read head architectures based on this idea has allowed for an increase in the density of computer hard disks, whose capacities have grown significantly over time, from a few Gigabytes at the start of the 1990 to current capabilities that can surpass the Terabyte. Other applications have also emerged, such as MRAM (Magnetic Random Access Memory), which has seen growing interest because it offers intriguing characteristics combining speed, rewriteability, and non-volatility of information even in the absence of supply voltage. Indeed, MRAMs would make it possible to replace DRAM (Dynamic Random Access Memory) memories in the RAM of current computers with much shorter access times. Thanks to magnetic tunnel junction technology, MRAM memories, contrary to DRAM memories, now store information as magnetic moments rather than electrical charges. Since this sort of non-volatile memory does not require continual data refreshing, it will use significantly less energy than existing DRAM memories, giving it a clear benefit of boosting the autonomy of all electronic applications, such as laptop computers.

Other possibilities for integrating spintronics with semiconductor technologies have attracted considerable research interest lately, including SpinLED (Spin Light Emitting Diode) and SpinFET (Spin Field Effect Transistor). The creation of such structures requires overcoming several significant physical challenges. One prerequisite for semiconductor nanostructures is the proper electrical injection of spin-polarized carriers. Solutions based on novel materials, such as diluted magnetic semiconductors, are being researched extensively currently. Then, these polarized carriers must maintain their spin orientation during transport in the semiconductor. Finally, we need to be capable of controlling these spins effectively to perform fundamental logical functions.

2.6.2 Photovoltaic cells

In the fifties of the previous century, modern solar photovoltaics research had been underway. Researchers at Bell Laboratories in the United States unintentionally found in 1954 that a pn junction diode produced a voltage when the light turned on. The same team manufactured a silicon pn junction solar cell with an efficiency of 6% less than a year later [109]. In 1956, it was employed for the first time to power geostationary satellites. In 1957, the Russians (former USSR) were the first to equip their Sputnik II satellite with silicon cells. Just one year later (1958), the Americans outfitted their first Vanguard I satellite with a photovoltaic power supply made of crystalline silicon cells [110]. The first selection of silicon relied on its electrical characteristics, which included four electrons on its outermost layer (column IV of Mendeleev periodic table). Each atom in solid silicon forms four bonds with its neighbors, utilizing all electrons in the surrounding layer. One electron can travel on the network when an atom of silicon is swapped out for an element from column V (like phosphorus), as it is not a part of the bonds. The semiconductor is referred to as n-type doped when there is electron conduction. In contrast, if an atom from column III (such as boron) replaces a silicon atom, an electron is missing to make all the bonds, a gap that an electron can fill. Subsequently, we define the semiconductor as p-type doped, and conduction via a hole is observed.

The photovoltaic effect refers to converting light into electricity, which was discovered by E. Becquerel in 1839. The type of material employed, the geometrical characteristics of the sensor, and its capacity to gather electrons before they recombine in the material can all affect how much electrical energy gets produced. When a semiconductor becomes illuminated with radiation of appropriate wavelength, the absorbed photon energy allows electronic shifts through the semiconductor's band valence to its conduction band, thus generating electron-hole pairs, which can contribute to the transport of current (photo-conductivity) by the material when it is polarized [111]. Heat or phonon emissions are the two ways that extra energy is released. The photon transmits through the semiconductor when its energy $h\nu$ is less than the band gap E_g.

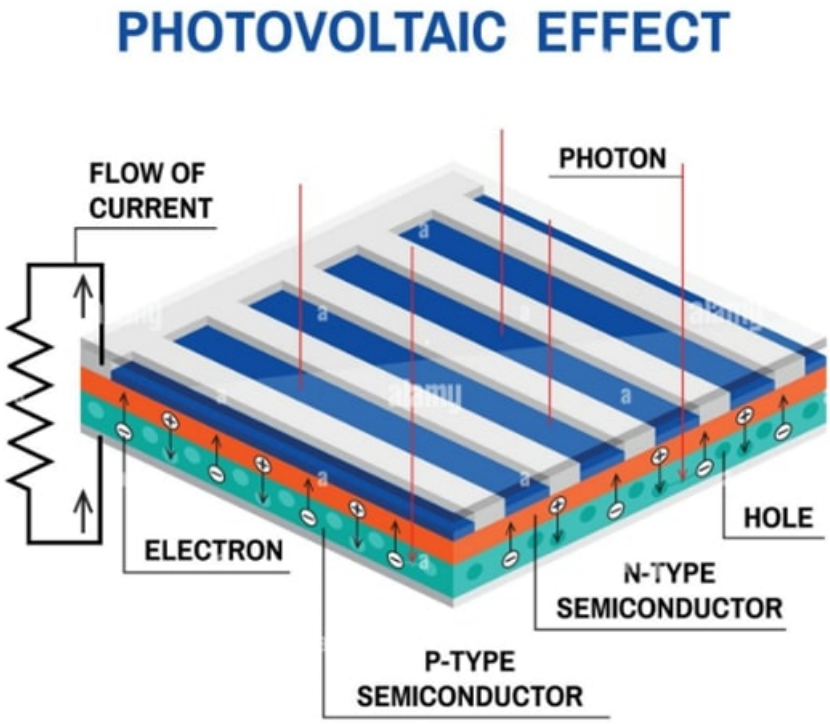

Figure 2.8: P-N junction in a photovoltaic cell [111, 112].

Solar cells are currently the subject of multiple research to achieve the best ratio between energy efficiency and cost price. The application of photovoltaic energy became apparent, and in recent years, significant endeavors have been developing to produce this energy. According to estimates, solar electricity could have an enormous long-term impact on global energy usage. According to a joint scenario produced by EPIA and Greenpeace, photovoltaics might supply enough energy in 2030 to power 3.7 million people globally, with the help of proper public policies in wealthy and developing nations. Most of them are located in isolated areas, lacking any access to the electricity network.

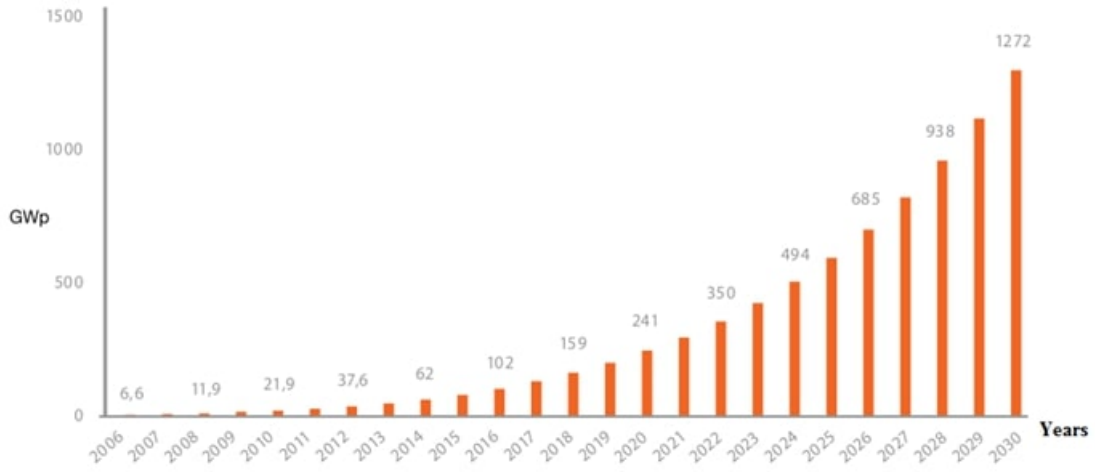

Figure 2.9: Cumulative global capacity until 2030-Advanced scenario [113].

However, the fabrication of the DMS for photovoltaic conversion has not been used yet, even if it could be a crucial component of future advancements in solar cell technology. According to some theoretical investigations, DMS SnO_2 doped with double impurities (Eu, Gd) might absorb up to 96% of visible light [209]. The impact of Mn and Co co-doped SnO_2 on optical properties has been reported by Lin et al. There was a significant improvement in the absorption capacity of Mn and Co co-doped SnO_2 in visible region [210]. Furthermore, double perovskites have emerged as a potential substitute for solar cells since researchers have laboriously constructed solar cells for photovoltaic devices [211 - 214].

2.7 Conclusion

In this chapter, we presented the different families of magnetic semiconductors and the different types of interaction between the magnetic moments in DMS with the models established to explain ferromagnetism in DMS. We also discussed a general review of the thermoelectric and optical characteristics. We will study in the next chapter the structure electronic, magnetic, optical, and thermoelectric characteristics of 3D materials (SnO_2 doped with doubles impurities, Double Perovskites) and 2D ZnO nanosheets doped by the transitions metal through FP-LAPW method.

Chapter 3

Study of the structural, electronic, magnetic, optical, and thermoelectric properties of SnO_2 coupled with double substitutions Mn and A=Mo/Tc

Introduction

Half-metallic materials have grown significantly in technological relevance over the last two decades due to their remaining physical properties. These compounds have an outstanding range of potential for usage in several technology applications, including thermoelectric, photovoltaic, and Spintronics. The study of new magneto-optical properties is possible by combining the magnetic and optical characteristics of half-metallic. Despite the numerous research investigations on this subject, spintronics combined with optoelectronics remains almost untouched. In the upcoming years, ferromagnetic material-based solar cell production could have a big impact on how solar cell technology develops.

Instead of the conventional single impurity, the current work studies oxide-based semiconductors doped with double impurities of transition metals M1 and M2 (different) for various reasons. One of these is the potential to prevent oxygen vacancies, which can lead to material deformation. It is feasible to create ferromagnetic half-metallic materials where the conduction electrons are 100% spin polarization by choosing a suitable choice of double impurity. These properties have inspired us to search for DMS ferromagnets based on rutile SnO_2 doped with double impurities to develop spin electronics and incorporate information storage functions, multiple sensors, and light transmitters into a single component. In this chapter, we essentially devoted ourselves to the study of the structural, magnetic, electronic, optical, and thermoelectric characteristics using TB-mBJ and GGA-PBE approaches, identifying the mechanisms responsible for the magnetic interactions of the diluted magnetic semiconductor SnO_2 doped by two magnetic elements Mn and A(=Mo or Tc). Our calculations involved determining the stability of the complex SnO_2 co-doped with coupled Mn and A=Mo/Tc as well as the total energy ferromagnetic (FM) and antiferromagnetic (AFM) state. We also discussed the density of states of co-doped SnO_2 and pristine SnO_2 without any doping elements. The thermoelectric and optical characteristics of the complex $Sn_{1-2x}Mn_xA_xO_2$ will then be discussed.

3.1 Tin dioxide SnO_2

Tin oxide or "stannic oxide" is found naturally in the form of the mineral cassiterite. Since ancient times, people have used cassiterite, an oxide that may vary in color from yellowish to black. SnO_2 is a semiconductor of n-type with approximately 97% optical transparency in visible region and a large band gap of 3.6eV. Because of its extensive availability as a raw material and lack of toxicity, SnO_2 is still in demand. This substance has unique physical characteristics that make it among the likely candidates for application in solar cells, optoelectronic devices, and thermoelectric materials [114, 115].

3.2 Crystal structure

Tin dioxide presents a single stable phase at ambient pressure [116] and takes the form of a quadratic cell of the rutile type with a space group P42/mnm [117]. The parameters of the crystalline lattice are: $a = b = 4.74\mathring{A}$ and $c = 3.18\mathring{A}$. The unit cell consists of two atoms of tin and four oxygen atoms. Six oxygen atoms form an almost regular octahedron around each tin atom, and three tin atoms are positioned at the vertices of an isosceles triangle to encircle each oxygen atom. Oxygen occupies position 4f by $[u, u, 0]$, $[1-u, 1-u, 0]$, $\left[u+\frac{1}{2}, \frac{1}{2}-u, \frac{1}{2}\right]$, and $\left[\frac{1}{2}-u, u+\frac{1}{2}, \frac{1}{2}\right]$ with $u = 0.306$. Tin is at positions 2a, $[0, 0, 0]$, and $\left[\frac{1}{2}, \frac{1}{2}, \frac{1}{2}\right]$. We created a supercell by repeating the $2\times2\times2$ unit cell, which generates 48 atoms $Sn_{16}O_{32}$ (see Figure 3.1(a)).

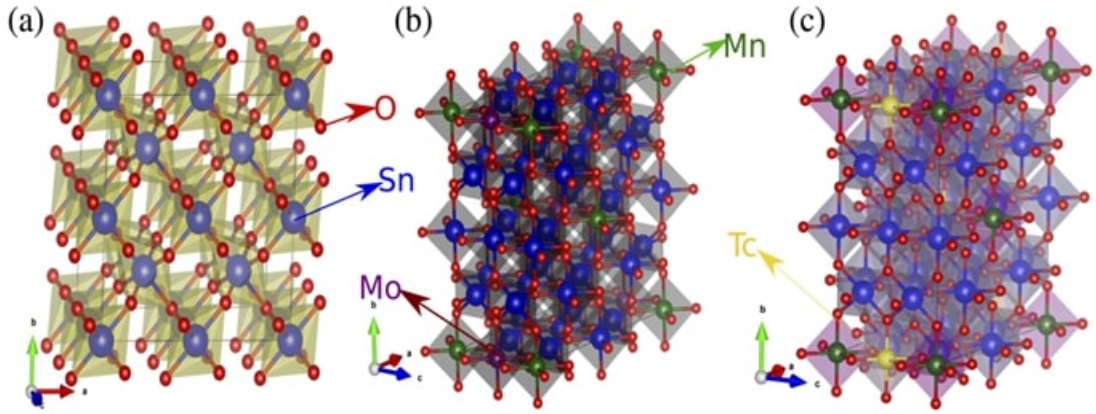

Figure 3.1: $2 \times 2 \times 2$ supercell structure of (a) SnO_2, (b) $Sn_{1-2x}Mn_xMo_xO_2$, and (c) $Sn_{1-2x}Mn_xTc_xO_2$ ($x = 0.0625$).

3.3 Calculation methods

We have employed in total calculations the FP-LAPW method founded on DFT carried out in the Wien2k package [65, 118]. We have used in this study the GGA-PBE [41, 119] and the TB-mBJ approaches [48, 120]. TB-mBJ aims to increase energy gap values. Two zones are formed in the space using the FP-LAPW method: region I, which is an interstitial area, and region II, which is a non-overlapping sphere around the R_{MT} Ray (Muffin-Tin) atomic sites. The size of the base in the interstitial area is determined by $R_{MT} \times K_{\max} = 7$. The highest wave vector utilized in the plane wave expansion of eigenfunctions is represented by $K_{\max}$, and R_{MT} is the smaller muffin-tin radius measured in atomic units (au). Considering a force of 0.1mRy/au, we employed self-consistent criteria for total energy, with an accurate $10^{-6}Ry$ and a charge difference of $10^{-6}e$ between

2 consecutive iterations. We have substituted two atoms of Sn with Mn and A=Mo/Tc with a concentration of $x = 0.0625$ in $Sn_{1-2x}Mn_xA_xO_2$ to create co-doped systems in the supercell [see Figure 3.1(b and c)].

3.4 Structural properties

The Murnaghan equation serves to minimize the total energy obtained for various volumes to determine the optimized mesh parameters [121], given by:

$$E(V) = E_0 + \frac{9V_0B_0}{16}\left[\left[\left(\frac{V_0}{V}\right)^{\frac{2}{3}} - 1\right]^3 B_0' + \left[\left(\frac{V_0}{V}\right)^{\frac{2}{3}} - 1\right]^2 \left[6 - 4\left(\frac{V_0}{V}\right)^{\frac{2}{3}}\right]\right] \tag{3.1}$$

Where E_0, V_0, V, B_0, B_0' represent the equilibrium energy, original volume, obtained volume change, bulk modulus, and first-order pressure derivative, respectively. The total energy against volume for pristine SnO_2 and co-doped co-doped SnO_2 with Mn and A=Mo/Tc are shown in Figure 3.2. These curves made it possible to determine the values of the balance parameter, a, and (B_0), from the Murnagham equation of state. Table 3.1 shows and compares the optimized parameters of the crystalline lattice with the previously published data. Using equation (3.2), we were able to calculate the formation energy E_{for} to further investigate the stability of the co-doped SnO_2 and pristine SnO_2 without any doping elements:

$$E_{for} = E_{tot} - \sum_x E_x \tag{3.2}$$

Where E_{tot}, x, and E_x represent the total energy in the ground state, the number of each element, and the energy of one element in its bulk form, respectively. For SnO_2 pure, $Sn_{1-2x}Mn_xMo_xO_2$, and $Sn_{1-2x}Mn_xTc_xO_2$, the computed E_{for} are -2.42eV, -1.57eV, and -1.54eV per atom, respectively. Our systems are stable, as evidenced by the negative values of E_{for}. The ferromagnetic and antiferromagnetic states are calculated to establish a more stable magnetic state. In the DMS, the calculation of the total energy differential, $\Delta E = E_{AFM} - E_{FM}$, computes the stability of the magnetic phase. Positive values indicate a consistent and stable FM condition, while negative values indicate a steady and stable AFM state. The comparison of the total energy of the ferromagnetic (FM) and antiferromagnetic (AFM) states shows that the ferromagnetic state is more stable in the complex $Sn_{1-2x}Mn_xMo_xO_2$. While in the compound $Sn_{1-2x}Mn_xTc_xO_2$, the antiferromagnetic state is more stable.

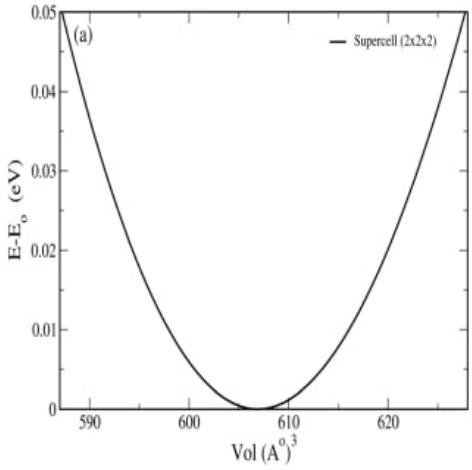

(a)

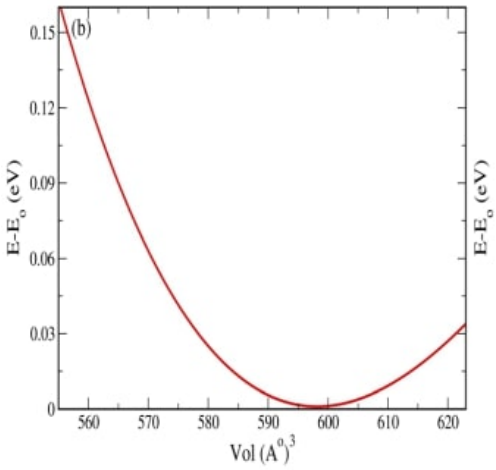

(b)

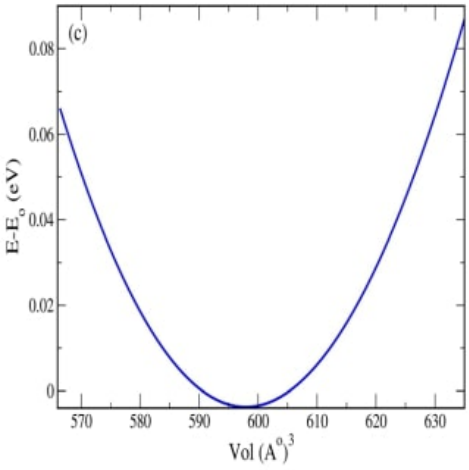

(c)

Figure 3.2: Structure of $2 \times 2 \times 2$ supercell of (a) SnO_2, (b) $Sn_{1-2x}Mn_xMo_xO_2$, and (c) $Sn_{1-2x}Mn_xTc_xO_2$ ($x = 0.0625$).

Systems	a=b	c	B_0	B_0'
SnO_2	4.737	3.186	186.028	4.249
Ref.122	4.767	3.129	–	–
Ref.117	4.74	3.18	–	–
$Sn_{1-2x}Mn_xMo_xO_2$	13.57	6.454	167.133	10.995
$Sn_{1-2x}Mn_xTc_xO_2$	13.662	6.498	177.672	0.454

Table 3.1: Results of the optimized lattice parameters, bulk modulus (B_0), and its pressure derivative (B_0').

3.5 Electronic and magnetic properties

3.5.1 Pristine SnO_2

Figure 3.3 shows the total and partial densities of states (DOS) of Pristine SnO_2 that we computed using the TB-mBJ potential. The line with a dash reflects the Fermi level ($E_f = 0eV$). The complete symmetry between the up and down spin states in the electronic structure suggests that SnO_2 is a non-magnetic semiconductor substance. The orbitals O-2p make up most of the valence band, which is totally full. The Sn-5s orbitals dominate the conduction band, which is empty. The GGA-PBE and TB-mBJ yielded band gap values of 1.85eV and 3.59eV, respectively. We have found similar results in the earlier theoretical computations [122 - 124]. As a result, the GGA-PBE approximation underestimates the energy gap. After using the TB-mBJ correction, we found the same value as the experimental data, which is 3.6eV [125]. The breadth of the valence band (O-2p orbital) is 7.1eV, according to the findings of prior theoretical studies and experiments [123, 126].

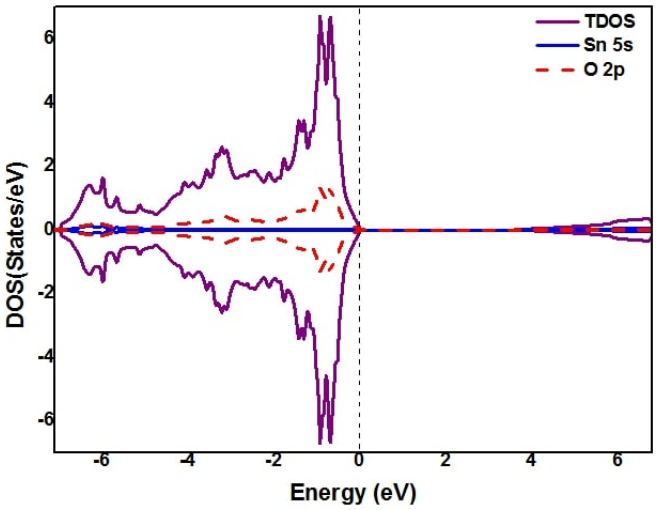

Figure 3.3: Diagram of DOS for pristine SnO_2 by applying the TB-mBJ.

3.5.2 SnO_2 co-doped with Mn and A=Mo/Tc

As can be seen in Figures 3.4 and 3.5, the DOS exhibits asymmetry, a characteristic of magnetic behavior. These figures show the half-metallic characteristic, in which the Fermi level appears in the majority spin band. It results in significant polarization of spin around the Fermi level. Asymmetric DOS refers to a situation where appropriate doping brings the Fermi level near the conduction band, resulting in a distinct number of states available

for carrier transport. In the spin majority bands of the complex $Sn_{1-2x}Mn_xMo_xO_2$ using the GGA-PBE, the Mn-3d and Mo-4d orbitals are mainly accountable for the half-metallic ferromagnetic feature close the Fermi level. We also observe the significant p-d hybridization among O-2p and 3d-4d orbitals. In contrast, the TB-mBJ correction split the impurity states Mn-3d and Mo-4d around the Fermi level. It may be easier to excite electrons to the conduction band when their energy levels are at the highest point of the band gap. Doping by coupled Mn-Mo decreases the band gap. An n-type material is formed when the Fermi level lies near the conduction band. Table 3.2 shows the overall and fractional magnetic moments of the several impurities within the compound $Sn_{1-2x}Mn_xMo_xO_2$. The compound $Sn_{1-2x}Mn_xMo_xO_2$ has a total magnetic moment of $5\mu_B$. Strong interaction between the double impurities is suggested by the significant overall magnetic moment value. The Mn and Mo atoms provide local magnetic moments of $3.51\mu_B$ and $0.81\mu_B$, respectively. They play a considerable role in the formation of the overall magnetic moment. The local magnetic moments in the simple doping by Mn ($Sn_{1-x}Mn_xO_2$) and Mo ($Sn_{1-x}Mo_xO_2$) are $2.87\mu_B$ and $1.3\mu_B$, respectively. When comparing the partial magnetic moments of Mn and Mo in simple doped (($Sn_{1-x}Mn_xO_2$) and ($Sn_{1-x}Mo_xO_2$)) and the doped with double impurities ($Sn_{1-2x}Mn_xMo_xO_2$), it is clear that several new states appear in the spin-up band of Mn-3d orbitals where a charge transfer from Mo to Mn occurs. We can infer that a charge transfer occurs among the Mo and the Mn electrons through the 2p-O atom. We can obtained an electronic configuration for $[Mn^{3+}(3d^5)]$ and $[Mo^{5+}(5d^1)]$. Thus, it is evident that the double Zener exchange is the process causing ferromagnetic coupling.

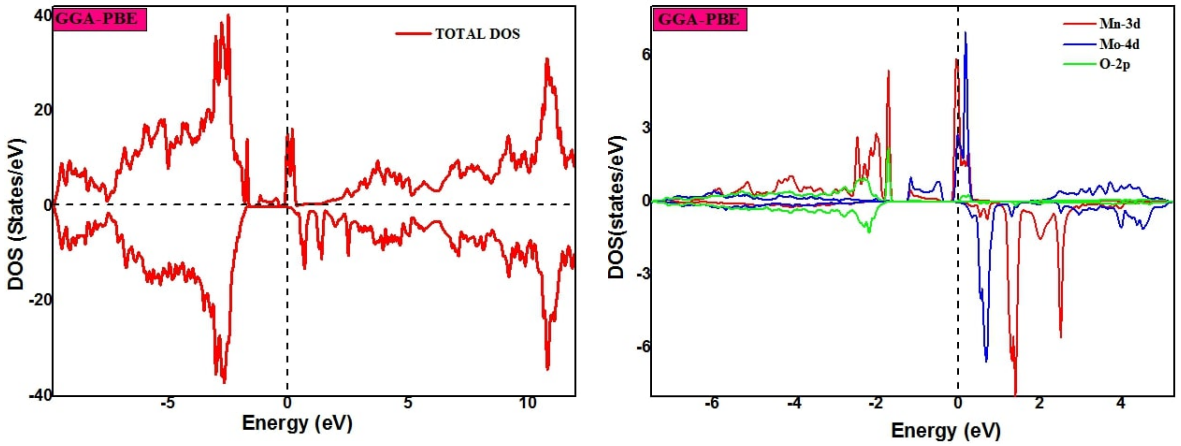

(a) (b)

Figure 3.4: (a) Total and (b) partial DOS of SnO_2 co-doped with Mn and Mo by applying the GGA-PBE approach.

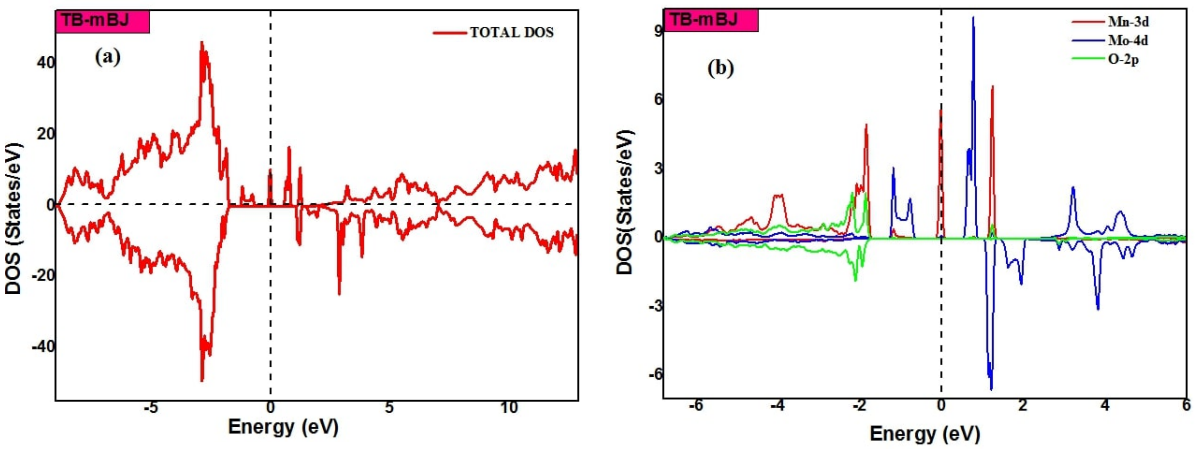

(a) (b)

Figure 3.5: (a) Total and (b) partial DOS of SnO_2 co-doped with Mn and Mo by applying the TB-mBJ approach.

The doping with dual impurities Mn and Mo has significantly altered the electronic and magnetic characteristics of SnO_2, as we have previously clarified. So, we carried out another co-doping with the dual impurities Mn and Tc. Figure 3.6 and Figure 3.7 depict the DOS calculations for $Sn_{1-2x}Mn_xTc_xO_2$ by applying the GGA-PBE and TB-mBJ, respectively. Near the Fermi level, double impurities cause the DOS to shift and become asymmetric. The novel states are created around the Fermi level by doping with the dual impurities Mn and Tc. High spin polarization in the spin-up band leads to the half-metallic characteristic The spin-down is empty and hybrid with the conduction band. Within the GGA-PBE, the 3d-Mn, 4d-Tc, and 2p-O orbitals appear around the Fermi level, leading to the robust hybridization p-d. The complex $Sn_{1-2x}Mn_xTc_xO_2$ has a significant total magnetic moment of $6\mu_B$. Table 3.2 shows the partial magnetic moments of Mn, Tc, and O atoms. Mn ($m_{Mn} = 2.97\mu_B$) and Tc ($m_{Tc} = 1.82\mu_B$) make up most of the overall magnetic moment. The local magnetic moments of the Mn and Mo atoms in the simple doped (($Sn_{1-x}Mn_xO_2$) and ($Sn_{1-x}Mo_xO_2$)) are $2.87\mu_B$ and $1.87\mu_B$, respectively. According to these findings, there is no evidence of a double Zener exchange (absence of charge transfer). Therefore, p-d hybridization can explain the ferromagnetism in SnO_2 co-doped with Mn and Tc.

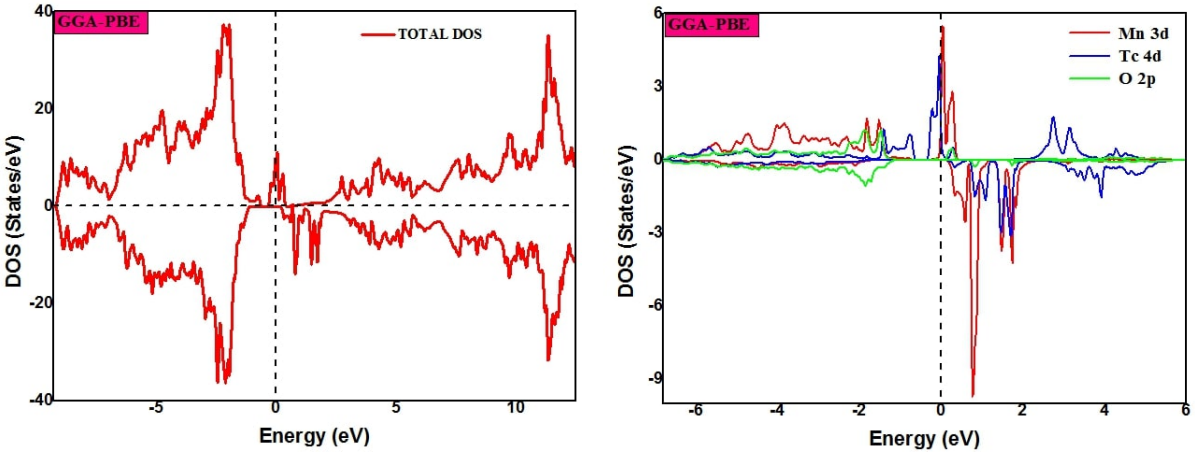

(a) (b)

Figure 3.6: (a) Total and (b) partial DOS of $Sn_{1-2x}Mn_xTc_xO_2$ using GGA-PBE approach.

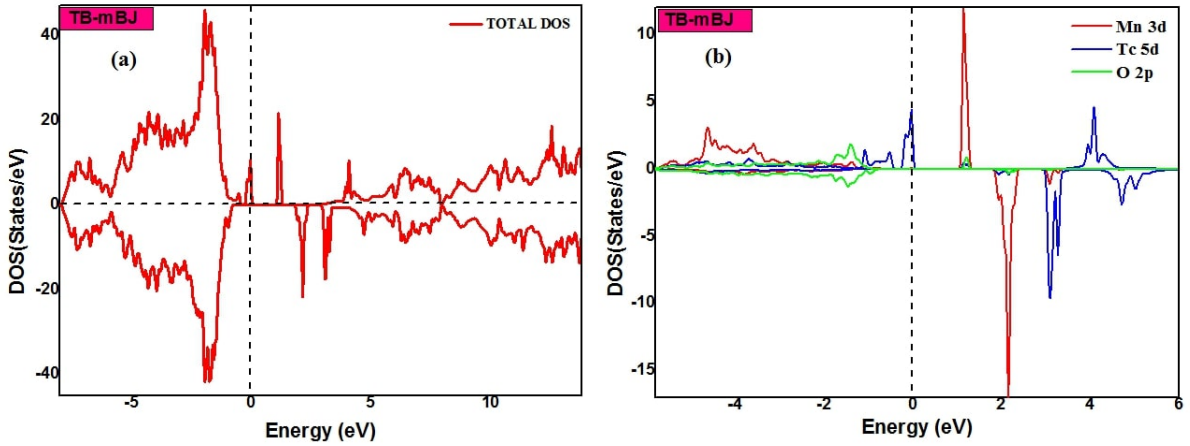

(a) (b)

Figure 3.7: (a) Total and (b) partial DOS of $Sn_{1-2x}Mn_xTc_xO_2$ using TB-mBJ approach.

	$Sn_{1-x}Mn_xMo_xO_2$	$Sn_{1-x}Mn_xTc_xO_2$
E_{FM}	-188249.705	-188723.737
E_{AF}	-188249.704	-188723.738
E_g	1.73/2.869	1.319/2.653
m_T	5.0/5.0	6.0/6.003
m_{Mn}	3.51/3.71	2.97/3.025
m_{Mo}	0.81/0.79	–
m_{Tc}	–	1.82/2.091
m_O	-0.005	-0.005

Table 3.2: Results of the total energy ferromagnetic $E_{FM}(Ry)$ and antiferromagnetic $E_{AFM}(Ry)$, energy gap $E_g(eV)$, total magnetic moment $m_T(\mu_B)$ and local magnetic moment $m_O(\mu_B)$ and $m_{TM}(\mu_B)$ using GGA-PBE/TB-mBJ approaches.

3.6 Optical properties

The optical characteristics are the result of the response of an electronic system to a time-dependent electromagnetic disturbance whose origin is incident light. Understanding the many ways that light interacts with matter—such as through absorption, transmission, reflection, scattering, and emission—is quite interesting. The atomic structure is ultimately connected to these optical features by their tight relationship with the electronic band structure [127]. The way a material responds to an electric field, such as an oscillating light wave, is described by the dielectric function $\varepsilon(\omega)$ [128]. Direct or indirect electronic transitions may result from interactions between electron-hole pairs and energy levels brought on by defects or impurities. $\varepsilon_2(\omega)$ originates from the complete direct transition and is related to absorption. When the energy of the bandgap is less than the energy of the incoming photon, the absorption process happens. $\varepsilon_2(\omega)$ is zero when a material is transparent, but it becomes non-zero when absorption starts. In this work, there exist two non-zero components that characterize the tensor of the dielectric function of the tetragonal structure, $\varepsilon_{xx} = \varepsilon_{yy} \neq \varepsilon_{zz}$.

The evolution of real $\varepsilon_1(\omega)$ and imaginary $\varepsilon_2(\omega)$ components versus the energy photon in the range 0-12eV are displayed in Figure 3.8 by employing GGA-PBE and TB-mBJ approaches for pure SnO_2 and co-doped SnO_2 with Mn and A(=Mo/Tc). Table 3.3 displays the values of $\varepsilon_1(0)$, the computed static dielectric constants and are higher when co-doping SnO_2 with coupled Mn-A, where A=Mo/Tc. The high value of $\varepsilon_1(\omega)$ at lower energy signifies a better polarization ability. The material displays metallic behavior because the $\varepsilon_1(\omega)$ has a negative value in the high-energies region, indicating complete reflection of the incident photon. The curves of $\varepsilon_2(\omega)$ versus the energy of the photon appears in Figure 3.8 (c, d). In the infrared and visible ranges, pure SnO_2 exhibits zero $\varepsilon_2(\omega)$ because of its high transmission in these areas. This computation is comparable to that of SnO_2 in the absence of doped components [129 - 131]. The SnO_2 co-doping effect by the coupled Mn and A=Mo/Tc is visible in the low energy range. We can observe novel peaks in visible and IR areas different from SnO_2 pristine. These peaks reflect the light absorption and show the interband electronic shifts among the occupied and unoccupied states. These compounds have the potential to be used in the development of optoelectronic applications that function well in the visible and infrared spectrum due to their capacity to absorb incoming radiation with a frequency in this range.

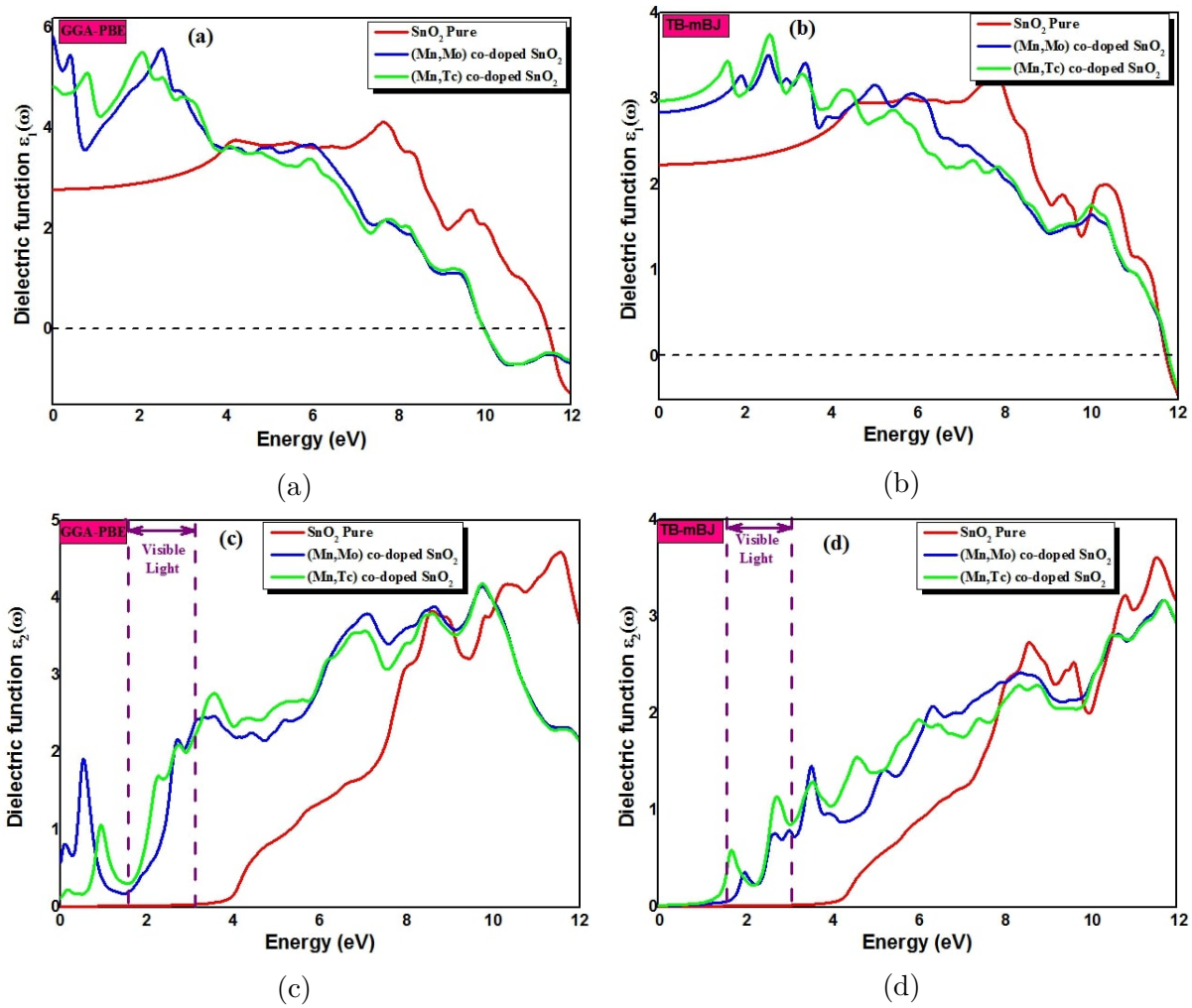

Figure 3.8: The real $\varepsilon_1(\omega)$ (a, b) and imaginary $\varepsilon_2(\omega)$ (c, d) components of the dielectric function versus energy photon using GGA-PBE and TB-mBJ approaches.

Parameter	SnO_2	$Sn_{1-x}Mn_xMo_xO_2$	$Sn_{1-x}Mn_xTc_xO_2$
$\varepsilon_1(0)$	2.79/2.23	5.83/2.84	4.83/2.97
$n(0)$	1.67/1.49	2.41/1.68	2.19/1.72
$R(0)\%$	6.26/3.93	17.13/6.51	13.99/7.06

Table 3.3: Outcomes of optical characteristics at zero energy of pure SnO_2 and SnO_2 co-doped with Mn and A=Mo/Tc using GGA-PBE/TB-mBJ approaches.

Other significant optical characteristics, like the refractive index $n(\omega)$, the optical absorption coefficient $\alpha(\omega)$, the loss function $L(\omega)$, and the reflectivity $R(\omega)$, can be found by determining the two components of $\varepsilon(\omega)$. A further metric for describing the photovoltaic properties of a material is the absorption coefficient. The spectra of $\alpha(\omega)$ versus photon energy for the pure SnO_2 and SnO_2 co-doped with Mn and A=Mo/Tc are shown in Figure 3.9 by applying the GGA-PBE and TB-mBJ. The electronic transitions are shown as the main peaks in the $\alpha(\omega)$ spectra. As compared to SnO_2, Figure 3.9

shows an improvement in the quantity of absorption in low-energy regions. The maximum absorption peaks appear in the high-energy regions (UV light). The absorption of visible and ultraviolet light by these materials indicates that they can be used as an absorbent layer for flat-screen displays and solar cells.

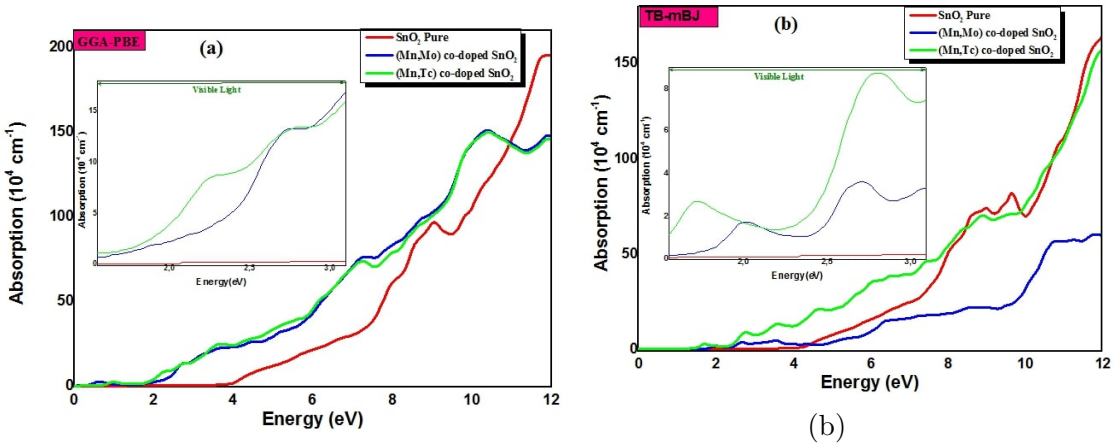

(a) (b)

Figure 3.9: Absorption coefficient $\alpha(\omega)$ against photon energy using a) GGA-PBE and b) TB-mBJ approaches.

The curves of the refractive index $n(\omega)$ with changes in photon energy are shown in Figure 3.10. The action of light within the material is described by $n(\omega)$, which varies depending on the incident photon. The static refractive index, $n(0)$, is shown in Table 3.3. At low frequencies ($\omega \approx 0$), we can conclude that $n(0) = \sqrt{\varepsilon_1(0)}$. The high values of $n(\omega)$ appear in low energies of photons. The reflectivity $R(\omega)$ of light is the crucial metrics that characterize the amount of energy reflected at the solid surface. The variation of $R(\omega)$ spectra of pristine SnO_2 and co-doped SnO_2 with Mn and A(=Mo/Tc) versus photon energy appears in Figure 3.11. The $R(\omega)$ values increase as we approach the high photon energies. Table 3.3 lists $R(0)$ of the reflectivity parameter at zero energy obtained from spectrum analysis. An electron traveling through a material quickly will lose energy; this may be explained by the energy loss function $L(\omega)$. Figure 3.12 represents the spectra of the variation of $L(\omega)$ obtained for the pure SnO_2 and co-doped SnO_2 with Mn and A(=Mo/Tc) versus photon energy. The loss happens during the electron shift from the valence band to the conduction band. The peaks in the $L(\omega)$ spectra are identified as plasma peaks, indicating ensemble excitations of the electronic charge density of the crystal.

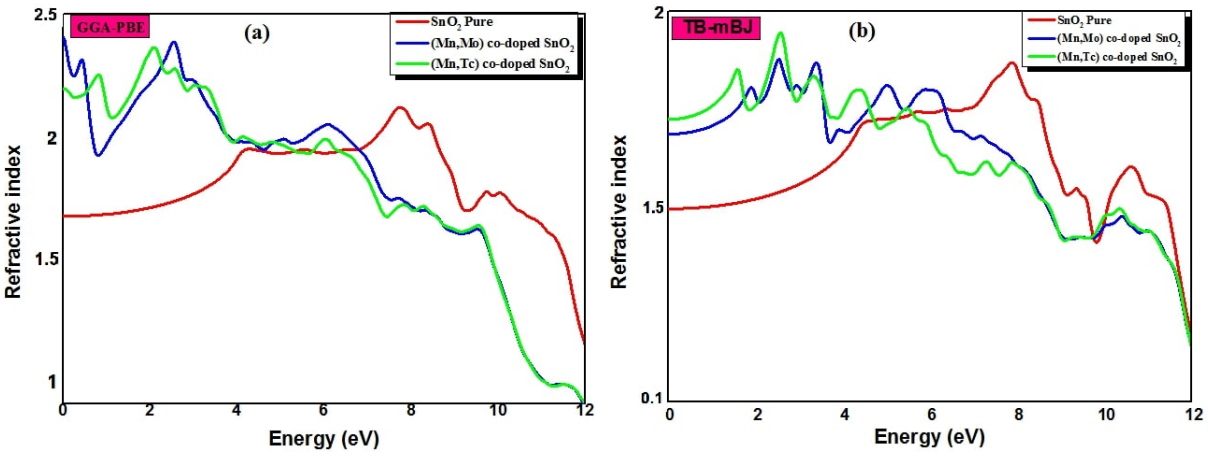

(a) (b)

Figure 3.10: Spectra of refractive index $n(\omega)$ against photon energy by applying a) GGA-PBE and b) TB-mBJ approaches.

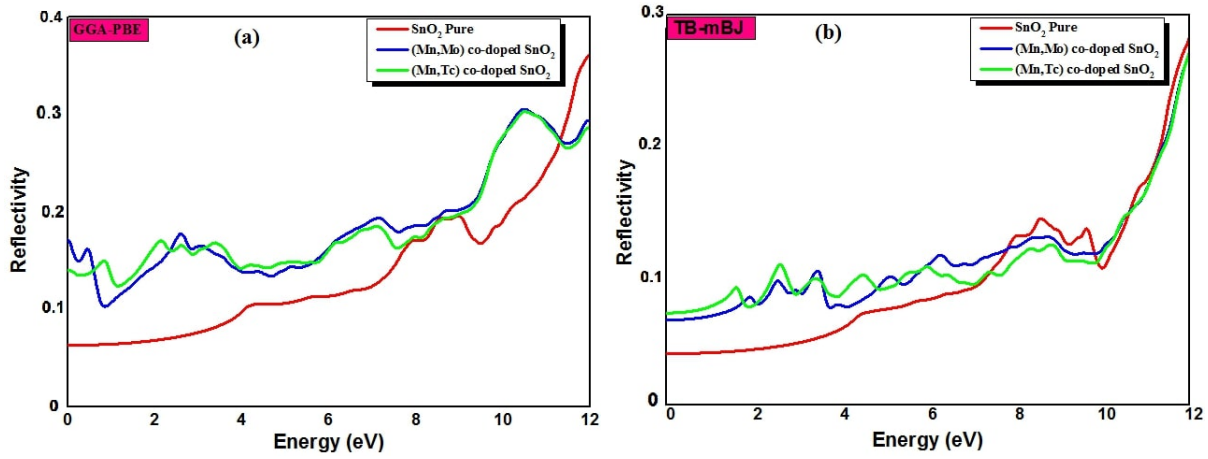

(a) (b)

Figure 3.11: Spectra of reflectivity $R(\omega)$ versus photon energy by applying a) GGA-PBE and b) TB-mBJ approaches.

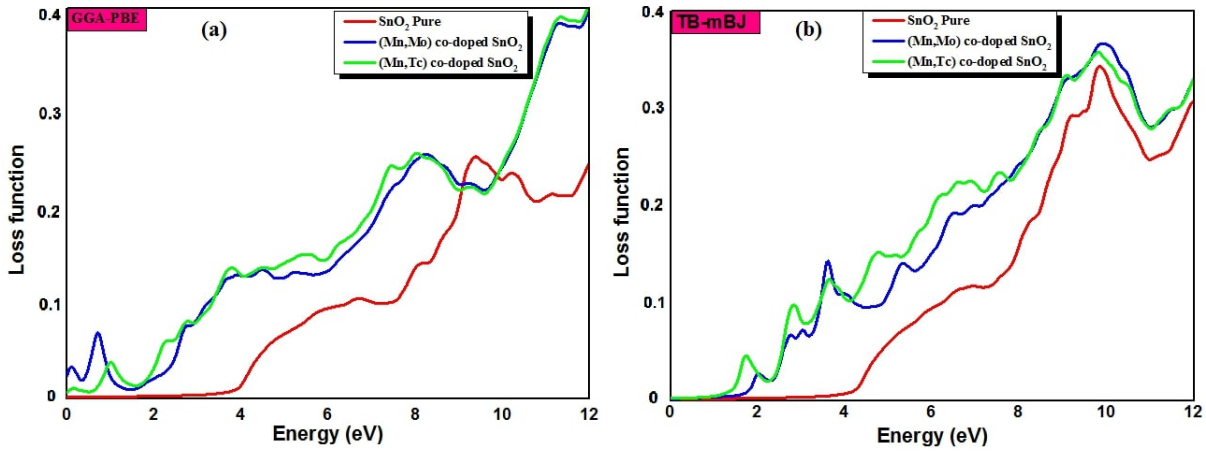

(a) (b)

Figure 3.12: Spectra of loss function $L(\omega)$ against photon energy by applying the a) GGA-PBE and b) TB-mBJ approaches.

3.7 Thermoelectric properties

We have used the BoltzTraP code [66] to calculate the thermoelectric characteristics. In our work, the relaxation time τ is considered constant ($\tau = 10^{-14}s$) [132, 133]. The most efficient thermoelectric substances need to have a low value of thermal conductivity (k) and a substantial electrical conductivity (σ) to minimize heat loss due to the Joule effect. $ZT = (S^2\sigma T/k)$ is the parameter that groups all these characteristics. We have used the GGA-mBJ approximation to perform the calculation in this section. We calculated the fundamental parameters like the electrical conductivity (σ), electronic thermal conductivity (k_e), Seebeck coefficient (S), and power factor (PF) against the chemical potential (μ) for different temperature values for SnO_2 co-doped with Mn and A=Mo/Tc. The n-type doping is associated with a positive chemical potential, while p-type doping is associated with a negative chemical potential.

Assessing the link between the electric potential and the thermal potential is made feasible by the Seebeck coefficient (S). A positive Seebeck value reflects a p-type of carriers (holes), while a negative Seebeck value reflects an n-type of carriers (electrons). Figures 3.13a and 3.14a represent the findings of the (S) values against the chemical potential (μ) for SnO_2 co-doped with Mn and A=Mo/Tc. In p-type doping, as we can see, the S values are positive; in n-type doping, they are negative. The variation of (S) shows a maximum at low temperatures and decreases with temperature rise. Due to the bipolar effect, which occurs when an electron and a hole cooperate to promote charge transport, the Seebeck coefficient gradually rises and falls [134]. These complexes exhibit high (S) values at room temperature, indicating their potential application as low-temperature thermoelectric materials.

The differences in electrical conductivity (σ) with chemical potential (μ) are presented in Figures 3.13b and 3.14b for SnO_2 co-doped with Mn and A=Mo/Tc. The movement of free electrons within a substance defines its electrical conductivity. A current of electricity is the flow of electrons from areas of increased temperature to zones of decreased temperature [135]. At 300K, The σ values are $5.7 \times 10^5 \Omega^{-1}.m^{-1}$ and $1.7 \times 10^5 \Omega^{-1}.m^{-1}$ for SnO_2 co-doped with Mn and Mo or Mn and Tc, respectively.

The capacity of a substance to transmit heat in response to a thermal gradient is measured by its thermal conductivity (k). Two contributions make this heat transfer possible: the electronic thermal conductivity (k_e), which occurs using the movement of charges, and the network thermal conductivity (k_l), which occurs by the network vibrations, also known as phonons. The total of these two contributions is the k. Figures 3.13c and 3.14c show the electronic thermal conductivity (k_e) versus the chemical potential for SnO_2 co-doped with Mn and Mo or Mn and Tc compounds. From these outcomes, we can see that the (k_e) increases with increasing temperature. Heating the material causes the atomic vibrations to rise to a point where they transfer energy in the form of kinetic energy, which is what causes the increase in (k_e).

Moreover, a good power factor ($PF = S^2\sigma$) is indicative of the optimum thermoelectric performance. The PF versus chemical potential appears in Figures 3.13d and 3.14d. At 300K, The PF values for $Sn_{1-2x}Mn_xMo_xO_2$ and $Sn_{1-2x}Mn_xTc_xO_2$ are 54×10^{-4} and $12 \times 10^{-4} (V^{2\cdot}K^{-2}.\Omega^{-1}.m^{-1})$, respectively.

To calculate the ZT, we need to determine the lattice thermal conductivity (k_l). By considering the minimal phonon mean free path, we will apply the approach to obtain the least (k_l) value. The following equation, which is derived using the bulk modulus and volume relationship of the unit cell using DFT, provides a ballpark estimate of $(k_l)_{\min}$ [136, 137]: $(k_l)_{\min} = 1.2K_B M_{av}^{-\frac{1}{2}} B^{\frac{1}{2}} V^{-\frac{1}{6}}$, With K_B, M_{av}, ($M_{av} = \frac{M}{nN_A}$), M, N_A, n, B, and V represent the Boltzmann constant, the average atomic mass, the molecular mass, the number of Avogadro, the number of atoms in the unit cell, the bulk modulus, and the average atomic volume, respectively. The calculated values $(k_l)_{\min}$ of SnO_2 co-doped with Mn and Mo and SnO_2 co-doped Mn and Tc are 11.15 and 3.08 ($W.m^{-1}.K^{-1}$), respectively. At 300K, The (k_e) values of SnO_2 co-doped with Mn and Mo and SnO_2 co-doped Mn and Tc are 3.03 and 1.21 ($W.m^{-1}.K^{-1}$), respectively. The ZT values at 300K for $Sn_{1-2x}Mn_xMo_xO_2$ and $Sn_{1-2x}Mn_xTc_xO_2$ have been estimated to be 0.114 and 0.11, respectively.

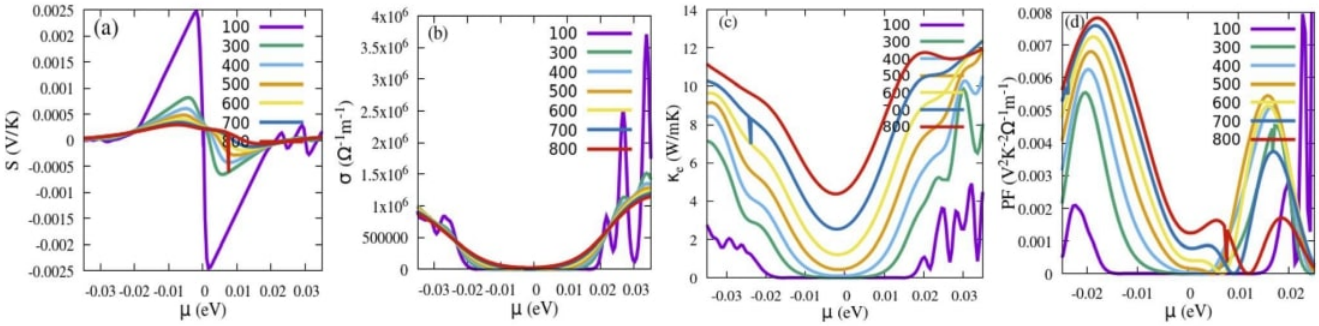

Figure 3.13: (a) Seebeck coefficient (S), (b) electrical conductivity (σ), (c) electronic thermal conductivity (k_e), and (d) power factor (PF) against chemical potential (μ) of $Sn_{1-2x}Mn_xMo_xO_2$.

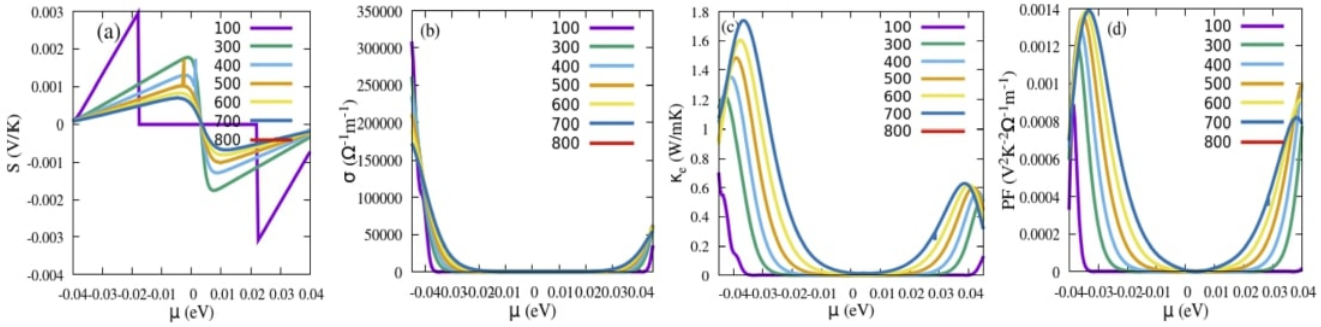

Figure 3.14: (a) Seebeck coefficient (S), (b) electrical conductivity (σ), (c) electronic thermal conductivity (k_e), and (d) power factor (PF) against chemical potential (μ) of $Sn_{1-2x}Mn_xTc_xO_2$.

3.8 Conclusion

In summary, we have discussed the magnetic, optical, structure electronic, and thermoelectric characteristics of SnO_2 system co-doped with Mn and A=Mo/Tc. Based on the computation from first principles, a comprehensive analysis has been conducted using the TB-mBJ and GGA-PBE approaches. The success of double doping of rutile SnO_2 is evident in the electronic and magnetic properties. The DOS makes it possible to observe that the majority spins and the minority spins exist in the band gap, which shows that the double impurity does not lead to the deformation of the host semiconductor's structure.. Our systems SnO_2 co-doped with Mn and Mo and SnO_2 co-doped Mn and Tc (x=0.0625) display the half-metallic behavior. We calculated the total energy differences among the ferromagnetic and antiferromagnetic states. We deduced that the ferromagnetic state is more stable in the $Sn_{1-2x}Mn_xMo_xO_2$ complex, whereas the antiferromagnetic state is

more stable in the $Sn_{1-2x}Mn_xTc_xO_2$ complex. Both co-doped systems have a significantly high total magnetic moment value. The double Zener exchange and the p-d hybridization govern ferromagnetism in $Sn_{1-2x}Mn_xMo_xO_2$ and $Sn_{1-2x}Mn_xTc_xO_2$, respectively. We studied the impact of co-doping SnO_2 on its optical characteristics. Compared to pristine SnO_2, optical absorption shows a noticeable enhancement in the low-energy regions. This feature makes these complexes SnO_2 system co-doped with Mn and A=Mo or Tc like absorbent layers for solar cells. The analysis of the thermoelectric properties shows excellent findings for SnO_2 co-doped with Mn and A=Mo/Tc. Consequently, the magnetic, optical, and thermoelectric characteristics of these complexes make them suitable for use in thermoelectric and photovoltaic devices.

RSC Advances

PAPER

Cite this: *RSC Adv.*, 2022, **12**, 28451

Electronic, magnetic, optical and thermoelectric properties of co-doped $Sn_{1-2x}Mn_xA_xO_2$ (A = Mo, Tc): a first principles insight

S. Laghzaoui,[a] A. Fakhim Lamrani,[ab] R. Ahl Laamara,[ac] E. Maskar,*[a] Botir Qonishevich Tuxtamishev,[d] Amel Laref[e] and D. P. Rai[f]

The electronic, magnetic, optical and thermoelectric (TE) properties of $Sn_{1-2x}Mn_xA_xO_2$ (A = Mo/Tc) have been examined using density functional theory (DFT) based on the FP-LAPW approach. The results suggested that all the doped compounds show a half-metallic ferromagnet property with a 100% spin polarization at the Fermi level within GGA and mBJ. Moreover, doping SnO_2 with double impurities reduces the bandgap. The reduced bandgaps are the result of impurity states which arise due to the Mn and Mo/Tc doping, leading to the shifts of the minima of the conduction band towards the Fermi energy caused by substantial hybridization between transition metals 3d–4d and O-2p states. Also, the (Mn, Mo) co-doped SnO_2 system exhibits a ferromagnetic ground state which may be explained by the Zener double exchange mechanism. While the mechanism that controls the ferromagnetism in the (Mn, Tc) co-doped SnO_2 system is p–d hybridization. Therefore, the role of this study is to illustrate the fact that half-metallic ferromagnet material is a good absorber of sunlight (visible range) and couples to give a combined effect of spintronics with optronics. Our analysis shows that $Sn_{1-2x}Mn_xMo_xO_2$ and $Sn_{1-2x}Mn_xTc_xO_2$ are more capable of absorbing sunlight in the visible range compared to pristine SnO_2. In addition, we report a significant result for the thermoelectric efficiency ZT of ~0.114 and ~0.11 for $Sn_{1-2x}Mn_xMo_xO_2$ and $Sn_{1-2x}Mn_xTc_xO_2$, respectively. Thus, the coupling of these magnetic, optical, and thermoelectric properties in (Mn, A = Mo or Tc) co-doped SnO_2 can predict that these materials are suitable for optoelectronic and thermoelectric systems.

Received 20th July 2022
Accepted 12th September 2022

DOI: 10.1039/d2ra04499d

rsc.li/rsc-advances

Chapter 4

Study of the structural, electronic, magnetic, optical, and thermoelectric properties of Half-metallic Double Perovskites

Introduction

Over the last two decades, double perovskites oxides have become essential due to their physical and thermoelectric properties. These materials find their application in renewable energy and spintronics. For potential spin-based devices to function, it is imperative to achieve high enough Tc and high spin polarization values. Furthermore, properties like higher diffusion lengths and powerful light absorptions are helpful in the advancement of solar cell technologies [16]. With significant improvements in fabrication technique, several perovskite solar cells now have efficiency levels of up to 22.7%, meaning they have a 3.8% practical applicability [140, 141]. The increasing requirement for renewable energies to fulfill energy needs and the expansion of industries have also made it more crucial than ever to identify other energy sources and minimize our energy consumption.The ability of thermoelectric (TE) substances to transform waste heat into useful energy has attracted attention globally as a potential source of renewable energy in the future [142 - 145].

4.1 Generality on double perovskites

The double perovskite oxide structure is composed of two materials having the perovskite structures ABO_3 and $AB'O_3$ coupled to form the structure $A_2BB'O_6$, where B and B' are ordered. An octahedron of oxygen surrounds each atom of the cation B or B'. However, six B' atoms surround every B atom, and vice versa. The cations A are alkaline earth metals or lanthanides. On site B, we find two cations surrounded by oxide anions forming octahedra BO_6 and $B'O_6$ joined by the vertices. Thus, two interlaced sublattices contain the BO_6 and $B'O_6$ octahedra. Other arrangements for double perovskites are also possible, such as $AA'B_2O_6$ or $AA'BB'O_6$. The half-metal double perovskites studied in our thesis present interesting optical, magnetic, electronic, and thermoelectric characteristics.

4.2 Study of Half-metallic Ferromagnetic Double Perovskites

This section discusses the structural,structure electronic, optical, magnetic, and thermoelectric characteristics of double perovskite ferromagnets by applying FP-LAPW method. The conventional DFT-GGA approach is known to underestimate the computation of the energy gaps. To address the issue of underestimation of the gap energy, we employed the Full hybrid Yukawa Screened-PBE0 (YS-PBE0) [146], GGA coupled with the Hubbard potential (U) (GGA+U), the GGA approximation with the Becke-Johnson potential modified within Tran and Blaha (GGA+mBJ) [48], and spin-orbit coupling (SOC) [147].

4.2.1 Study of Ca_2XMnO_6 (X = Ti/Cr)

4.2.1.1 Crystallographic structure

The tetragonal structure of Ca_2TiMnO_6 (CTMO) and Ca_2CrMnO_6 (CCMO) has space group I/4 m ($N^\circ = 87$) (Figure 4.1). Atomic positions for Ca, Ti/Cr, Mn, O1, and O2 are 4d(0, 1/2, 1/4), 2a(0, 0, 0), 2b(1/2, 1/2, 0), and 8h(0.1983, 0.3101, 0), respectively [148]. With identical Wyckoff position of the atoms of CTMO, CCMO is obtained by simply substituting the Cr atom for the Ti atom.

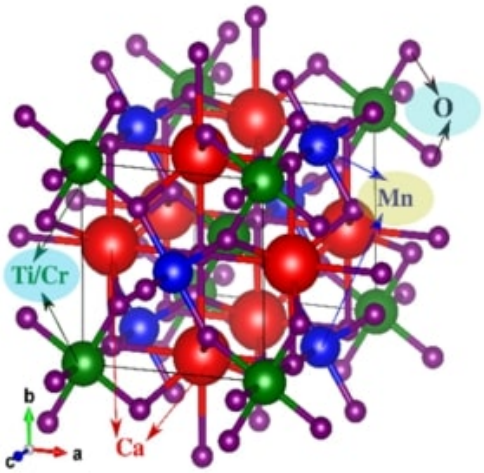

Figure 4.1: Crystal structure of Ca_2XMnO_6 (X = Ti/Cr).

4.2.1.2 Computational Detail and structural optimization

Many approximations, such as PBEsol-GGA [149], YS-PBE0, GGA +U, and TB-mBJ have been used to compute the electronic structure. The bandgap can be more accurate with the help of the TB-mBJ. The physical properties of compounds involving strongly correlated electrons appear to be better described by the GGA+U. By combining semi-locality with Hartree-Fock (HF) exchange, the hybrid functional may be applied to all electrons. The relation is as follows: $E_{xc}^{hybrid} = E_{xc}^{GGA} + \alpha_x \left(E_x^{HF} - E_x^{GGA}\right)$. The functional $\alpha_x \epsilon [0, 1]$ represents the fraction of accurate exchange, where E_x^{HF} and E_x^{GGA} denote the HF and GGA exchange functionals, respectively. For electronic, optical, and thermo-electric computations, the number of k-points utilized to sample the first Brillouin zone remains equal to $10 \times 10 \times 10$. The plane waves are limited to $R_{MT} \times K_{\max} = 7$. We reduced the forces to 0.1 mRy/au, the charge difference to $\Delta Q = 10^{-6}e$, and the total energy convergence to $10^{-6}Ry$ to guarantee correctness in the self-consistent calculations.

Employing the Birch-Murnaghan equation [121], we computed the total energy versus the volume in a self-consistent manner to find the structural parameters at equilibrium. The total energy curves for the Ca_2XMnO_6 (X = Ti/Cr) compounds appear in Figure 4.2 versus unit cell volume. Table 4.1 displays the optimum lattice parameters obtained from the GGA, which align with experimental and theoretical findings [148, 150, 151]. The lattice parameter values rise when a magnetic atom (Cr) replaces a non-magnetic (Ti) atom, as Table 4.1 illustrates.

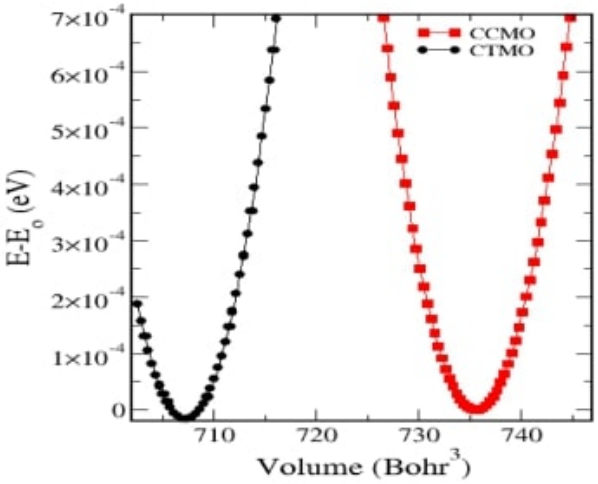

Figure 4.2: Total energy against volume for Ca_2XMnO_6 (X = Ti/Cr).

Systems	Ca_2TiMnO_6	Ca_2CrMnO_6
Ref.148	$a = 5.339\AA, b = 7.736\AA$	–
Ref.150	$a = 5.585\AA, b = 7.751\AA$	–
GGA	$a = 5.34\AA, b = 7.737\AA$	$a = 5.534\AA, b = 8.019\AA$

Table 4.1: Optimized lattice parameters for Ca_2XMnO_6 (X = Ti/Cr) compounds.

The following expression represents the tolerance factor known as "Goldschmith's tolerance factor," which regulates the stability of our compounds in the tetragonal structure:

$$t = \frac{r_{Ca} + r_O}{\sqrt{2}(\frac{r_{Ti/Cr}+r_{Mn}}{2}) + r_O} \tag{4.1}$$

Where r_{Ca}, r_O, $r_{Ti/Cr}$, and r_{Mn} are the ionic radius of Ca, O, Ti/Cr, and Mn atoms. The doubles perovskites are stable if t among 0.81 and 1.11 [163]. The t value for our compounds CTMO and CCMO is 0.98, indicating the stability of the tetragonal structure.

4.2.1.3 Electronic and magnetic properties

Initially, we studied the electronic and magnetic characteristics of our first compound, CTMO. We have computed the DOS of compound CTMO by applying the PBEsol-GGA approach, as shown in Figure 4.3. We can observe that the CTMO has a band gap of 1.16eV for majority-spin and 1.51eV for minority-spin, which indicates the semiconductor character. These outcomes concur with the prior findings [148]. We observed the characteristic asymmetry of the DOS of a magnetic semiconductor. We detected a subgap in the spin-up band between 3.51eV and 4.9eV in the conduction band, but no subgaps occurred in the valence band. A subgap between 4.03 and 4.9eV is present in the spin-down band. Our studies revealed that the Mn atom gives a substantial part of the total magnetic moment, while Ca, Ti, and O atoms make smaller contributions, as shown in Table 4.2. The total magnetic moment is $3\mu_B$.

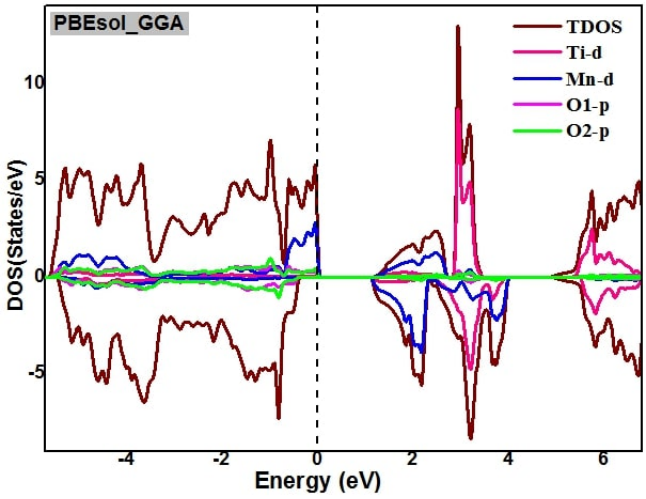

Figure 4.3: Spin-polarized DOS of double perovskite CTMO.

		m_T	$m_{Ti/Cr}$	m_{Mn}	m_{O1}	m_{O2}	E_g
CTMO	PBEsol-GGA	3	0.012	2.51	0.036	0.035	1.16(↑)/1.51(↓)
CCMO	PBEsol-GGA	5	1.819	2.56	0.023	0.029	1.390
CCMO	GGA+U	5	1.968	2.72	-0.027	-0.007	2.099
CCMO	TB-mBJ	5	1.963	2.65	-0.011	0.034	2.560
CCMO	YS-PBE0	5	1.839	2.57	0.021	0.027	1.399

Table 4.2: Results of the total and local magnetic moments (μ_B) and gap energy values (eV) of Ca_2XMnO_6 (X = Ti/Cr) compounds.

Step two involved employing a variety of approaches, including PBEsol-GGA, TB-mBJ, YS-PBE0, and GGA+U, to investigate the electronic and magnetic characteristics

of CCMO. Simply replacing the Ti in the CTMO compound with Cr yields the CCMO. We have studied the CCMO unstrained and CCMO under compressive uniaxial strains of -1% to -5% along z-axes. We also examined the effects of strain on the magnetic and electronic characteristics of CCMO.

- ***CCMO unstrained***

Figure 4.4 displays the spin-polarized DOS of CCMO without strain by applying PBEsol-GGA, TB-mBJ, YS-PBE0, and GGA+U. From Figures 3(a)–3(d), the DOS shows asymmetry among the spin-up/-down bands. The half-metallicity behavior is shown in the CCMO compound, where the conduction electrons are 100% spin-polarized around the Fermi level. The spin-down band reveals a semiconductor nature, whereas the majority spin channel displays a metallic nature. The results of the energy band appear in Table 4.2. The TB-mBJ, GGA+U, and YS-PBE0 enhance the band gap value of CCMO. The magnetic phase transitions from a magnetic semiconductor to a half-metal ferromagnetic when replacing Ti with Cr atoms. This feature helps double perovskites have better electrical conductivity. The majority spin band, formed of the 3d-Cr, 3d-Mn and 2p-O atoms, overlaps with the Fermi level. Thus, ferromagnetism in CCMO appears to result from p–d hybridization. All approximations maintain the total magnetic moment. The total magnetic moment of CCMO confirms its half-metallicity nature as it has a positive integer value of $5\mu_B$. Table 4.2 shows that the magnetic moments mainly come from the Cr and Mn atoms, with negligible contribution from the O atoms. These features suggest that the CCMO is an excellent choice for applications in spintronics.

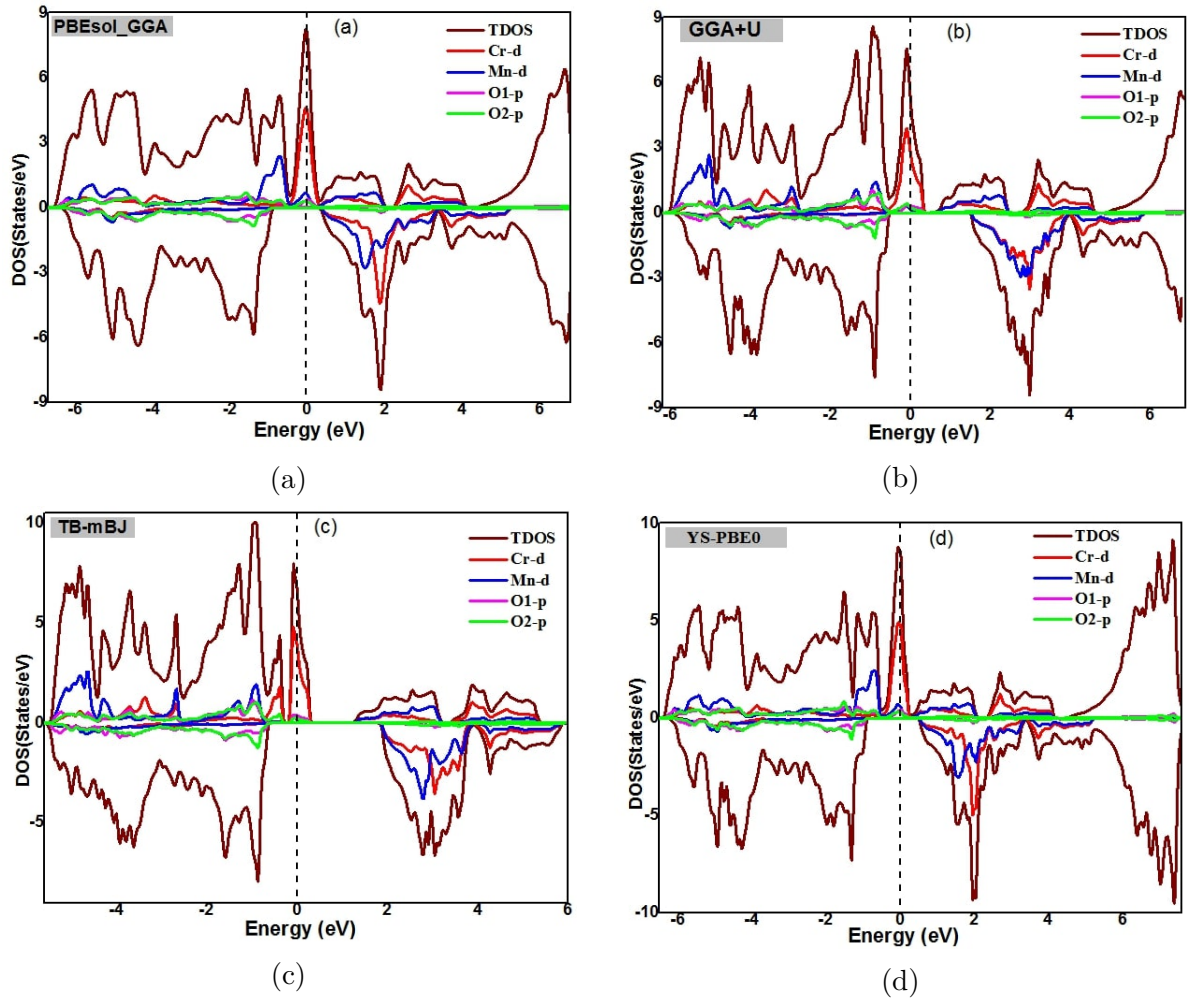

Figure 4.4: Total DOS and Partial DOS of CCMO by applying (a) PBEsol-GGA, (b) GGA+U, (c) TB-mBJ and (d) YS-PBE0.

- ***CCMO strained***

We applied the uniaxial strains within the -1% to -5% range in response to the change in the value of the lattice along the c-axis. The symbol "-" indicates the compressive strains. The relation of the strain is calculated by $a - a_0/a_0$, with a and a_0 represent the lattice constants of CCMO under the applied strain and the ambient condition, respectively. Figures 4.5(a)–4.5(e) display the spin-polarized DOS of CCMO under compressive strains along the c-axis of -2% to -5% by applying GGA+U. From Figures 4.5(b), 4.5(c), 4.5(d), and 4.5(e), DOS displays the same behavior as seen in the CCMO unstrained. Thus, the half-metal property remains unchanged under the compressive strains along the c-axis from -2% to -5%. The minority spins band presents a semiconductor character, and the majority spins band has a metallic property. At the Fermi level, orbitals 2p-O and 3d-Cr/Mn make up most states. Figure 4.5(a) shows the change of DOS of CCMO under -1% uniaxial compressive strain, in which the minority spins band displays a metallic character, and the majority spins band shows a semiconductor

behavior. This case could still be a half-metallic magnet. Table 4.3 lists the local and total magnetic moments of CCMO strained. In the range of −2% to −5% compressive uniaxial strain, the total magnetic moment does not change. For the −1% case, the total magnetic moment is 3.73 μ_B, which is not an integer. This result lends credence to the metallic character in this case. Therefore, it is possible to maintain the HM feature of CCMO material under compressive uniaxial strains of −2% to −5%.

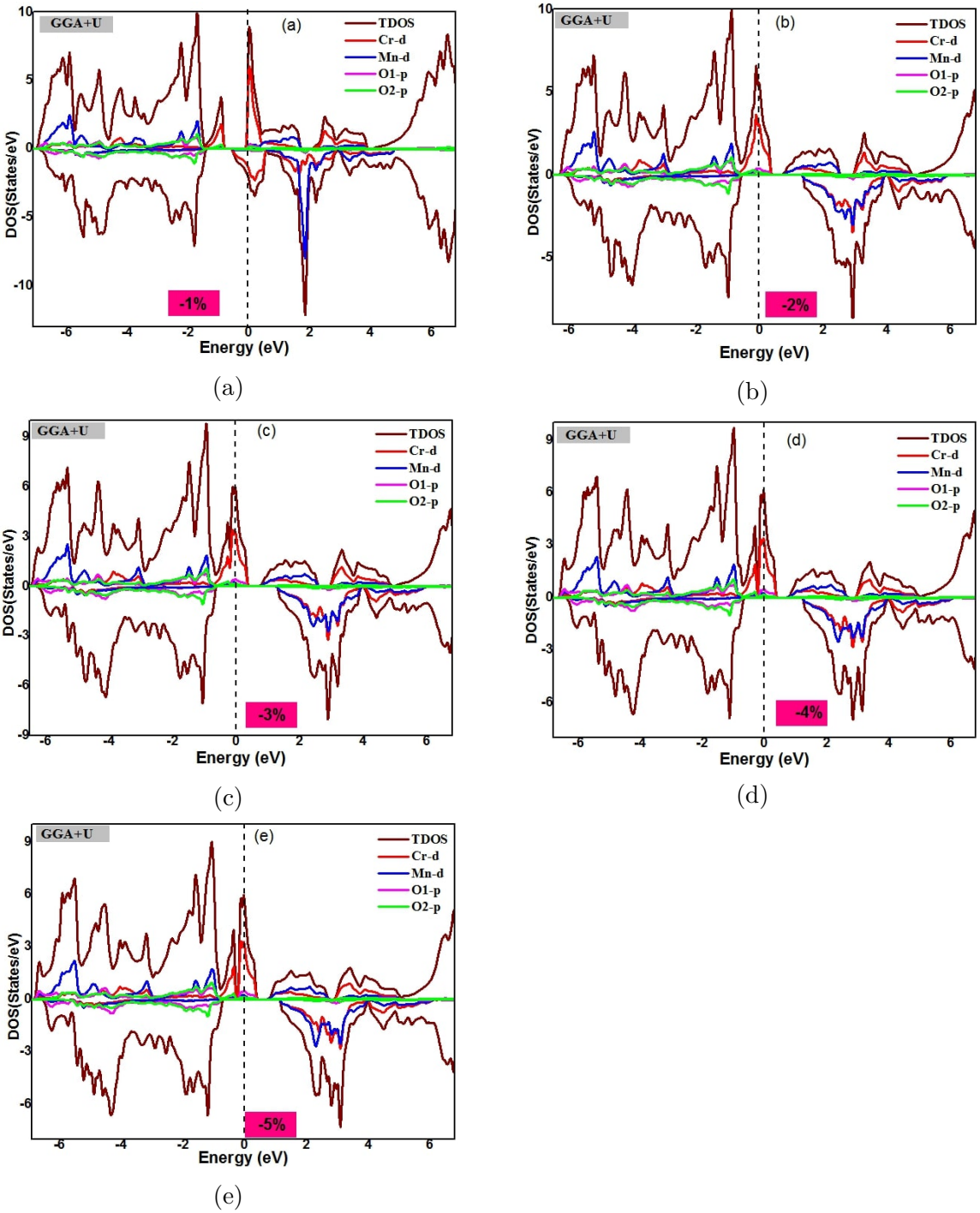

Figure 4.5: Spin-polarized TDOS and PDOS of CCMO under (a) −1%, (b) −2%, (c) −3%, (d) −4%, and (e) −5% uniaxial compressive strain by applying GGA+U.

Strain	m_T	$m_{Ti/Cr}$	m_{Mn}	m_{O1}	m_{O2}
-1%	3.73	0.693	2.623	0.005	0.035
-2%	5	1.919	2.672	-0.021	0.004
-3%	5	1.898	2.652	-0.018	0.009
-4%	5	1.878	2.624	-0.015	0.014
-5%	5	1.860	2.594	-0.012	0.019

Table 4.3: Results of the total and local magnetic moments (μ_B) of CCMO under the uniaxial compressive strain of -1% to -5% by applying GGA+U.

4.2.1.4 Optical properties

In this work, we are interested in half-metallic ferromagnetic materials. For this, we studied the optical characteristics of the ferromagnetic CCMO with and without strain compressive along the c-axis. We calculated the variations of $\varepsilon_1(\omega)$ the real and $\varepsilon_2(\omega)$ imaginary components of the dielectric function between 0 and 12eV photon energy using GGA+U. From Figure 4.6(a), the $\varepsilon_1(\omega)$ shows the high values at zero energy photon, suggesting high polarization ability. Table 4.4 lists the static dielectric constant $\varepsilon_1(0)$. At high energy photons after 8eV, $\varepsilon_1(\omega)$ becomes negative. The incident photon beam becomes fully attenuated in the optical medium in these energy ranges. Note that in these energy intervals, these materials have a metallic appearance [152]. Figure 4.6(b) illustrates the variation of $\varepsilon_2(\omega)$, which is frequently used to define the electronic transition. The low energy regions (IR range) contain the principal peaks. These peaks correlate with electrons moving from the occupied to the unoccupied states through interband transitions. $\varepsilon_2(\omega)$ with or without uniaxial strain compressive shows similar curves.

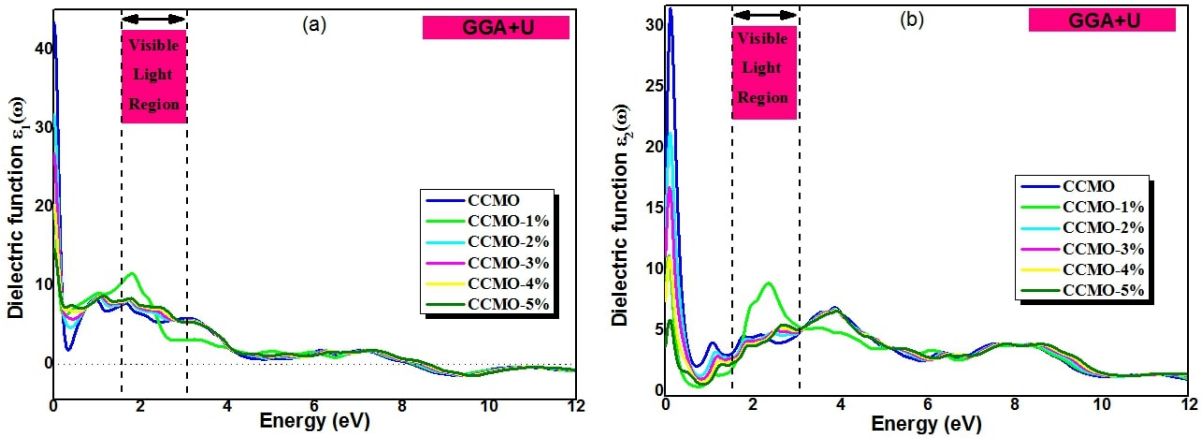

(a) (b)

Figure 4.6: Variation of (a) the real $\varepsilon_1(\omega)$ and (b) the imaginary $\varepsilon_2(\omega)$ parts of the dielectric function versus photon energy of CCMO with and without strain compressive calculated by GGA+U.

	0%	−1%	−2%	−3%	−4%	−5%
$\varepsilon_1(0)$	43.42	19.73	31.77	26.71	20.21	14.59
n(0)	6.69	4.53	5.75	5.28	4.56	3.84
R(0)	0.55	0.42	0.51	0.48	0.42	0.35

Table 4.4: Results of the optical parameters at zero energy photon of CCMO with and without strain compressive calculated by GGA+U.

An additional crucial metric for determining the portion of energy absorbed at the solid surface is the absorption coefficient $\alpha(\omega)$. Figure 4.7 illustrates the $\alpha(\omega)$ spectra of CCMO with and without strain compressive along the c-axis versus photon energy using GGA+U. As we can see, the CCMO in both cases (with or without uniaxial compressive) can absorb a sizable amount of light at many energy regions (IR, visible, and UV). There is a large amount of absorption in the UV range,. This compound is beneficial for various types of optical and optoelectronic applications operating in the visible and UV ranges, like solar cells, as demonstrated by its broad absorption range.

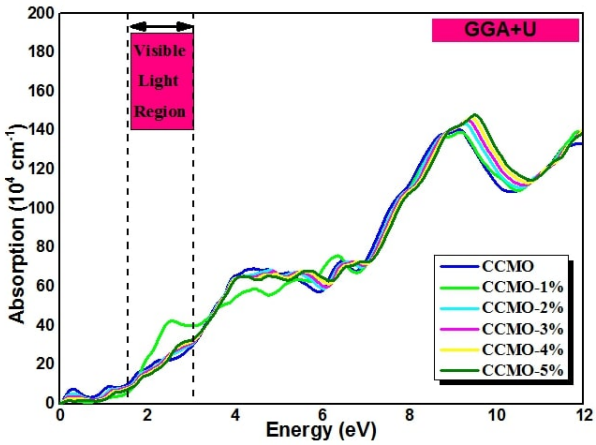

Figure 4.7: Absorption coefficient $\alpha(\omega)$ against energy of photon of CCMO with and without strain compressive calculated by GGA+U.

Figure 4.8(a) displays the variation of the refractive index $n(\omega)$ against photon energy. The result presented in Table 4.4 regarding static values $n(0)$. The relation $n(0) = \sqrt{\varepsilon_1(0)}$ also allows for the calculation of these values, n(0). The $n(\omega)$ begins to drop because of optical dispersion as photon energy rises. The reflectivity $R(\omega)$ describes the fraction of energy that represents at the surface of the solid. Figure 4.8(b) provides an illustration of the results obtained. The reflectivity R(0) at zero energy, which corresponds to the high reflectivity values, is listed in Table 4.4. The unstrained CCMO shows a maximum quantity of reflectivity compared to the strained CCMO. The extinction coefficient $k(\omega)$ variation is seen in Figure 4.8(c). The $\varepsilon_2(\omega)$ curves and the $k(\omega)$ curves resemble each

other. The $k(\omega)$ maximum values appear in the low-energy photon ranges. Photon energy is lost when light interacts with matter because electrons move from the valence band to the conduction band. An energy loss function helps to determine the energy loss that occurs during the electron transition. Figure 4.8(d) displays the loss function spectra $L(\omega)$ against photon energy. We can see that the maximum peaks appear in high-energy regions, indicating the high energy loss. As a result, uniaxial compressive strain has less of an impact on the optical characteristics of CCMO.

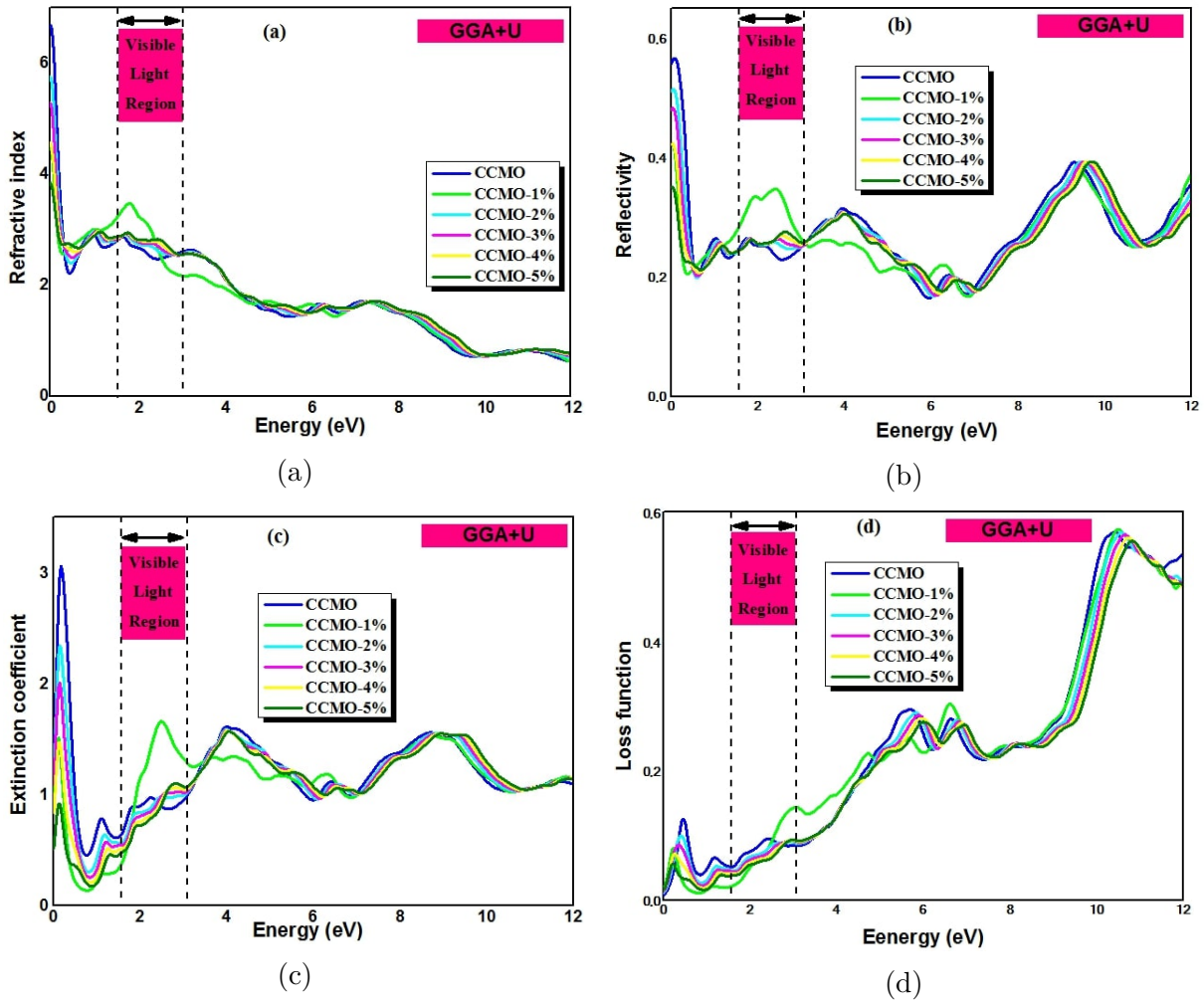

Figure 4.8: Variation of the (a) refractive index $n(\omega)$, (b) reflectivity $R(\omega)$, (c) extinction coefficient $k(\omega)$, and (d) loss function $L(\omega)$ against photon energy of CCMO with and without strain compressive calculated by GGA+U.

4.2.1.5 Thermoelectric properties

Improving electrical conductivity and Seebeck transport qualities to maximize the figure of merit ($ZT = (S^2\sigma T/k)$) is part of optimizing materials for thermoelectric energy conversion. ZT is higher than or equal to close to unity for superior thermometric materials [153]. The study solely considers the electrical part of thermal conductivity. In this section,we explored ferromagnetic materials CCMO without or with strain compressive

along the c-axis from -1% to -5%. Using the GGA+U, we investigated how this strain affected the thermoelectric characteristics.

Figure 4.9 shows the Seebeck coefficient (S) against temperature for CCMO with and without strain compressive along the c-axis in both spin channels up/down. Positive values are seen for S in the spin-down band, indicating that p-type behavior predominates and that holes exist in most carriers. The CCMO in the spin-up channel, both with and without strain compression, exhibits negative values of S below 500K, indicating that electrons comprise the bulk of charge carriers. It demonstrates that n-type behavior exists. Figure 4.10 illustrates the variation of the electrical conductivity (σ/τ) per relaxation time versus temperature. By gradually reducing the values of σ/τ versus temperature increase, the spin-up channel validates the metallic nature for CCMO with and without strain compressive of -2% to -5%. The increase in carrier concentration, combined collisions, and diffusion phenomena at high temperatures explain the modest decrease in electrical conductivity as temperature rises. Electronic and network contributions are responsible for heat conduction in a material [155]. Figure 4.11 displays the electron thermal conductivity k_e/τ per relaxation time versus the temperature. The k_e/τ rises linearly with temperature, as seen in Figure 4.11(a). The Wiedemann-Franz law [6], which determines the connection between k_e and T ($k_e = \sigma LT$), is compatible with these results. From Figure 4.11(b), k_e/τ values of CCMO under -1% compressive strain are less than CCMO without and with strain compressive of -2%, -3%, -4%, and -5%. The figure of merit ZT versus the temperature in both spin channels up/down appears in Figure 4.12. The compound CCMO with and without strain compressive -2%, -3%, -4%, and -5% exhibit maximum values of ZT equal to 1 in the spin-down band. This feature of the CCMO without or with uniaxial strain compressive is desirable for thermoelectric devices. The increase in k_e is the cause of the decline in the values of ZT in the majority-spin band.

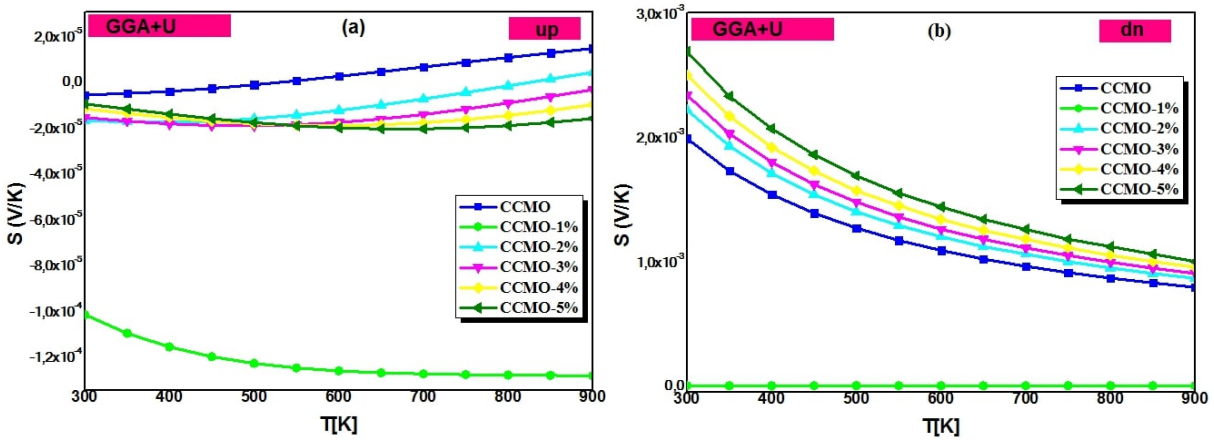

(a) (b)

Figure 4.9: Seebeck coefficient (S) versus the temperature for (a) spin-up and (b) spin-down channels.

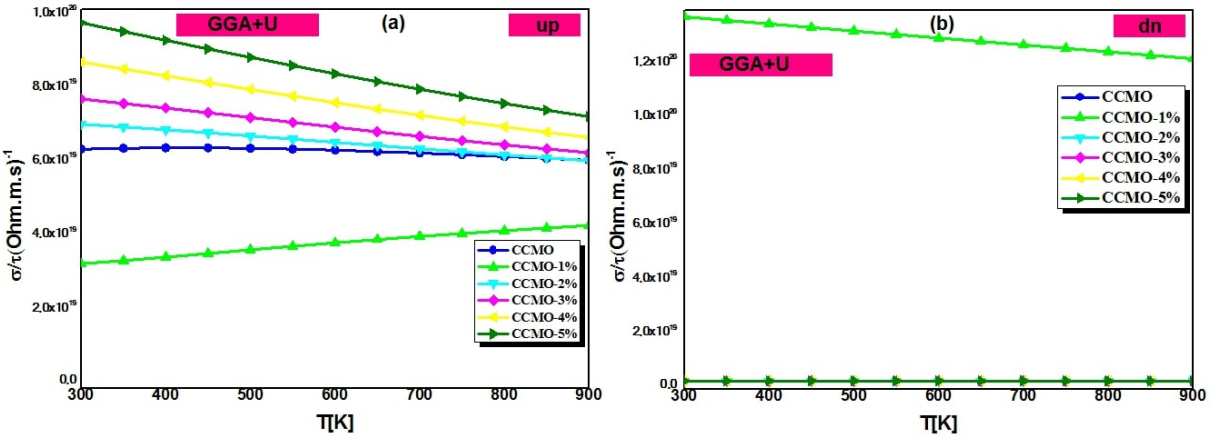

(a) (b)

Figure 4.10: Electrical conductivity (σ/τ) versus the temperature for (a) spin-up and (b) spin-down channels.

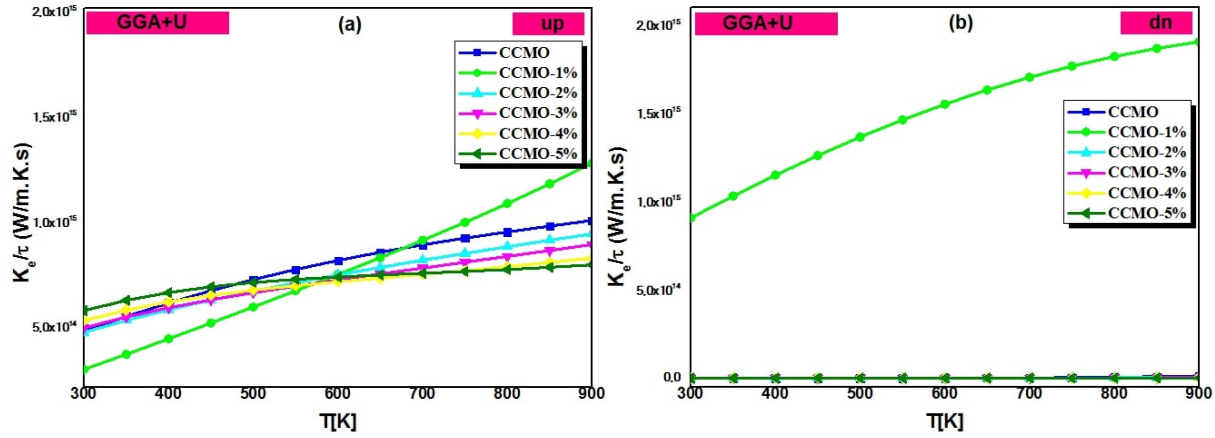

(a) (b)

Figure 4.11: Electron thermal conductivity (k_e/τ) as a function the temperature for (a) spin-up and (b) spin-down channels.

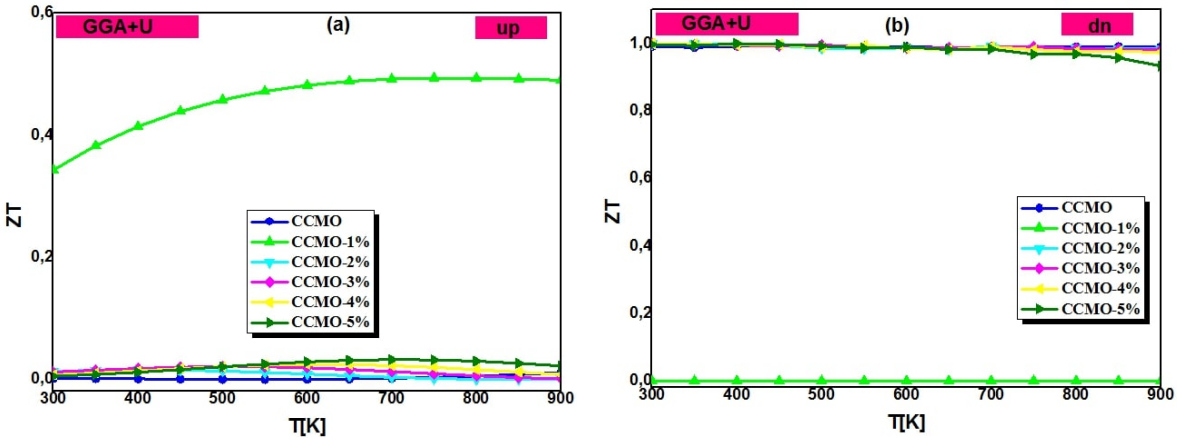

(a) (b)

Figure 4.12: Figure of merit (ZT) as a function the temperature for (a) spin-up and (b) spin-down channels.

4.2.2 Study of Sr_2ACoO_6 (A = Ti, Dy, Ho, Er, or Tm)

4.2.2.1 Crystallographic structure

Our initial compound is double perovskite oxide Sr_2TiCoO_6 (STCO). The STCO exhibits a cubic structure and belongs to the space group Fm-3m ($N° = 225$). According to [156, 157, 158], the lattice constant in experiment is $a = 7.894\mathring{A}$. In that order, the locations of the Sr, Ti, Co, and O are as follows: (0.25, 0.25, 0.25), (0.5, 0.5, 0.55), (0, 0, 0), and (0.25, 0, 0). We swapped out the Ti atom in Sr_2TiCoO_6 (STCO) with Dy, Ho, Er, or Tm atoms, leaving Sr, Ti, Co, and O atom positions unchanged. Figure 4.13 displays the crystalline structures Sr_2TiCoO_6 and Sr_2RECoO_6 (where RE might be Dy, Ho, Er, or Tm).

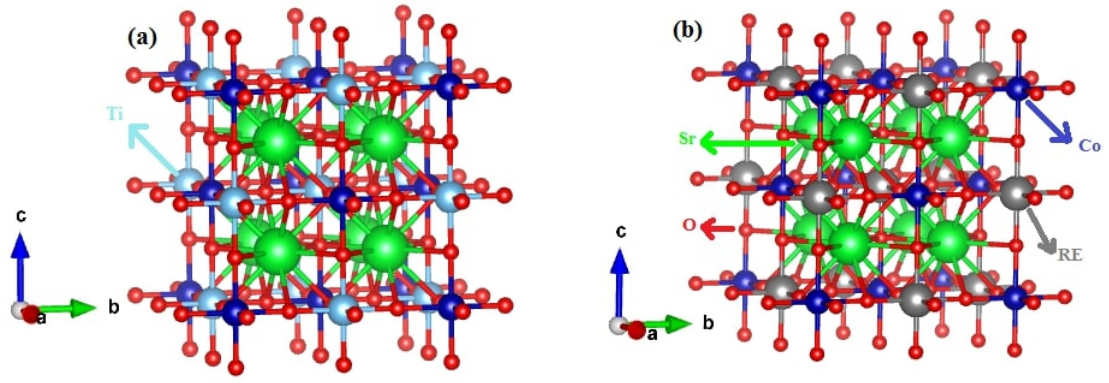

(a) (b)

Figure 4.13: Crystal structure of double perovskites in the cubic phase of a) Sr_2TiCoO_6 and b) Sr_2RECoO_6 (RE = Dy, Ho, Er, or Tm).

4.2.2.2 Computational Detail and structural optimization

We have computed the exchange-correlation function by applying the GGA-WC approximation. GGA-WC generally underestimates the bandgap of materials, so we used the GGA+U potential. U = 1eV, 7eV, 6eV, 5eV, and 4eV represented corresponding Hubbard values for the d-Co, f-Dy, f-Ho, f-Er, and f-Tm orbitals. We further have investigated the impact of spin-orbit coupling (SOC) [147] on the electronic properties of our investigated compounds. To prevent the spheres from overlapping, we chose values for the Muffin-tin radii or average radius of the atomic spheres (R_{MT}). For Sr, Ti, Co, RE, and O atoms, these values correspond to 2.5, 1.88, 1.93, 1.97, and 1.66 u.a., respectively. An energy of -6.0Ry is maintained as the separation between the valence states and the core.We have used $10 \times 10 \times 10$ mesh in the irreducible Brillouin zone (IBZ), which turns out to be sufficient for convergence.

As the development of the subsequent computations relies on the optimized crystal parameter, determining the structural properties of materials is the most crucial step toward comprehending and forecasting their many physical properties. The optimal values of the crystal lattice characterizing our materials SACO (A = Ti, Dy, Ho, Er, or Tm) are computed by applying GGA approximations. The equilibrium volume (V_0), and consequently the mesh parameter a, the compressibility modulus (B_0), and the first derivative of the compressibility modulus B_0' correspond to the minimum total energy (E_0). To determine the more stable structure, we plot the energy against volume using the Murnaghan equation of state [121]. Figure 4.14, below, represents the total energies versus volume for SACO compounds. Our results for the equilibrium structural parameters appear in Table 4.5. Our first compound STCO results are still in reasonable accord with the earlier data [159, 160, 161].

The tolerance factor is stable in cubic structure for t=0.78–1.05[162]. Our compounds Sr_2TiCoO_6 (STCO), Sr_2DyCoO_6 (SDYCO), Sr_2HoCoO_6 (SHOCO), Sr_2ErCoO_6 (SERCO), and Sr_2TmCoO_6(STMCO) have calculated tolerance factors of 0.876, 0.84, 0.88, 0.88, and 0.88, respectively, indicating that the cubic structure is stable.

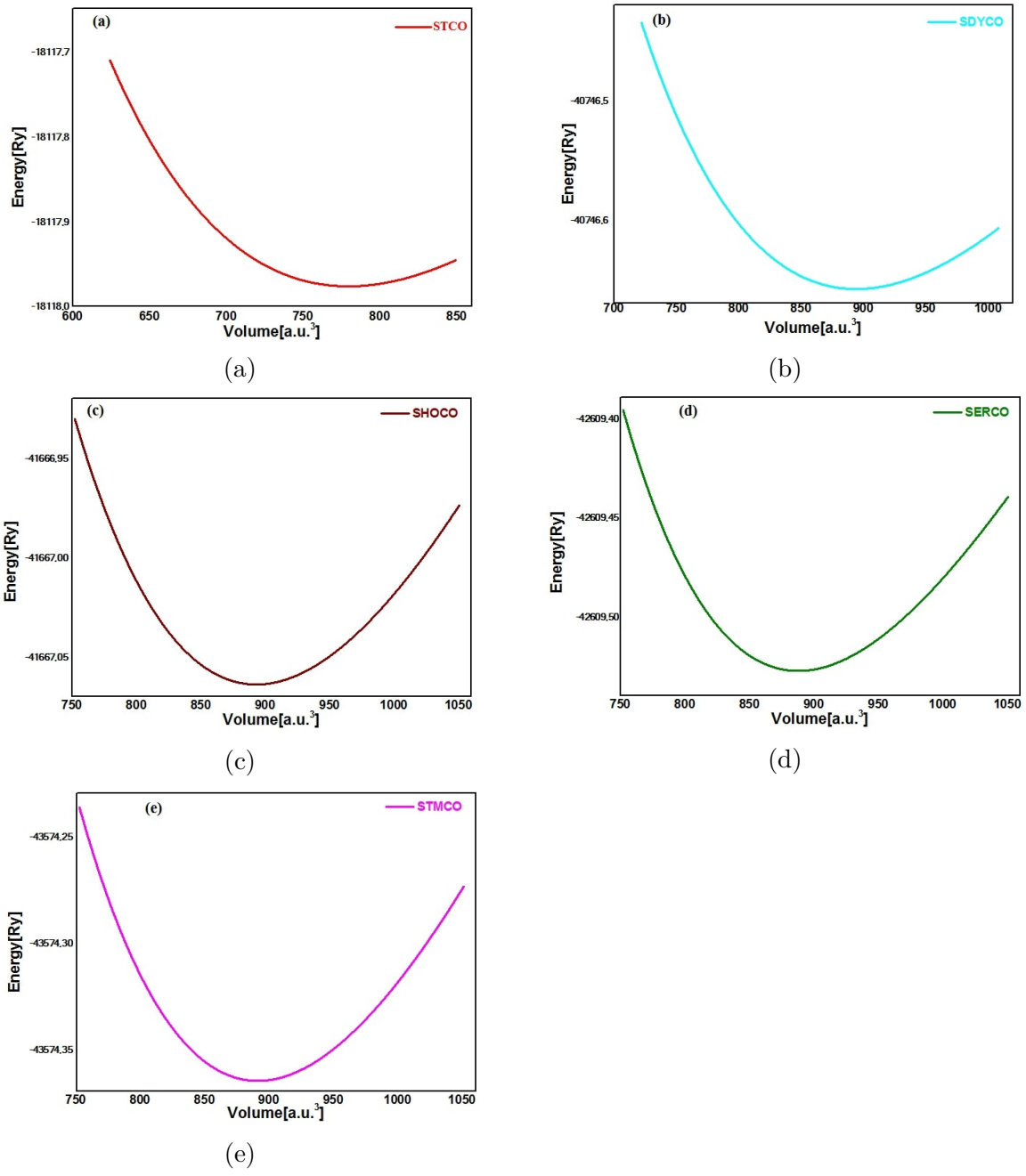

Figure 4.14: Total energy versus volume of a) Sr_2TiCoO_6, b) Sr_2DyCoO_6, c) Sr_2HoCoO_6, d) Sr_2ErCoO_6, and e) Sr_2TmCoO_6.

	STCO	SDYCO	SHOCO	SERCO	STMCO
$a = b = c(\AA)$	7.722	8.095	8.114	8.114	8.114
$V_0(a.u.)^3$	779.429	894.224	893.158	887.864	890.689
$B_0(GPa)$	168.782	130.621	129.380	127.852	128.334
B_0'	4.599	4.534	4.534	5.907	4.651

Table 4.5: Optimized parameters (a), (B_0) Bulk Modulus and (B_0') its Pressure derivative of Sr_2ACoO_6 (A = Ti, Dy, Ho, Er, or Tm).

4.2.2.3 Electronic and magnetic properties

The spin-polarized total DOS and Partial DOS of the STCO compound appear in Figure 4.15 by applying WC-GGA, SOC, and GGA+U. From Figure 4.15, the DOS shows asymmetrical between majority and minority-spin bands, together with high polarization around the Fermi level, suggesting that our compound is half-metallic. The channel of the majority-spins shows the semiconductor character, while the minority-spins band displays the metallic nature under all approximations. These results correspond well with the theoretical DFT calculations [164]. The band gap values of the material STCO by applying WC-GGA, GGA+U, and SOC are 0.49eV, 0.77eV, and 0.34eV. The GGA+U enhances the band gap of STCO compared to other approximations. The 3d-Co and 2p-O orbitals make up the minority-spins band. The Co atom is the source of magnetism. It indicates the robust p-d hybridization between p-O and d-Co orbitals. Thus, the STCO compound exhibits a ferromagnetic half-metallic behavior. The half-metallic behavior proved appropriate and suited for several technical applications, such as Spintronic, magnetic recording, high-efficiency magnetic sensors, and computational manipulation [138, 139]. STCO has a total magnetic moment equal $1\mu_B$. The magnetic moment results for Co, Ti, and O are in Table 4.6. The Co atom contributes significantly to the overall magnetic moment.

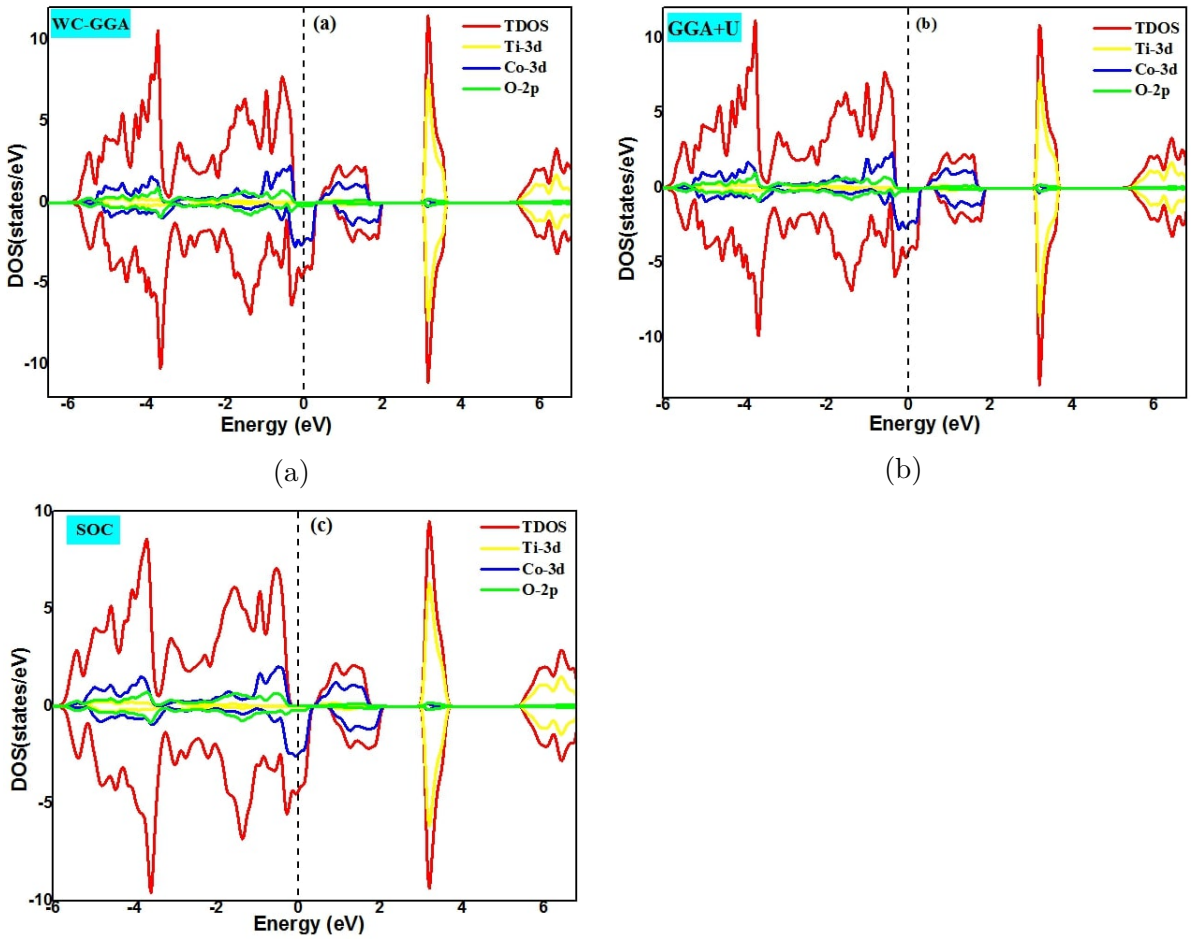

Figure 4.15: Spin-polarized Total DOS and Partial DOS of Sr_2TiCoO_6 by applying a) WC-GGA, b) GGA+U, and c) SOC.

Compounds	$E_g(eV)$	$m_t(\mu_B)$	$m_A(\mu_B)$	$m_{Co}(\mu_B)$	$m_O(\mu_B)$
STCO	0.77/0.34	1/0.99	-0.027/-0.026	0.64/0.68	0.056/0.049
SDYCO	1.28/0.76	7/6.9	5.16/5.13	0.88/0.91	0.13/0.12
SHOCO	1.45/0.7	6/5.87	4.15/4.08	0.77/0.84	0.15/0.13
SERCO	1.28/0.76	5/4.81	3.08/2.97	0.84/0.89	0.15/0.13
STMCO	0.89/0	4/3.79	1.96/1.86	1.06/1.07	1.14/0.12

Table 4.6: Outcomes of band gap E_g, total and local magnetic moment m_t, m_A, m_{Co} and m_O of Sr_2ACoO_6 (A= Ti, or RE) by applying the GGA+U/SOC.

By substituting an RE (=Dy, Ho, Er, or Tm) ion into the Ti position in the host material Sr_2TiCoO_6, we obtain the following structures Sr_2DyCoO_6, Sr_2HoCoO_6, Sr_2ErCoO_6, and Sr_2TmCoO_6. Figures 4.16, 4.17, 4.18, and 4.19 display the DOS versus energy by applying the WC-GGA and GGA+U approaches. New states were observed near the Fermi level after replacing the Ti with rare earth elements. The 4f orbitals of the atoms of Dy, Ho, Er, and Tm are responsible for these novel states. Electrons are easily stimulated to

the conduction band when their energy levels are at the highest part of the band gap. Asymmetric states between the spin-up band, which has a semiconductor nature, and the spin-down band, which has a metallic nature, support the ferromagnetic character structures. The primary orbitals forming the spin-minority channel are RE-f and Co-d. Consequently, ferromagnetism comes via the p-f hybridization among the O-2p, RE-4f, and Co-3d orbitals. The bandgap value differs between WC-GGA and GGA+U, although both exhibit half-metallic ferromagnetic. The magnetic properties of Sr_2TiCoO_6 are also enhanced. The total magnetic moment of Sr_2TiCoO_6 is changed from $1\mu_B$ to $7\mu_B$, $6\mu_B$, $5\mu_B$, and $4\mu_B$ for Sr_2DyCoO_6, Sr_2HoCoO_6, Sr_2ErCoO_6, and Sr_2TmCoO_6, respectively. Table 4.6 shows the local moments of the RE, Ti, Co, and O atoms. The RE atoms give most of the magnetic moment, with Co and O making smaller contributions. Thus, the features of these compounds are suitable for spintronic applications.

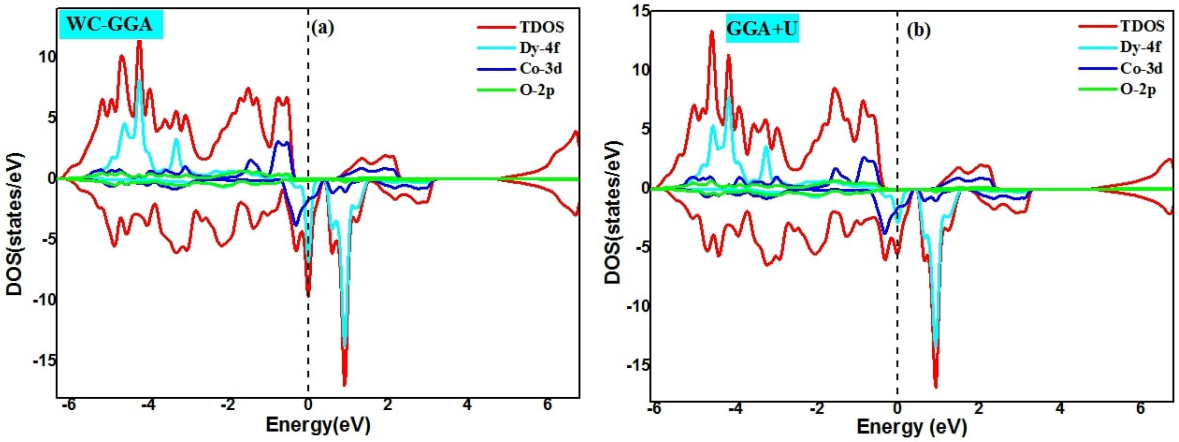

(a) (b)

Figure 4.16: Total DOS and Partial DOS of Sr_2DyCoO_6 by applying a) WC-GGA, and b) GGA+U.

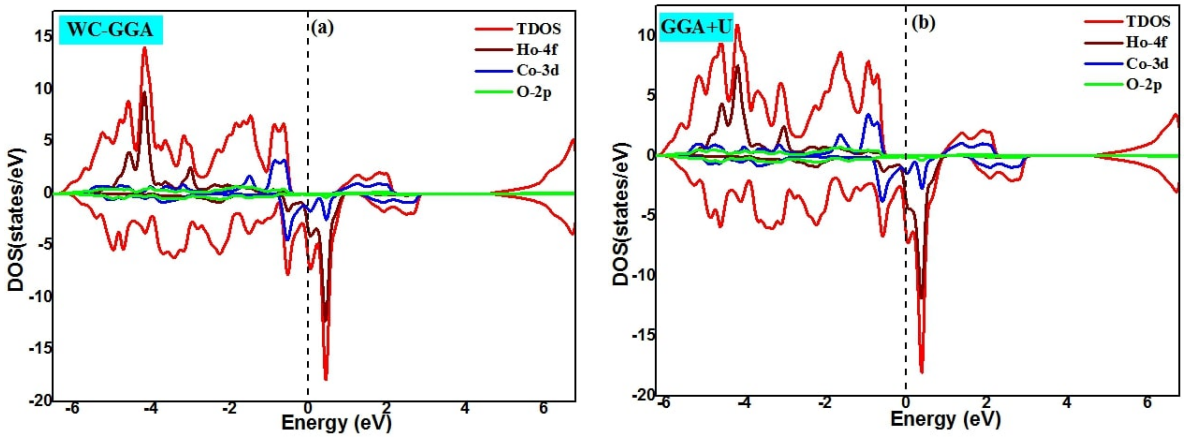

(a) (b)

Figure 4.17: Total DOS and Partial DOS of Sr_2HoCoO_6 by applying a) WC-GGA, and b) GGA+U.

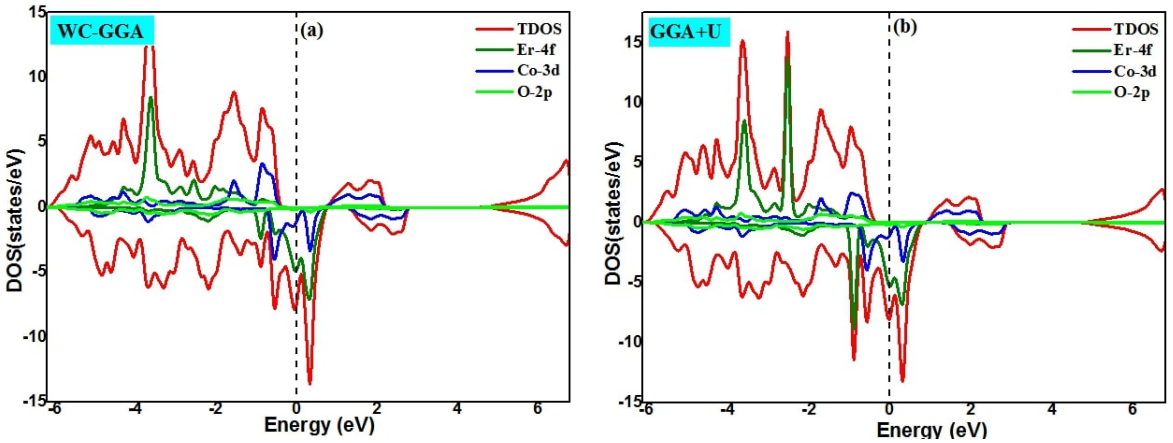

(a) (b)

Figure 4.18: Total DOS and Partial DOS of Sr_2ErCoO_6 by applying a) WC-GGA, and b) GGA+U.

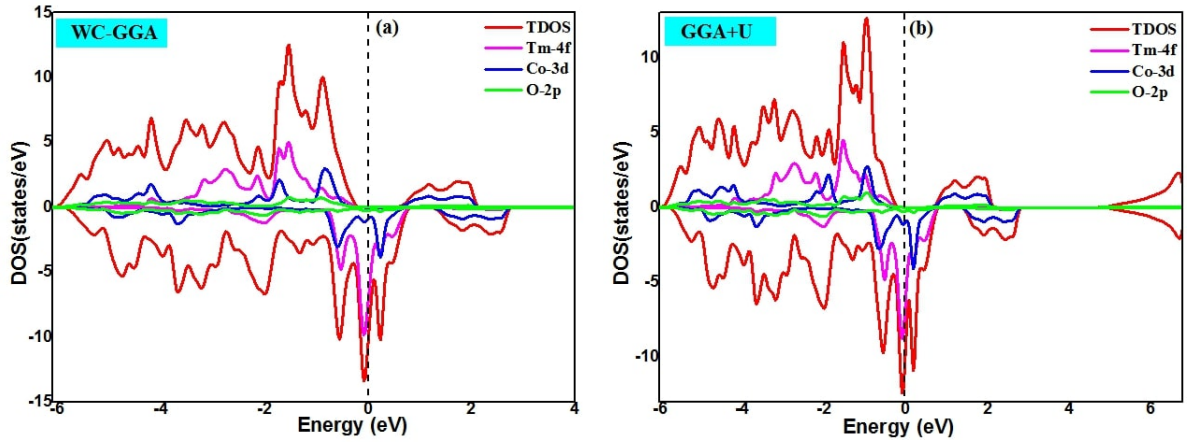

(a) (b)

Figure 4.19: Total DOS and Partial DOS of Sr_2TmCoO_6 by applying a) WC-GGA, and b) GGA+U.

In this part, we have discussed the effect of spin-orbit coupling (SOC), as seen in Figure 4.20. Usually, only the magnetic electron spin is considered, with the magnetic orbital being ignored. SOC is responsible for introducing the magnetic moment of an atomic orbit. When atoms become heavier, their orbital magnetic moment becomes significant and cannot be disregarded. From Figure 4.20, Sr_2DyCoO_6, Sr_2HoCoO_6, and Sr_2ErCoO_6 maintain their intense spin-polarization close to the Fermi level in the minority-spins band, thus maintaining their half-metallicity character. The band gap value drops when the majority-spins band peaks approach the Fermi level when the SOC is applied (See Table 4.6). The band gap narrows with the application of SOC with robust hybridization between the RE-4f and Co-3d. The compound Sr_2TmCoO_6 is metallic due to the absence of a band gap in majority-spin and minority-spin-channels. Table 4.6 lists the overall and partial magnetic moments of Sr_2RECoO_6 obtained by applying the SOC. We can notice

that the magnetic moments of Sr_2RECoO_6 are lower than those obtained via GGA+U. Thus,GGA+U approach offers the best description for the magnetic and electronic of SRECO.

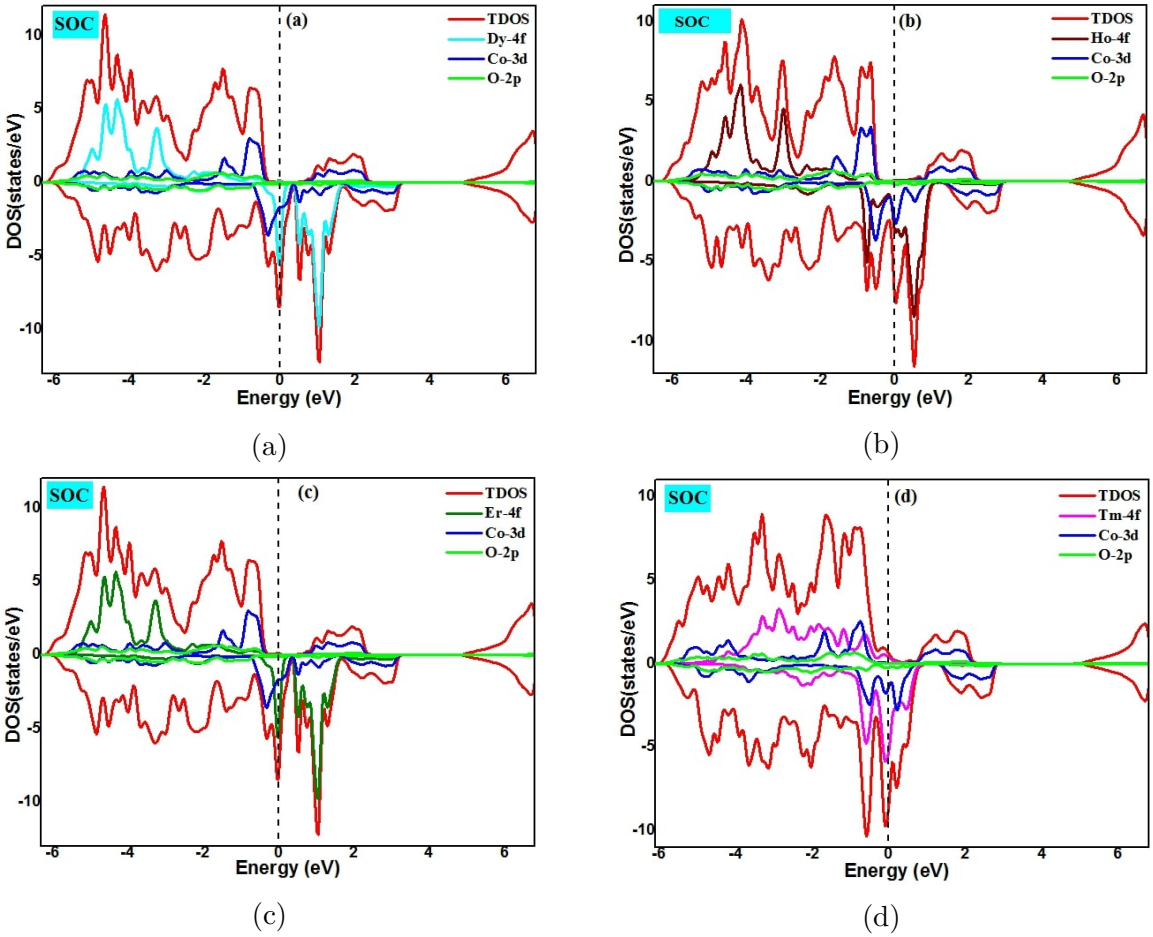

Figure 4.20: Total DOS and Partial DOS of a) Sr_2DyCoO_6, b) Sr_2HoCoO_6, c) Sr_2ErCoO_6, and d) Sr_2TmCoO_6 compounds by applying SOC.

4.2.2.4 Optical properties

The discipline of spintronics coupled with optoelectronics is a promising area for new research projects. We have investigated the optical characteristics employing the GGA+U approach. Figure 4.21 shows the evolution of the real $\varepsilon_1(\omega)$ and imaginary $\varepsilon_2(\omega)$ components of dielectric function for double perovskites Sr_2TiCoO_6, Sr_2DyCoO_6, Sr_2HoCoO_6, Sr_2ErCoO_6, and Sr_2TmCoO_6 versus photon energy. As shown in Figure 4.21(a), we can see that the principal peaks in $\varepsilon_2(\omega)$ appear in the IR region.The peaks in $\varepsilon_2(\omega)$ are caused by electrons moving from above the valence band to below the conduction band through interband transitions. By substituting RE atoms, the intensity of the peaks in the visible and infrared is improved, increasing the amount of absorption. The existence of specific impurity energy levels around the Fermi level can serve to explain this, leading to an enhanced chance of the electron transition. $\varepsilon_1(0)$ ($\omega \sim 0$) (static dielectric constant)

is the essential value for the $\varepsilon_1(\omega)$. From Figure 4.21(b), the $\varepsilon_1(0)$ values of Sr_2TiCoO_6, Sr_2DyCoO_6, Sr_2HoCoO_6, Sr_2ErCoO_6, and Sr_2TmCoO_6 are 24.66, 60.4, 39.98, 114.8, and 111.98, respectively. These elevated values indicate a greater capacity for polarization. $\varepsilon_1(\omega)$ curves decrease with increasing energy photons and eventually tend to zero at higher energies. $\varepsilon_1(\omega)$ curves become negative in specific energy ranges. The optical medium attenuates the incident photon beam at these energies. When $\varepsilon_1(\omega) = 0$, our compounds do not react to incident light.

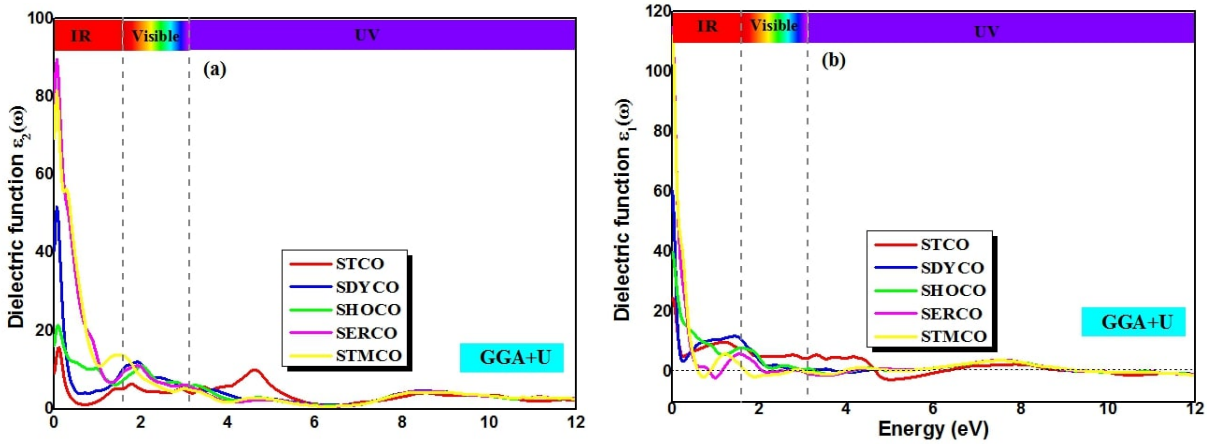

(a) (b)

Figure 4.21: Variation of (a) the imaginary $\varepsilon_2(\omega)$ and (b) real $\varepsilon_1(\omega)$ components of dielectric function of Sr_2ACoO_6 (A= Ti, Dy, Ho, Er, or Tm) against photon energy by applying GGA+U.

Figure 4.22 displays the result of the absorption coefficient $\alpha(\omega)$ spectra of SACO versus photon energy. We can notice that the SRECO compounds exhibit significant absorption compared to STCO in the IR and visible regions. Photovoltaic and solar cell applications demand a significant absorption quantity, especially in the visible spectrum.

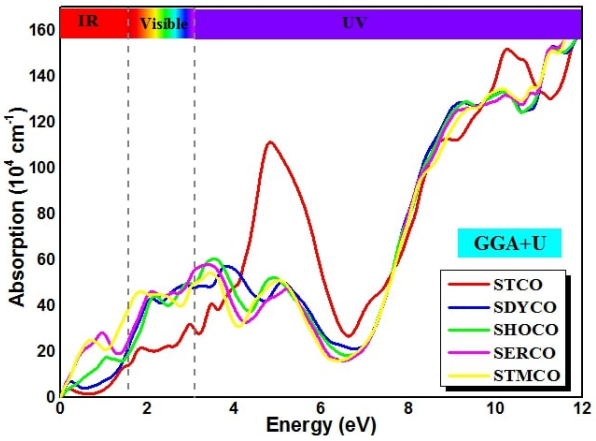

Figure 4.22: Spectra of the absorption coefficient $\alpha(\omega)$ of Sr_2ACoO_6 (A= Ti, Dy, Ho, Er, or Tm) against photon energy by applying GGA+U.

The wavelength of the incident light beam determines the refractive index $n(\omega)$, which explains how light behaves in a material. Figure 4.23(a) shows the variation of $n(\omega)$ of the SACO compounds versus the incident photon energy. The principal peaks appear at zero photon energy. At zero energy, the n(0) values of Sr_2DyCoO_6, Sr_2HoCoO_6, Sr_2ErCoO_6, and Sr_2TmCoO_6, and Sr_2TiCoO_6 are 5.05, 8.16, 6.44, 11.25, and 11.03, in that order. The principal peak on all $n(\omega)$ curves occurs by resonance-approaching frequencies and is associated with electrons migrating via the valence band to the conduction band. Figure 4.23(b) shows the loss function curves $L(\omega)$ against photon energy. Electron excitations, resulting from rapid electron passage through a material, are the origin of the $L(\omega)$. As input photon energy increases, this increases energy loss. The extinction coefficient curves $k(\omega)$ vs photon energy appear in Figure 4.23(c). From the $k(\omega)$ curves, we can observe several peaks at different photon energies. Every peak in the $k(\omega)$ spectra corresponds to a peak in $\varepsilon_2(\omega)$. Figure 4.23(d) displays the reflectivity spectra $R(\omega)$ against photon energy. From the spectrum analysis, the reflectivity parameter values R(0) at zero frequency are 46%, 64%, 55%, 72%, and 71% of Sr_2TiCoO_6, Sr_2DyCoO_6, Sr_2HoCoO_6, Sr_2ErCoO_6, and Sr_2TmCoO_6, respectively. The cause for the increased $R(\omega)$ value is the interband transition of electrons [165].

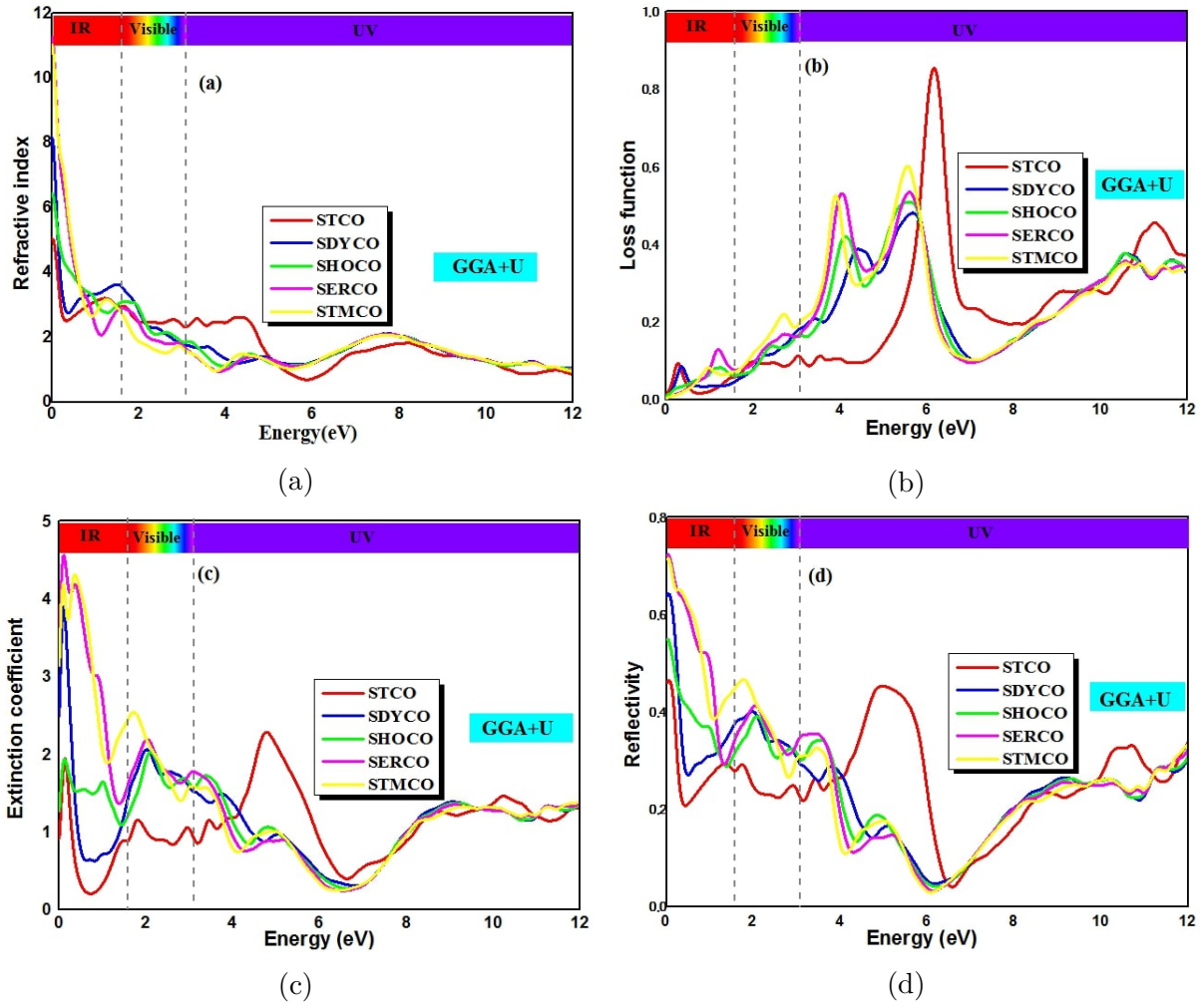

Figure 4.23: Spectra of the (a) refractive index $n(\omega)$, (b) loss function $L(\omega)$, (c) extinction coefficient $k(\omega)$ and (d) reflectivity $R(\omega)$ of Sr_2ACoO_6 (A= Ti, Dy, Ho, Er, or Tm) against photon energy by applying GGA+U.

4.2.2.5 Thermoelectric properties

The electronic thermal conductivity (k_e), Seebeck coefficient (S), figure of merit (ZT), and electrical conductivity (σ) have all been computed over a range of temperatures from 300 to 900 K. We have applied the GGA+U approximation to determine these properties.

Figure 4.24 illustrates the electrical conductivity (σ) versus temperature. In the spin-up channel, the σ values rise with increasing temperature. In the low temperature, the σ values are minimal. When the temperature rises, the spin-down band for Sr_2TiCoO_6, Sr_2ErCoO_6, and Sr_2TmCoO_6 exhibits a progressive reduction of σ, which shows maximum values at 300 K. At 300K in spin-down band, the σ values are 1.38×10^6, 8.36×10^5, 1.02×10^6, 1.16×10^6, and $9.47 \times 10^5 (\Omega m)^{-1}$ for Sr_2TiCoO_6, Sr_2DyCoO_6, Sr_2HoCoO_6, Sr_2ErCoO_6, and Sr_2TmCoO_6, respectively. The large values of σ made the Sr_2ACoO_6 compounds very interesting in microelectronics and photovoltaics. Figure 4.25 shows the

change in electron thermal conductivity (k_e) with temperature. From these results, we can see that the k_e values increase with increasing temperature. The material heats up to a point where atomic vibrations increase to the point where they transfer energy as kinetic energy, which accounts for the increase in k_e. Figure 4.26 compiles the findings of the Seebeck coefficient (S) versus the temperature. We find that for all of our compounds, the S values in the spin-up channel are positive across the whole temperature range, suggesting that our compounds are p-type and that the holes function as charge carriers. Sr_2TmCoO_6 has negative values of S and electrons function as charge carriers in the spin-down band. The figure of merit (ZT) defines the efficiency of thermoelectric devices. From the results obtained for the three transport properties (S, σ, and k_e), we calculated the ZT (See Figure 4.27). Our materials have a maximum ZT factor equal to 1 in low-temperature ranges in the spin-up channel. These features are suitable for the development of thermoelectric devices.

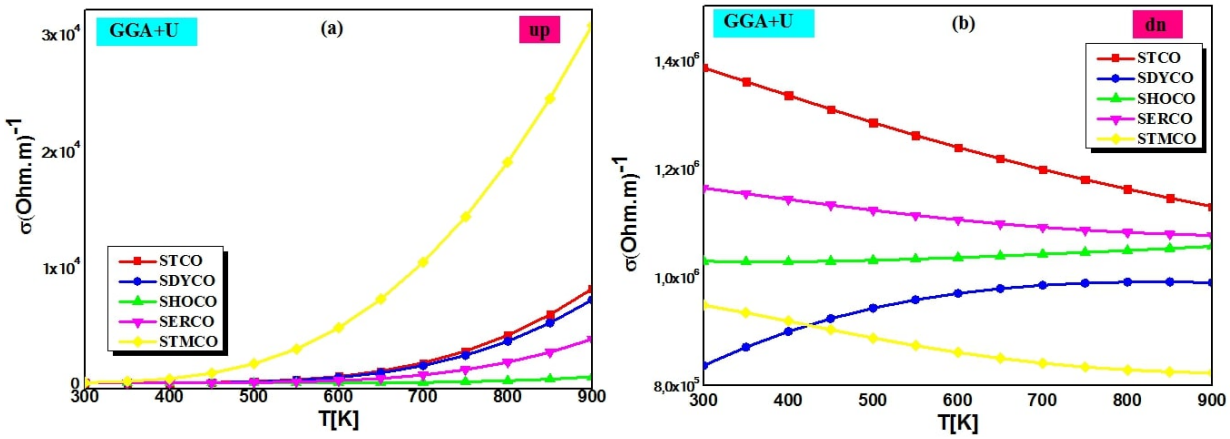

(a) (b)

Figure 4.24: Electrical conductivity (σ) versus temperature of Sr_2ACoO_6 (A= Ti, Dy, Ho, Er, or Tm) for a) spin-up and b) spin-down by applying GGA+U.

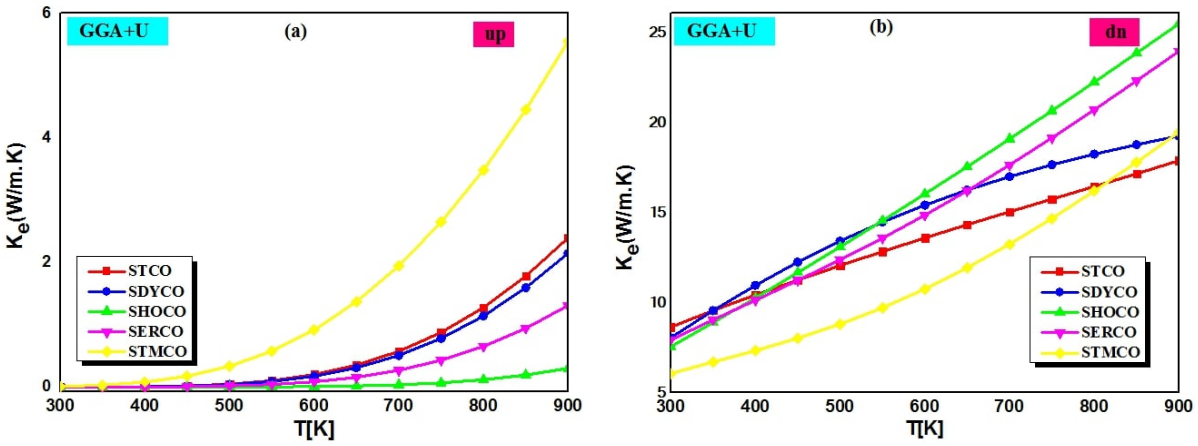

(a) (b)

Figure 4.25: Electronic thermal conductivity (k_e) versus temperature of Sr_2ACoO_6 (A= Ti, Dy, Ho, Er, or Tm) for a) spin-up and b) spin-down by applying GGA+U.

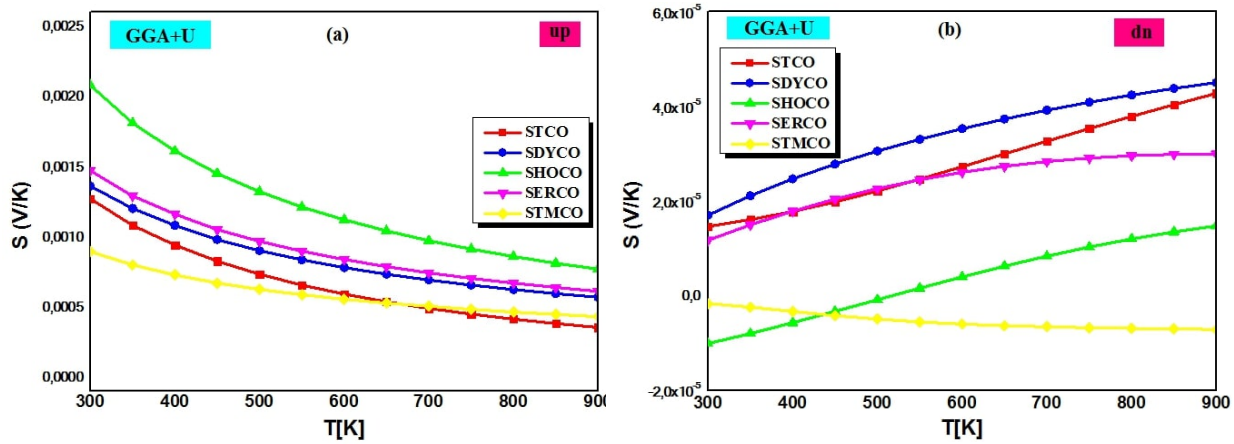

(a) (b)

Figure 4.26: Seebeck coefficient (S) versus temperature of Sr_2ACoO_6 (A= Ti, Dy, Ho, Er, or Tm) for a) spin-up and b) spin-down by applying GGA+U.

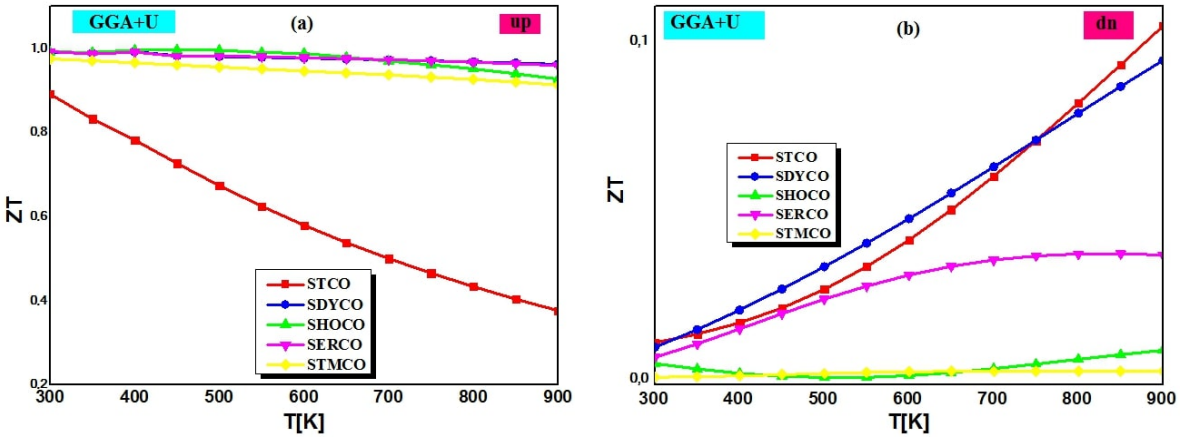

(a) (b)

Figure 4.27: Figure of merit (ZT) versus temperature of Sr_2ACoO_6 (A= Ti, Dy, Ho, Er, or Tm) for a) spin-up and b) spin-down by applying GGA+U.

4.3 Study of Half-metallic Antiferromagntic Double Perovskite Sr_2TcReO_6

As we have already seen, double perovskite ferromagnetic materials have interesting properties in different fields, such as Spintronics, optoelectronics, photovoltaic cells, and thermoelectrics. Double perovskites have a relatively high magnetic transition temperature (T_c), which implies that conduction electrons are more spin-polarized. Among these, Sr_2CrReO_6 has a Curie temperature of $T_c = 635K$ [14, 15]. Given that half-metallic antiferromagnetics (HM-AFMs) exhibit high spin polarization around the Fermi level, have zero magnetic moments, and lose less energy if employed in spintronic devices, multiple investigations have shown that double perovskites may be a promising option for HM-AFM materials [166]. Van Leukenet al. [167] provided the first half-metallic antiferromagnetics using the Heusler compound ($V_7MnFe_8Sb_8In$), and the first suggestion of HM-AFM in perovskite oxides was made by Pickett [168, 169].Since the current in HM-AFM is entirely spin polarization and produced by electrons near the Fermi level, it does not generate a magnetic field. Thus, the electrons responsible for magnetism do not participate in electronic conduction. Spin-Polarized Scanning Tunnel Microscopy (SP-STM) is one experiment that benefits from these features. The presence of a persistent magnetic tip that is roughly located on the (magnetic) surface that one wants to study is the foundation of SP-STM [167].

In this section, we have used FP-LAPW to study the structure electronic, magnetic, optical, and thermoelectric characteristics of the antiferromagnetic material Sr_2TcReO_6, which comes from the ferrimagnetic double perovskite oxide Sr_2CrReO_6 within the GGA-

PBEsol [149] and GGA+U [43] approaches.

4.3.1 Calculation details

We performed semi-relativistic computations, ignoring the spin-orbit effect. The GGA-PBEsol and PBEsol+U approaches provide a foundation for discussing the exchange and correlation potential. The number of particular points used for the mesh of the first Brillouin zone is set at 1000, resulting in a $10\times10\times10$ grid. The process of self-consistency occurs when the energy difference between iterations converges to $10^{-6}Ry$. The charge density of $\Delta Q = 10^{-6}e$ is selected to enhance the precision of the computations with spin-polarized, while the forces decrease to 0.1mRy/au. Separating the valence state from the core state requires a cut-off energy of -6.5Ry. The optimal muffin-tin radii values for Sr, Cr, Re, Tc, and O atoms are 2.5, 1.92, 1.93, 1.78, and 1.66 Bohr, respectively. Plane-wave functions $R_{MT} \times K_{\max}$ are limited to equal 7.0. We applied the GGA+ U technique to investigate the correlation on a site at the 3d-5d transition metal level. In the Hubbard Hamiltonian, U is the parameter for electrostatic repulsion. Using the U parameter in SCRO and STRO, the orbitals of Cr-3d, Re-5d, and Tc-4d are chosen to have U = 3eV, 1eV, and 2eV.

4.3.2 Structural properties

The structure of our first double perovskite Sr_2CrReO_6 (SCRO is tetragonal and belongs to space group I4/mmm ($N^\circ = 139$). $a = b = 5.52\AA$ and $c = 7.82\AA$ are the lattice constants in the experiment [14]. In Sr_2CrReO_6, the five atoms Sr, Cr, Re, O1, and O2 occupy the following positions: 4d(1/2, 0, 1/4), 2a(0, 0, 0), 2b(0, 0, 1/2), 8h(0.249, 0.249, 1/2), and 4e(0, 0, 0.254), respectively. For Sr_2TcReO_6 (STRO), we have replaced the Cr with a Tc atoms while maintaining the identical Wyckoff locations of the SCRO atoms. The representation of the crystal structures of the compounds SCRO and STRO are shown in Figure 4.28.

To determine the parameters of the equilibrium mesh and to find how the total energy varies against these parameters, we performed structural optimizations on the SCRO and STRO compounds. We used the GGA approximation to perform the calculation. Minimizing the total energy versus volume V is the structural optimization method. Repetition of the optimization cycle continues until convergence remains achieved. The total energy against volume is designated by E(V), which is adjusted by the Murnaghan equation [121], which leads to the determination of the structural parameters.The grouping of the optimal parameters, a and c, for SCRO and STRO is displayed in Table 4.7. Our results agree with published experimental and theoretical investigations. It confirms the success of GGA function in predicting the structural properties of solids. Figure 4.28 shows the

variations in total energy versus volume.

The tolerance factor governs the stability in the tetragonal structure, given by the following expression:

$$t = \frac{r_{Sr} + r_O}{\sqrt{2}(\frac{r_{R/Tc}+r_{Cr}}{2}) + r_O} \tag{4.2}$$

Where r_{Sr}, r_O, $r_{R/Tc}$, and r_{Cr} are the ionic radius of Sr, O, Re/Tc, and Cr atoms [170, 171]. It turns out that these compounds in tetragonal form are stable for t= 0.81–1.11 [163]. For SCRO and STRO, the t value is 0.877.

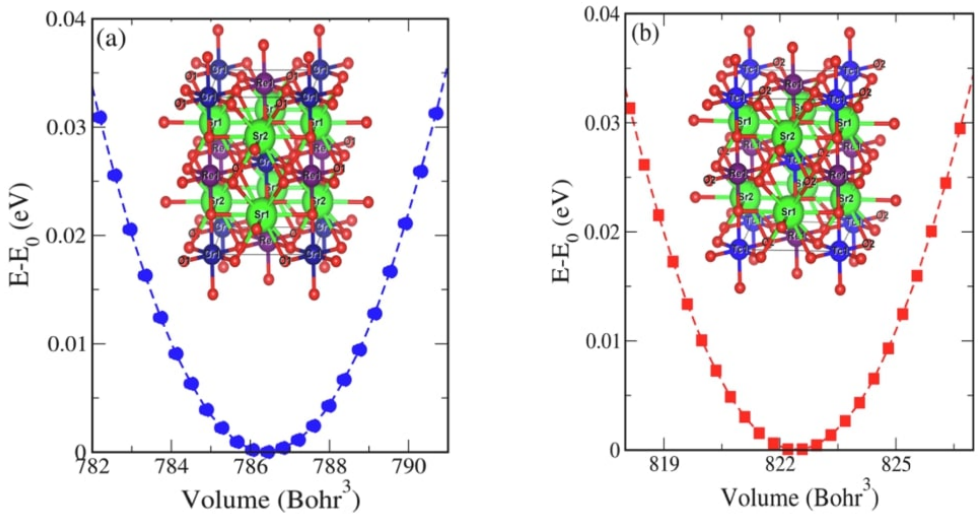

Figure 4.28: Structure crystallin and energy optimization versus volume of a) Sr_2CrReO_6 (SCRO) and b) Sr_2TcReO_6 (STRO).

	SCRO	STRO
Exp[38]	a=5.520, c=7.820	-
Ref.[47]	a=5.513, c=7.795	-
Ref.[48]	a=5.530, c=7.835	-
Present work PBE-GGA	a=5.530, c=7.835	a=5.590, c=7.930

Table 4.7: Equilibrium network parameters $a(\AA)$ and $c(\AA)$ of SCRO and STRO compounds by applying PBE-GGA.

4.3.3 Electronic and magnetic properties

It is feasible to determine if a compound is semiconductor, conductive, or insulating by analyzing its electronic structures. Indeed, there is a clear connection between most physical and electronic properties. We have determined the density of electronic states

(DOS) of SCRO and STRO by applying GGA-PBEsol and GGA+U to describe the electronic structure.

The DOS reflects an asymmetry among the majority- and minority-spin bands, shown in Figures 4.29 and 4.30, resulting in high spin polarization near the Fermi level using both approximations GGA-PBEsol and GGA+U. These results indicate that our compounds STRO and SCRO display a half-metallic character. The spin-up band in both compounds SCRO and STRO confirms a semiconductor characteristic (presence of forbidden band), and the structure of spin-up (majority) bands has intersections at the Fermi level, which shows the metallic properties. The band gap values calculated for the compounds studied SCRO and STRO utilizing GGA-PBEsol/GGA+U are 1.020eV/2.108eV and 0.418eV/1.146eV, respectively. Using PBEsol+U improves the energy band gap. The Hubbard U can improve the energy of the bandgap, thanks to the spin-up gap widening as the Tc-4d, Re-5d and Cr-3d bands shift farther from the Fermi level. The theoretical findings from DFT [174, 175] and the experimental data [176, 177, 178] agree well with our computations of the DOS of SCRO.

For SCRO, the total magnetic moment of $1\mu_B$ accords with the values obtained theoretically [15, 179] and the experimental result of $0.9\mu_B$. The partial moments of the Re and Cr atoms appear in Table 4.8. The outcomes demonstrate an anti-parallel interaction caused by the positive and negative partial moments of Cr and Re. We found that the Re and Cr generate the most of the total magnetic moment. The calculated Cr and Re moments agree rather well with values measured empirically and previously reported [180]. Re-5d orbitals are the main cause of half-metallic ferrimagnetism (HM-FiM), while Cr-3d orbitals have no contribution (Figure 4.29). The octahedral crystal field splits the Cr-3d and Re-5d atoms into t_{2g} and e_g states, which are the primary orbitals contributing to DOS. There are d_{xy}, d_{xz}, and d_{yz} orbitals in the states t_{2g}, and $d_{x^2-y^2}$ and d_{z^2} orbitals in the states e_g. The t_{2g} orbitals have a lower energy level than e_g orbitals. In the spin-minority band, the Re$-t_{2g}$ orbitals are partially occupied and have two electron ($5d : t_{2g}$ $2 \downarrow$). The $t_{2g} - Cr$ in spin-up channel are occupied, while the $t_{2g} - Cr$ orbitals in the minority-spin band are empty. They have three electrons ($3d : t_{2g}$ $3 \uparrow$). We can find the electronic configuration d^2 on Re^{5+} and d^3 on Cr^{3+}. Re and $Cr - t_{2g}$ states can hybridize with one another, allowing an electron in spin-down jumps from the Re^{5+} sites to the Cr^{3+} sites via O-2p orbitals. As a result, we may deduce that the O-2p atoms aid in the charge transfer among the Re-5d and Cr-3d electrons. The mechanism that controls the ferromagnetism in the SCRO compound is the Zener double exchange.

The anti-parallel alignment of the two magnetic moments produces the total magnetic moment of $0\mu_B$ in the STRO compound. The magnetic moment of the Re is negative,

while that of Tc is positive, as indicated in Table 4.8. The STRO compound displays the half-metallic antiferromagnetic behavior. Since this compound STRO does not alter the magnetic characteristics of the material surface, it seems to have great potential as a spin-polarized STM tip. From Figure 4.30, the $Tc - t_{2g}$ states are occupied in the spin-up band, while the minority-spin band shows the empty states. It has three electrons $Tc^{4+}(4d^3 : t_{2g}\ 3\uparrow)$. In the majority spin band, the $t_{2g} - Re$ states are empty, but the minority-spin band has some partial filling. It contains 3 electrons $Re^{4+}(5d^3 : t_{2g}\ 3\downarrow)$. The minority-spin band, made up of 5d-Re and 2p-O- states, is traversed by the Fermi level. The p-d hybridization can explain the antiferromagnetism in STRO. This study suggests that half-metallic antiferromagnets find suitable conditions in the double perovskite group of compounds. More experimental validation for these possible HM-AFM candidates will come in the future.

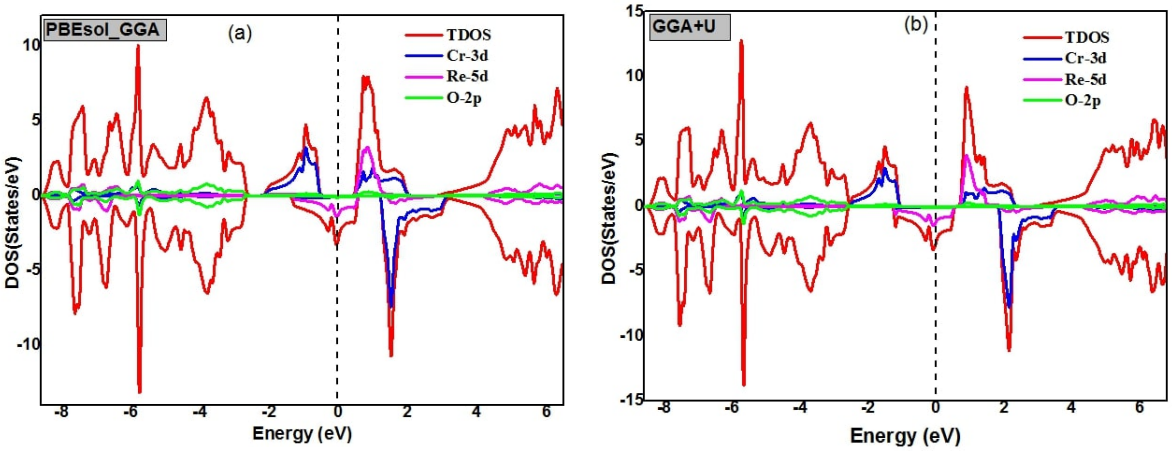

(a) (b)

Figure 4.29: Spin-polarized Total DOS and Partial DOS of SCRO by applying a) GGA-PBEsol and b) GGA+U.

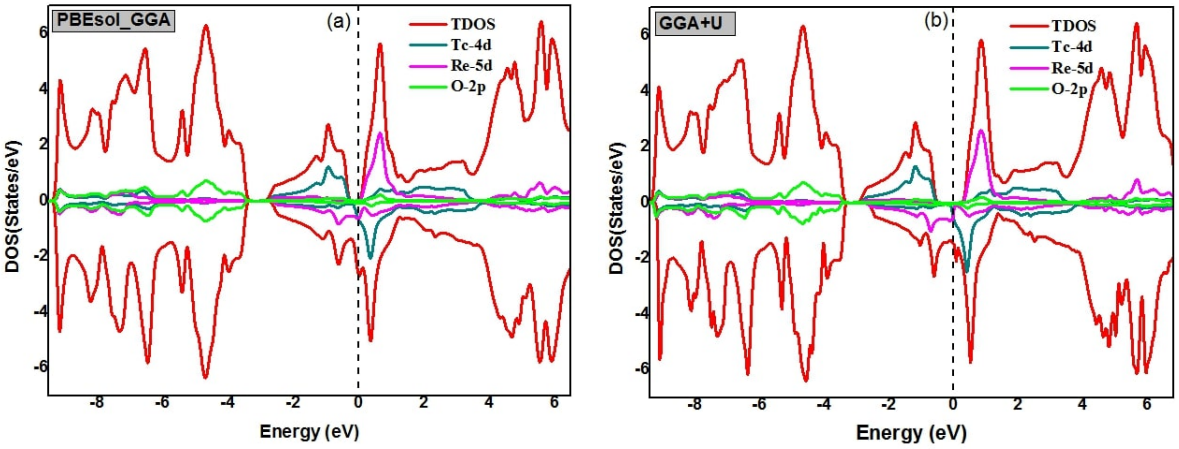

(a) (b)

Figure 4.30: Spin-polarized Total DOS and Partial DOS of STRO by applying a) GGA-PBEsol and b) GGA+U.

	$Sr_2Cr\mathrm{ReO}_6$	$Sr_2Tc\mathrm{ReO}_6$
$E_T(Ry)$	-49138.824/-49138.643	-55607.868/-55607.690
$E_g(eV)$	1.020/2.108	0.418/1.146
$m_t(\mu_B)$	1/1	0/0
$m_{Cr}(\mu_B)$	2.086/2.373	-
$m_{Tc}(\mu_B)$	-	0.905/1.220
$m_{\mathrm{Re}}(\mu_B)$	-0.821/-0.992	-0.871/-1.155
$m_{O1}(\mu_B)$	-0.019/-0.026	-0.001/-0.003
$m_{O2}(\mu_B)$	-0.026/-0.032	-0.010/-0.016

Table 4.8: Results of total energies, total and partial magnetic moments, and band gap energy of SCRO and STRO by applying GGA-PBEsol/GGA+U.

4.3.4 Optical properties

In this part, we have investigated the optical characteristics of half-metal ferrimagnetic and antiferromagnetic compounds versus photon energy. The spectra of the $\varepsilon_2(\omega)$ against energy of the electromagnetic radiation is presented in Figures 4.31a and 4.32a using PBEsol+U and PBEsol-GGA. We can note the maximum intensity peak of $\varepsilon_2(\omega)$ for STRO and SCRO at 0.52eV/0.69eV and 1.66eV/2.45eV using PBEsol-GGA/PBEsol+U, respectively. The peaks in the $\varepsilon_2(\omega)$ define the interband transitions of electrons. Optical transitions occur above the valence band (VBM) and below the conduction band (CBM). When compared to PBEsol-GGA, PBEsol+U increased absorption in the visible spectrum, whereas the peaks in the infrared spectrum for STRO and SCRO moved into the visible spectrum. Figures 4.31b and 4.32b show the evolution of $\varepsilon_1(\omega)$ versus photon energy. The constants $\varepsilon_1(0)$, static dielectric, show high values at zero photon energy, as a shown in Table 4.9. The $\varepsilon_1(\omega)$ significant values suggest a higher polarization ability. The materials display metallic behavior because the $\varepsilon_1(\omega)$ remains negative at certain places, indicating complete reflection of the input electromagnetic waves. The $\varepsilon_1(\omega)$ tends to zero at high energy, which may reflect the appearance of oscillations of the plasmonic kind.

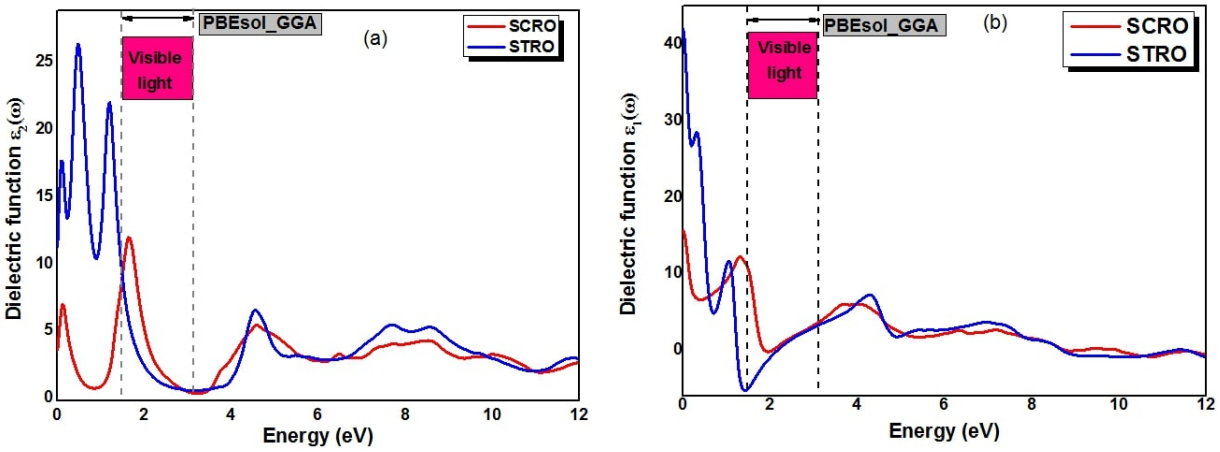

(a) (b)

Figure 4.31: Variation of the (a) imaginary $\varepsilon_2(\omega)$ and (b) real $\varepsilon_1(\omega)$ parts of the dielectric function of SCRO and STRO by applying GGA-PBEsol.

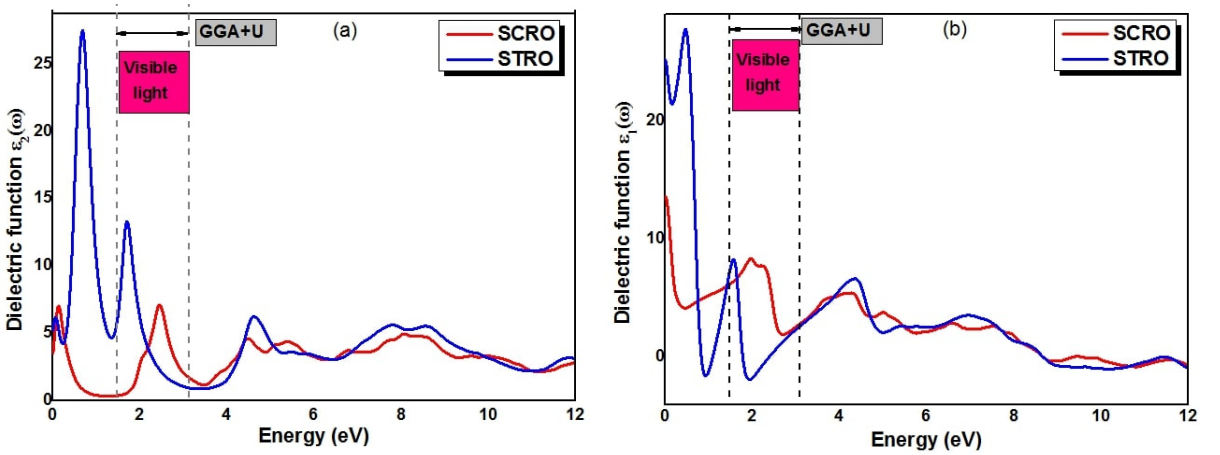

(a) (b)

Figure 4.32: Variation of the (a) imaginary $\varepsilon_2(\omega)$ and (b) real $\varepsilon_1(\omega)$ parts of the dielectric function of SCRO and STRO by applying GGA+U.

	Sr_2CrReO_6	Sr_2TcReO_6
$\varepsilon_1(0)$	15.62/13.61	42.03/25.18
n(0)	3.98/3.71	6.54/5.04
R(0)	36.41/33.82	54.61/45.16

Table 4.9: Results of the optical parameters at zero photon energy of STRO and SCRO by applying GGA-PBEsol/GGA+U

Moreover, we investigated the absorption coefficient $\alpha(\omega)$ of the STRO and SCRO by applying GGA-PBEsol and GGA-GGA, as shown in Figure 4.33. The quantities $\alpha(\omega)$ and $\varepsilon_2(\omega)$ are closely linked. These two parameters explain the attenuation of the incident

beam of light. We can see that these compounds can absorb light in several regions (IR, visible, and UV). The STRO material has a significant amount of absorption compared to SCRO. These results show that our compounds, as best absorbers, are suitable for optoelectronic and photovoltaic devices.

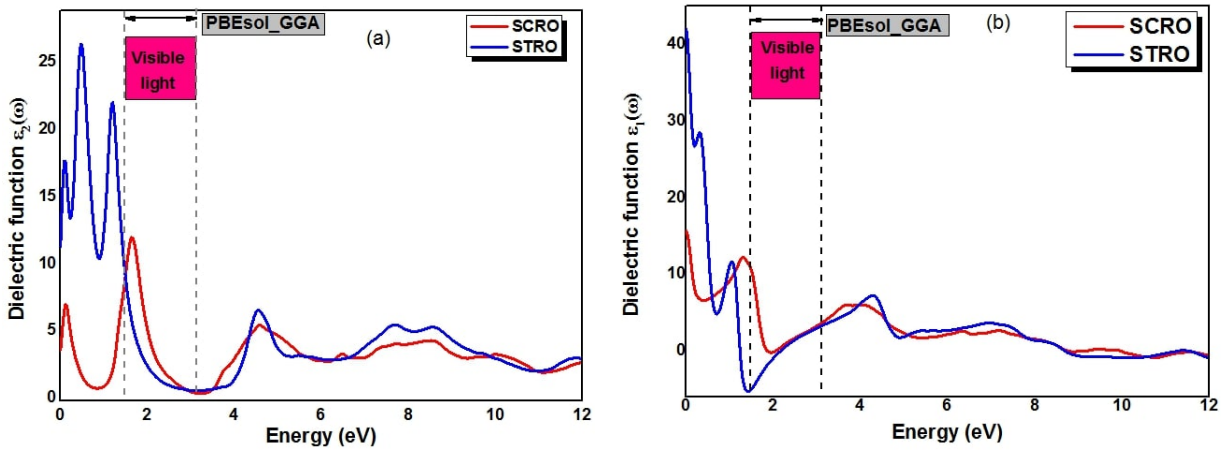

(a) (b)

Figure 4.33: Spectra of the absorption coefficient $\alpha(\omega)$ of STRO and SCRO by applying a) GGA-PBEsol and b) GGA+U.

Figures 4.34a and 4.35a show the evolution of the refractive index $n(\omega)$ against photon energy by applying PBEsol+U and PBEsol-GGA. The $n(\omega)$ spectra present a maximum at low photon energy (IR region) for STRO and SCRO using both GGA+U and GGA-PBEsol approach. The static values at zero photon energy n(0) of STRO and SCRO appear in Table 4.9. We find the same findings from $n(0) = \sqrt{\varepsilon_1(0)}$. The optical dispersion of light causes the $n(\omega)$ values to drop as photon energy increases. The spectra of the loss function, $L(\omega)$, of STRO and SCRO, is illustrated in Figures 4.34b and 4.35b using PBEsol+U and PBEsol-GGA. We note that the energy loss is considerably high in visible areas. Losses of energy happen by excitations of electrons. Using PBEsol+U and PBEsol-GGA, the reflectivity spectra $R(\omega)$ for the STRO and SCRO are displayed in Figures 4.34c and 4.35c. These Figures make it quite evident that, for both compounds, the $R(\omega)$ curves increase at low photon energy. The R(0) values at zero photon energy appear in Table 4.9. These maxima of $R(\omega)$ result from interband transitions. The extinction coefficient evolution $k(\omega)$ against photon energy is displayed in Figures 4.34d and 4.35d using PBEsol+U and PBEsol-GGA. The maximum peaks in $k(\omega)$ spectra appear in the IR range for STRO at 1.27eV/0.64eV and in the visible region for SCRO at 1.78eV/2.11eV by applying PBEsol-GGA/PBEsol+U. Every peak in the $k(\omega)$ represents a high percentage of light absorption.

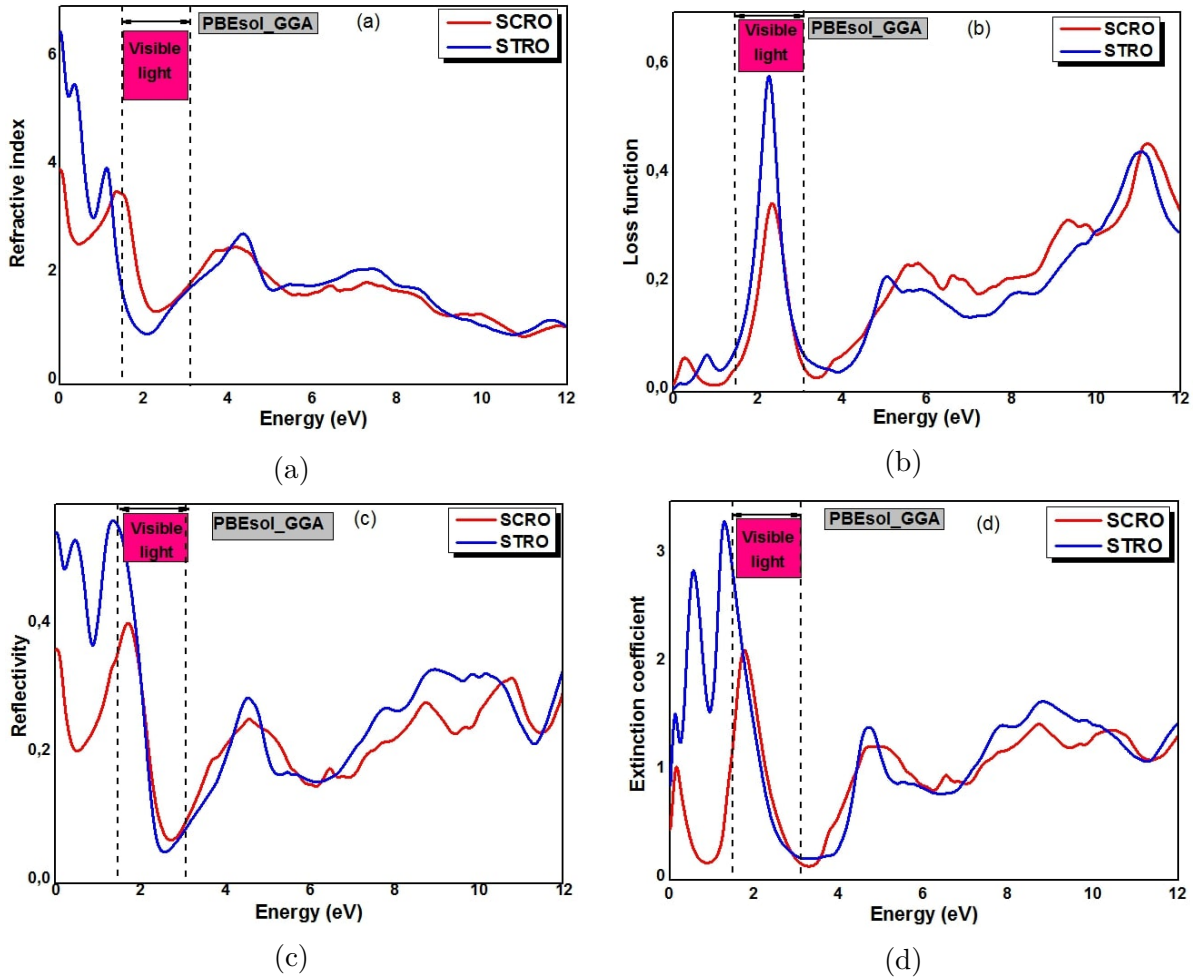

Figure 4.34: Spectra of the (a) refractive index $n(\omega)$, (b) loss function $L(\omega)$, (c) reflectivity $R(\omega)$, and (d) extinction coefficient $k(\omega)$ of SCRO and STRO by applying GGA-PBEsol.

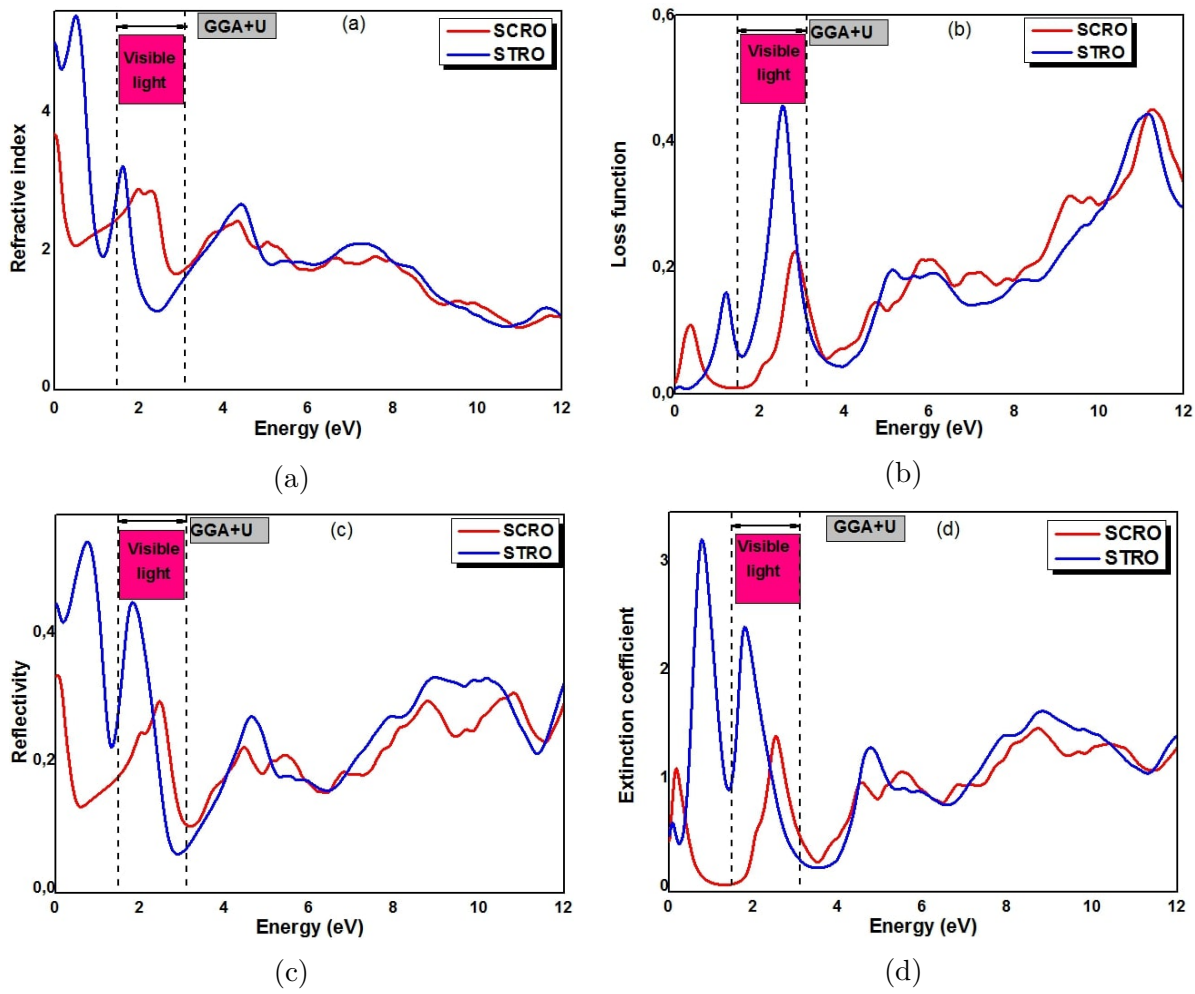

Figure 4.35: Spectra of the (a) refractive index $n(\omega)$, (b) loss function $L(\omega)$, (c) reflectivity $R(\omega)$, and (d) extinction coefficient $k(\omega)$ of SCRO and STRO by applying GGA+U.

4.3.5 Thermoelectric properties

An option for solving the energy crisis is thermoelectric materials (TE), which convert heat into electricity. Because this class of materials manages energy efficiently and in an environmentally benign manner, research into them is currently proceeding more quickly than with other technologically significant materials [154, 181].

Figure 4.36 displays the electrical conductivity (σ/τ) curves against temperature for the materials STRO and SCRO. For STRO, σ/τ increases with temperature rise. The σ/τ values of SCRO are small compared to STRO. The modest value of σ/τ at low temperatures indicates the lack of carriers. Increased electrical conductivity and the creation of electron-hole pairs are outcomes of electrons receiving high thermal energy to jump to the conduction band when the temperature rises. Considering that the electronic component of thermal conductivity, k_e, depends on the relaxation time, τ, we obtain k_e/τ in the current calculations. Figure 4.37 shows the electronic thermal conductivity (k_e/τ)

against temperature. The STRO compound shows high values of k_e when temperature rises compared to SCRO. Higher temperatures enhance the density of charge via electronic vibrations. Quantifying the link between the electrical potential and the thermal potential is made feasible by the Seebeck coefficient. A positive Seebeck reflects a p-type of carriers (holes), while a negative Seebeck reflects an n-type of carriers (electrons). Figure 4.38 represents the Seebeck coefficient variation against temperature for SCRO and STRO. Negative values of S suggest the conduction of the material by electrons, which increase with temperature rise. SCRO and STRO are n-type materials in both approximations GGA-PBEsol and GGA+U. The figure of merit (ZT) defines the thermoelectric efficacy. Figure 4.39 displays the merit factor (ZT) curves versus the temperature of the SCRO and STRO compounds. The ZT values are 0.86/0.99 for SCRO and 0.97/1.01 for STRO using PBEsol-GGA/PBEsol+U at 300K. For thermoelectric devices, materials having a ZT around or over unity are generally suitable choices [182]. These materials STRO and SCRO exhibit exceptional performance, making them viable options for thermoelectric devices in the alternative energy sector.

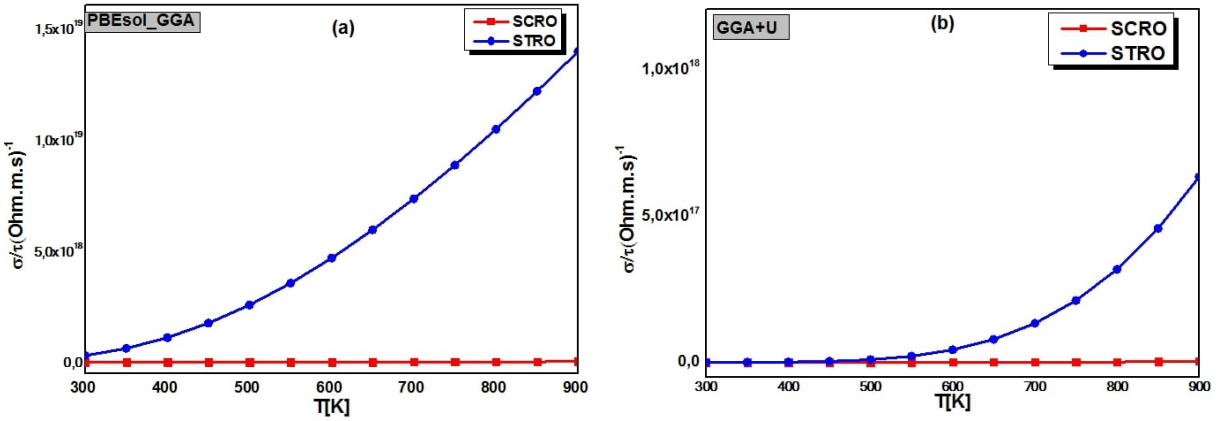

(a) (b)

Figure 4.36: Electrical conductivity (σ/τ) against temperature of STRO and SCRO by applying (a) GGA-PBEsol and (b) GGA+U.

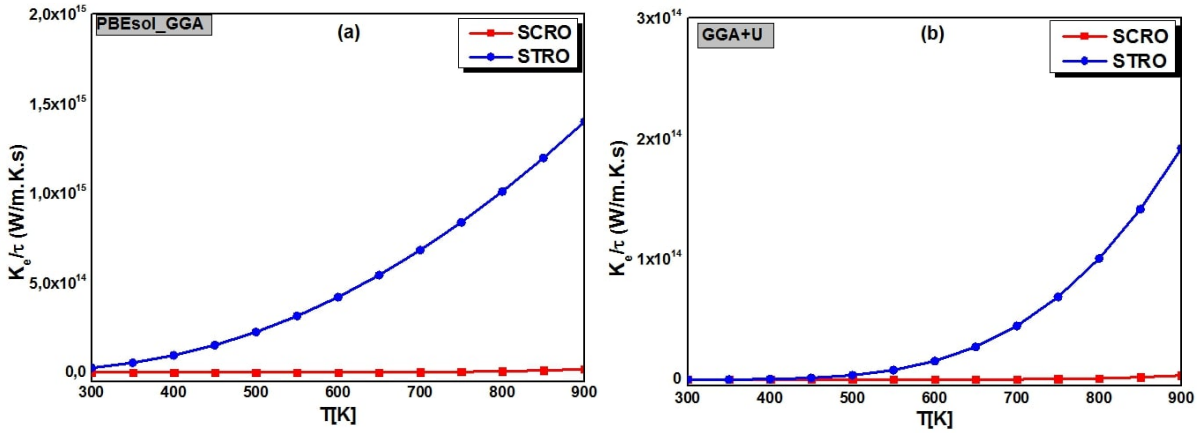

(a) (b)

Figure 4.37: Electronic thermal conductivity (k_e/τ) against temperature of STRO and SCRO by applying (a) GGA-PBEsol and (b) GGA+U.

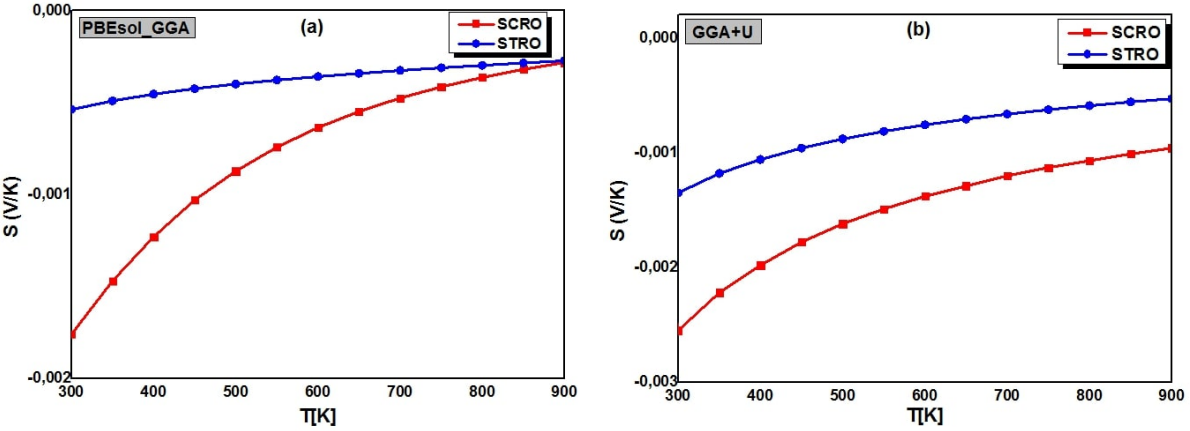

(a) (b)

Figure 4.38: Seebeck coefficient (S) against temperature of STRO and SCRO by applying (a) GGA-PBEsol and (b) GGA+U.

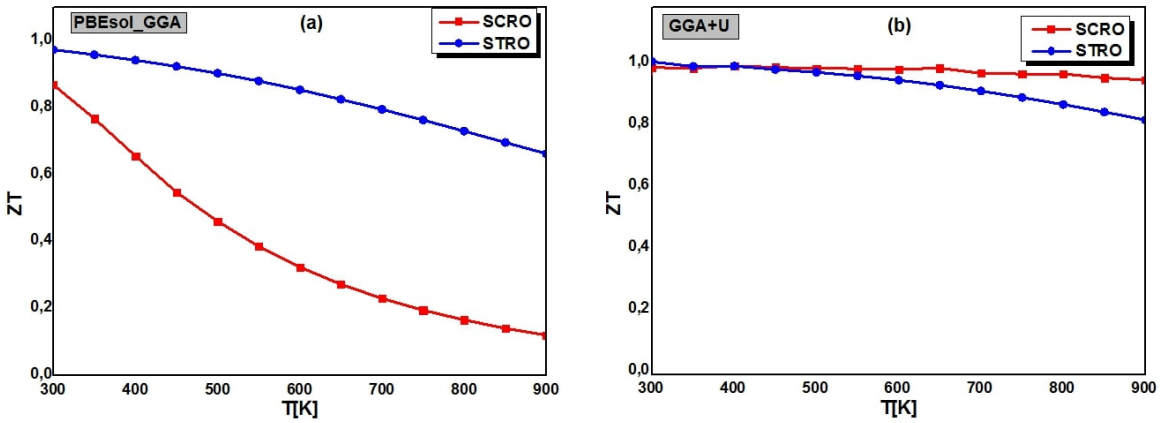

(a) (b)

Figure 4.39: Figure of merit (ZT) against temperature of STRO and SCRO by applying (a) GGA-PBEsol and (b) GGA+U.

4.4 Conclusion

To conclude, we presented the results of the electronic, structural, magnetic, optical, and thermoelectric characteristics of Ferromagnetic and Antiferromagnetic Double perovskites using for this the functional density theory based on the FP-LAPW method. We have applied various approximations in this chapter, such as GGA, GGA+U, YS-PBE0, GGA+mBJ, and SOC. The substitution by the best choice of the impurity in our initial double perovskites can improve the physical properties. All compounds in this study display the half-metallic behavior when replaced by transition metals or rare-earth elements. These features are suitable for Spintronic applications. These compounds can function as light absorbers in solar cells because they can absorb light in the visible, UV, and infrared photon energy areas. We found intriguing room-temperature findings for these antiferromagnetic and ferrimagnetic materials, including a near unity figure of merit and a very high optimum Seebeck coefficient. These encouraging characteristics imply that the investigated compounds might make suitable thermoelectric and photovoltaic materials.

Modern Physics Letters B
(2023) 2350026 (20 pages)

DOI: 10.1142/S0217984923500264

Study of electronic, magneto-optical and transport properties of double perovskite Ca_2XMnO_6 (X = Ti, Cr) under uniaxial compressive strain by using a DFT method

S. Laghzaoui*, A. Fakhim Lamrani*,†, R. Ahl Laamara*,‡, E. Maskar*, Amel Laref§, Mattipally Prasad¶, J. Sivakumar¶ and D. P. Rai‖,**

*LPHE-Modeling and Simulation, Faculty of Sciences, Mohammed V University in Rabat, Rabat, Morocco

†ENS-Rabat Physics Department, Mohammed V University in Rabat, B. P. 5118, Morocco

‡Centre of Physics and Mathematics, CPM, Faculty of Sciences, Mohammed V University in Rabat, Rabat, Morocco

§Department of Physics and Astronomy, College of Science, King Saud University, Riyadh 11451, Saudi Arabia

¶Department of Physics, University College of Science, Osmania University, Hyderabad 500007, Telangana, India

‖Physical Sciences Research Center (PSRC), Department of Physics, Pachhunga University College, Mizoram University, Aizawl 796001, Mizoram, India

** dibyaprakashrai@gmail.com

Received 27 December 2022
Revised 25 January 2023
Accepted 29 January 2023
Published

Journal of Physics and Chemistry of Solids 183 (2023) 111639

Contents lists available at ScienceDirect

Journal of Physics and Chemistry of Solids

journal homepage: www.elsevier.com/locate/jpcs

Robust half-metallic ferromagnet in doped double perovskite Sr_2TiCoO_6 by rare-earth elements for photovoltaic and thermoelectric conversion: A DFT method

S. Laghzaoui [a], A. Fakhim Lamrani [a,b,*], R. Ahl Laamara [a,c]

[a] LPHE-Modeling and Simulation, Faculty of Sciences, Mohammed V University in Rabat, Rabat, Morocco
[b] ENS-Rabat Physics Department, Mohammed V University in Rabat, B. P. 5118, Morocco
[c] Centre of Physics and Mathematics, CPM, Faculty of Sciences, Mohammed V University in Rabat, Rabat, Morocco

ARTICLE INFO

Keywords:
Half-metallic ferromagnet
GGA+SOC
p-f hybridization
Photovoltaic solar cells
Thermoelectric applications

ABSTRACT

In this study, we have discovered a novel candidate series of half-metals by replacement of the Ti atom with the rare-earth elements RE (=Dy, Ho, Er, or Tm) in the double perovskite Sr_2TiCoO_6. We methodically investigated the electronic, magneto-optical, and thermoelectric characteristics of the compounds $Sr_2(RE)CoO_6$ using the FP-LAPW method. The spin-polarized electronic structure studied within GGA-WC and GGA + U showed a robust half-metallic character for all compounds. The substitution by the rare-earth elements RE enhanced the magnetic characteristics of Sr_2TiCoO_6, which exhibits a transition from a total magnetic moment of $1\mu_B$ for Sr_2TiCoO_6 to $7\mu_B$, $6\mu_B$, $5\mu_B$, and $4\mu_B$ for Sr_2DyCoO_6, Sr_2HoCoO_6, Sr_2ErCoO_6, and Sr_2TmCoO_6, respectively. However, the hybridization between RE-4f, Co-3d, and O-2p is responsible for robust half-metallic ferromagnet in $Sr_2(RE)CoO_6$ compounds. We have also studied the effect of spin-orbit coupling (SOC) on electronic structure. The Sr_2DyCoO_6, Sr_2HoCoO_6, and Sr_2ErCoO_6 compounds maintained their half-metallicity under GGA + SOC, whereas Sr_2TmCoO_6 became a magnetic metal. An in-depth analysis of the optical and thermoelectric characteristics was performed by GGA + U. According to the absorption coefficient and imaginary part of the dielectric function, we have found that the compounds $Sr_2(RE)CoO_6$ have better absorption quantities at different frequencies (IR, visible, and UV) than Sr_2TiCoO_6. Due to their high ZT and good Seebeck coefficient in a spin-up canal, the investigated compounds have excellent thermoelectric efficiency. These characteristics make the double perovskites $Sr_2(RE)CoO_6$ as a high absorber an attractive choice for photovoltaic solar cells and thermoelectric applications.

Inorganic Chemistry Communications 146 (2022) 110172

Contents lists available at ScienceDirect

Inorganic Chemistry Communications

journal homepage: www.elsevier.com/locate/inoche

Short communication

Realization of half-metal antiferromagnetic (HM-AFM) behaviour in double perovskite Sr_2CrReO_6 on substitution of Tc at Cr site: Promising material for optoelectronics and thermoelectric applications via DFT framework

S. Laghzaoui [a], A. Fakhim Lamrani [a,b], R. Ahl Laamara [a,c], E. Maskar [a], Amel Laref [d], Mohammed Ezzeldien [e,f], D.P. Rai [g,*]

[a] LPHE-Modeling and Simulation, Faculty of Sciences, Mohammed V University in Rabat, Rabat, Morocco
[b] ENS-Rabat Physics Department, Mohammed V University in Rabat, B. P. 5118, Morocco
[c] Centre of Physics and Mathematics, CPM, Faculty of Sciences, Mohammed V University in Rabat, Rabat, Morocco
[d] Department of Physics and Astronomy, College of Science, King Saud University, Riyadh 11451, Saudi Arabia
[e] Physics Department, College of Science, Jouf University, P.O. Box 2014, Sakaka, Al-Jouf, Saudi Arabia
[f] Metallurgy & Material Science Tests (MMST) Lab, Department of Physics, Faculty of Science, South Valley University, Qena, Egypt
[g] Physical Sciences Research Center (PSRC), Department of Physics, Pachhunga University College, Mizoram University, Aizawl 796001, India

ARTICLE INFO

Keywords:
FP-LAPW
Half-metallic antiferromagnet materials
Spin device
Zener double exchange
Photovoltaic
Thermoelectric properties

ABSTRACT

Using the first principles approach within the Full Potential Linearized Augmented Plane wave (FP-LAPW) method, the electronic, magnetic, optical and thermoelectric properties of double perovskite oxides Sr_2AReO_6 (A = Cr, Tc) were systematically investigated. We have used the most appropriate functionals like PBEsol-GGA and PBEsol + U. The replacement of Cr atom by Tc atom in Sr_2CrReO_6 leads to the transition of the magnetic configuration from ferrimagnet to complete antiferromagnet half-metal (AFM-HM) with zero magnetic moments. The mechanisms that govern the ferrimagnetism/antiferromagnetism in the two double perovskites are the Zener double exchange and p-d hybridization, respectively. A careful analysis of the optical and thermoelectric properties in this study leads to the conclusion that the antiferromagnet double perovskite Sr_2TcReO_6 (STRO) has the power to convert the maximum amount of sunlight in the visible range as compared to Sr_2CrReO_6(SCRO). Further, we have obtained an optimal figure of merit (ZT ~ 1) and high electrical conductivity. Finally, the half-metallic antiferromagnetic double perovskite STRO is a potential energy material for the spintronic device, photovoltaic solar cells and thermoelectric applications.

Chapter 5

Study of electronic, magnetic, optical, and thermoelectric properties of doped two-dimensional ZnO nanosheets

Introduction

Two-dimensional (2D) materials have garnered a great deal of attention since the discovery of graphene because of their exceptional optical and electrical capabilities. The initial discovery of graphene in 2004 [23], a substance with extraordinarily high conductivity, and its integration with several other materials marked the beginning of the 2D study. Graphene is a material composed of hexagon-shaped sp^2 hybridized carbon atoms that are atomically thick. It stands out by its extreme qualities, including exceptional conductivity, high thermal conductivity, and durable chemical and mechanical resistance. Despite its extraordinary qualities, graphene is not appropriate for many device applications because of the absence of bandgap [183]. One method to overcome this graphene limitation is to open the graphene bandgap or use a different 2D material with electrical properties similar to graphene but a limited bandgap [184, 185, 186]. Research has shown that nanosheets are one of the most significant challenges in current studies, as is evident by the number of publications on the subject. Zinc oxide (ZnO) is a highly promising 2D nanosheet in technology due to its large direct band gap and outstanding efficacy in fields like spintronics and optoelectronic devices [187, 188]. Similar to graphene, ZnO nanosheets crystallize in a planar honeycomb shape [189] in contrast to bulk ZnO, which forms crystals in a wurtzite structure. Because of this structural modification and the quantum confinement effect, 2D-ZnO exhibits several unique features. Compared to the ZnO bulk, which has a band gap of 3.4eV [190], 2D-ZnO has a band gap ranging from 3.54 to 4.0eV [189]. Various techniques are currently employed to alter the magnetic and electronic characteristics of 2D-ZnO, such as external strain [191] and doping [192, 193, 194]. One of the best strategies is doping. By doping ZnO nanosheets (ZnONSs) with foreign atoms, it has recently become possible to efficiently manufacture 2D nanostructures, namely single-layer (SL) graphite-like ZnO nanosheets [195]. It allows for obtaining half-metallic (HM) ferromagnetic (FM) characteristics.

We investigated in this chapter the structure electronic, magnetic, optical, and thermoelectric properties of metal transitions TM(=Fe, Co, Ni, or Cu) doped ZnO nanosheets through the FP-LAPW method by applying the PBEsol-GGA approach. Our results show the half-metallic behavior when doped ZnO nanosheet by TM doping. Our findings may guide the development of ferromagnetic ZnO nanosheets utilized in optoelectronic and spintronic devices and provide a basic understanding of these materials.

5.1 Calculation details

All computations are performed with the WIEN2k package [196], which relies on DFT [1, 2] and employs the FP-LAPW method [197]. We have applied the PBEsol-GGA

approach [149] to characterize the exchange and correlation function. The process of self-consistency occurs when the energy difference between iterations converges to $10^{-6}Ry$. The charge density of $\Delta Q = 10^{-6}e$ is selected to enhance the precision of the computations with spin-polarized, while the forces decrease to 0.1mRy/au. To specify the distance between the core and the valence states, a cut-off energy of -6.5Ry is used. The muffin-tin (MT) spheres radius are 1.89, 1.63, and 1.89 Bohr for Zn, O, and TM atoms, respectively. We have used the 200 k-point meshes using the Monkhorst-Pack grid [198] to acquire the optical characteristics and DOS.

5.2 Crystal structure

In Figure 5.1, a TM-3d atom has been used instead of one Zn atom represented in the $3\times3\times1$ supercell. Some theoretical studies examined the total energy against band gap for various nanosheet configurations by altering the spacing between $5\mathring{A}$ and $15\mathring{A}$ to analyze the interaction between neighboring ZnONS sheets. The findings demonstrate that the energy of the bandgap and total energy becomes constant beyond $10\mathring{A}$, indicating that at spacings above $10\mathring{A}$, the contact between nanosheets becomes extremely negligible, and the nanosheet is considered isolated [199]. A vacuum space of $15\mathring{A}$ in this work is applied along the z-axis perpendicular to the ZnONS sheets and positioned on the x-y plane to prevent interactions among adjacent ZnO sheets. The computed bond length (Zn-O) of $1.8942\mathring{A}$ in the ZnO nanosheet (ZnONS) accords with the experimental value of $1.9\mathring{A}$ [200] and the earlier theoretical findings of $1.86\mathring{A}$ [201, 202]. The Zn-O bond shrinks in the nanosheet because the sp^2 hybridization of the bond length is stronger than the sp^3 bonding in bulk, which is $1.98\mathring{A}$ [199, 203]. The structure of the optimized pure ZnONS is akin to that of honeycomb structures [204, 205], as shown in Figure 5.1. The atoms of zinc and oxygen make 120° angles. The honeycomb structures of silicon carbon (SiC), graphene, and boron nitride exhibit a like pattern [205].

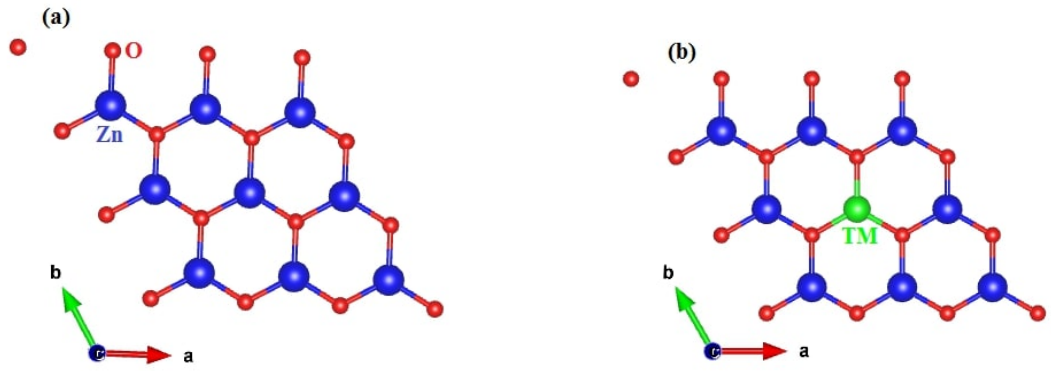

(a) (b)

Figure 5.1: Crystal structure of a) pure ZnO nanosheet and b) ZnO nanosheet doped with TM placed on the x–y plane.

The formation energy (E_f) was computed using the following formula to provide a more comprehensive thermodynamic stability investigation of TM doped ZnO nanosheets [192, 206]:

$$E_f = E_{ZnO:TM} - E_{ZnO} + \mu_{Zn} - \mu_{TM} \tag{5.1}$$

Where E_{ZnO} and $E_{ZnO:TM}$ denote the total energies of the pure ZnO nanosheets and TM doped ZnO nanosheets, respectively. The chemical potential is $\mu(X)$ (where X = Zn/TM). We get E_f values of 2.14, 2.063, 3.022, and 2.32eV for ZnONS doped with Fe, Co, Ni, and Cu, respectively. For structures in experiments, lower E_f values are preferable.

5.3 Electronic and magnetic properties

Figure 5.2(a) displays the TDOS and PDOS for pristine ZnONS by applying the PBEsol-GGA approach. The DOS indicates that pure ZnO exhibits a semiconductor nature and has a band gap of 1.615eV, which accords with earlier theoretical studies [192, 199, 206]. The ZnONS pure seems to be a nonmagnetic material due to the perfect symmetry between the spin-up/-down bands in the DOS. The O-2p orbitals constitute the highest occupied molecular orbitals (HOMO) and lowest unoccupied molecular orbitals (LUMO)[207]. Figure 5.2(b) displays the band structure using the potential of PBEsol-GGA. ZnONS pure has a direct band gap, meaning that the conduction band minimum (CBM) and valence band maximum (VBM) are located at the same place Γ.

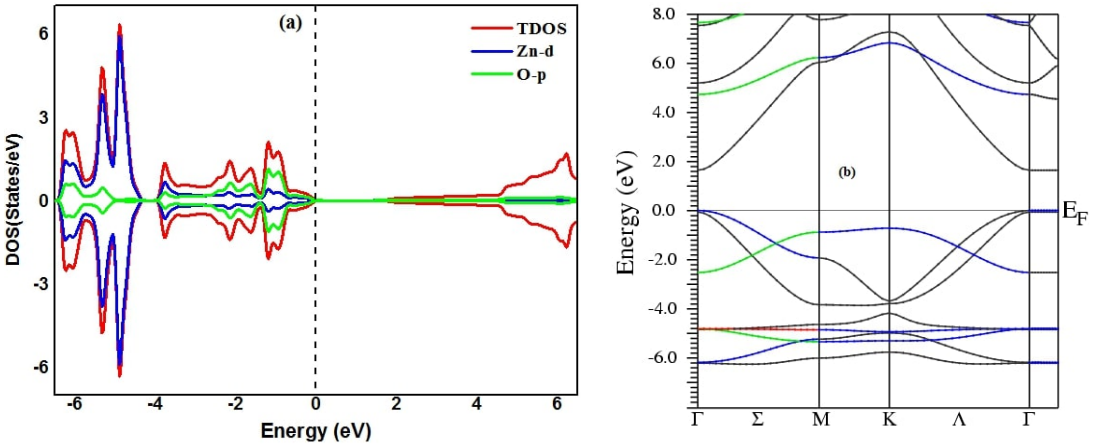

(a) (b)

Figure 5.2: a) Total DOS and Partial DOS and b)band structure of pure ZnO nanosheet.

As seen in Figures 5.3–5.6, we used PBEsol-GGA to compute the Total DOS and Partial DOS of the TM-doped ZnONS. This work will help further investigate the effects of TM doping on the structure magnetic and electronic properties of pristine ZnO nanosheet. Magnetic moments are present in the DOS because of spin-split close to the Fermi level. It appears that the DOS of ZnONS doped with TM exhibits notable asymmetry. These figures show the high spin polarisation around the Fermi level, indicating the presence of half-metal character in all systems doped. From Figures 5.4, 5.5, and 5.6, the spin-down band, composed of the O-2p, and Co, Ni, or Cu-3d orbitals, is crossed by the Fermi level. It suggests significant p-d hybridization among 2p-O and 3d-Co/3d-Ni/3d-Cu states. We can use the p-d hybridization to explain the ferromagnetism in systems doped. ZnO films doped with C have also shown evidence of p-p interaction and p-d exchange hybridization [208]. Furthermore, in Fe-, Co-, or Ni-doped ZnO nanosheets systems, we find that the Fermi level rises to the conduction band, suggesting an n-type material that could exhibit a low resistivity characteristic. While the Cu-doped ZnO nanosheet displays a p-type system. Table 5.1 lists the computed total and partial magnetic moments by applying PBEsol-GGA. The total magnetic moment of ZnO nanosheets doped with Fe-, Co, Ni, and Cu show the net values of $4\mu_B$, $3\mu_B$, $2\mu_B$, and $1\mu_B$, respectively. We find that the TM atoms contribute primarily to the magnetic moments of the TM-doped ZnONS. The ZnO nanosheets doped with TM are promising DMS for use in spintronic devices. One zinc atom gets replaced with the TM atom, and an anion (O) receives two electrons from the TM. Each of the four parallel-spin electrons can occupy the 3d orbital of Fe^{2+}. Similarly, Co^{2+} has three parallel-spin electrons, Ni^{2+} has two parallel-spin electrons, and Cu^{2+} has one parallel-spin electron.

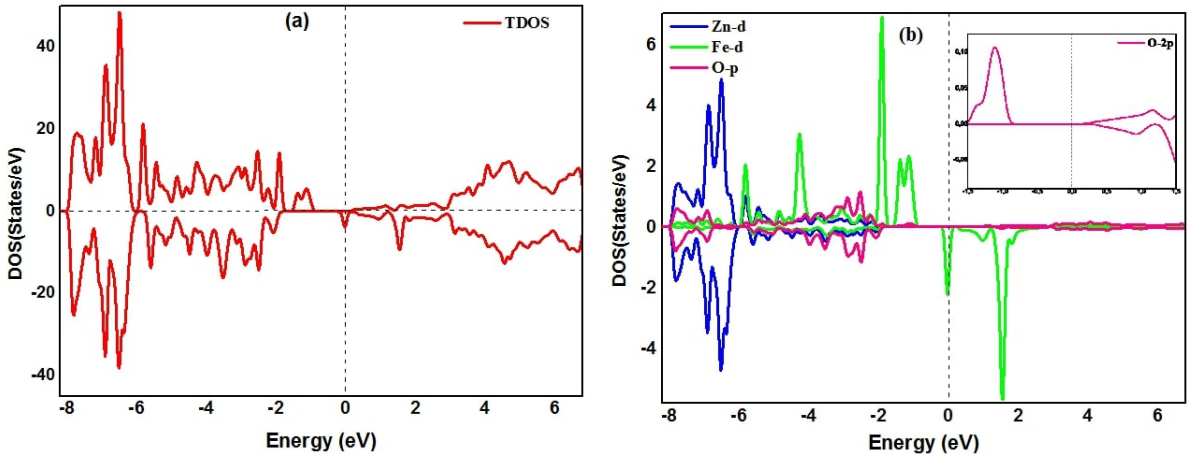

(a) (b)

Figure 5.3: Total DOS and Partial DOS of Fe-doped ZnONS.

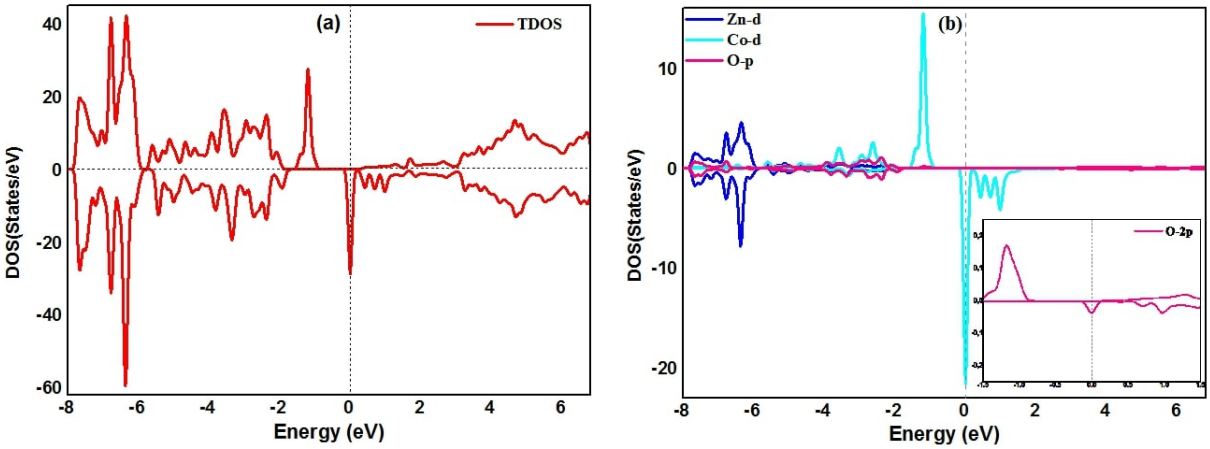

(a) (b)

Figure 5.4: Total DOS and Partial DOS of Co-doped ZnONS.

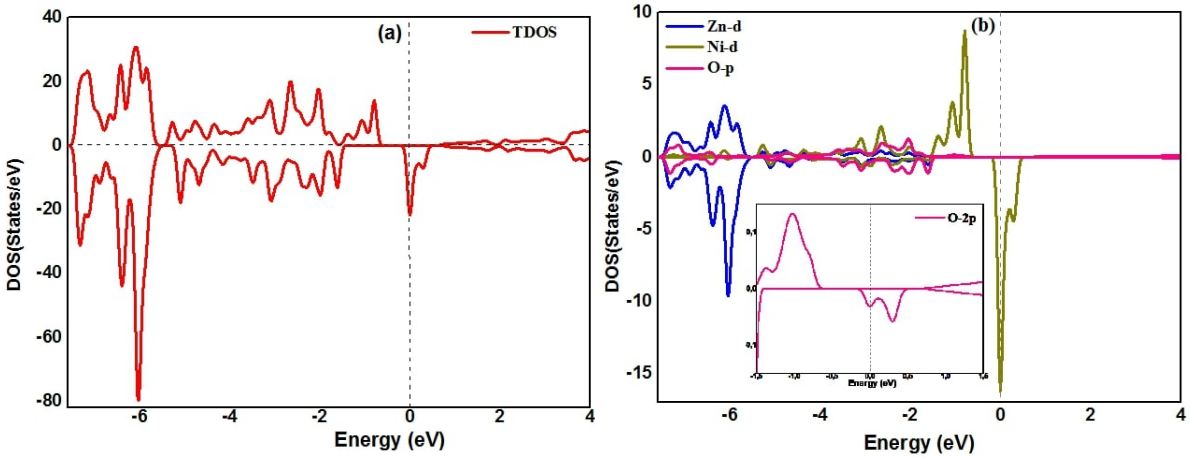

(a) (b)

Figure 5.5: Total DOS and Partial DOS of Ni-doped ZnONS.

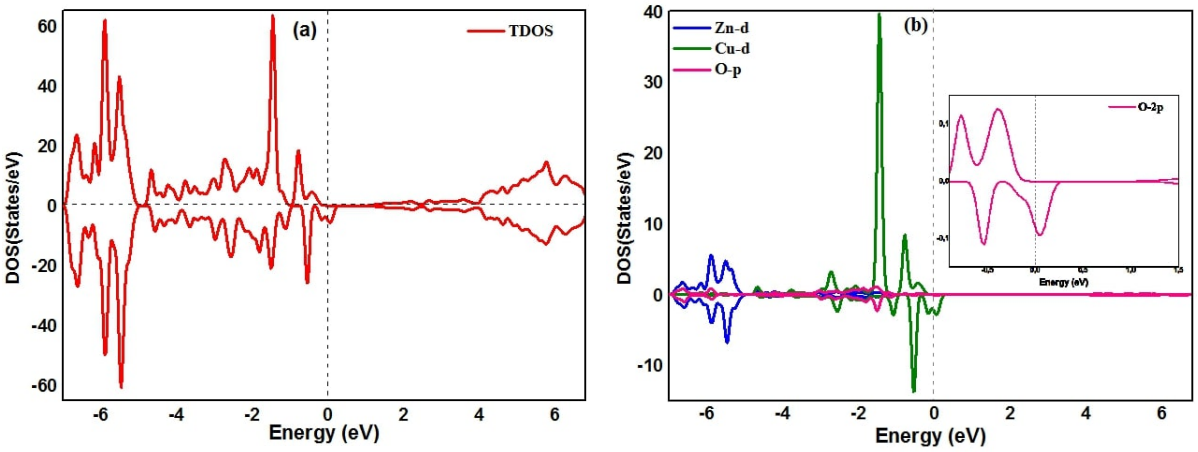

(a) (b)

Figure 5.6: Total DOS and Partial DOS of Cu-doped ZnONS.

TM	$E_g(eV)$	$m_T(\mu_B)$	$m_{TM}(\mu_B)$	$m_O(\mu_B)$
Fe	0.364	4	3.357	-0.002
Co	0.292	3	2.370	0.0007
Ni	0.102	2	1.436	0.003
Cu	1.549	1	0.525	0.009

Table 5.1: Results of the band gap, the total and partial magnetic moments of ZnONS doped with TM by applying PBEsol-GGA.

Spin-polarized band structures of doped ZnONS withFe, Co, Ni, or Cu atoms appear in Figure 5.7. To indicate the spin of an electron, we used the symbols (↑) / (↓) for spin-up/-down. The spin-up channel displays the semiconductor character. The new energy levels, which come from the TM atom in the spin-down band, are visible around the Fermi level. Thus, the electronic transition may become more active because of impurity energy levels close to the Fermi level. The minority-spin band exhibits a metallic nature. The hybridization of the 2p-O and 3d-TM orbitals is made possible by the existence of energy levels around the Fermi level. The band gap nature is direct in all systems doped. The presence of semiconductor character in the majority-spin band and metallic character in the minority-spin band confirm the half-metallic behavior in TM-doped ZnONS.

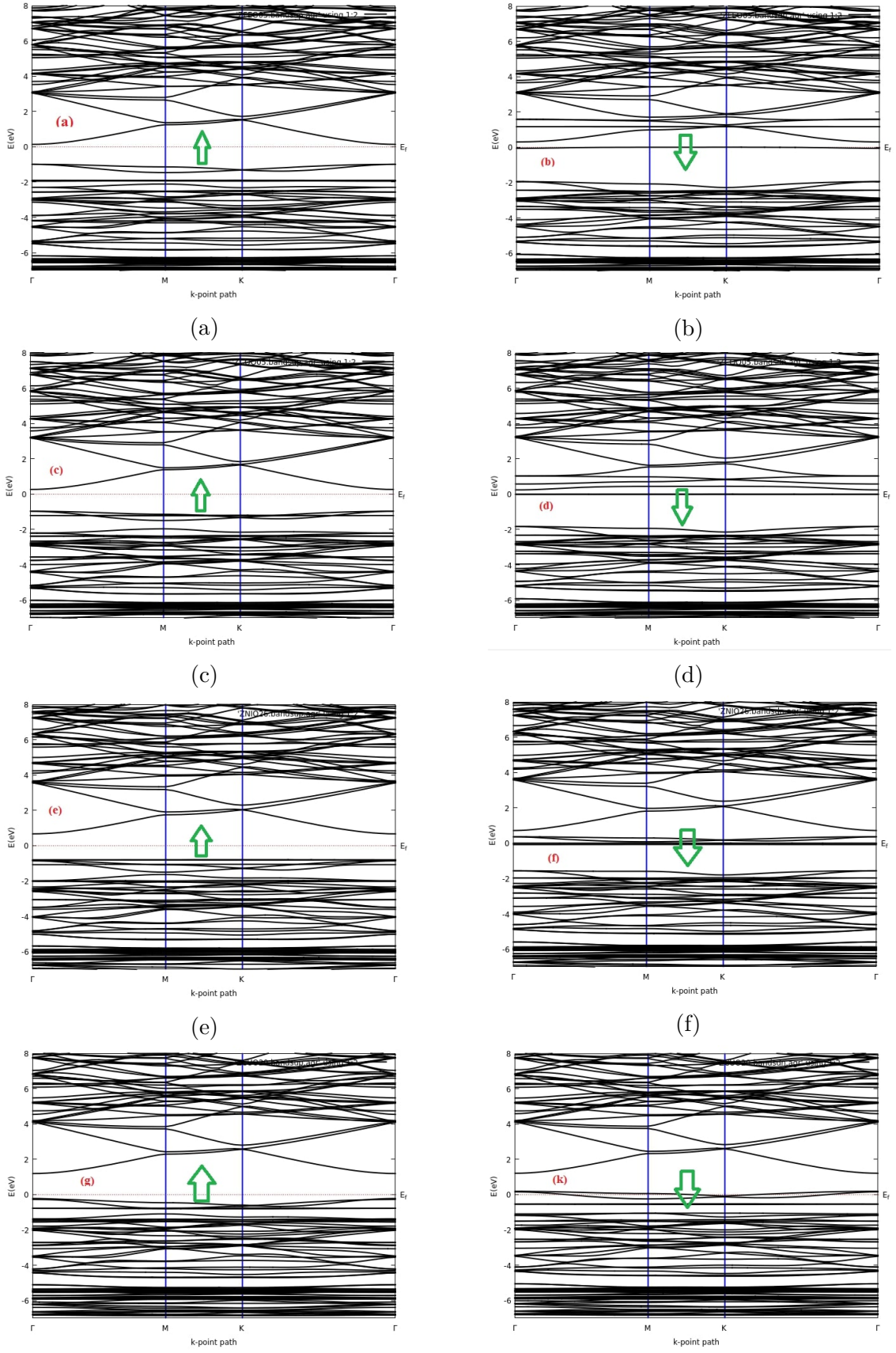

Figure 5.7: Spin-polarized band structure of ZnO nanosheets doped with (a, b) Fe, (c, d) Co, (e, f) Ni, and (g, k) Cu for spin-up/-down.

5.4 Optical properties

We discuss in this section the optical results in both directions of electric field polarizations parallel ($E \parallel X$) and perpendicular ($E \parallel Z$). The PBEsol-GGA approximation framework becomes utilized to compute the optical characteristics.

Figures 5.8a and 5.8b report the variation of the imaginary part $\varepsilon_2(\omega)$ in the energy region [0-12] eV for the pure ZnONS and TM-doped ZnONS along the ($E \parallel X$) and ($E \parallel Z$) polarization directions. It is possible to determine the sources of the $\varepsilon_2(\omega)$ peaks by analyzing the DOS and energy band structures. We can determine the various inter-band transitions from these curves, which show the absorption of the material. The study of these spectra reveals the existence of absorption peaks in the low photon energy (IR and visible) compared to pristine ZnONS in the ($E \parallel X$) polarization direction. It takes 2.08eV to reach a transition for the pure ZnONS. We can see the peaks at 0.50eV, 1.37eV, 1.93eV, and 0.17eV for ZnO nanosheets with Fe, Co, Ni, and Cu, respectively. The peaks are a signature of the incident photon energy absorption. These peaks result from the interband electronic transitions. The $\varepsilon_2(\omega)$ in the IR and visible ranges becomes zero, as shown in Figure 5.8b, making all these nanosheets highly transparent systems in these ranges. The $\varepsilon_1(\omega)$ quantifies the level to which a material can be polarized. A high value of $\varepsilon_1(\omega)$ indicates a high degree of polarization. Figures 5.8c and 5.8d represent the spectra of $\varepsilon_1(\omega)$ against photon energy for the pure ZnONS and TM-doped ZnONS along the ($E \parallel X$) and ($E \parallel Z$) polarization directions. Table 5.2 lists the static values of $\varepsilon_1(0)$ at zero frequency in the ($E \parallel X$) polarization direction. Increased $\varepsilon_1(0)$ value with TM atom incorporation in ZnO nanosheet indicates increased polarization capacity.

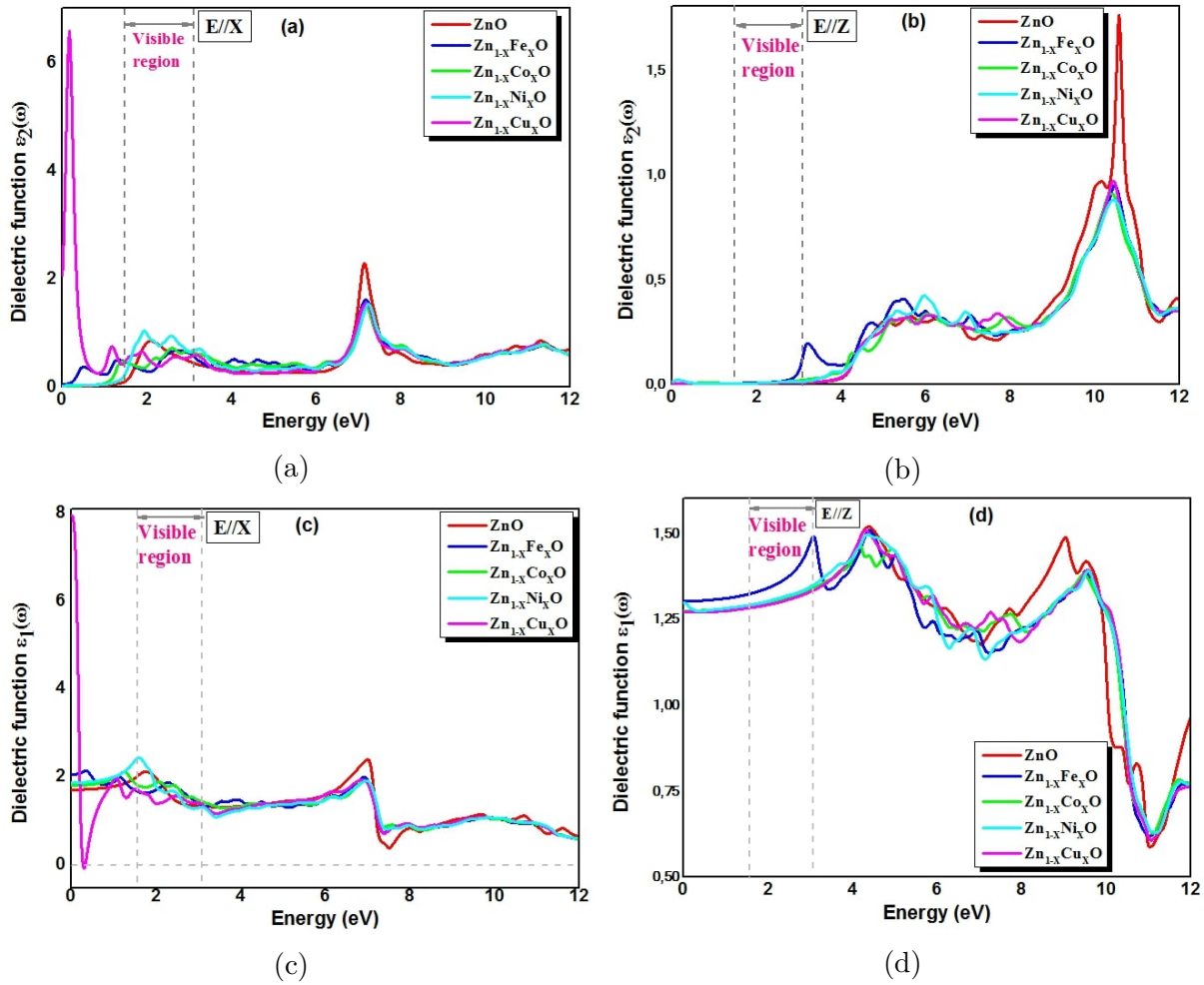

Figure 5.8: Spectra of the imaginary $\varepsilon_2(\omega)$ (a and b) and the real $\varepsilon_1(\omega)$ (c and d) parts of the dielectric function against photon energy of ZnO nanosheeet pure and TM-doped ZnO nanosheets along $(E \parallel X)$ and $(E \parallel Z)$ polarization directions.

	ZnO	$Zn_{1-x}FeO$	$Zn_{1-x}CoO$	$Zn_{1-x}NiO$	$Zn_{1-x}CuO$
$\varepsilon_1(0)$	1.73	2.06	1.82	1.90	7.96
n(0)	1.31	1.44	1.35	1.38	2.85

Table 5.2: Optical parameters at zero frequency of ZnO nanosheet pure and TM doped ZnO nanosheets in the $(E \parallel X)$ polarization direction.

Figure 5.9 displays the absorption coefficient $\alpha(\omega)$ spectra for the ZnONS pure and ZnONS doped with TM in $(E \parallel X)$ and $(E \parallel Z)$ polarization directions. Below 1.63eV, the absorption starts from the low incident photon energy compared to the pristine ZnO nanosheet in the $(E \parallel X)$ polarization direction. In the UV regions, we obtain a large absorption band in $(E \parallel X)$ and $(E \parallel Z)$. The red-shift phenomenon occurs in $(E \parallel X)$ direction when the absorption edge moves to the low energy range in comparison to pure ZnO nanosheets. The ability to absorb incoming light with a frequency in the visible re-

gion makes these doped systems potential candidates for the fabrication of optoelectronic components and photovoltaic solar cells operating efficiently in this spectral region.

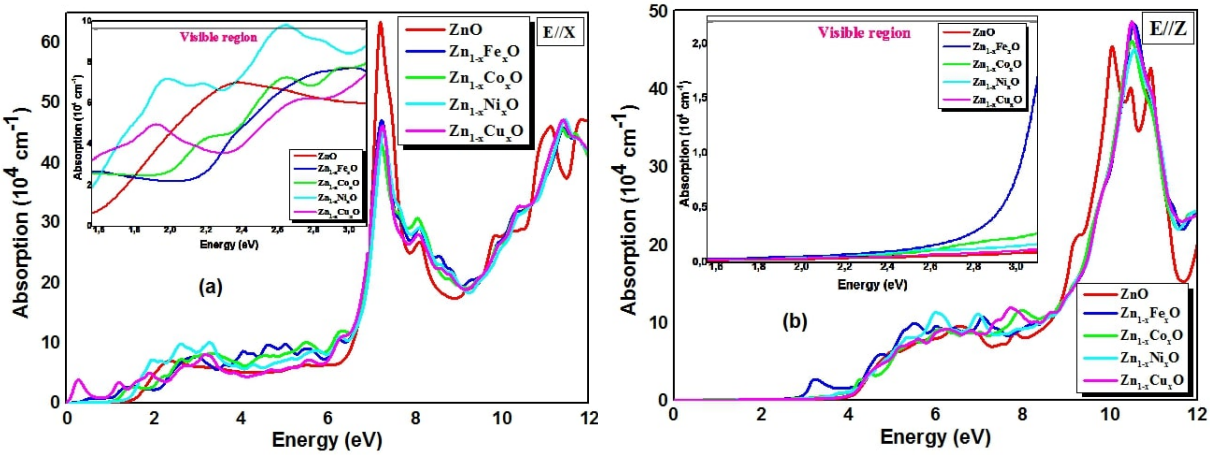

(a) (b)

Figure 5.9: Absorption coefficient $\alpha(\omega)$ against photon energy for pristine ZnONS and TM-doped ZnONS along a) $E \parallel X$ and b) $E \parallel Z$ polarization directions.

Figure 5.10 displays the energy loss function variation $L(\omega)$ of pure ZnO nanosheets and ZnO nanosheets doped with TM. It measures the energy loss of fast electrons moving through a material. The complex dielectric function serves to calculate this function. The plasmonic oscillations and optical transitions correspond to the $L(\omega)$ peaks. The peaks in $L(\omega)$ spectra correspond to the new peaks in $\varepsilon_2(\omega)$ for TM-doped ZnONS along $(E \parallel X)$ polarization direction, as proven by the DOS compared to ZnONS pure. Generally speaking, the maximum peaks in the $L(\omega)$ spectra are identified as plasma peaks, indicating collective excitations of the electronic charge density. Because of negligible absorption along the $(E \parallel Z)$ in the IR and visible bands, the $L(\omega)$ of both TM-doped ZnONS and pure ZnONS shrinks to zero. Figure 5.11 displays the evolution of reflectivity $R(\omega)$ spectra versus photon energy for TM-doped ZnONS and pure ZnONS along the $(E \parallel X)$ and $(E \parallel Z)$. The $R(\omega)$ maximum values correspond to interband transitions. Figure 5.12 displays the refractive index $n(\omega)$ spectra against photon energy for ZnONS doped with TM and pure ZnONS along the $(E \parallel X)$ and $(E \parallel Z)$. The $n(\omega)$ curves are similar to those of $\varepsilon_1(\omega)$. Table 5.2 lists the static n(0) value at zero frequency. We can find the same n(0) values from $n(0) = \sqrt{\varepsilon_1(0)}$. The extinction coefficient $k(\omega)$ serves to control the quantity of light scattered. It describes how electromagnetic radiation becomes attenuated when it passes through a substance. The variation of $k(\omega)$ of TM-doped ZnONS and pure ZnONS along the $(E \parallel X)$ and $(E \parallel Z)$ polarization directions appears in Figure 5.13. A higher amount of light absorbed is indicated by each $k(\omega)$ peak. As a result, according to the graphs of optical characteristics, all nanosheets show a significant level of anisotropy.

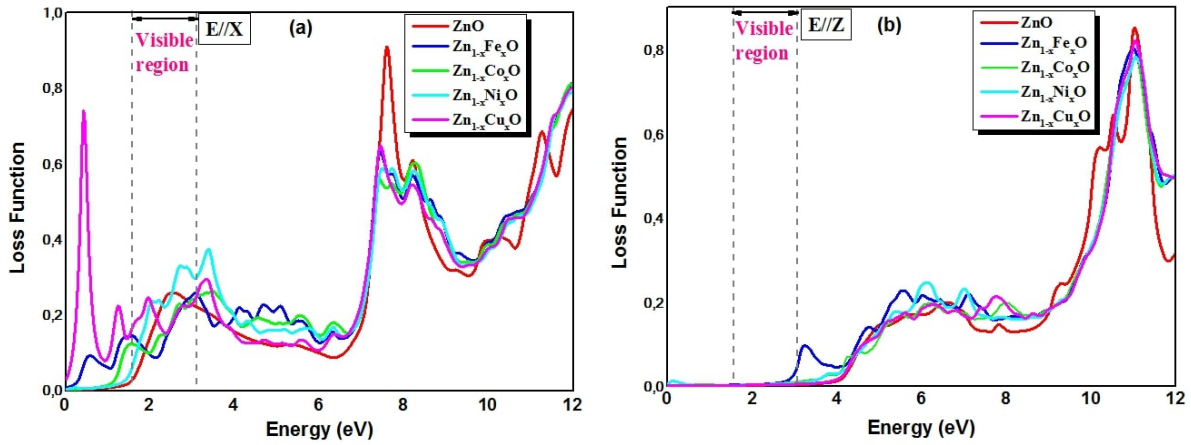

(a) (b)

Figure 5.10: Spectra of the loss function $L(\omega)$ against photon energy for ZnO nanosheeet pure and TM-doped ZnO nanosheets along a) $E \parallel X$ and b) $E \parallel Z$ polarization directions.

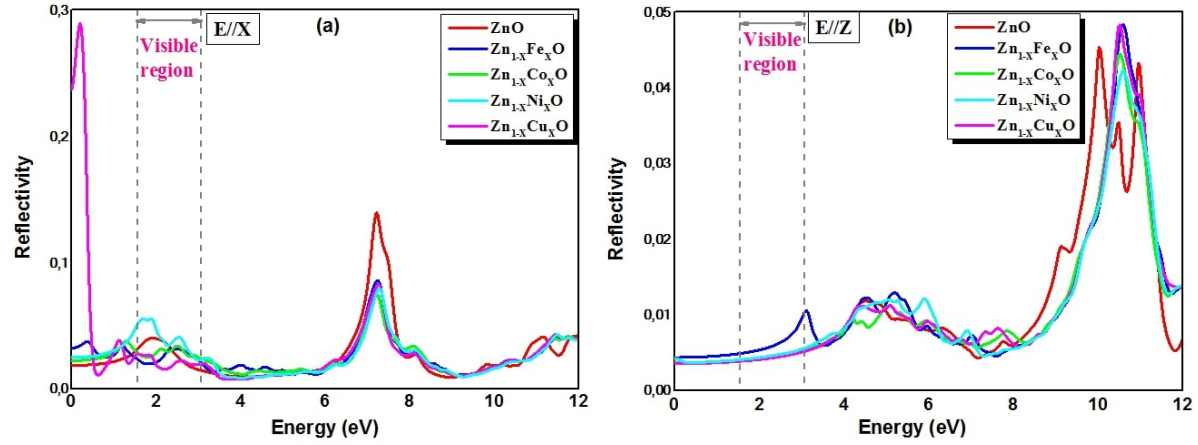

(a) (b)

Figure 5.11: Spectra of reflectivity $R(\omega)$ against photon energy for ZnO nanosheeet pure and TM-doped ZnO nanosheets along a) $E \parallel X$ and b) $E \parallel Z$ polarization directions.

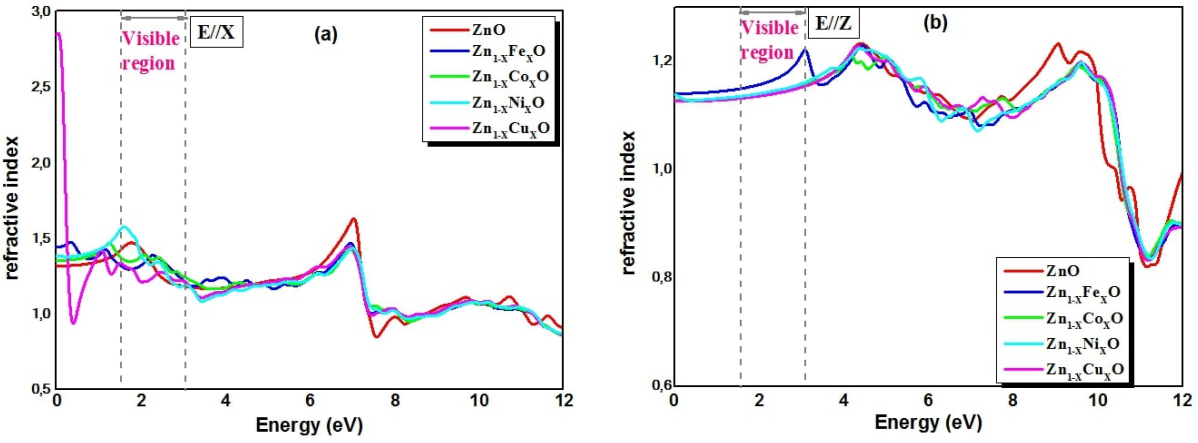

(a) (b)

Figure 5.12: Spectra of the refractive index $n(\omega)$ against photon energy for ZnO nanosheeet pure and TM-doped ZnO nanosheets along a) $E \parallel X$ and b) $E \parallel Z$ polarization directions.

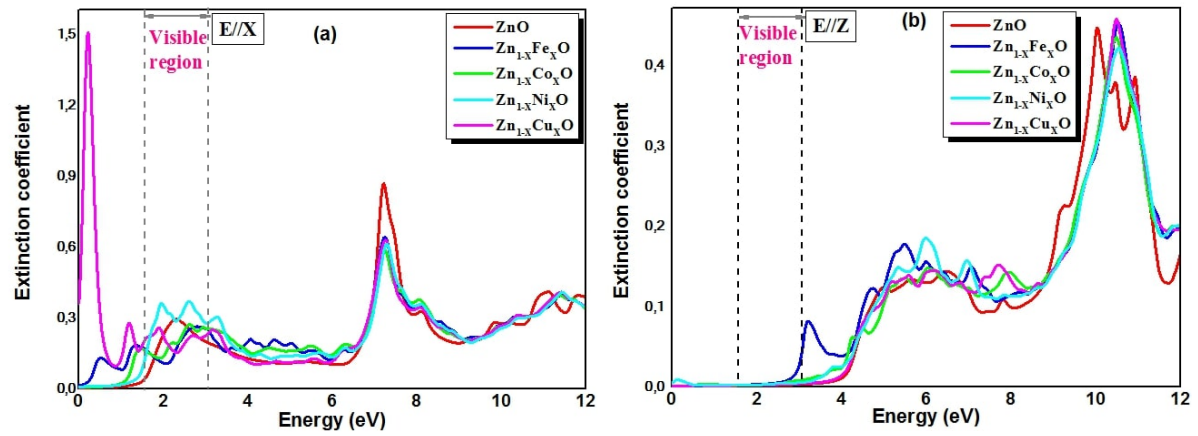

(a) (b)

Figure 5.13: Spectra of the extinction coefficient $k(\omega)$ against photon energy for ZnO nanosheeet pure and TM-doped ZnO nanosheets along a) $E \parallel X$ and b) $E \parallel Z$ polarization directions.

5.5 Thermoelectric properties

Based on the semi-classical Boltzmann theory with constant relaxation time approximation (τ) [132, 133], we calculated the thermoelectric properties using the BolzTraP2 code [132]. Thermoelectric properties are calculated in the range of temperature of 100 to 900 K using PBEsol-GGA. The parameters σ, k_e, and S can be expressed respectively by:

$$\sigma_{\alpha\beta}(T,\mu) = \frac{1}{\Omega}\int \sigma_{\alpha\beta}(\varepsilon)\left[-\frac{\partial f_\mu(T,\varepsilon)}{\partial \varepsilon}\right] d\varepsilon \tag{5.2}$$

$$k_{\alpha\beta}(T,\mu) = \frac{1}{e^2 T\Omega}\int \sigma_{\alpha\beta}(\varepsilon)\,(\varepsilon-\mu)^2\left[-\frac{\partial f_\mu(T,\varepsilon)}{\partial\varepsilon}\right]d\varepsilon \tag{5.3}$$

$$S = \frac{8\pi^2 k_B^2 m^* T}{3eh^2}\left(\frac{\pi}{3n}\right)^{\frac{2}{3}} \tag{5.4}$$

With μ, T, f_μ, $\sigma_{\alpha\beta}(\varepsilon)$, Ω, k_B, m^*, e, h, n, and ε are the chemical potential, the absolute temperature, the Fermi distribution function, the expected conductivity tensors of energy, the volume, Boltzmann number, the effective mass, the electronic charge, the Planck constant, the carrier concentration, the electron-band energies, respectively.
Along the x, y, and z axes, we can express three-dimensional tensors of σ, S, and k_e by:

$$\sigma = \frac{1}{3}Tr(\sigma) = \frac{1}{3}(\sigma^{xx}+\sigma^{yy}+\sigma^{zz}) \tag{5.5}$$

$$S = \frac{1}{3}Tr(S) = \frac{1}{3}(S^{xx}+S^{yy}+S^{zz}) \tag{5.6}$$

$$k_e = \frac{1}{3}Tr(k_e) = \frac{1}{3}(k_e^{xx}+k_e^{yy}+k_e^{zz}) \tag{5.7}$$

In this investigation, we used a $15\mathring{A}$ separation along the z-axis between single sheets to prevent interactions between successive nanosheets. We can consider nanosheets to be isolated. Along the x-axis, we examined the parameters σ, S, k_e, and PF ($\sigma^{xx}=\sigma^{yy}, S^{xx}=S^{yy}, k_e^{xx}=k_e^{yy}$,and $PF^{xx}=PF^{yy}$). The transport properties σ^{xx}, S^{xx}, k_e^{xx}, and PF^{xx} for half-metallic $Zn_{1-x}TM_xO$ nanosheets are computed against the chemical potential (μ). The n-type and p-type doping correspond to the positive and negative chemical potentials (μ), respectively.

The electrical conductivity (σ/τ) against chemical potential (μ) curves are shown in Figures 5.14a, 5.15a, 5.16a, and 5.17a for ZnONS doped with Fe, Co, Ni, and Cu. These Figures show the higher electrical conductivity in n-type doping compared to p-type doping in our doped nanosheets. Because of the peaks in the σ/τ that are close to the Fermi level, more of the electrons can move from the valence band to the conduction band. Figures 5.14b, 5.15b, 5.16b, and 5.17b represent the evolution of the Seebeck coefficient (S) against chemical potentials (μ) for TM-doped ZnO nanosheets. If S is positive, the holes are the primary charge carriers; if S is negative, then electrons are the dominating charge carriers. The maximum peaks of S are decreased when the temperature rises. The Seebeck coefficient values are more sensitive to temperature than electrical conductivity. S reaches its maximum value near the Fermi level at $\mu = -0.02eV(1.57\times10^{-3}VK^{-1})$, $\mu = -0.02eV(1.56\times10^{-3}VK^{-1})$, $\mu = -0.03eV(1.58\times10^{-3}VK^{-1})$, $\mu = 0.02eV(1.57\times10^{-3}VK^{-1})$ for ZnONS doped with Fe, Co, Ni, and Cu, respectively. Figures 5.14c, 5.15c, 5.16c, and 5.17c show the variations of the electron thermal conductivity (k_e/τ) versus chemical potential (μ). The k_e/τ gradually rises with temperature rise. We can see that

the k_e/τ values are increasing depending on the temperature, this characteristic results from the increase in the energy of the free electrons. The power factor (PF) is represented versus chemical potential (μ) in Figures 5.14d, 5.15d, 5.16d, and 5.17d. PF is a crucial metric for assessing thermoelectric material efficiency. Seebeck coefficient and electrical conductivity data can determine this factor ($PF = \sigma S^2$). The maximum values of PF along the x-axis are 2.94×10^{11}, 2.61×10^{11}, 2.66×10^{11} and 2.57×10^{11} for ZnO anosheets doped with Fe, Co, Ni, and Co at $\mu = 0.16eV$, 0.19eV, 0.12eV, and 1.14eV, respectively. The PF increases gradually with temperature, suggesting a high potential of these doped nanosheets for commercial thermoelectric applications at high temperatures.

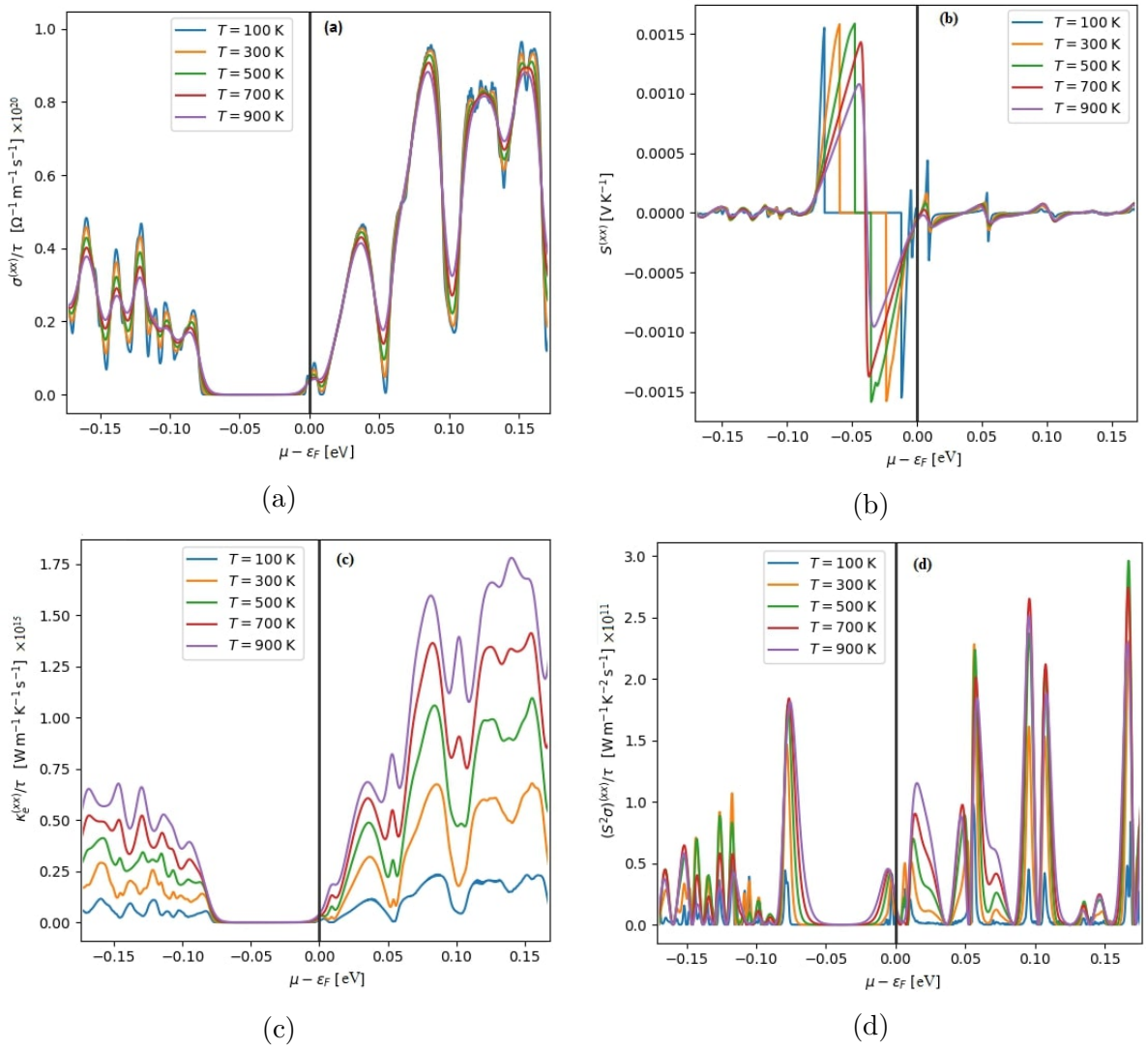

Figure 5.14: a) Electrical conductivity, b) Seebeck coefficient, c) Electron thermal conductivity, and d) Power factor versus chemical potential for Fe-doped ZnONS along the x-axis.

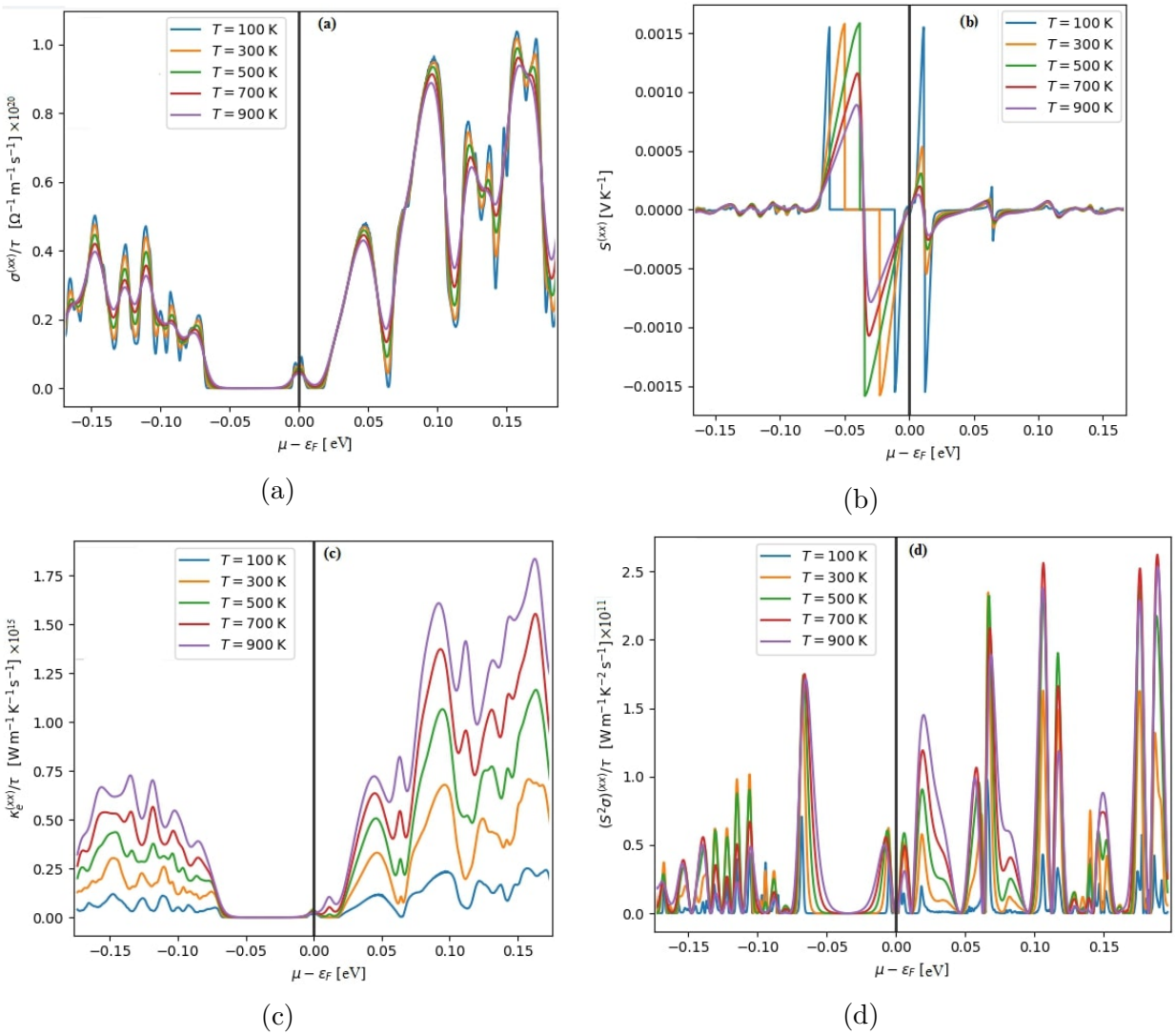

Figure 5.15: a) Electrical conductivity, b) Seebeck coefficient, c) Electron thermal conductivity, and d) Power factor versus chemical potential for Co-doped ZnONS along the x-axis.

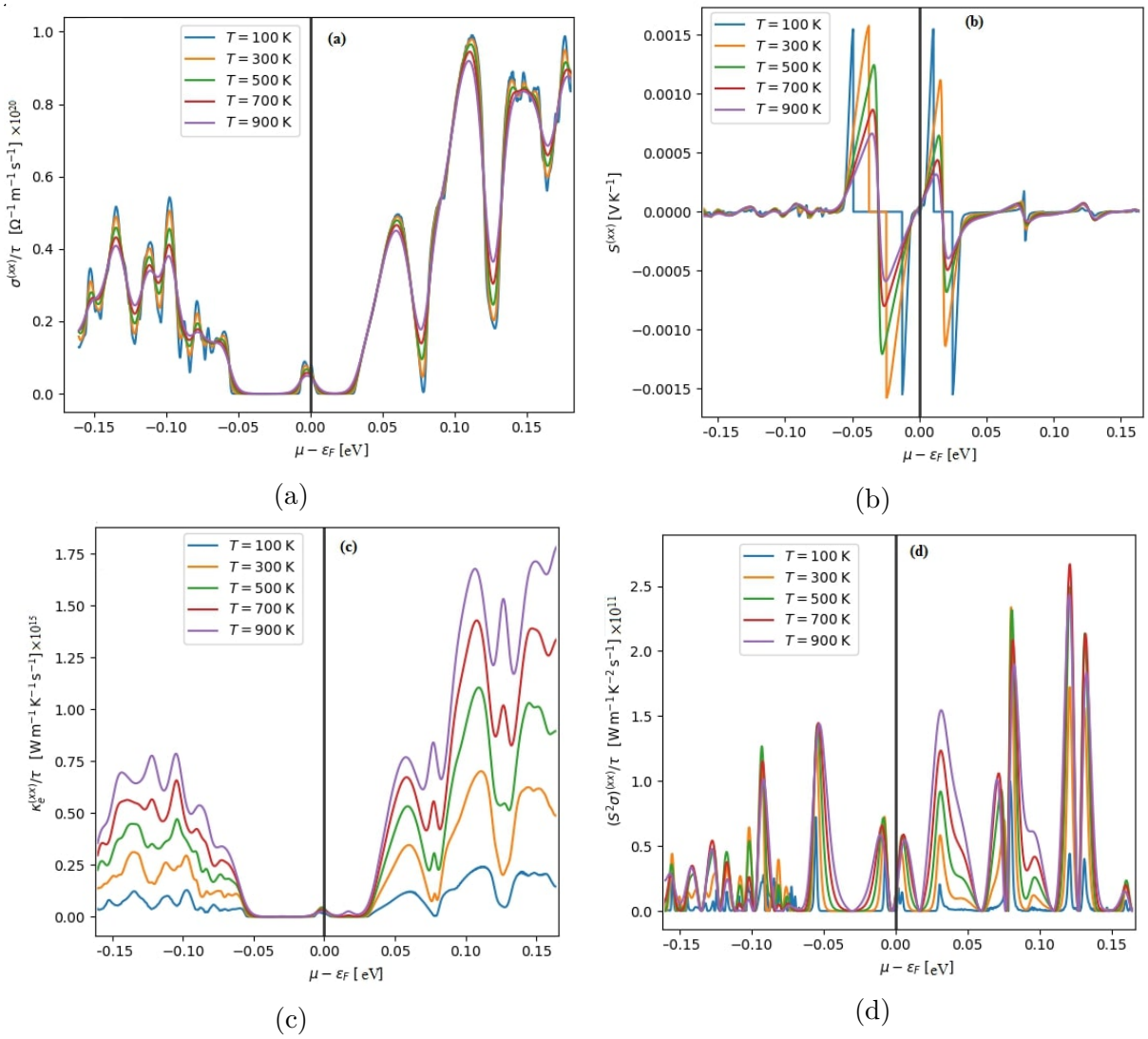

Figure 5.16: a) Electrical conductivity, b) Seebeck coefficient, c) Electron thermal conductivity, and d) Power factor versus chemical potential for Ni-doped ZnONS along the x-axis.

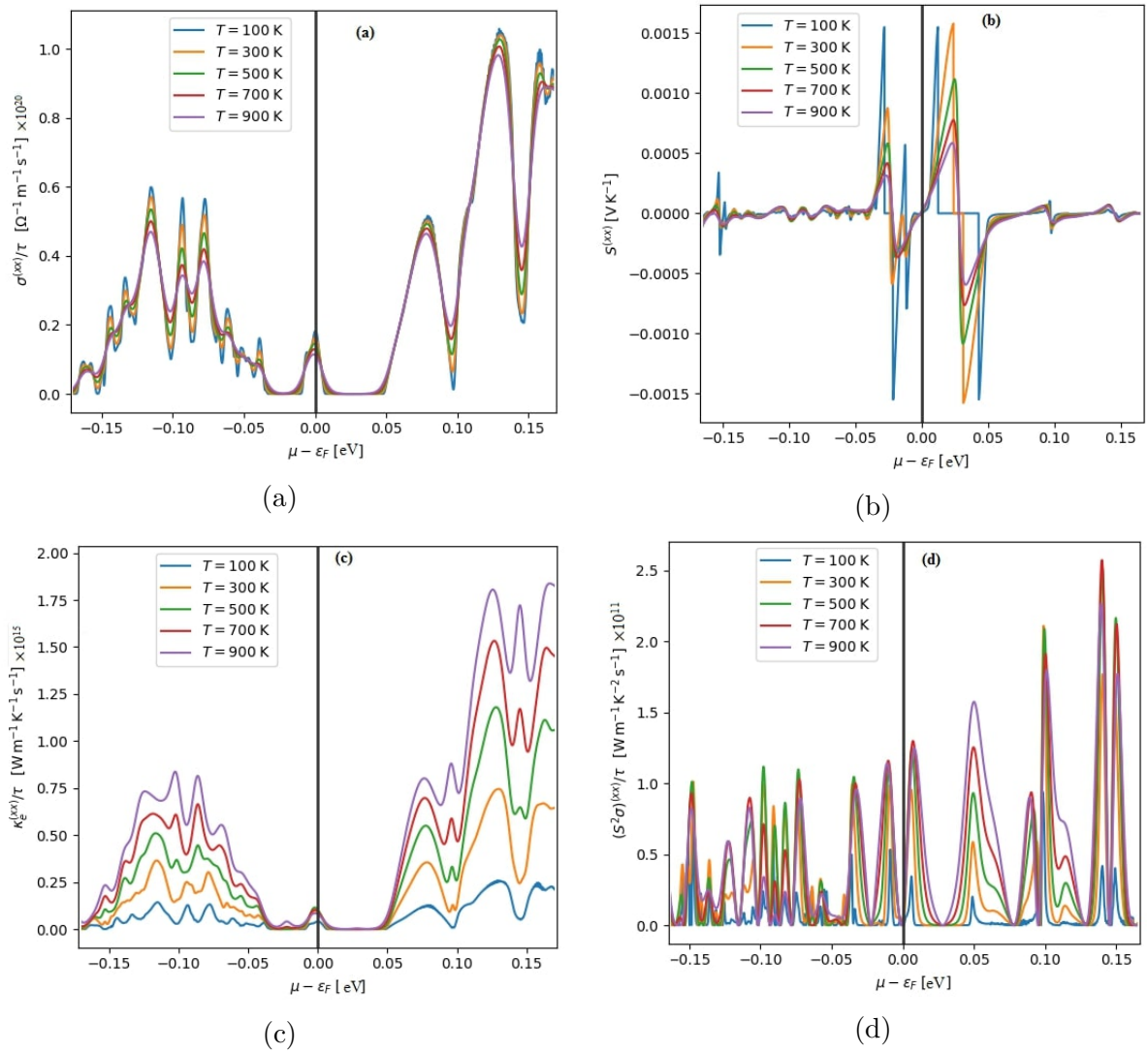

Figure 5.17: a) Electrical conductivity, b) Seebeck coefficient, c) Electron thermal conductivity, and d) Power factor versus chemical potential for Cu-doped ZnONS along the x-axis.

5.6 Conclusion

To summarize, the electronic, magnetic, thermoelectric, and optical characteristics of ZnO nanosheets doped with TM (Fe, Co, Ni, or Cu) have been theoretically calculated based on the DFT framework, which applies the FP-LAPW method by applying PBEsol-GGA. The electronic structure of pure ZnONS displays the semiconductor character with a direct band gap. Doping with TM atoms changes the symmetry of DOS of pristine ZnO nanosheets, allowing the formation of new energy levels close to the Fermi level. Around the Fermi level, doped ZnO nanosheets with TM show high spin polarization and half-metallic behavior. It is implied that the doping of TM atoms induces magnetization by the asymmetry of DOSs between the spin-down/-up bands. The ferromagnetism in doped ZnO nanosheets with Co-, Ni-, or Cu- originates from the hybridization p-d between

the 2p-O and 3d-Co (or 3d-Ni, or 3d-Cu) orbitals. These features of TM-doped ZnO nanosheets are suitable for Spintronic applications. Furthermore, at low energy regions in the ($E \parallel X$) polarization direction, there is a considerable rise in both the absorption coefficient and the imaginary part of the dielectric function for nanosheets doped. The red-shift phenomenon occurs in the ($E \parallel X$) direction when the absorption edge moves to the low energy range in comparison to pure ZnO nanosheets, and the ZnO nanosheets with TM doping also have enhanced optical characteristics in the infrared region. Theoretical underpinnings for optoelectronic and photovoltaic solar cell device design and execution in visible and infrared spectrums are provided by these studies. Superior thermoelectric characteristics, including the power factor, electrical conductivity, and Seebeck coefficient, were observed along the x-axis. These findings suggest that ZnO nanosheets doped with TM are suitable for future thermoelectric applications.

Physica B 668 (2023) 415241

Contents lists available at ScienceDirect

Physica B: Condensed Matter

journal homepage: www.elsevier.com/locate/physb

Excellent optical and thermoelectric features of two-dimensional half-metallic ferromagnet $Zn_{1-x}(TM)_xO$: A first principle investigation

S. Laghzaoui [a], A. Fakhim Lamrani [a,b,*], R. Ahl Laamara [a,c]

[a] LPHE-Modeling and Simulatiaon, Faculty of Sciences, Mohammed V University in Rabat, Rabat, Morocco
[b] ENS-Rabat Physics Department, Mohammed V University in Rabat, B. P. 5118, Morocco
[c] Centre of Physics and Mathematics, CPM, Faculty of Sciences, Mohammed V University in Rabat, Rabat, Morocco

ARTICLE INFO

Keywords:
Two-dimensional half-metallic
p-d hybridization
Electric field polarization
Photovoltaic cells
Thermoelectric properties

ABSTRACT

The electronic, magneto-optical, and thermoelectric properties of graphene-like ZnO nanosheets doped with transition-metal TM (= Fe, Co, Ni, or Cu) were analyzed using spin-polarized first-principles computations. When a TM atom substitution with the Zn atom, the resultant material exhibits significant spin-polarization around the Fermi level and displays a half-metallic ferromagnet within the PBEsol-GGA. Doped ZnO nanosheets by Fe-, Co-, Ni-, and Cu-dopants generate the total magnetic moment of $4\mu_B$, $3\mu_B$, $2\mu_B$, and $1\mu_B$, respectively, which is produced primarily by the TM-3d atoms. The p-d hybridization explains the ferromagnetic interactions caused by the robust coupling among Co-, Ni-, or Cu-3d and anion O-2p orbitals. We have investigated the optical characteristics of TM-doped ZnO nanosheets in parallel (E∥X) and perpendicular (E∥Z) polarization directions. Our analysis demonstrates that the $Zn_{1-x}(TM)_xO$ two-dimensional nanosheets can absorb visible sunlight in the (E∥X) polarization direction comparatively to pristine ZnONS. Along the x-axis, we studied the Seebeck coefficient, electrical, electronic thermal conductivities, and power factor for various temperatures. All the TM-doped ZnO (2D) nanosheets demonstrate superior electrical conductivity and high power factor in n-type doping than in p-type doping. According to these findings, TM-doped ZnO nanosheets could represent the next evolution in Spintronic, photovoltaic cells, and thermoelectric technologies.

General conclusion and perspectives

In this work, which is theoretical, we studied the structure electronic, magnetic, optical, and thermoelectric properties of $Zn_{1-x}TM_xO$ nanosheets (TM= Fe, Co, Ni, and Cu), $Sn_{1-2x}Mn_xA_xO_2$ (A=Mo or Tc), and double perovskites oxides in DFT by the FP-LAPW method executed in the WIEN2k package using many approaches such as GGA, GGA+U, mBJ-GGA, GGA+SOC, and YS-PBE0, as well as the BoltzTrap code for calculating the thermoelectric properties.

The first section addressed co-doped SnO_2 with Mn and A=Mo/Tc. The results were checked for compliance with experimental data and with earlier theoretical investigations of SnO_2 pure using the GGA-PBE. We determined the lattice parameter, the compressibility modulus, and its pressure derivative to study equilibrium structural characteristics. The acquired results are in accordance with the theoretical and experimental outcomes. We use the formation energy calculation to confirm the stability of our materials SnO_2 pure and SnO_2 co-doped with Mn and A=Mo/Tc. We calculated for the two co-doping the total energy for the two parallel and antiparallel configurations between the spins of the impurities. The $Sn_{1-2x}Mn_xMo_xO_2$ complex suggests that the ferromagnetic (FM) state is more stable than the antiferromagnetic (AFM) state; in contrast, the $Sn_{1-2x}Mn_xTc_xO_2$ complex suggests that the AFM state is more stable than the FM state. On the one hand, our calculation of the electronic structure indicates the presence of the half-metallic character with 100% spin-majority polarization close to the Fermi level in $Sn_{1-2x}Mn_xTc_xO_2$ and $Sn_{1-2x}Mn_xMo_xO_2$ by applying mBJ-GGA and GGA-PBE. The origin of ferromagnetism in $Sn_{1-2x}Mn_xMo_xO_2$ and $Sn_{1-2x}Mn_xTc_xO_2$ systems is explained by the double Zener exchange and p-d hybridization, respectively. The total magnetic moments of all co-doped materials are sufficiently large. This investigation demonstrates the effectiveness of Mn and A=Mo/Tc in SnO_2 co-doping. It shows that the double impurity does not distort the host semiconductor nature since the DOS displays the spins-up and spins-down positioned in the band gap. These features are suitable for Spintronic. To study the behavior of SnO_2 pure and SnO_2 co-doped with Mn and A=Mo/Tc materials under sunlight, we calculated their optical characteristics like the dielectric function, absorption, reflectivity, etc. The low-energy regions (visible and infrared) exhibit a discernible boost in the optical absorption of $Sn_{1-2x}Mn_xTc_xO_2$ and $Sn_{1-2x}Mn_xMo_xO_2$. It implies that

technological applications like optoelectronics and photovoltaic solar cells may benefit from these systems. By analyzing the thermoelectric properties, we found the best results for Seebeck coefficient, power factor and electrical conductivity for $Sn_{1-2x}Mn_xTc_xO_2$ and $Sn_{1-2x}Mn_xMo_xO_2$ systems, which make these systems demonstrate good thermoelectric performance.

The second section of this work examined ferromagnetic double perovskite oxides by substitution with transition metals or rare-earth elements. We have used a variety of approximations, including GGA, GGA+U, YS-PBE0, GGA+mBJ, and SOC. Due to the substitution by magnetic atoms, all compounds Ca_2CrMnO_6, Sr_2RECoO_6 (RE=Dy, Ho, Er, or Tm) in this investigation exhibit a half-metallic character. Also, these compounds Ca_2CrMnO_6, Sr_2RECoO_6 improve the magnetic properties in our initial compounds Ca_2TiMnO_6 and Sr_2TiCoO_6. Ca_2CrMnO_6 and Sr_2RECoO_6 can absorb light in the visible, ultraviolet, and infrared photon energy ranges, which enables them to serve as light absorbers in solar cells. Next, we studied the thermoelectric characteristics of the chosen substances. These materials show the best Seebeck coefficient and a figure of merit close to unity, which makes it possible to use in thermoelectric applications.

The double perovskite Sr_2CrReO_6 is given another desired magnetic characteristic by replacing the Cr atom with Tc. It is the antiferromagnetic half-metal property. The GGA+U calculation preserves the half-metallic character in Sr_2TcReO_6. The parameter U considers the correlation between the electrons of the d orbitals. This compound Sr_2TcReO_6 shows a high polarization close to the Fermi level with zero total magnetic moment. These features serve a purpose in the fabrication of spin-polarized tunneling microscopies. By analyzing the optical and thermoelectric properties of Sr_2TcReO_6, we found that this material can absorb sunlight in various photon energies and convert heat into electricity. These results suggest that the half-metallic antiferromagnetic material Sr_2TcReO_6 can be advantageous for thermoelectric, optoelectronic, and solar cell applications.

The third section focused on two-dimensional doped ZnO nanosheets with TM (=Fe, Co, Ni, and Cu). The doped systems shows a half-metallic character using PBEsol-GGA. The substitution by TM enhanced the magnetic properties of ZnO nanosheet pure. The TM atoms are the primary source of most of the total magnetic moments. Ferromagnetic interactions resulting from the strong coupling between the anion O-2p orbitals and Co-, Ni-, or Cu-3d orbitals are explained by the p-d hybridization. Through parallel ($E//X$) and perpendicular ($E//Z$) electric field polarizations, we have examined the optical properties of ZnO nanosheets doped with TM. Along the ($E//X$), the doped nanosheets enhance the optical absorption in low-energy photon regions (IR and visible). The investigation of thermoelectric characteristics along the x-axis reveals excellent

electrical conductivity, high power factor, and outstanding Seebeck coefficient. Thanks to these characteristics, ZnO nanosheets doped with TM may be the future advances in thermoelectric, spintronic, and solar cell devices.

In the end, this work has enabled the opening up of several perspectives. It would seem intriguing to extend the research to study the electronic, magnetic, optical, and thermoelectric properties of 2D nanosheets coupled with double impurities and compare these properties with three-dimensional materials. Then, we propose to use other more precise approximations, such as the meta-GGA and the HSE hybrid functions.

Bibliography

[1] P. Hohenberg, and W. Kohn, Inhomogeneous Electron Gas, Phys. Rev. 136 (1964) 864. **https://doi.org/10.1103/PhysRev.136.B864**.

[2] W. Kohn, and L. J. Sham, Self-Consistent Equations Including Exchange and Correlation Effects, Phys. Rev. A 140 (1965) A1133. **https://doi.org/10.1103/PhysRev.140.A1133**.

[3] M. N. Baibich, J. M. Broto, A. Fert, F. Nguyen Van Dau, F. Petroff, P. Etienne, G. Creuzet, A. Friederich, and J. Chazelas, Giant Magnetoresistance of (001)Fe/(001)Cr Magnetic Superlattices, Phys. Rev. Lett. 61 (1988) 2472. **https://doi.org/10.1103/PhysRevLett.61.2472**

[4] G. Binasch, P. Grünberg, F. Saurenbach, and W. Zinn, Enhanced magnetoresistance in layered magnetic structures with antiferromagnetic interlayer exchange, Phys. Rev. B 39 (1989) 4828. **https://doi.org/10.1103/PhysRevB.39.4828**.

[5] S. Parkin, X. Jiang, K. R. Christian Kaiser, A. Panchula, and M. Samant, Magnetically engineered spintronic sensors and memory, Proc. IEEE 91 (2003) 661. **https://doi.org/10.1109/JPROC.2003.811807**.

[6] T. Miyazaki, and N. Tezuka, Spin polarized tunneling in ferromagnet/insulator/ferromagnet junctions, J. Magn. Magn. Mater. 151 (1995) 403. **https://doi.org/10.1016/0304-8853(95)00563-3**.

[7] F. Heusler, W. Starck, and E. Haupt, Magnetisch-chemische studien, Verh DPG 5 (1903) 219.

[8] R. A. de Groot, F. M. Mueller, P. G. van Engen, and K. H. J. Buschow, New Class of Materials: Half-Metallic Ferromagnets, Phys. Rev. Lett. 50 (1983) 2024. **https://doi.org/10.1103/PhysRevLett.50.2024**.

[9] Y. Matsumoto, M. Murakami, T. Shono, T. Hasegawa, T. Fukumura, M. Kawasaki, P. Ahmet, T. Chikyow, S. Koshihara, and H. Koinuma, Room-temperature ferromagnetism in transparent transition metal-doped titanium dioxide, Science 291 (2001) 854. **https://doi.org/10.1126/science.1056186**

[10] K. Ueda, H. Tabata, and T. Kawai, Magnetic and electric properties of transition-metal-doped ZnO films, Appl. Phys. Lett. 79 (2001) 988. **https://doi.org/10.1063/1.1384478**.

[11] A. H. MacDonald, P. Schiffer, and N. T. Samarth, Ferromagnetic semiconductors: Moving beyond (Ga,Mn)As, Nat. Mater. 4 (2005) 195. **https://doi.org/10.1038/nmat1325**.

[12] T. Dietl, H. Ohno, F. Matsukura, J. Cibert, and D. Ferrand, Zener model description of ferromagnetism in zinc-blende magnetic semiconductors, Science 287 (2000) 1019. **https://doi.org/10.1126/science.287.5455.1019**.

[13] K. I. Kobayashi, T. Kimura, H. Sawada, K. Terakura, and Y. Tokura, Room-temperature magnetoresistance in an oxide material with an ordered double-perovskite structure, Nature 395 (1998) 677. **https://doi.org/10.1038/27167**.

[14] H. Kato, T. Okuda, Y. Okimoto, and Y. Tomioka, Metallic ordered double-perovskite with maximal Curie temperature of 635 K, Appl. Phys. Lett. 81 (2002) 328. **https://doi.org/10.1063/1.1493646**.

[15] H. Asano, N. Kozuka, A. Tsuzuki, and M. Matsui, Growth and properties of high-Curie-temperature Sr_2CrReO_6 thin films, Appl. Phys. Lett. 85 (2004) 263. **https://doi.org/10.1063/1.1769085**.

[16] T. Hoseinzadeh, S. Solaymani, S. Kulesza, A. Achour, Z. Ghorannevis, Ş. Ţălu, M. Bramowicz, M. Ghoranneviss, S. Rezaee, A. Boochani, and N. Mozaffari, Microstructure, fractal geometry and dye-sensitized solar cells performance of CdS/TiO_2 nanostructures, J. Electroanal. Chem. 830 (2018) 80. **https://doi.org/10.1016/j.jelechem.2018.10.037**.

[17] X. J. Tan, H. Z. Shao, J. He, G. Q. Liu, J. T. Xu, J. Jiang, and H. C. Jiang, Band engineering and improved thermoelectric performance in M-doped SnTe (M = Mg, Mn, Cd, and Hg), Phys. Chem. Chem. Phys. 18 (2016) 7141. **https://doi.org/10.1039/C5CP07620J**.

[18] C. Berger, Z. Song, T. Li, X. Li, A. Y. Ogbazghi, R. Feng, Z. Dai, A. N. Marchenkov, E. H. Conrad, P. N. First, and W. A. de Heer, Ultrathin Epitaxial Graphite: 2D Electron Gas Properties and a Route toward Graphene-based Nanoelectronics, J. Phys. Chem. B 108 (2004) 19912. **https://doi.org/10.1021/jp040650f**.

[19] A. Hashimoto, K. Suenaga, A. Gloter, K. Urita, and S. Iijima, Direct evidence for atomic defects in graphene layers, Nature 430 (2004) 870. **https://doi.org/10.1038/nature02817**.

[20] Y. Zhang, Y. Tan, H. L. Stormer, and P. Kim, Experimental observation of the quantum Hall effect and Berry's phase in graphene, Nature 438 (2005) 201. **https://doi.org/10.1038/nature04235**.

[21] L. D. Landau, On the theory of phase transitions, Phys. Z. Sowjetunion 11 (1937) 26. **https://doi.org/10.1016/B978-0-08-010586-4.50034-1**.

[22] R. Peierls, Bemerkungen über Umwandlungstemperaturen, Helv. Phys. Acta 7 (1934) 81. **https://doi.org/10.5169/seals-110415**.

[23] K. S. Novoselov, A. K. Geim, S. V. Morozov, D. Jiang, Y. Zhang, S. V. Dubonos, I. V. Grigorieva, and A. A. Firsov, Electric field effect in atomically thin carbon films, Science 306 (2004) 666. **https://doi.org/10.1126/science.1102896**.

[24] K. S. Novoselov, D. Jiang, F. Schedin, T. J. Booth, V. V. Khotkevich, S. V. Morozov, and A. K. Geim, Two-dimensional atomic crystals, Proc. Natl. Acad. Sci. 102 (2005) 10451. **https://doi.org/10.1073/pnas.0502848102**.

[25] Y. Zhu, S. Murali, W. Cai, X. Li, J. W. Suk, J. R. Potts, and R. S. Ruoff, Graphene and Graphene Oxide: Synthesis, Properties, and Applications, Adv. Mater. 22 (2010) 3906. **https://doi.org/10.1002/adma.201001068**.

[26] M. Velický, and P. S. Toth, From two-dimensional materials to their heterostructures: An electrochemist's perspective, Appl. Mater. Today 8 (2017) 68. **https://doi.org/10.1016/j.apmt.2017.05.003**.

[27] H. L. Zhuang, and R. G. Hennig, Computational identification of single-layer CdO for electronic and optical applications, Appl. Phys. Lett. 103 (2013) 212102. **https://doi.org/10.1063/1.4831972**.

[28] G. A. Trisaris, B. D. Malone, and E. Kaxiras, Optoelectronic properties of single-layer, double-layer, and bulk tin sulfide: A theoretical study, J. Appl. Phys. 113 (2013) 233507. **https://doi.org/10.1063/1.4811455**.

[29] F. B. Zheng, C. W. Zhang, H. X. Luan, S. S. Li, and P. J. Wang, Design of half-metallic properties induced by 2p impurities in ZnO nanosheet, J. Solid State Chem. 200 (2013) 299. **https://doi.org/10.1016/j.jssc.2013.02.004**.

[30] M. Born, and J. R. Oppenheimer, On the quantum theory of molecules, Ann. der Phys. 84 (1927) 457. **http://dx.doi.org/10.1002/andp.19273892002**.

[31] D. R. Hartree, The wave mechanics of an atom with a non-Coulomb central field. Part I. Theory and methods, Proc. Camb. Phil. Soc. 24 (1928) 89. **https://doi.org/10.1017/S0305004100011919**.

[32] L. H. Thomas, The calculation of atomic fields, Proc. Camb. Phil. Soc. 23 (1927) 542.**https://doi.org/10.1017/S0305004100011683**.

[33] E. Fermi, Eine statistische Methode zur Bestimmung einiger Eigenschaften des Atoms und ihre Anwendung auf die Theorie des periodischen Systems der Elemente, Z. Phys. 48 (1928) 73. **https://doi.org/10.1007/BF01351576**.

[34] M. C. Payne, M. P. Teter, D. C. Allan, T. A. Arias, and J. D. Joannopoulos, Iterative minimization techniques for ab initio total-energy calculations: molecular dynamics and conjugate gradients, Rev. Mod. Phys. 64 (1992) 1045. **https://doi.org/10.1103/RevModPhys.64.1045**.

[35] J. P. Perdew, and A. Zunger, Self-interaction correction to density-functional approximations for many-electron systems, Phys. Rev. B 23 (1981) 5048. **https://doi.org/10.1103/PhysRevB.23.5048**.

[36] J. P. Perdew, and Y. Wang, Accurate and simple analytic representation of the electron-gas correlation energy, Phys. Rev. B 45 (1992) 13244. **https://doi.org/10.1103/PhysRevB.45.13244**.

[37] J. P. Perdew, Accurate Density Functional for the Energy: Real-Space Cutoff of the Gradient Expansion for the Exchange Hole, Phys. Rev. Lett. 55 (1985) 2370. **https://doi.org/10.1103/PhysRevLett.55.1665**.

[38] J. P. Perdew, Generalized gradient approximations for exchange and correlation: A look backward and forward, Phys. B: Condens. Matter. 172 (1991) 1. **https://doi.org/10.1016/0921-4526(91)90409-8**.

[39] J. P. Perdew , J. A. Chevary, S. H. Vosko, K. A. Jackson, M. R. Pedreson, D. J. Singh, and C. Fiolhais, Atoms, molecules, solids, and surfaces: Applications of the generalized gradient approximation for exchange and correlation, Phys. Rev. B 46 (1992) 6671. **https://doi.org/10.1103/PhysRevB.46.6671**.

[40] J. P. Perdew, J. A. Chevary, S. H. Vosko, K. A. Jackson, M. R. Pederson, D. J. Singh, and C. Fiolhais, Atoms, molecules, solids, and surfaces: Applications of the generalized gradient approximation for exchange and correlation, Phys. Rev. B 48 (1993) 4978. **https://doi.org/10.1103/PhysRevB.48.4978.2**.

[41] J. P. Perdew, K. Burke, and M. Ernzerhof, Generalized Gradient Approximation Made Simple, Phys. Rev. Lett. 77 (1996) 3865. **https://doi.org/10.1103/PhysRevLett.77.3865**.

[42] J. P. Perdew, K. Burke, and M. Ernzerhof, Generalized Gradient Approximation Made Simple, Phys. Rev. Lett. 78 (1997) 1396. **https://doi.org/10.1103/PhysRevLett.77.3865**.

[43] V. I. Anisimov, J. Zaanen, and O. K. Andersen, Band theory and Mott insulators: Hubbard U instead of Stoner I, Phys. Rev. B. 44 (1991) 943. **https://doi.org/10.1103/PhysRevB.44.943**.

[44] A. I. Liechtenstein, V. I. Anisimov, and J. Zaanen, Density-functional theory and strong interactions: Orbital ordering in Mott-Hubbard insulators, Phys. Rev. B 52 (1995) R5467. **https://doi.org/10.1103/PhysRevB.52.R5467**.

[45] S. L. Dudarev, G. A. Botton, S. Y. Savrasov, C. J. Humphreys, and A. P. Sutton, Electron-energy-loss spectra and the structural stability of nickel oxide: An LSDA+U study, Phys. Rev. B 57 (1998) 1505. **https://doi.org/10.1103/PhysRevB.57.1505**.

[46] S. L. Dudarev, A. I. Liechtenstein, M. R. Castell, G. A. D. Briggs, and A. P. Sutton, Surface states on NiO (100) and the origin of the contrast reversal in atomically resolved scanning tunneling microscope images, Phys. Rev. B 56 (1997) 4900. **https://doi.org/10.1103/PhysRevB.56.4900**.

[47] A. D. Becke, and E. R. Johnson, A simple effective potential for exchange, J. Chem. Phys. 124 (2006) 221101. **https://doi.org/10.1063/1.2213970**.

[48] F. Tran, and P. Blaha, Accurate Band Gaps of Semiconductors and Insulators with a Semilocal Exchange-Correlation Potential, Phys. Rev. Lett. 102 (2009) 226401. **https://doi.org/10.1103/PhysRevLett.102.226401**.

[49] A. D. Becke, and M. R. Roussel, Exchange holes in inhomogeneous systems: A coordinate-space model, Phys. Rev. A 39 (1989) 3761. **https://doi.org/10.1103/PhysRevA.39.3761**.

[50] A. D. Becke, A new mixing of Hartree–Fock and local density functional theories, J. Chem. Phys. 98 (1993) 1372. **https://doi.org/10.1063/1.464304**.

[51] J. P. Perdew, M. Ernzerhof, and K. Burke, Rationale for mixing exact exchange with density functional approximations, J. Chem. Phys. 105 (1996) 9982. **https://doi.org/10.1063/1.472933**.

[52] M. A. L. Marques , J. Vidal, M. J. T. Oliveira, L. Reining, and S. Botti, Density-based mixing parameter for hybrid functionals, Phys. Rev. B. 83 (2011) 035119. **https://doi.org/10.1103/PhysRevB.83.035119**.

[53] V. N. Staroverov, G. E. Scuseria, J. Tao, and J. P. Perdew, Comparative assessment of a new nonempirical density functional: Molecules and hydrogen-bonded complexes, J. Chem. Phys. 119 (2003) 12129. **https://doi.org/10.1063/1.1626543**.

[54] K. Kim, and K. D. Jordan, Comparison of Density Functional and MP2 Calculations on the Water Monomer and Dimer, J. Phys. Chem. 98 (1994) 10089. **https://doi.org/10.1021/j100091a024**.

[55] W. Jones, and N. H. March, Theoretical solid state physics Dover Publications, New York (1985) c1973.

[56] O. K. Andersen, Linear methods in band theory, Phys. Rev. B 12 (1975) 3060. **https://doi.org/10.1103/PhysRevB.12.3060**.

[57] A. Y. Liu, R. M. Wentzcovitch, and M. L. Cohen, Atomic arrangement and electronic structure of BC_2N, Phys. Rev. B 39 (1989) 1760. **https://doi.org/10.1103/PhysRevB.39.1760**.

[58] R. Wentzcovitch, K. J. Chang, and M. L. Cohen, Electronic and structural properties of BN and BP, Phys. Rev. B 34 (1986) 1071. **https://doi.org/10.1103/PhysRevB.34.1071**.

[59] J. C. Slater, Wave Functions in a Periodic Potential, Phys. Rev. 51 (1937) 846. **https://doi.org/10.1103/PhysRev.51.846**.

[60] R. M. Martin, Electronic Structure: Basic Theory and Practical Methods, Cambridge university press (2004).

[61] A. P. Sutton, Electronic Structure of Materials, Clarendon Press (1993).

[62] D. D. Koelling, and G.O. Arbman, Use of energy derivative of the radial solution in an augmented plane wave method: application to copper, J Phys. F Met. Phys. 5 (1975) 2041. **https://doi.org/10.1088/0305-4608/5/11/016**.

[63] P. Blaha, K. Schwarz, and R. Augustyn, improved and updated UNIX version of the original copyrighted WIEN-code, WIEN93, Technical University, Vienna (1993).

[64] P. Blaha, K. Schwarz, P. Dufek, and J. Luitz, A full-potential linearized augmented plane wave package for calculating crystal properties, WIEN97, Technical University, Vienna (1997).

[65] P. Blaha, K. Schwarz, G.K.H. Madsen, D. Kvasnicka, and J. Luitz, An Augmented Plane Wave Plus Local Orbitals Program for Calculating Crystal Properties, University Technology, Austria (2001).

[66] G. K. H. Madsen, and D. J. Singh, BoltzTraP. A code for calculating band-structure dependent quantities, Comp. Phys. Commun. 175 (2006) 67. **https://doi.org/10.1016/j.cpc.2006.03.007**.

[67] G. S. Nolas, J. Sharp, and H. J. Goldsmid, Thermoelectrics: Basic Principles and New Materials Development, 45 (2001).

[68] G. Henryk, Integration of the boltzmann equation in the relaxation time approximation, J. Stat. Phys. 29 (1982) 617. **https://doi.org/10.1007/BF01342190**.

[69] Y. D. Park, A. T. Hanbicki, J. E. Mattson, and B. T. Jonker, Epitaxial growth of an n-type ferromagnetic semiconductor $CdCr_2Se_4$ on GaAs(001) and GaP(001), Appl. Phys. Lett. 81 (2002) 1471. **https://doi.org/10.1063/1.1498503**.

[70] R. Goswami, G. Kioseoglou, A. T. Hanbicki, B. T. Jonker, and G. Spanos, Interfacial phase formation during growth of ferromagnetic $CdCr_2Se_4$ on AlGaAs and ZnSe/AlGaAs, Acta Mater. 55 (2007) 4625. **https://doi.org/10.1016/j.actamat.2007.04.032**.

[71] V. Zestrea, V. Y. Kodash, V. Felea, P. Petrenco, D. V. Quach, J. R. Groza, and V. Tsurkan, Structural and magnetic properties of $FeCr_2S_4$ spinel prepared by field-activated sintering and conventional solid-state synthesis, J Mater. Science 43 (2008) 660. **https://doi.org/10.1007/s10853-007-2168-7**.

[72] P. G. Steeneken, L. H. Tjeng, I. Elfimov, G. A. Sawatzky, G. Ghiringhelli, N. B. Brookes, and D. J. Huang, Exchange Splitting and Charge Carrier Spin Polarization in EuO, Phys. Rev. Lett. 88 (2002) 047201. **https://doi.org/10.1103/PhysRevLett.88.047201**.

[73] Z. Wang, W. Wang, J. Tang, L. Tung, L. Spinu, and W. Zhou, Extraordinary Hall effect and ferromagnetism in Fe-doped reduced rutile, Appl. Phys. Lett. 83 (2003) 518. **https://doi.org/10.1063/1.1593825**.

[74] N. Hong, J. Sakai, W. Prellier, A. Hassini, A. Ruyter, and F. Gervais, Ferromagnetism in transition-metal-doped TiO_2 thin films, Phys. Rev. B 70 (2004) 195204. **https://doi.org/10.1103/PhysRevB.70.195204**.

[75] S. B. Ogale, R. J. Choudhary, J. P. Buban, S. E. Lofland, S. R. Shinde, S. N. Kale, V. N. Kulkarni, J. Higgins, C. Lanci, J. R. Simpson, N. D. Browning, S. Das Sarma, H. D. Drew, R. L. Greene, and T. Venkatesan, High Temperature Ferromagnetism with a Giant Magnetic Moment in Transparent Co-doped $SnO_{2-\delta}$, Phys. Rev. Lett. 91 (2003) 077205. **https://doi.org/10.1103/PhysRevLett.91.077205**.

[76] N. H. Hong, J. Sakai, W. Prellier, and A. Hassini, Transparent Cr-doped SnO_2 thin films: ferromagnetism beyond room temperature with a giant magnetic moment, J. Condens. Matter Phys. 17 (2005) 1697. **https://doi.org/10.1088/0953-8984/17/10/023**.

[77] C. Fitzgerald, M. Venkatesan, L. Dorneles, R. Gunning, P. Stamenov, J. Coey, P. Stampe, R. Kennedy, E. Moreira, and U. Sias, Magnetism in dilute magnetic oxide thin films based on SnO_2, Phys. Rev. B 74 (2006) 115307. **https://doi.org/10.1103/PhysRevB.74.115307**.

[78] W. Prellier, A. Fouchet, B. Mercey, C. Simon, and B. Raveau, Laser ablation of Co:ZnO films deposited from Zn and Co metal targets on (0001) Al_2O_3 substrates, Appl. Phys. Lett. 82 (2003) 3490. **https://doi.org/10.1063/1.1578183**.

[79] M. Venkatesan, C. B. Fitzgerald, J. G. Lunney, and J. M. D. Coey, Anisotropic Ferromagnetism in Substituted Zinc Oxide, Appl. Phys. Lett. 93 (2004) 177206. **https://doi.org/10.1103/PhysRevLett.93.177206**.

[80] D. B. Buchholz, R. P. H. Chang, J. H. Song, and J. B. Ketterson, Room-temperature ferromagnetism in Cu-doped ZnO thin films, Appl. Phys. Lett. 87 (2005) 082504. **https://doi.org/10.1063/1.2032588**.

[81] K. Kittilstved, W. Liu, and D. Gamelin, Electronic structure origins of polarity-dependent high-TC ferromagnetism in oxide-diluted magnetic semiconductors, Nat. Mater. 5 (2006) 291. **https://doi.org/10.1038/nmat1616**.

[82] N. H. Hong, N. Poirot, and J. Sakai, Evidence for magnetism due to oxygen vacancies in Fe-doped HfO_2 thin films, Appl. Phys. Lett. 89 (2006) 042503. **https://doi.org/10.1063/1.2236105**.

[83] J. Philip, N. Theodoropoulou, G. Berera, J. Moodera, and B. Satpati, High-temperature ferromagnetism in manganese-doped indium–tin oxide films, Appl. Phys. Lett. 85 (2004) 777. **https://doi.org/10.1063/1.1773617**.

[84] J. He, S. Xu, Y. Yoo, Q. Xue, H. Lee, S. Cheng, X. Xiang, G. Dionne, and I. Takeuchi, Room temperature ferromagnetic n-type semiconductor in $(In_{1-x}Fe_x)_2\,O_{3-\sigma}$, Appl. Phys. Lett. 86 (2005) 052503. **https://doi.org/10.1063/1.1851618**.

[85] J. Philip, A. Punnoose, B. Kim, K. Reddy, S. Layne, J. Holmes, B. Satpati, P. Leclair, T. Santos, and J. Moodera, Carrier-controlled ferromagnetism in transparent oxide semiconductors, Nat. Mater. 5 (2006) 298. **https://doi.org/10.1038/nmat1613**.

[86] N. H. Hong, J. Sakai, N. T. Huong, A. Ruyter, and V. Brizé, Magnetism in transition-metal-doped In_2O_3 thin films, J. Condens. Matter Phys. 18 (2006) 6897. **https://doi.org/10.1088/0953-8984/18/29/027**.

[87] G. Peleckis, X. Wang, and S. X. Dou, High temperature ferromagnetism in Ni-doped In_2O_3 and indium-tin oxide, Appl. Phys. Lett. 89 (2006) 022501. **https://doi.org/10.1063/1.2220529**.

[88] J. Stankiewicz, F. Villuendas, and J. Bartolomé, Magnetic behavior of sputtered Co-doped indium-tin oxide films, Phys. Rev. B 75 (2007) 235308. **https://doi.org/10.1103/PhysRevB.75.235308**.

[89] A. Tiwari, V. M. Bhosle, S. Ramachandran, N. Sudhakar, J. Narayan, S. Budak, and A. Gupta, Ferromagnetism in Co doped CeO_2: Observation of a giant magnetic moment with a high Curie temperature, Appl. Phys. Lett. 88 (2006) 142511. **https://doi.org/10.1063/1.2193431**.

[90] B. Vodungbo, Y. Zheng, F. Vidal, D. Demaille, V. H. Etgens, and D. H. Mosca, Room temperature ferromagnetism of Co doped $CeO_{2-\delta}$ diluted magnetic oxide: Effect of oxygen and anisotropy, Appl. Phys. Lett. 90 (2007) 062510. **https://doi.org/10.1063/1.2472520**.

[91] A. Thurber, K. M. Reddy, and A. Punnoose, High-temperature magnetic-field-induced activation of room-temperature ferromagnetism in $Ce_{1-x}Ni_xO_2$, J. Appl. Phys. 101 (2007) 09N506. **https://doi.org/10.1063/1.2709413**.

[92] G. H. Jonker, and J. H. Van Santen, Ferromagnetic compounds of manganese with perovskite structure, Physica 16 (1950) 337. **https://doi.org/10.1016/0031-8914(50)90033-4**.

[93] J. B. Goodenough, A. Wold, R. J. Arnot, and N. Menyuk, Relationship Between Crystal Symmetry and Magnetic Properties of Ionic Compounds Containing Mn^{3+}, Phys. Rev. 124 (1961) 373. **https://doi.org/10.1103/PhysRev.124.373**.

[94] C. Zener, Interaction between the d-Shells in the Transition Metals. II. Ferromagnetic Compounds of Manganese with Perovskite Structure, Phys. Rev. 82 (1951) 403. **https://doi.org/10.1103/PhysRev.82.403**.

[95] C. Zener, Interaction Between the d Shells in the Transition Metals, Phys. Rev. 81 (1951) 440. **https://doi.org/10.1103/PhysRev.81.440**.

[96] M. A. Ruderman, and C. Kittel, Indirect Exchange Coupling of Nuclear Magnetic Moments by Conduction Electrons, Phys. Rev. 96 (1954) 99. **https://doi.org/10.1103/PhysRev.96.99**.

[97] P. Bruno, and C. Chappert, Oscillatory Coupling between Ferromagnetic Layers Separated by a Nonmagnetic Metal Spacer, Phys. Rev. Lett. 67 (1991) 2592. **https://doi.org/10.1103/PhysRevLett.67.1602**.

[98] R. Skomski, J. Zhou, J. Zhang, and D. Sellmyer, Indirect exchange in dilute magnetic semiconductors, J. Appl. Phys. 99 (2006) 08D504. **https://doi.org/10.1063/1.2159394**.

[99] H. Tompkins, and E. A. Irene, Handbook Of Ellipsometry, William Andrew, (2005).

[100] L D Landau, L. P. Pitaevskii, and E. M. Lifshitz, Electrodynamics of Continuous Media, 2nd Ed 8 (1984).

[101] H. Ehrenreich, and H. R. Philips, Optical Properties of Ag and Cu, Phys. Rev. 128 (1962) 1622. **https://doi.org/10.1103/PhysRev.128.1622**.

[102] F. Wooten, Optical properties of solids, Academic press, New York (1972).

[103] H. J. Goldsmid, Introduction to Thermoelectricity, Springer Series in Materials Science 121 (2010).

[104] T. M. Tritt, Thermoelectric Phenomena, Materials, and Applications, Annu. Rev. Mater. Res. 41 (2011). **https://doi.org/10.1146/annurev-matsci-062910-100453**.

[105] J. R. Sootsman, D. Y. Chung , and M. G. Kanatzidis, New and Old Concepts in Thermoelectric Materials, Angew. Chem. Int. Ed. Engl. 48 (2009) 8616. **https://doi.org/10.1002/anie.200900598**.

[106] D. M. Rowe, and C. M. Bhandari, Modern Thermoelectrics, Holt, Rinehart and Winston (1983).

[107] P. Singh, and S. K. Shukla, Advances in polyaniline-based nanocomposites, J. Mater. Sci. 55 (2020) 1331. **https://doi.org/10.1007/s10853-019-04141-z**.

[108] K. Uchida, M. Murata, A. Miura, and R. Iguchi, Observation of the Magneto-Thomson Effect, Phys. Rev. Lett. 125 (2020) 106601. **https://doi.org/10.1103/PhysRevLett.125.106601**.

[109] D. M. Chapin, C. S. Fuller, and G. L. Pearson, A New Silicon p-n Junction Photocell for Converting Solar Radiation into Electrical Power, J. Appl. Phys. 25 (1954) 676. **https://doi.org/10.1063/1.1721711**.

[110] R. L. Easton, and M. J. Votaw, Vanguard I IGY Satellite (1958 Beta), Rev. Sci. Instrum. 30 (1959) 70. **https://doi.org/10.1063/1.1716492**.

[111] C. Lerouge, Recherche and Industrie Photovoltaïque (PV) aux Etats-Unis, Sciences physique. États-Unis (2006).

[112] J. C. MULLER, Électricité photovoltaïque - Principes, Techniques de l'Ingénieur, BE8578, (2007).

[113] S. Teske, and G. Masson, Solar generation 6. Solar photovoltaic electricity empowering the world, European Photovoltaic Industry Association EPIA (2011).

[114] S. A. Wolf, D. D. Awschalom, R. A. Buhrman, J. M. Daughton, S. V. Molnar, M. L. Roukes, A. Y. Chtchelkanova, and D. M. Treger, Spintronics: a spin-based electronics vision for the future, Science 294 (2001) 1488. **https://doi.org/10.1126/science.1065389**.

[115] M. Hammi, O. El Rhazouani, M. Arejdal, and A. Slassi, Ab initio study of semiclassic transport coefficients of SnO_2 thermoelectric material, Chin. J. Phys. 55 (2017) 187. **https://doi.org/10.1016/j.cjph.2016.10.016**.

[116] S. R. Shieh, A. Kubo, T. S. Duffy, V. B. Prakapenka, and G. Shen, High-pressure phases in SnO_2 to 117 GPa, Phys. Rev. B 73 (2006) 014105. **https://doi.org/10.1103/PhysRevB.73.014105**.

[117] A. A. Bolzan, C. Fong, B. J. Kennedy, and C. J. Howard, Structural Studies of Rutile-Type Metal Dioxides, Acta Cryst. B 53 (1997) 373. **https://doi.org/10.1107/S0108768197001468**.

[118] G. K. H. Madsen, P. Blaha, K. Schwarz, E. Sjostedt, and L. Nordstrom, Efficient linearization of the augmented plane-wave method, Phys. Rev. B 64 (2001) 195134. **https://doi.org/10.1103/PhysRevB.64.195134**.

[119] Y. Zhang, and W. Yang, Comment on "Generalized Gradient Approximation Made Simple", Phys. Rev. Lett. 80 (1998) 890. **https://doi.org/10.1103/PhysRevLett.80.890**.

[120] P. E. Blochl, O. Jepsen, and O. K. Andersen, Improved tetrahedron method for Brillouin-zone integrations, Phys. Rev. B 49 (1994) 16223. **https://doi.org/10.1103/PhysRevB.49.16223**.

[121] F. D. Murnaghan, The Compressibility of Media under Extreme Pressures, Proc Natl Acad Sci U S A 30 (1944) 244. **https://doi.org/10.1073/pnas.30.9.244**.

[122] D. P. Rai, A. Laref, A. Shankar, A. P. Sakhya, R. Khenata, and R. K. Thapa, Spin-induced transition metal (TM) doped SnO_2 a dilute magnetic semiconductor (DMS): A first principles study, J. Phys. Chem. Solids 120 (2018) 104. **https://doi.org/10.1016/j.jpcs.2018.04.006**.

[123] M. A. Maki-Jaskari, and T. T. Rantala, Band structure and optical parameters of the SnO_2 (110) surface, Phys. Rev. B 64 (2001) 075407. **https://doi.org/10.1103/PhysRevB.64.075407**.

[124] A. F. Lamrani, M. Belaiche, A. Benyoussef, and A. El Kenz, Electronic structures and ferromagnetism of SnO_2 (rutile) doped with double-impurities: First-principles calculations, J. Appl. Phys. 115 (2014) 013910. **https://doi.org/10.1063/1.4852475**.

[125] M. Batzill, and U. Diebold, The surface and materials science of tin oxide, Prog. Surf. Sci. 79 (2005) 47. **https://doi.org/10.1016/j.progsurf.2005.09.002**.

[126] J. Themlin, R. Sporken, J. Darville, R. Caudano, J. Gilles, and R. Johnson, Resonant-photoemission study of SnO_2: Cationic origin of the defect band-gap states, Phys Rev B Condens Matter. 42 (1990) 11914. **https://doi.org/10.1103/PhysRevB.42.11914**.

[127] M. Fox, Optical Properties of Solids, Oxford: Oxford Univ. Press (2008).

[128] Md. Afjalur Rahman, Md. Zahidur Rahaman, and Md. Atikur Rahman, The structural, elastic, electronic and optical properties of MgCu under pressure: A first-principles study, Int. J. Mod. Phys. B 30 (2016) 1650199. **https://doi.org/10.48550/arXiv.1510.02020**.

[129] T. Serin, N. Serin, S. Karadeniz, H. Sari, N. Tugluoglu, and O. Pakma, Electrical, structural and optical properties of SnO_2 thin films prepared by spray pyrolysis, J. Non-Cryst. Solids 352 (2006) 209. **https://doi.org/10.1016/j.jnoncrysol.2005.11.031**.

[130] P. Saikia, A. Borthakur, and P. K. Saikia, Structural, optical and electrical properties of tin oxide thin film deposited by APCVD method, Indian J. Phys. 85 (2011) 551. **https://doi.org/10.1007/s12648-011-0058-y**.

[131] L. Yanlu, F. Weiliu, S. Honggang, C. Xiufeng, L. Pan, Z. Xian, H. Jingcheng, and J. Minhua, Optical properties of the high-pressure phases of SnO_2: first-principles calculation, J. Phys. Chem. A 114 (2010) 1052. **https://doi.org/10.1021/jp909021r**.

[132] G. K. H. Madsen, J. Carrete, and M. J. Verstraete, BoltzTraP2, a program for interpolating band structures and calculating semi-classical transport coefficients, Comput. Phys. Commun. 231 (2018) 140. **https://doi.org/10.1016/j.cpc.2018.05.010**.

[133] B. Ryu, and M. Oh, Computational Simulations of Thermoelectric Transport Properties, J. Korean Ceram. Soc. 53 (2016) 273. **https://doi.org/10.4191/kcers.2016.53.3.273**.

[134] G. J. Snyder, and E. S. Toberer, Complex thermoelectric materials, Mater. sci. eng. (2010) 101. **https://doi.org/10.1038/nmat2090**.

[135] H. A. Rahnamaye Aliabad, and M. Kheirabadi, Thermoelectricity and superconductivity in pure and doped Bi_2Te_3 with Se, Physica B Condens. Matter. 433 (2014) 157. **https://doi.org/10.1016/j.physb.2013.10.035**.

[136] I. Ohkubo, and T. Mori, Origin of Projected Excellent Thermoelectric Transport Properties in d0-Electron AMN_2 (A = Sr or Ba; M = Ti, Zr, Hf) Layered Complex Metal Nitrides, Eur. J. Inorg. Chem. 2015 (2015) 3715. **https://doi.org/10.1002/ejic.201500350**.

[137] I. Ohkubo, and T. Mori, Anisotropic Anomalies of Thermoelectric Transport Properties and Electronic Structures in Layered Complex Nitrides AMN_2 (A = Na, Cu; M = Ta, Nb), Chem. Mater. 27 (2015) 7265. **https://doi.org/10.1021/acs.chemmater.5b02015**.

[138] J. -H. Park, E. Vescovo, H. -J. Kim, C. Kwon, R. Ramesh, and T. Venkatesan, Direct evidence for a half-metallic ferromagnet, Nature 392 (1998) 794. **https://doi.org/10.1038/33883**.

[139] W. E. Pickett, and J. S. Moodera, Half Metallic Magnets, Phys. Today. 54 (2001) 39. **https://doi.org/10.1063/1.1381101**.

[140] X. Sun, R. Asadpour, W. Nie, A. D. Mohite, and M. A. Alam, A Physics-Based Analytical Model for Perovskite Solar Cells, IEEE J. Photovolt. 6 (2016) 1390. **https://doi.org/10.48550/arXiv.1505.05132**.

[141] L. Rakocevic, R. Gehlhaar, T. Merckx, W. Qiu, U. W. Paetzold, H. Fledderus, and J. Poortmans, Loss Analysis in Perovskite Photovoltaic Modules, IEEE J. Photovolt. 7 (2016) 404. **https://doi.org/10.1002/solr.201900338**.

[142] G. J. Snyder, and E. S. Toberer, Complex thermoelectric materials, Nat. Mater. 7 (2008) 105. **https://doi.org/10.1038/nmat2090**.

[143] B. G. Levi, Simple compound manifests record-high thermoelectric performance, Phys. Today, 67 (2014) 14. **https://doi.org/10.1038/srep09567**.

[144] X. Zhang, and L.-D. Zhao, Thermoelectric materials: Energy conversion between heat and electricity, J. Materiomics 1 (2015) 92. **https://doi.org/10.1016/j.jmat.2015.01.001**.

[145] A. D. LaLonde, Y. Pei, H. Wang, and G. J. Snyder, Lead telluride alloy thermoelectrics, Mater. Today 14 (2011) 526. **https://doi.org/10.1016/S1369-7021(11)70278-4**.

[146] B. G. Yalcin, S. Bagci, M. Ustundag, and M. Aslan, Electronic and optical properties of BBi and AlBi: Hybrid (YS-PBE0) function, Comput. Mater., Sci. 98 (2015) 136. **https://doi.org/10.1016/j.commatsci.2014.11.010**.

[147] A. H. MacDonald, W. E. Picket, and D. D. Koelling, A linearised relativistic augmented-plane-wave method utilising approximate pure spin basis functions, J. Solid State Phys. 13 (1980) 2675. **https://doi.org/10.1088/0022-3719/13/14/009**.

[148] J. P. Garzón López, R. Cardona, A. S. Santos, D. A. Landínez Téllez, J. Roa-Rojas, Crystallographic and electronic structure of the Ca_2TiMnO_6 double perovskite, Physica B Condens. Matter. 455 (2014) 53. **https://doi.org/10.1016/j.physb.2014.07.044**.

[149] J. P. Perdew, A. Ruzsinszky, G. I. Csonka, O. A. Vydrov, G. E. Scuseria, L. A. Constantin, X. Zhou, and K. Burke, Restoring the Density-Gradient Expansion for Exchange in Solids and Surfaces, Phys. Rev. Lett. 100 (2008) 136406. **https://doi.org/10.1103/PhysRevLett.100.136406**.

[150] R. O. Burgos, D. Martinez, C. A. P. Vargas, D. A. Landínez Téllez, E. V. Lopez, A. S. Santos, and J. Roa-Rojas, Magnetic and ferroelectric response of Ca_2TiMnO_6 manganite-like perovskite, J. Rev. Mex. de Fis. 58 (2012) 44.

[151] G. Tsea, and D. Yu, The electronic and structural properties in Ca_2TiMnO_6 double perovskite: The first principle study, Comput. Condens. Matter 9 (2016) 35. **https://doi.org/10.1016/j.cocom.2016.09.002**.

[152] G. Murtaza, I. Ahmad, and A. Afaq, Shift of indirect to direct bandgap in going from K to Cs in $MCaF_3$ (M = K, Rb, Cs), Solid State Sci. 16 (2013) 152. **https://doi.org/10.1016/j.solidstatesciences.2012.10.002**.

[153] H. A. R. Aliabad, M. Ghazanfari, I. Ahmad, and M. A. Saeed, Ab initio calculations of structural, optical and thermoelectric properties for $CoSb_3$ and ACo_4Sb_{12} (A= La, Tl and Y) compounds, Comput. Mater. Sci. 65 (2012) 509. **https://doi.org/10.1016/j.commatsci.2012.08.013**.

[154] G. K. H. Madsen, Automated Search for New Thermoelectric Materials: The Case of LiZnSb, J. Am. Chem. Soc. 128 (2006) 12140. **https://doi.org/10.1021/ja062526a**.

[155] H. A. R. Aliabad, and Z. Parvizi, Structural, electronical and thermal properties of XVO_4 (X = Y, Gd) vanadate crystals, Comput. Mater. Sci. 93 (2014) 125. **https://doi.org/10.1016/j.commatsci.2014.06.025**.

[156] M. Acharya, and T. Maiti, Effect of bismuth doping on thermoelectric properties of Sr_2TiCoO_6, Ferroelectrics 532 (2018) 28. **https://doi.org/10.1080/00150193.2018.1430432**.

[157] M. Saxena, and T. Maiti, Compositional modification of Sr_2TiCoO_6 double perovskites by Mo and La for high temperature thermoelectric applications, Ceram. Int. 44 (2018) 2732. **https://doi.org/10.1016/j.ceramint.2017.11.003**.

[158] M. S. Sudha, K. Balani, and T. Maiti, Structure and thermoelectric properties of calcium doped Sr_2TiCoO_6 double perovskites, Mater. Sci. Eng. B 244 (2019) 65. **https://doi.org/10.1016/j.mseb.2019.04.025**.

[159] S. Haid, W. Benstaali, A. Abbad, B. Bouadjemi, S. Bentata, and Z. Aziz, Thermoelectric, Structural, Optoelectronic and Magnetic properties of double perovskite Sr_2CrTaO_6: First principle Study, Mater. Sci. Eng. B 245 (2019) 68. **https://doi.org/10.1016/j.mseb.2019.05.013**.

[160] P. Roy, V. Waghmare, and T. Maiti, Environmentally friendly $Ba_xSr_{2-x}TiFeO_6$ double perovskite with enhanced thermopower for high temperature thermoelectric power generation, RSC Adv. 6 (2016) 54636. **https://doi.org/10.1039/C6RA09629H**.

[161] P. Roy, I. Bose, and T. Maiti, Synthesis and characterization of Sr_2TiMoO_6 (M = Fe,Co) double perovskites for high temperature thermoelectric applications, Integr. Ferroelectr. 174 (2016) 34. **https://doi.org/10.1080/10584587.2016.1190253**.

[162] B. Rameshe, M. Rajagopalan, and B. Palanivel, Electronic structure, structural phase stability, optical and thermoelectric properties of $Sr_2AlM'O_6$ (M' = Nb and Ta) from first principle calculations, Comput. Condens. Matter 4 (2015) 13. **https://doi.org/10.1016/j.cocom.2015.03.003**.

[163] F. Aslam, B. Sabir, and M. Hassan, Structural, electronic, optical, thermoelectric, and transport properties of indium-based double perovskite halides Cs_2InAgX_6 (X=Cl, Br, I) for energy applications, Appl. Phys. A 127 (2021) 1. **https://doi.org/10.1007/s00339-020-04178-x**.

[164] L. F. Blaha, A. Maafa, H. Rozale, A. Chahed, M. A. H. Boukli, and A. Sayade, The first principle calculations of structural, magneto-electronic, elastic, mechanical, and thermoelectric properties of half-metallic double perovskite oxide Sr_2TiCoO_6, Rev. Mexic. Fisica 67 (2021) 114. **https://doi.org/10.31349/RevMexFis.67.114**.

[165] S. A. Dar, R. Sharma, V. Srivastava, and U. Kumar Sakalle, Investigation on the electronic structure, optical, elastic, mechanical, thermodynamic and thermoelectric properties of wide band gap semiconductor double perovskite Ba_2InTaO_6, RSC Adv. 9 (2019) 9522. **https://doi.org/10.1039/C9RA00313D**.

[166] J. H. Park, S. K. Kwon, and B. I. Min, Half-metallic antiferromagnetic double perovskites: $LaAVRuO_6$ (A=Ca, Sr, and Ba), Phys. Rev. B 65 (2002) 174401. **https://doi.org/10.1103/PhysRevB.65.174401**.

[167] H. van Leuken, and R. A. de Groot, Half-Metallic Antiferromagnets, Phys. Rev. Lett. 74 (1995) 1171. **https://doi.org/10.1103/PhysRevLett.74.1171**.

[168] W. E. Pickett, Single Spin Superconductivity, Phys. Rev. Lett. 77 (1996) 3185. **https://doi.org/10.1103/PhysRevLett.77.3185**.

[169] W. E. Pickett, Spin-density-functional-based search for half-metallic antiferromagnets, Phys. Rev. B 57 (1998) 10613. **https://doi.org/10.1103/PhysRevB.57.10613**.

[170] C. J. Bartel, C. Sutton, B. R. Goldsmith, R. Ouyang, C. B. Musgrave, L. M. Ghiringhelli, and M. Scheffler, New tolerance factor to predict the stability of perovskite oxides and halides, Sci. Adv. 5 (2019) eaav0693. **https://doi.org/10.1126/sciadv.aav0693**.

[171] A. E. Fedorovskiy, N. A. Drigo, and M. K. Nazeeruddin, The Role of Goldschmidt's Tolerance Factor in the Formation of A_2BX_6 Double Halide Perovskites and its Optimal Range, Small Methods 4 (2020) 1900426. **https://doi.org/10.1002/smtd.201900426**.

[172] S. Nazir, and Qurat-Ul-Ain, Impact of uniaxial strain on the electronic and magnetic properties of Sr_2CrReO_6, J. Alloys Compd. 847 (2020) 155906. **https://doi.org/10.1016/j.jallcom.2020.155906**.

[173] C. Q. Tang, Y. Zhang, and J. Dai, Electronic and magnetic structure studies of double perovskite Sr_2CrReO_6 by first-principles calculations, Solid State Commun. 133 (2005) 219. **https://doi.org/10.1016/j.ssc.2004.11.006**.

[174] G. Vaitheeswaran, V. Kanchana, and A. Delin, Pseudo-half-metallicity in the double perovskite Sr_2CrReO_6 from density-functional calculations, Appl. Phys. Lett. 86 (2005) 032513. **https://doi.org/10.1063/1.1855418**.

[175] G. Vaitheeswaran, V. Kanchana, and A. Delin, Electronic structure of the ferromagnetic double-perovskites Sr_2CrReO_6, Sr_2CrWO_6, and Ba_2FeReO_6, J Phys. Conf. Ser. 29 (2006) 50. **https://doi.org/10.1088/1742-6596/29/1/008**.

[176] H. Kato, T. Okuda, Y. Okimoto, Y. Tomioka, K. Oikawa, T. Kamiyama, and Y. Tokura, Structural and electronic properties of the ordered double perovskites A_2MReO_6 (A=Sr,Ca; M=Mg,Sc,Cr,Mn,Fe,Co,Ni,Zn), Phys. Rev. B 69 (2004) 184412. **https://doi.org/10.1103/PhysRevB.69.184412**.

[177] P. Majewski, S. Geprägs, O. Sanganas, M. Opel, R. Gross, F. Wilhelm, A. Rogalev, and L. Alff, X-ray magnetic circular dichroism study of Re 5d magnetism in Sr_2CrReO_6, Appl. Phys. Lett. 87 (2005) 202503. **https://doi.org/10.1063/1.2131178**.

[178] P. Majewski, S. Geprägs, A. Boger, M. Opel, A. Erb, R. Gross, G. Vaitheeswaran, V. Kanchana, A. Delin, F. Wilhelm, A. Rogalev, and L. Alff, Magnetic moments of W 5d in Ca_2CrWO_6 and Sr_2CrWO_6 double perovskites, Phys. Rev. B 72 (2005) 132402. **https://doi.org/10.1103/PhysRevB.72.132402**.

[179] A. Winkler, N. Narayanan, D. Mikhailova, K.G. Bramnik, H. Ehrenberg, H. Fuess, G. Vaitheeswaran, V. Kanchana, F. Wilhelm, A. Rogalev, A. Kolchinskaya, and L. Alff, Magnetism in Re-based ferrimagnetic double perovskites, New J. Phys. 11 (2009) 073047. **https://doi.org/10.1088/1367-2630/11/7/073047**.

[180] T. K. Mandal, C. Felser, M. Greenblatt, and J. Kübler, Magnetic and electronic properties of double perovskites and estimation of their Curie temperatures by ab initio calculations, Phys. Rev. B 78 (2008) 134431. **https://doi.org/10.1103/PhysRevB.78.134431**.

[181] S.A. Khandy, and D. C. Gupta, Electronic structure, magnetism and thermoelectricity in layered perovskites: Sr_2SnMnO_6 and Sr_2SnFeO_6, J. Magn. Magn. Mater. 441 (2017) 166. **https://doi.org/10.1016/j.jmmm.2017.05.058**.

[182] T. Takeuchi, Conditions of Electronic Structure to Obtain Large Dimensionless Figure of Merit for Developing Practical Thermoelectric Materials, Mater Trans. 50 (2009) 2359. **https://doi.org/10.2320/matertrans.M2009143**.

[183] V. K. Sangwan, and M. C. Hersam, Electronic Transport in Two-Dimensional Materials, Annu. Rev. Phys. Chem. 69 (2018) 299. **https://doi.org/10.1146/annurev-physchem-050317-021353**.

[184] J. Liu, Q. Ma, Z. Huang, G. Liu, and H. Zhang, Recent Progress in Graphene-Based Noble-Metal Nanocomposites for Electrocatalytic Applications, Adv. Mater. 31 (2019) 1800696. **https://doi.org/10.1002/adma.201800696**.

[185] M. Liu, P. A. Gurr, Q. Fu, P. A. Webley, and G. G. Qiao, Two-dimensional nanosheet-based gas separation membranes, J. Mater. Chem. 6 (2018) 23169. **https://doi.org/10.1039/C8TA09070J**.

[186] C. Tan, X. Cao, X.-J. Wu, Q. He, J. Yang, X. Zhang, J. Chen, W. Zhao, S. Han, G.-H. Nam, M. Sindoro, and H. Zhang, Recent Advances in Ultrathin Two-Dimensional Nanomaterials, Chem. Rev. 117 (2017) 6225. **https://doi.org/10.1021/acs.chemrev.6b00558**.

[187] A. L. Schoenhalz, J. T. Arantes, A. Fazzio, and G. M. Dalpain, Surface magnetization in non-doped ZnO nanostructures, Appl. Phys. Lett. 94 (2009) 162503. **https://doi.org/10.1063/1.3119640**.

[188] Y. Li, X. Zhao, and W. Fan, Structural, Electronic, and Optical Properties of Ag-Doped ZnO Nanowires: First Principles Study, J. Phys. Chem. C 115 (2011) 3552. **https://doi.org/10.1021/jp1098816**.

[189] H .K. Hong, J. Jo, D. Hwang, J. Lee, N. Y. Kim, S. Son, J. H. Kim, M.J. Jin, Y. C. Jun, R. Erni, S. K. Kwak, J. W. Yoo, and Z. Lee, Atomic Scale Study on Growth and Heteroepitaxy of ZnO Monolayer on Graphene, Nano Lett. 17 (2017) 120. **https://doi.org/10.1021/acs.nanolett.6b03621**.

[190] S. J. Pearton, D. P. Norton, K. Lp, Y. W. Heo, and T. Steiner, Recent progress in processing and properties of ZnO, Prog. Mater. Sci. 50 (2005) 293. **10.1016/j.pmatsci.2004.04.001**.

[191] B. Rakshit, and P. Mahadevan, Indirect to direct bandgap transition under uniaxial strain in layered ZnO, Appl. Phys. Lett. 102 (2013) 143116. **https://doi.org/10.1063/1.4801314**.

[192] F. Li, C. Zhang, and M. Zhao, Magnetic and optical properties of Cu-doped ZnO nanosheet: First-principles calculations, Phys. E: Low-Dimens. Syst. Nanostructures. 53 (2013) 101. **https://doi.org/10.1016/j.physe.2013.04.026**.

[193] W. X. Zhang, T. Li, C. He, X. L. Wu, L. Duan, H. Li, L. Xu, and S. B. Gong, First-principle study on Ag-2N heavy codoped of p-type graphene-like ZnO nanosheet, Solid State Commun. 204 (2015) 47. **https://doi.org/10.1016/j.ssc.2014.12.014**.

[194] T. M. Schmidt, R. H. Miwa, and A. Fazzio, Ferromagnetic coupling in a Co-doped graphenelike ZnO sheet, Phys. Rev. B 81 (2010) 195413. **https://doi.org/10.1103/PhysRevB.81.195413**.

[195] C. Tusche, H. L. Meyerheim, and J. Kirschner, Observation of Depolarized ZnO(0001) Monolayers: Formation of Unreconstructed Planar Sheets, Phys. Rev. Lett. 99 (2007) 026102. **https://doi.org/10.1103/PhysRevLett.99.026102**.

[196] P. Blaha, K. Schwarz, G.K.H. Madsen, D. Kvasnicka, J. Luitz, R. LasKowsk, F. Tran, and L. Marks, WIEN2k: An Augmented Plane Wave Plus Local Orbitals Program for Calculating Crystal Properties, (2019).

[197] K. Schwarz, P. Blaha, and G. K. H. Madsen, Electronic structure calculations of solids using the WIEN2k package for material sciences, Comput. Phys. Commun. 147 (2002) 71. **https://doi.org/10.1016/S0010-4655(02)00206-0**.

[198] H. J. Monkhorst, and J. D. Pack, Special points for Brillouin-zone integrations, Phys. Rev. B 13 (1976) 5188. **https://doi.org/10.1103/PhysRevB.13.5188**.

[199] M. Khuili, N. Fazouan, H. Abou El Makarim, E. H. Atmani, M. Houmad, Improvement of optical properties of Mg doped ZnO by nanostructuring for applications in optoelectronics, Mater. Res. Express 7 (2020) 025043. **https://doi.org/10.1088/2053-1591/ab748b**.

[200] D. Q. Fang, A. L. Rosa, R. Q. Zhang, and T. Frauenheim, Theoretical Exploration of the Structural, Electronic, and Magnetic Properties of ZnO Nanotubes with Vacancies, Antisites, and Nitrogen Substitutional Defects, J. Phys. Chem. C 114 (2010) 5760. **https://doi.org/10.1021/jp909937u**.

[201] M. Topsakal, S. Cahangirov, E. Bekaroglu, and S. Ciraci, First-principles study of zinc oxide honeycomb structures, Phys. Rev. B 80 (2009) 235119. **https://doi.org/10.1103/PhysRevB.80.235119**.

[202] X. Y. Feng, Z. Wang, C. W. Zhang, and P. J. Wang, Electronic Structure and Energy Band of IIIA Doped Group ZnO Nanosheets, J. Nanomater. 6 (2013). **https://doi.org/10.1155/2013/181979**.

[203] M. Khuili, N. Fazouan, H. A. E. Makarim, G. El Halani, E. Atmani, Comparative first principles study of ZnO doped with group III elements, J. Alloys Compd. 688 (2016) 368. **https://doi.org/10.1016/j.jallcom.2016.06.29**.

[204] C. Shi, H. Qin, Y. Zhang, J. Hu, and L. Ju, Magnetic properties of transition metal doped AlN nanosheet: First-principle studies, J. Appl. Phys. 115 (2014) 053907. **https://doi.org/10.1063/1.4864262**.

[205] H. Şahin, S. Cahangirov, M. Topsakal, E. Bekaroglu, E. Akturk, R. T. Senger, and S. Ciraci, Monolayer honeycomb structures of group-IV elements and III-V binary compounds: First-principles calculations, Phys. Rev. B 80 (2009) 155453. **https://doi.org/10.1103/PhysRevB.80.155453**.

[206] C. W. Zhang, F. B. Zheng, P. J. Wang, F. Li, and P. Li, First-principles study on ferromagnetism in two-dimensional ZnO nanosheet, Chem. Phys. Lett. 548 (2012) 60. **https://doi.org/10.1021/jp2104177**.

[207] F. B. Zheng, C. W. Zhang, P. J. Wang, and H. X. Luan, Tuning the electronic and magnetic properties of carbon-doped ZnO nanosheets: First-principles prediction, J. Appl. Phys. 111 (2012) 044329. **https://doi.org/10.1063/1.3688233**.

[208] X. Wang, X. Chen, R. Dong, Y. Huang, and W. Liu, Ferromagnetism in carbon-doped ZnO films from first-principle study, Phys. Lett. A 373 (2009) 3091. **https://doi.org/10.1016/J.PHYSLETA.2009.06.049**.

[209] A. F. Lamrani, Ferromagnetic alloy for high-efficiency photovoltaic conversion in solar cells: first-principles insights when doping SnO_2 rutile with coupled Eu-Gd, RSC Adv. 11 (2021) 7096. **https://doi.org/10.1039/D1RA00088H**.

[210] L. Lin, R. Chen, C. He, H. Tao, J. Huang, L. Zhu, L. Yan, and J. Zhang, Magnetic and optical properties of (Mn, Co) co-doped SnO_2, Vacuum 182 (2020) 109681. **https://doi.org/10.1016/j.vacuum.2020.109681**.

[211] S. S. Nair, L. Krishnia, A. Trukhanov, P. Thakur, and A. Thakur, Prospect of double perovskite over conventional perovskite in photovoltaic applications, Ceram. Int. 48 (2022) 34128. **https://doi.org/10.1016/j.ceramint.2022.08.184**.

[212] G. Longo, S. Mahesh, L. R. V. Buizza, A. D. Wright, A. J. Ramadan, M. Abdi-Jalebi, P. K. Nayak, L. M. Herz, H. J. Snaith, Understanding the Performance Limiting Factors of $Cs_2AgBiBr_6$ Double-Perovskite Solar Cells, ACS Energy Lett. 5 (2020) 2200. **https://doi.org/10.1021/acsenergylett.0c01020**.

[213] M. Kumar, A. Raj, A. Kumar, A. Anshul, Theoretical evidence of high power conversion efficiency in double perovskite solar cell device, Opt. Mater. 111 (2021) 110565. **https://doi.org/10.1016/j.optmat.2020.110565**.

[214] A. Soni, K. C. Bhamu, and J. Sahariya, Investigating effect of strain on electronic and optical properties of lead free double perovskite $Cs_2AgInCl_6$ solar cell compound: A first principle calculation, J. Alloys Compd. 817 (2020) 152758. **https://doi.org/10.1016/j.jallcom.2019.152758**.